Spallation Neutron Source
Accumulator Ring and Transport
Design Manual

(DRAFT; June 2, 2003)

Preface

This document describes the design of the accumulator ring and the transport lines of the Spallation Neutron Source Project.

Contents

Figure 1: Layout of the Spallation Neutron Source.

1 Overview

1.1 Introduction

The Spallation Neutron Source (SNS) project is designed to reach an average beam power above 1.4 MW for pulsed neutron production (Fig. 1). The accelerator system operates at a repetition rate of 60 Hz and an average current of 1.6 mA. It consists of an H^- RF volume source of 48 mA peak current at 6% duty, a low-energy beam transport (LEBT) housing a first-stage beam chopper with ±20 ns rise/fall time; a 402.5 MHz, 4-vane radio-frequency-quadrupole (RFQ); a medium-energy beam transport (MEBT) housing a second-stage chopper ($< \pm 10$ ns rise/fall), an adjustable beam-halo scraper, diagnostics devices, and matching quadrupoles; a 402.5 MHz, 6-tank drift-tube-linac (DTL) with permanent-magnet quadrupoles; a 805 MHz, 4-module coupled-cavity-linac (CCL); a 805 MHz, superconducting RF (SRF) linac of medium- and high-β cavities accelerating the beam to the full energy; a high-energy beam transport (HEBT) for diagnostics, transverse and longitudinal collimation, matching, energy correction and painting; and an accumulator ring compressing the 1 GeV, 1 ms pulse to 650 ns for delivery onto the target through a ring-target beam transport (RTBT).

Table 1 lists major parameters.

Table 1.1 shows evolution of beam parameters during the cycle including expected energy, horizontal (H), vertical (V), and longitudinal (L) acceptances and emittances, and controlled and uncontrolled beam losses.

Table 1: Spallation Neutron Source primary parameters.

Quantity	Value	Unit
Kinetic energy, E_k	1000	[MeV]
Uncertainty, ΔE_k (95%)	± 15	[MeV]
SRF cryo-module number	$11 + 12$	
SRF cavity number	$33 + 48$	
Peak field E_p ($\beta = 0.61$)	27.5	[MV/m]
ΔE_p ($\beta = 0.61$)	± 2.5	[MV/m]
Peak field E_p ($\beta = 0.81$)	35	[MV/m]
ΔE_p ($\beta = 0.81$)	$+2.5/-7.5$	[MV/m]
Beam power on target, P_{max}	1.4	[MW]
Pulse length on target	695	[ns]
Chopper beam-on duty factor [%]	68	
Linac macro pulse duty factor	6.0	[%]
Average macropulse H$^-$ current	26	[mA]
Linac average beam current	1.6	[mA]
Ring rf frequency	1.058	[MHz]
Ring injection time	1.0	[ms]
Ring bunch intensity	1.6	[10^{14}] per pulse
Ring space-charge tune spread	0.15	

Table 2: Beam parameter evolution across the SNS accelerators. The aperture and acceptance do not include scrapers and collimators. Notes are: a) corresponding to 27% chopped beam; b) corresponding to 5% chopped beam; c) beam loss on the transverse and momentum collimators; d) including total 4% of beam escaping foil and 0.2% beam loss on collimators; e) including 4% beam scattered on the target window; and f) corresponding to 20% beam loss averaged over RFQ length.

	LEBT	RFQ	MEBT	DTL	CCL	SRF 1	SRF 2	HEBT	Ring	RTBT	Unit
E_k (out)	0.065	2.5	2.5	86.8	185.6	387	1000	1000	1000	1000	MeV
Length	0.12	3.8	3.6	36.6	55.1	64.2	94.7	169.5	248.0	150.8	m
Peak current	47	38	38	38	38	38	38	38	9×10^4	9×10^4	mA
Min. trans. aperture		7	32	25	30	80	80	50	200		mm
Min. H acceptance			250	38	19	57	50	26	480	480	μm
H emit. out, $\epsilon_{un,rms}$	17	2.9	3.7	0.75	0.59	0.41	0.23	0.26	24	24	μm
Min. V acceptance			51	42	18	55	39	26	480	400	μm
V emit. out, $\epsilon_{un,rms}$	17	2.9	3.7	0.75	0.59	0.41	0.23	0.26	24	24	μm
Min. L acceptance			4.7	2.4	7.4	7.2	18		$19\times10^5/\pi$		$10^{-5}\pi$eVs
L emit. out, rms		7.6	10	12	14	17	23		$2\times10^7/\pi$		$10^{-7}\pi$eVs
Loss (control)	0.05[a]	N/A	0.2[b]	N/A	N/A	N/A	N/A	5[c]	62[d]	58[e]	kW
Loss (uncontroll)	70	100[f]	2	1	1	0.2	0.2	< 1	1	< 1	W/m
H emit. out, $\epsilon_{N,rms}$	0.2	0.21	0.27	0.33	0.39	0.41	0.41	0.46	44	44	μm
V emit. out, $\epsilon_{N,rms}$	0.2	0.21	0.27	0.33	0.39	0.41	0.41	0.46	44	44	μm

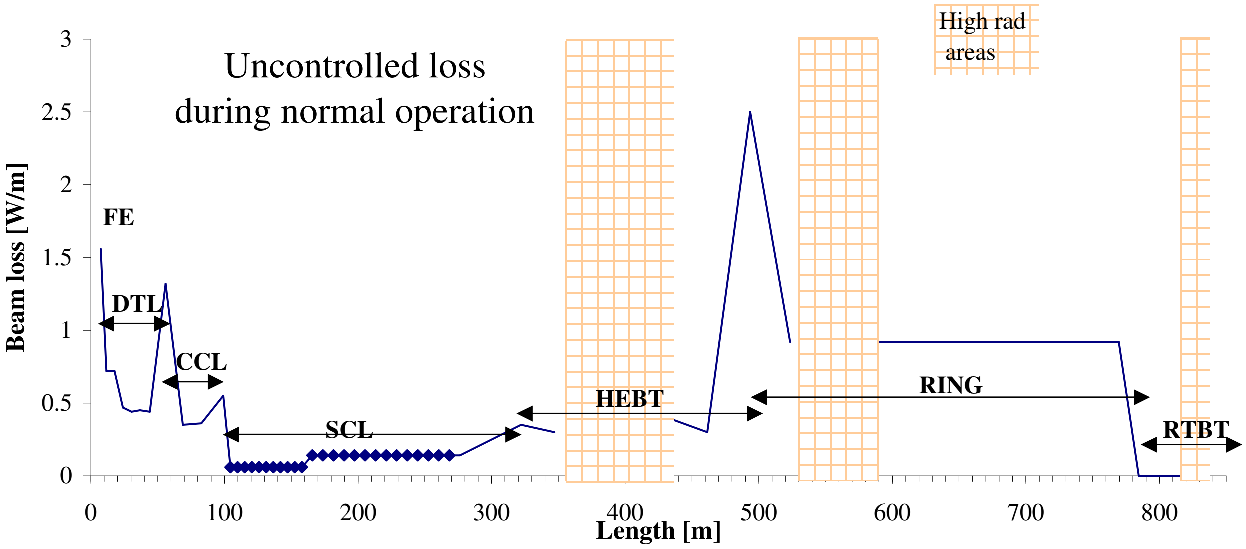

Figure 2: Expected beam loss across the SNS accelerator complex. The uncontrolled beam loss is at 1 W/m level.

1.2 Design Philosophy

The primary concern of building such a high-intensity accelerator is that radio-activation caused by excessive uncontrolled beam loss can limit the machine's availability and maintainability. Based on operational experiences, hands-on maintenance demands that the average uncontrolled beam loss does not exceed 1 W beam power per tunnel-meter. Uncontrolled mismatch upon change of linac structure, lattice, and frequency; 2) space-charge effects including envelope and parametric resonances and non-equipartition in the linac, and resonance crossing and instability enhancement in ring; 3) limited physical and momentum acceptance; 4) premature H^- and H^0 stripping and ring injection foil scattering; 5) magnetic errors, fringe fields, and misalignments; 6) instabilities (resistive impedances due to e.g. extraction kicker, and electron cloud); and 7) accidental loss due to system malfunction (ion source and linac, ring extraction kickers).

SNS addresses the above seven issues by adopting a low-loss design philosophy. Above all, foreseen losses are localized to shielded areas using 1) adjustable scrapers in the MEBT; 2) transverse and momentum collimators in the HEBT prior ring injection; 3) two-stage transverse collimation and momentum cleaning with beam-in-gap (BIG) kicker in the ring; 4) collimator protection in the RTBT, and 5) beam-gap cleaning with LEBT and MEBT choppers and ring BIG kicker (Fig. 2).

Emphasis is also put on machine's flexibility and reliability. The SRF linac allows operation with one failed cavity/klystron; the ring accepts ±5% variation in linac output energy; a wide ring tuning range avoids resonances; a robust injection allows independent horizontal, vertical, and longitudinal painting; adjustable collimation systems accommodate variable beam size; and design reserve and redundancy ensure a high availability (e.g., spare cryo-module for a quick replacement, power supplies compatible with 1.3 GeV energy, multi-foil exchange, spare kicker power supply (PFN), and aperture clearance for one-kicker failure).

Finally, the facility is designed with the potential to reach a beam energy up to 1.3 GeV and a beam power higher than 2 MW, capable of supplying a second neutron target. The higher energy can be reached by upgrading the superconducting RF cavity gradient and klystron power supplies, and by filling the presently unoccupied linac tunnel spaces with up to 9 additional cryo-modules. The ring is capable of accommodating the energy and power increase without extensive hardware change – space is reserved for two additional extraction kickers, and for the replacement of 2 injection-chicane dipoles to satisfy H^0 stripping conditions.

1.3 Performance Requirements

1.4 Interface Requirements

1.4.1 Linac/HEBT interface requirements

1.4.1.1 Introduction

The Linac, WBS 1.4, accelerates the H^- up to 1.0 GeV and delivers H^- to the High Energy Beam Transport (HEBT) line, WBS 1.5. This document deals with the interface between the Linac and HEBT including the functional interface with beam and the physical interface between systems.

1.4.1.2 Interface

The following are the interfaces between WBS 1.4 and WBS 1.5.

Functional:

1. Beam line elevation
2. H- beam
3. Vacuum system
4. RF signal interface
5. Beam diagnostics in the transport line
6. The last 6 quadrupoles in the SRF linac
7. Energy corrector and energy spreader cavities
8. Shielding

Physical:

1. Flange connection on the H- beam line vacuum pipe downstream of last SRF quadrupoles
2. Flange connection on the energy corrector cavity (both ends)
3. Flange connection on the energy spreader cavity (both ends)
4. Flange connection on the Beam In Gap (BIG) monitor system

The Linac to High Energy Beam Transport interface is shown in Fig. 3. The interface point is at the gate valve at the end of the SRF. LANL is responsible for this gate valve, which is intended to protect the Linac from vacuum perturbations generated in the HEBT and/or the Ring.

1.4.1.3 General interface criteria

The parameters being used here are consistent with the SNS Parameter List, Rev. 6. In addition, the design of the HEBT System allows it to be compatible with future machine upgrades to 2 MW and beyond. The design basis H^- beam characteristics at the end of the Linac are given below:

Table 3: Linac parameter for a 1.4 MW beam.

Average H^- particles per second (at 60 Hz)	9.4×10^{15}
Maximum pulses per second	60 Hz
H^- particles per macro pulse	1.56×10^{14}
Average H^- energy	1.0 GeV
Average beam current	1.5 mA
Average beam power	1.5 MW
Maximum macro pulse length	1.0 ms
Average H^- current during macro pulse	26 mA
Peak H^- current (between chopper gaps)	38 mA
Chopping frequency	1.188 MHz
MINI pulse length	645 ns
Chopper Gap	300 ns
Rise and fall time	10 ns
Chopper transmission	68%

The parameters above are consistent with a design power level of 1.4 MW.

1.4.1.4 Functional interface

1. Beam Height:

Beam axis will be 127 cm (50.0 inches) above the floor.

2. H^- Beam:

The Normal and the off normal conditions of the beam at the interface with HEBT are listed below:

Transverse beam emittance (norm, rms)	$< 0.41\pi$mm-mrad
Transverse jitter	< 0.25 mm
Effective transverse beam emittance (norm, rms)	$< 0.45\pi$mm-mrad
Beam microstructure	402.5 MHz
Bunch spread (rms at 805 MHz)	1.5 deg
Energy spread	± 0.33 MeV (rms)
Energy centriod jitter	± 1.5 MeV (max)
Phase centriod Jitter	± 3.7 deg (max)
Beam halo outside 5 s	$< 1 \times 10^{-4}$
Beam charge inside chopper gap	$< 1 \times 10^{-4}$ of total charge

Off-normal beam conditions for beam shutdown:

Maximum effective transverse emittance (rms)	1.0πmm-mrad
Beam halo	$< 3 \times 10^{-4}$
Beam charge in chopper gap	$< 3 \times 10^{-5}$ of total charge ll
Accelerator trips > 5 sec and < 5 Min	< 50 per day
Accelerator trips > 5 min	< 10 per day

Beam interruptions are likely to occur due to ion source problems, RF power trips, or perhaps due to Linac beam loss exceeding a pre-specified limit. Accelerator beam delivery interruptions impact the target system. Accelerator trips that allow the target window to cool down from normal operating temperature will produce fatigue cycles. The time constant is estimated at ∼5 sec. The time constant for the entire mercury loop to cool down from normal operating temperature is estimated at ∼5 minutes.

3. Vacuum System

Pressure at Linac interface 1×10^{-8} torr

Any significant increase in pressure will lead to excessive stripping of the H^- beam by the residual gas.

4. RF Signal and Control Signals

The design basis signal interface includes the following reference signals:

To the Ring System (WBS 1.5):

Linac vacuum status	TBD
RF carrier frequency	805 MHz
RFQ carrier frequency	402.5 MHz

From the Ring System (WBS 1.5):

Chopper timing signal	1.188 MHz
Macro pulse beam trigger	TBD

Control Signals:

A “Ring-Ready” control signal shall be provided by BNL for input signal to the LANL-supplied low-level RF controller. A chopper sync signal will also be provided by BNL. The interface to the main control system shall be provided by LANL.

LANL will provide input signals to the main control system for “Fast Protect” and “Run Permit”. LANL will also provide 402.5 and 805 MHz RF sync signals.

5. Beam Diagnostics

The design basis interface includes the following signals from System 1.5.1 (Transport Line) to System 1.4.5 (Linac beam diagnostics). Except for the laser system, these diagnostic systems should be in the zero-degree transport line upstream of the first dipole magnet.

Beam current measurement
Beam position measurement
Beam energy measurement
Measurement of beam in chopper gap (laser H- stripping system in transport line)
Beam profile measurement
Beam energy and phase spread measurement
Beam halo measurement system in transport line
Fast beam abort signal
Beam enable signal for Linac injector
Beam halo collimator
Beam current measurement before linac dump

6. The Last SRF Quadrupoles

For matching from doublet lattice (LINAC) to the FODO lattice (HEBT) BNL will use last six quadrupoles (six independent knobs).

7. Energy Corrector and Energy Spreader Cavity

LANL will be responsible (including cost) for the design and fabrication of the energy corrector and energy spreader cavity system, and all its signal interfaces to the Linac. LANL will install these cavities in the HEBT:

Cavity	Frequency	Voltage
Energy Corrector	805 MHz	4.0 MV
Energy Spreader	805 MHz ±100 kHz	4.0 MV

8. Shielding (TBD)

1.4.1.5 Physical interface

The physical interface is shown in Fig. 4.

1. Proton beam line vacuum tube flange interface

The proton line vacuum pipe will have a flange interface downstream of the last quadrupole in the SRF linac as shown in Figure II. WBS 1.4 will supply the vacuum pipe upstream of the gate valve interface and WBS 1.5 shall provide the pipe downstream of the interface.

Seal Location	TBD
Beam Tube	12 cm in diameter
Type of seal	Metallic
Flange Type	TBD

2. Flange connection on the energy Corrector cavity (both ends)

The energy corrector cavity shall be located between quadrupoles QH10 and QV11 in HEBT. Design details of this interface will be provided by LANL.

Seal location	In flange
Beam tube diameter (I.D.)	5.15 cm diameter
Type of seal	Metallic, Copper
Flange type	6.75 Conflat, Rotatable
Overall length of cavity across flanges	71.736 inches
Total overall length of insert module	79.00 inches
Cavity bore diameter	5.00 cm

3. Flange Connection on the Energy Spreader Cavity (both ends)

The Energy spreader cavity shall be located between quadrupoles QV19 and QH20 in the HEBT. Design details of this interface will be provided by LANL.

Seal location	In flange
Beam tube diameter (I.D.)	5.15 cm diameter
Type of seal	Metallic, Copper
Flange type	6.75 Conflat, Rotatable
Overall length of cavity across flanges	71.736 inches
Total overall length of insert module	79.00 inches
Cavity bore diameter	5.00 cm

4. Flange Connection on the Beam In Gap Monitor System

The Beam In Gap monitor shall be located after the 6th dipole (DH16). Design details of this interface will be provided by LANL.

Seal Location	TBD
Beam Tube	12 cm in diameter
Type of seal	Metallic
Flange Type	TBD

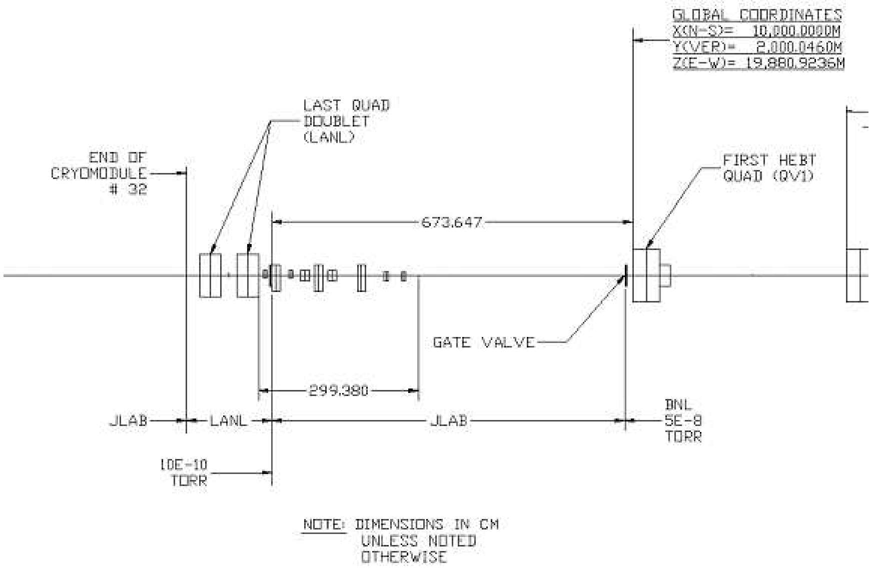

Figure 3: Linac to High Energy Beam Transport - Interface Point.

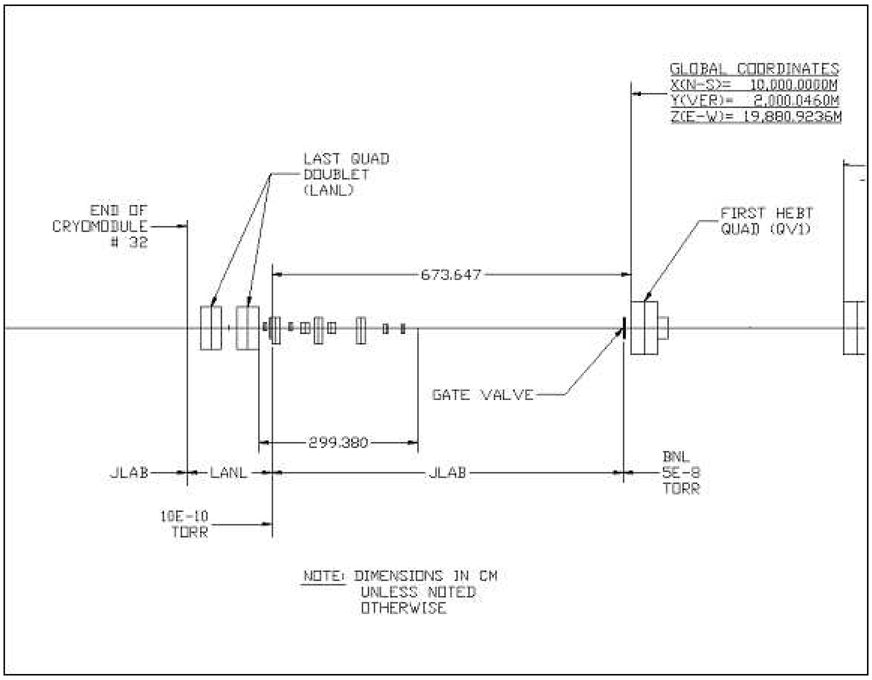

Figure 4: Linac and HEBT Interface.

1.4.2 RTBT/Target interface requirements

1.4.2.1 Introduction

The Ring to Target Beam Transfer (RTBT) Line, WBS 1.5, transports the proton beam from the ring to the neutron-producing Target System, WBS 1.6. This document deals with the interface between the RTBT and target system including the functional interface with the beam and the physical interface.

1.4.2.2 Interfaces

The following are the interfaces between WBS 1.5 and WBS 1.6.
Functional:

1. Proton beam on the target
2. Proton beam from flange interface to proton beam window
3. Vacuum systems
4. Radiation shielding
5. Handling and maintenance

Physical:

1. Flange connection on proton beam line vacuum pipe downstream of last optical element.

1.4.2.3 General Interface Criteria

The design basis proton beam characteristics on the target are given in Table 4. The target location parameters are given in Table 5. The last section of the RTBT line entering the target building is shown in Fig. 5.

Table 4: Normal proton beam parameters at the target station.

Proton beam power	2.0 MW
Protons per pulse	2.1×10^{14}
Average proton energy	1.0 GeV
Maximum pulses per second	60
Pulse duration	$< 0.7 \times 10^{-6}$ sec

These parameters are consistent with a design power level of 1.4 MW.

Table 5: Target location parameters.

Proton beam elevation	$103'5''$
Target liner radius	200-in
Nominal target center (x, y)	$0.0''$, $0.00''$

1.4.2.4 Functional Interfaces

1. Proton Beam-Target Interface

The normal and off-normal conditions of the beam at the interface with the target are listed in Table 6. Table 7 lists general target parameters. The beam spot and target cross section are shown in Figure 6. Figure 7 shows the beam density distribution used in the target design in both the horizontal and vertical directions at the target face. The beam density shall decrease monotonically with distance from the center.

Some parameters of the target are given in Table 7. The target assembly will consist of a mercury vessel and a water cooled shroud. The beam interface requirements are given for the inner mercury vessel.

2. Proton Beam to Window Interface

The proton beam window is located 2.3 m from the front of the target. The beam parameters are to be defined so that the interface requirements at the target are satisfied, including beam divergence and the effects of scattering in the beam window. WBS 1.5 shall provide beam profile information from the last optical element to the proton beam window. Normal and off-normal conditions at the window are given in Table 8. Proton window parameters are listed in Table 8.

3. Vacuum Systems Interface

The proton beam line provided by WBS 1.5 will be sealed at a flange interface downstream of the last optical element. WBS 1.6 shall provide a vacuum pipe from this flange connection to the proton beam window assembly.. WBS 1.5 shall define the seal type, provide the seal and be responsible for handling of the optical components and their beamline vacuum pipe. At the proton beam window an inflatable seal will be used to make the high vacuum seal between the beam vacuum and the bulk shield atmosphere. The maximum leak rate specification from the proton beam window assembly into the beam vacuum line is given in Table 10. When the window is changed, the design is to vent the assembly up to air.

Failure modes for the proton beam window include a singe shell failure releasing activated water into the beam line, a seal failure releasing air and or helium into the beamline and a double wall failure which releases water and possibly helium. The helium release would occur with the core vessel operated at approximately 1 atmosphere helium pressure.

4. Radiation Shielding

There are several radiation issues associated with the radiation shielding interface:

1. Radiation doses to beam line equipment during operation. WBS 1.5 shall provide radiation hard components so that there is no operational limit on dose rate.

2. Dose rate and activation of components after shutdown. WBS 1.6 shall provide shielding to limit backstreaming neutrons from the target assembly. The goal is to reduce activation and allow magnet replacement to be accomplished without the use of remote handling equipment.

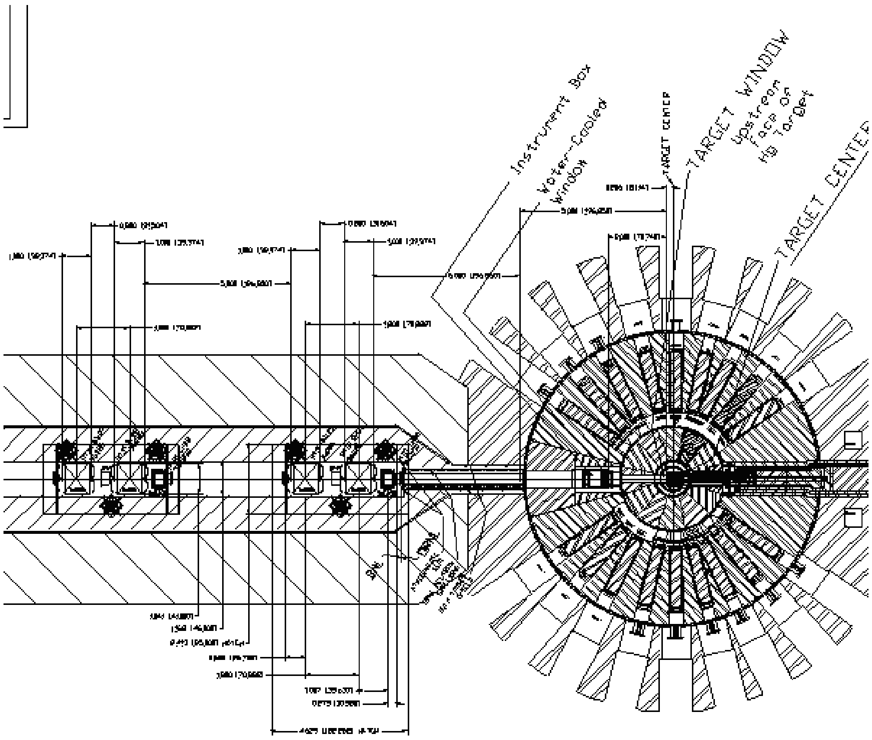

Figure 5: Configuration of the last RTBT section and Target.

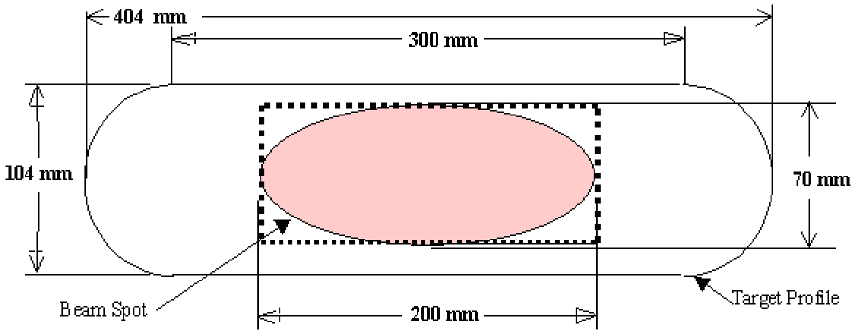

Figure 6: Total mercury target vessel cross section and beam spot.

3. Dose rate external to the RTBT shielding within the high bay and on the instrument floor. The shielding provided by WBS 1.6 downstream of the flange interface will be design to limit the external dose to 0.25 mrem/hr in combination with the RTBT shielding provided by WBS 1.8 and WBS 1.5.

WBS 1.6 shall provide all shielding and activation calculations.

5. Handling and maintenance

WBS 1.5 shall be responsible for all handling of components upstream of the flange interface. WBS 1.6 shall be responsible for all handling of components downstream of the flange interface. The section between the flange and the proton beam window assembly will be designed to allow replacement by retraction upstream and removal through the overhead hatches. WBS 1.6 shall specify features such as rails for rollers within the tunnel required for transport and replacement.

1.4.2.5 Physical Interfaces

The physical interface is diagrammed in Figure 8.

1. Proton beam line vacuum tube flange interface

The proton beam line vacuum pipe will have a flange interface downstream of the last optical element as shown in Figure fig:rtbtiddIV-1. WBS 1.5 will supply the vacuum pipe upstream of the interface and WBS 1.6 shall provide the pipe downstream of the interface and any shielding required for reducing the backstreaming neutron dose. WBS 1.6 shall also provide an atmospheric seal to isolate the bulk shielding air from the RTBT tunnel.

An interface control drawing shall be established for the flange interface defining dimensions, tolerances, loads, component parts and other essential features.

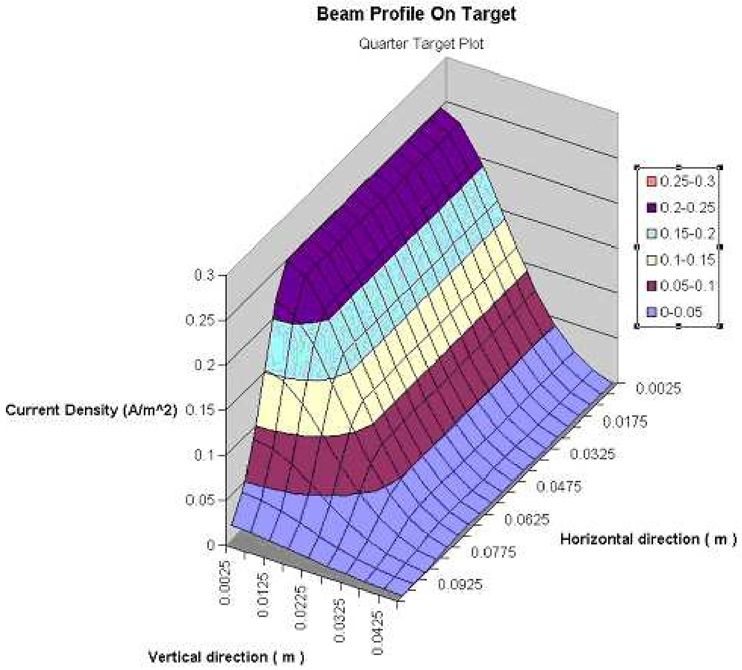

Figure 7: Normal beam profile at target face.

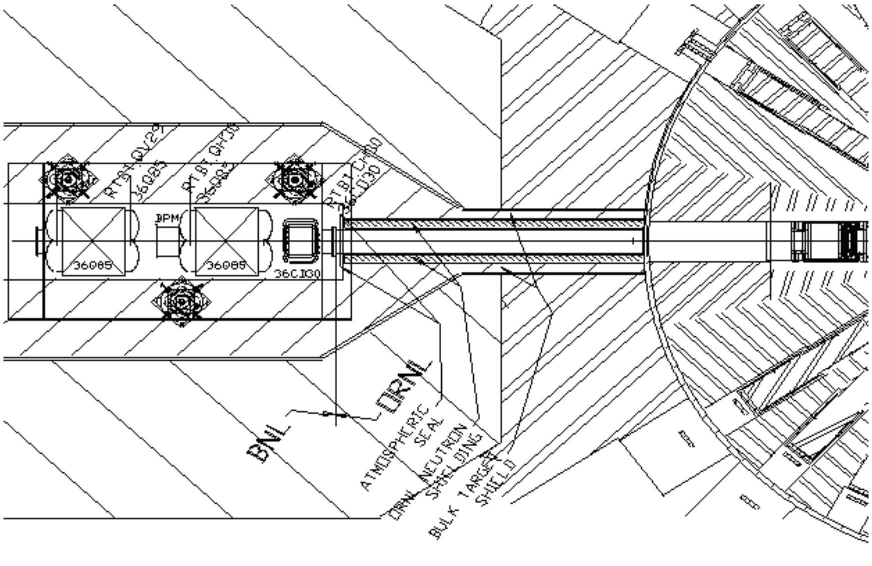

Figure 8: Systems physical interface diagram.

Table 6: 2-MW Beam interface requirements with the target shroud face.

	Normal condition	Off-normal condition	Duration of fault
Target cross-section width	404 mm		
height	104 mm		
Beam spot width	200 mm		
height	70 mm		
Beam power within nominal beam spot[3]	$\geq 90\%$	$> 50\%$ power outside spot	≤ 2 pulses
Time-average beam current density over spot	≤ 0.143 A/m^2		
Peak time-average beam current density[1,2]	≤ 0.25 A/m^2	≤ 0.28 A/m^2	10 sec.
Peak single pulse density[4]	$\leq 2.6 \times 10^{16}$ p/m^2	$\leq 3.20 \times 10^{16}$ p/m^2	≤ 2 pulses
Tolerance on beam centroid			
horizontal	±2 mm		
vertical	±2 mm		
Unscheduled beam-off[5,6]			
> 5 sec.	≤ 50 per day		
> 5 min.	≤ 10 per day		

1. The peak time-average current density is the most concentrated beam the target must survive without causing a failure within the planned target lifetime.

2. The off-normal peak time-average current density allows a 10% increase over ten seconds and assumes a failure that concentrates the beam for multiple pulses prior to detection. The target will be designed to handle this concentrated heat load for the specified time within the beam spot.

3. The power outside the spot in an off-normal condition represents beam error for two pulses. Target system components are to be designed to survive this failure.

4. The off-normal peak single pulse density allows two consecutive pulses with 25% higher than normal pulse densities.

5. Missing beam that allows the target structure to cool down from normal operating temperature ($>$ 5 seconds) will produce fatigue cycles that need to be included in the design for expected fatigue life.

6. Missing beam that allows the entire mercury loop to cool down from normal operating temperature ($>$ 5 minutes) will produce fatigue cycles that need to be included in the design for expected fatigue life.

Table 7: General target parameters.

Target material	Mercury
Target structure	Stainless steel type 316
Atmosphere surrounding target	Helium ($\leq$ 0.1 MPa) or vacuum
Target face radius	52 mm
Mercury Target leading edge	8.1 in. from target station center

Table 8: Proton beam parameters at the beam window.

	Normal condition	Off-normal[4,5] condition	Duration of fault
Beam spot width (95%)	204 mm		
height (95%)	74 mm		
Beam power outside	$\leq$ 5%	$\leq$ 50%	$\leq$ 2 pulses
nominal spot[3]	$\leq$ 5%	$\leq$ 50%	2 pulses
Time-average beam current density over beam spot	$\leq$ 0.143 A/m^2		
Peak time averaged beam current density[1,2]	0.28 A/m^2	TBD	

1. The peak time-average current density should be the most concentrated beam the window must survive without failure within the planned lifetime.

2. The off-normal peak time-average current density over ten seconds assumes a failure which concentrates the beam for multiple pulses prior to detection. The window would be designed to handle this concentrated heat load for the specified time within the beam spot.

3. The power outside the spot in an off-normal condition represents a beam error for two pulses. Window system components are to be designed to survive this failure.

4. Beam trips, as given in Table 6, that allows the window to cool down from normal operating temperature will produce fatigue cycles that need to be included in the design for expected fatigue life.

5. A rupture type failure of the water cooled Inconel window will release water into the high vacuum beam line for a single wall failure, or helium for a double wall or seal failure.

Table 9: Proton beam window parameters

Configuration	Dual walls with flowing water
Window material	Inconel
Metal thickness	Two 2.0 mm thick plates
Vertical radius of curvature	52 mm
Coolant	Deionized water
Coolant temperature:	40°C
Coolant pressure	TBD
Coolant thickness	1.5 mm
Window to target face separation	2.33 m

Table 10: Vacuum interface.

Beam window seal leakage	TBD
Net pumping speed at flange location	TBD
Provision for bake-out	none
Environment during window change-out	air at 1 atm

Table 11: Proton beam line Flange interface seal.

Seal location	TBD approximately 7 m from target center
Beam tube	14-inch Schedule 10 pipe (13.5 inch ID 14.0 inch OD)
Type seal	Metallic
Flange Type	Helicoflex or Cefilac
Attachments	Bolted (vertical access)

1.4.3 Beam dump interface requirements

1.4.3.1 Introduction

The ring system and the target system have interfaces at each of the three beam dumps that are similar in some ways to target station. The three dumps are described briefly below:

Linac Dump (passive) - Dissipate as much beam power as possible at the end of the Linac using the earth as a heat sink with no active cooling (approximately 7.5 kW). Ring Injection Dump (active) - Dissipate 200 kW of beam power at the ring Ring Extraction Dump (passive) - Dissipate as much beam power as possible immediately before the Target Station using the earth as a heat sink with no active cooling (approximately 7.5 kW).

1.4.3.2 Interfaces

The following are the beam dump interfaces between WBS 1.5 and WBS 1.6

Functional:

1. Proton Beam on the beam stops
2. Flight tube Vacuum systems
3. Flight tube Helium systems

Physical:

1. Welded Pipe connection at external face of beam dump vault

1.4.3.3 General Interface Criteria

The beam parameters are shown on Table 12.

The project lattice drawing (100000000-G8E- 8000-A001 latest revision) controls the beam dump locations.

1.4.3.4 Functional Interfaces

1. Proton Beam-Beam Stop Interface

2. Proton Beam-Vacuum Window Interface for Ring Injection Dump

3. Vacuum Systems Interface

The flight tube between the ring facility and the Ring Injection Dump will be vacuum containment system. The flight tube from the immediately outside of the beam dump vault and into the beam stop enclosure will be the responsibility of WBS 1.6.9. The system will be capped with a vacuum window inside the beam stop enclosure and is the complete responsibility of WBS 1.6.9. Some parameters include:

Beam window seal leakage	TBD
Net pumping speed at flange location	TBD
Provision for bake-out	none
Environment during window change-out	air at 1 atm

4. Helium Systems Interface

The flight tubes for the two passive dumps are filled with helium between the ring facility

Table 12: Beam Characteristics At Beam Dump.

Parameter	Linac	Injection	Extraction
Maximum average power (kW)	∼7.5	200	∼7.5
Beam energy (GeV)	1.0	1.0	1.0
Pulse length (ms)	∼1.0	∼1.0	∼0.0006
Nominal pulse energy (kJ)	33.4	3.33	33.3
Max single pulse energy (kJ)	50.1	45.8	41.6
Frequency (Hz)	0.20	60	0.20
Max power (kW) (less than 30 sec)	∼10	200	∼10
Duty cycle (%)[1]	10	100	10
Annual Operating time (hr)	500	5000	500
Max Proton Current density (A/m^2)	0.005	0.015	0.002
Horizontal beam size (cm)	6	20	20
Vertical beam size (cm)	6	10	20
Tolerance on beam center (cm)	±5	±5	±5
Minimum stop diameter (cm)	35	35	35

1. Duty cycle shall be defined as the operating time in a one year period divided by 5000 hrs.

and the beam stop. The flight tubes can be filled and sealed with atmospheric pressure helium. All provisions for gas connections shall be near the Ring facility.

5. Instrumentation Interface

The passive beam stops will be equipped with a total of 20 thermocouples that will be contained in four thermocouple probes with five thermocouple junctions per probe. The access to these thermocouples shall be through a stainless steel conduit generally parallel to the flight tube leading from the Ring facility to the beam dump facility. WBS 1.5 will provide the conduit and WBS 1.6 will provide the thermocouple probes terminating in the ring facility. WBS 1.5 will provide the equipment to monitor these thermocouples.

1.4.3.5 Physical Interfaces

1. Ring Injection Dump

The physical interface for the Ring Injection Dump is shown in Figure 9.

2. Passive Dumps

The physical interface for the Linac and Ring Extraction Dump is shown in Figure IV-2??.

1.5 Coordinates and Polarity Conventions

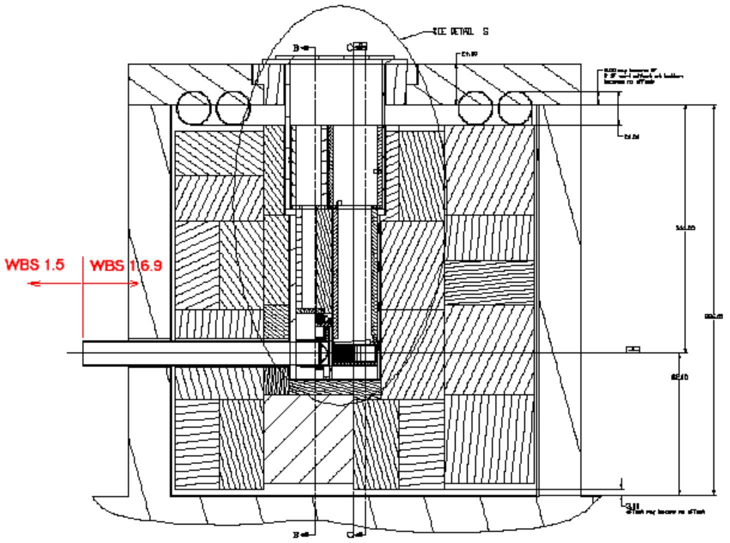

Figure 9: Physical interface for the ring injection dump.

1.6 Acknowledgments

Co-authors:

1.1	J. Wei
1.2	J. Wei
1.4	D. Raparia
2.1	D. Raparia, J. Wei
2.2	D. Raparia, J. Wei
2.2.4	J. Holmes
2.3	N. Catalan-Lasheras
2.4	Y. Papaphilippou
2.5	A.V. Fedotov
2.5.3	H. Hahn
2.5.6	M. Blaskiewicz
3.1	D. Raparia
3.2	R. Lambiase
3.3	Y. Papaphilippou
3.5.1	Y.Y. Lee, N. Catalan-Lasheras
3.6.5	H. Hahn
3.7	N. Catalan-Lasheras, S. Cousineau, H. Ludewig
3.8	D. Raparia
3.9	M. Blaskiewicz, A. Zaltsman
3.10	P. Cameron, A.V. Fedotov, D. Raparia
4.1	L. Hoff
4.2	D. Gurd
4.3	L. Hoff

Acknowledgments:

Editor:

J. Wei

2 Accelerator Design and Beam-dynamics Issues

2.1 Layout

2.1.1 HEBT layout

HEBT is about 180 meter long and carry $^-$ ion with peak average current of 38 mA in 1 ms long pulses at the rate of 60 Hz. The HEBT not only carry the H^- ion but also optically matches linac and ring, correct the energy jitter from the linac, increase the energy spread of beam to avoid beam stability in the ring, clean the transverse and longitudinal halo coming from the linac, characterize the beam from linac, and protect ring from the fault conditions. The general features of this line are, the magnetic filed in dipole and quadrupoles and vacuum are low enough to control Lorentz and gas stripping of H^- for energies 800 - 1300 MeV. The ratio of aperture to the rms beam size is kept greater than 10 through out the line except energy corrector, spreader and collimators. Fig. 10 shows the layout of the HEBT. For ease of operation and stability reasons the lattice of the is chosen is FODO which matches the linac and ring doublet-FODO lattices. We can consider the HEBT as having three sections: Linac-Achromat Matching Section (LAMS), Achromat, and Achromat-Ring Matching Section (ARMS). In addition to the bend to the ring, there is a straight beam line used for linac beam characterization, as shown in Fig. 10. The first five cells (8 m/cell) after the linac (LAMS) are used to characterize the linac beam, match beam into the achromat, collimate beam halo. The energy corrector cavity is located in the last half cell of the LAMS. Following this, the four cell long achromat (14 m/cell) provides momentum selection by cleaning up the beam energy halo at the point of maximum dispersion (η_x=6.4 m). The remaining six cells (8 m/cell) are used for matching the beam into the accumulator ring, diagnostics. The energy spreader cavity is located in the first cell following the achromat (in the ARMS), where the dispersion and its derivative are zero. There are eight horizontal and eight vertical dipole correctors placed in strategic positions of small apertures in the line. The line has following new features to control losses.

2.1.2 Ring layout

2.1.3 RTBT layout

Ring to Target Beam Transfer (RTBT) line is about 150 meter long and carry the beam from the ring extraction region to the target and provide the desired footprint for the accelerator complex. The general features of this line are, the line is immune to one kicker failure and the ratio of acceptance to rms emittance is more than 20. Fig. 12 shows the layout of RTBT.

The line has following function (a) extraction (b) beam dump (c) protect from device failure (d) beam spreader and (e) diagnostics. Following the extraction system beam can be dumped straight through a 16.8° dipole magnet. After the magnet two cell are used for the collimator system which protect line from the dipole failure. Following another six cells of transport, the last five quadrupoles in the line are used for final beam spreading to produced the beam sized required at the target. The phase advance between kickers and target is an integral multiple of π, so that in event of a kicker failure beam will not move at the target.

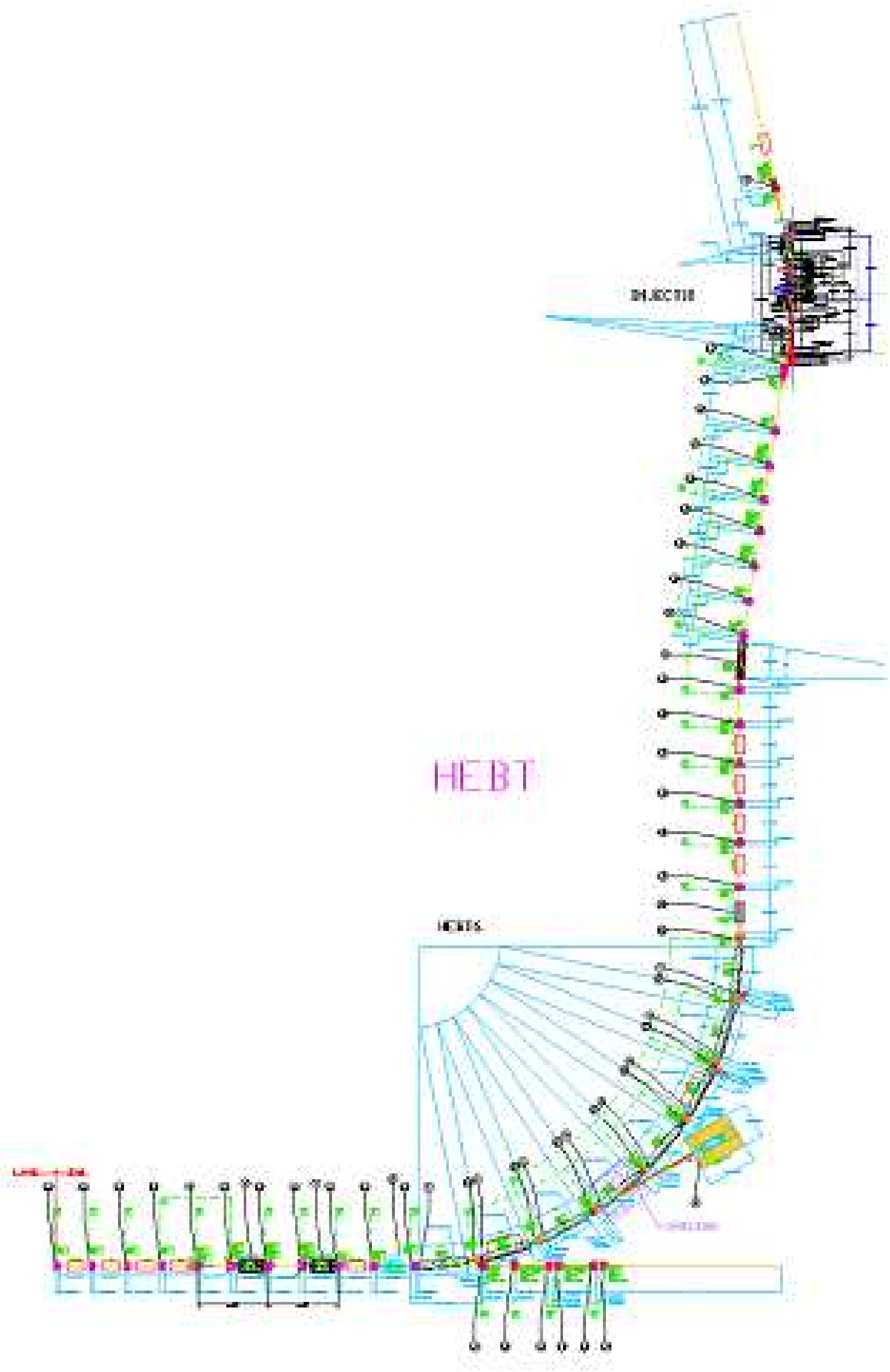

Figure 10: High Energy Beam Transport layout.

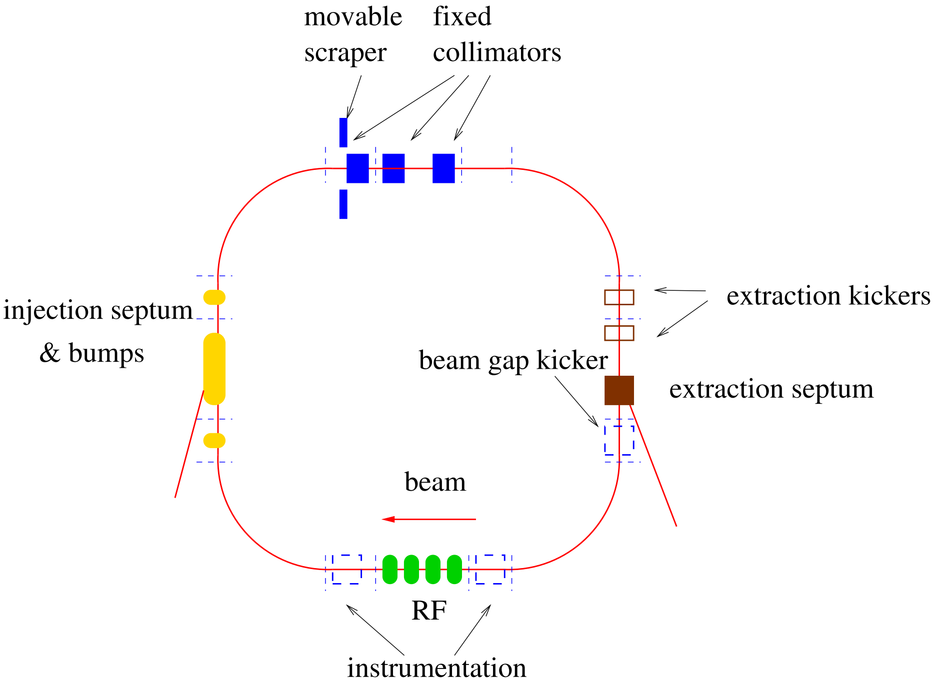

Figure 11: Schematic layout of the SNS accumulator ring. The four straight sections are designed for injection, collimation, the RF system, and extraction.

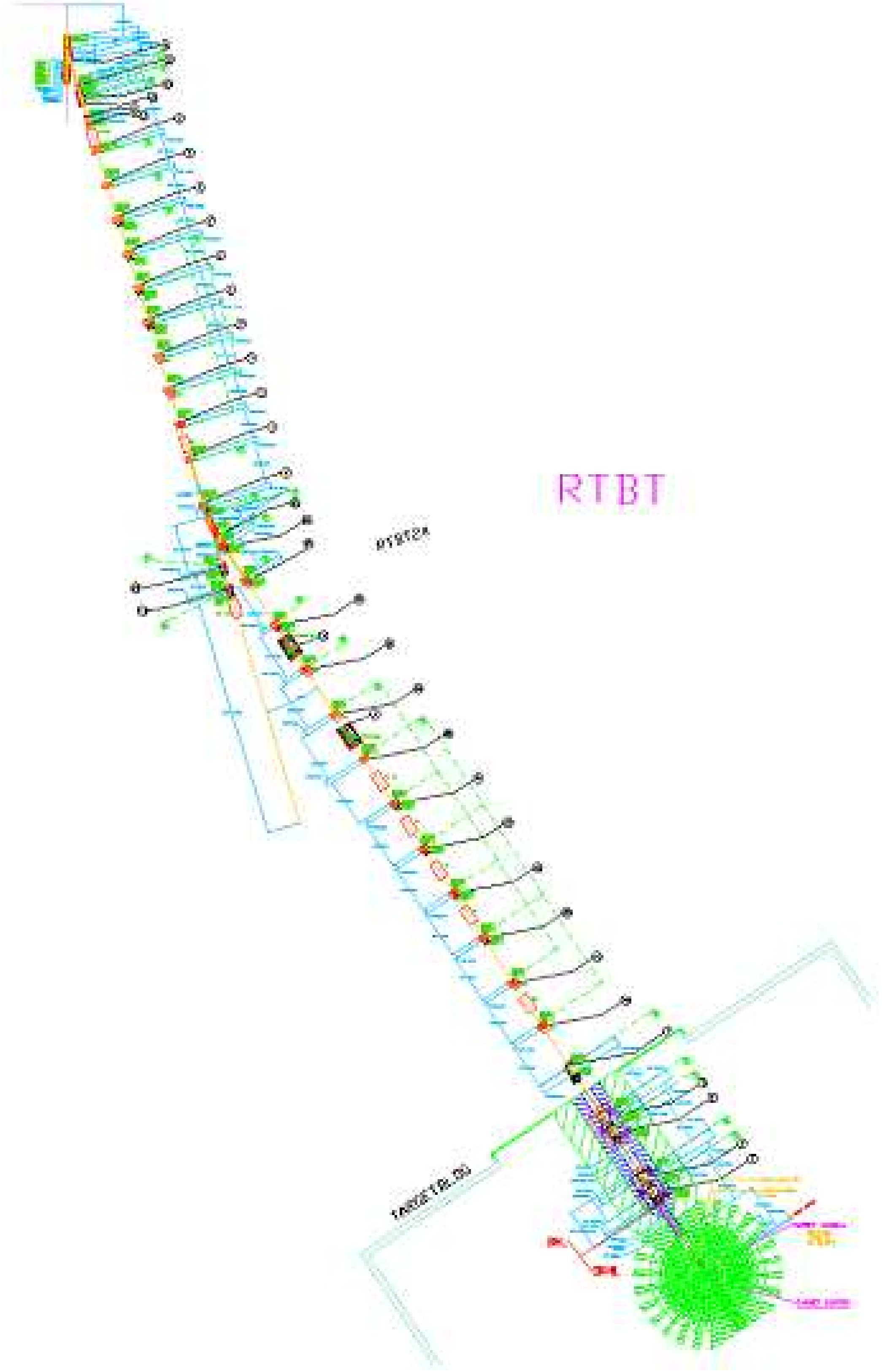

Figure 12: Ring to Target Beam Transport layout.

2.2 Lattice

2.2.1 HEBT optics

2.2.1.1 Introduction

The SNS High Energy Beam Transport line (HEBT) connects the 1 GeV linac to an accumulator ring. The HEBT not only matches the beam into the accumulator, but also determines the beam quality at injection. HEBT also capable to transport 1.3 GeV H minus to the accumulator ring [3].

2.2.1.2 Design Requirements

Table 13 gives the required Courant-Snyder parameters at the entrance (middle of the first HEBT quadrupole) and exit (injection stripping foil) of the HEBT. In addition, a major requirement of all parts of this accelerator is minimization of uncontrolled beam losses to allow hands-on maintenance. This is achieved by maintaining adequate tolerances on elements, appropriately located collimators, and sufficient beam diagnostics.

Table 13: Courant-Snyder parameters at the entrance and exit of the HEBT for a 1.4 MW beam.

Quantity	Entrance (end of linac)	Exit (stripping foil)	Units
α_x	0.00	0.053	
β_x	2.377	10.44	π mm/mrad
ϵ_x	1.26	1.40	mm mrad (5 rms, unnorm.)
α_y	0.00	0.045	
β_y	13.543	12.12	mm/mrad
ϵ_y	1.26	1.40	π mm mrad (5 rms, unnorm.)
α_z	0.0005	0.14	
β_y	0.005	0.05	deg/keV
ϵ_z	1500	1500	π keV deg (5 rms)

2.2.1.3 Description of the HEBT Line

The HEBT has following functions: (a) matching of the beam from the linac into the transport line, (b) momentum correction, (c) momentum spread, (d) matching bean into the accumulator ring, (e) characterization of the beam out of the linac and before injection, and (f) halo and momentum tails cleanup. We have managed to decouple the first four of these functions, and can consider the HEBT as having three sections: Linac-Achromat Matching Section (LAMS), Achromat, and Achromat-Ring Matching Section (ARMS). In addition to the 90° bend to the ring, there is a 0° beamline used for linac beam characterization.

The first four and half cells (8.0 m/cell) after the linac (LAMS) are used to characterize the linac beam, match beam into the achromat, collimate beam halo. Following this section, the four cell long achromat (14 m/cell) bends the beam 90° and provides momentum selection by cleaning up the beam energy halo at the point of maximum dispersion (η=6.4 m). The energy spreader cavity is located in the first cell following the achromat (in the ARMS), where the dispersion and its derivative are zero. The remaining six cells (8 m/cell) are used for matching the beam into the accumulator ring, diagnostics. There are 16 small dipole magnets for steering of the beam in the quadrupole focusing-plane located strategically to align the beam in the narrow apertures. To reduce the probability of uncontrolled beam losses, HEBT is equipped with five sets of beam halo scrapers and three beam absorbers. The collimators are the minimum apertures in the line, chosen to be 10 times the rms beam size. The maximum magnetic field in dipoles and quadrupoles is kept less than 2.1 kG, to keep H^- stripping losses below 0.1 nA/m. The alignment tolerances required to keep the beam losses low (Raparia, 97) are given in Table 14.

Table 14: Expected misalignment for the HEBT magnets.

Translation (x and y)	±0.1 mm
Pitch and yaw	±1 mrad
Rotation	±0.5 deg

2.2.1.4 Linac to Achromat Matching Section

The linac has a FDOO lattice with a phase advance of about 90°/cell, and the achromat has a FODO lattice with 90°/cell phase advance. To remove any linac beam halo, there are four movable (two in each plane) and two fixed collimators located in the 3rd through 7th half-cells in this section (details of the configuration are discussed in the section on halo scraping). The space between quadrupoles in the first cell of the HEBT is occupied by beam diagnostics, as discussed in a later section.

2.2.1.5 Momentum Selection (Achromat)

A 90° achromatic bend starts at the 5th cell of the HEBT line, and finishes in four cells, containing eight 11.25° dipoles. The total phase advance in the achromat is 360°. A beam energy-halo scraper is located at the middle cell of the achromat, where the dispersion is maximum (6.4 meter). The first dipole of the achromat is a switching magnet to provide beam to the 0° linac dump.

2.2.1.6 Momentum Correction and Momentum Spread

The H minus beam from the linac suffers from the energy (2.0 MeV)and pahse (3.5°) jitter due to the phase and amplitude errors of 0.5° and 0.5% respectively. To correct this energy jitter there is corrector cavity in the HEBT which operate at the same frequency as linac namely 805 MHz and phase lock with last cavity of the linac such that the particle with design energy (synchronous) sees the $-90°$ (zero voltage) hence does not change the energy. The particle having more energy than the design energy arrives earlier than the synchronous particle and sees the negative voltage hence lose the excess energy. The particle having less energy then the synchronous particle arrive later than the synchronous and sees the positive voltage and gain the required energy. The energy gain (lose) depend on the time difference (phase difference) between the off energy particles and the synchronous particle and the cavity voltage. There is a limit to this correction scheme, which is if the phase difference is more than 90° than the particle does not gain (lose) the correct amount of energy. Ideally we want maximum phase difference of less than 60°. The phase slip per MeV for a distance L is given

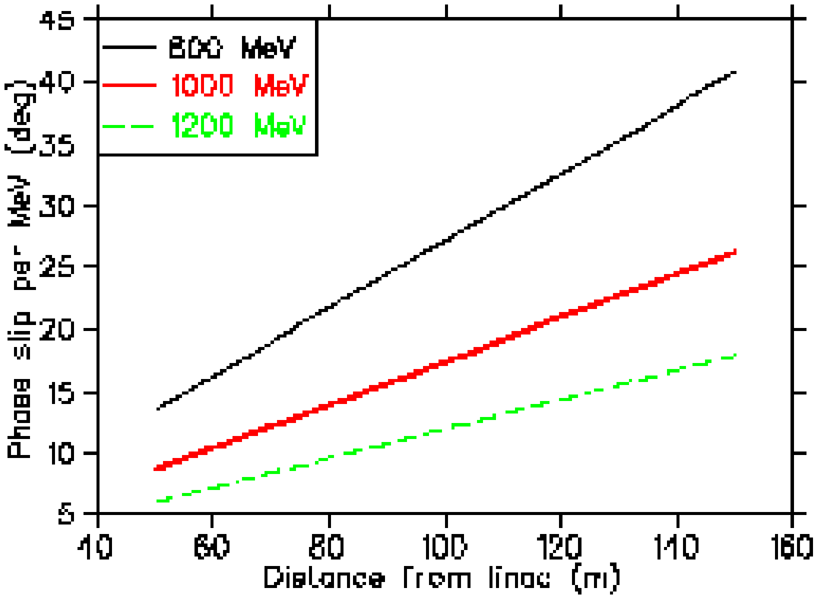

Figure 13: Phase slip per MeV as function of distance for three different energies.

by

$$\Delta\phi_L \equiv \frac{\gamma}{\gamma(\gamma+1)}\frac{\Delta T}{T}\frac{L}{\beta c}2\pi f \qquad (1)$$

where β and γ are the relativistic parameters, c is the speed of light, f is the RF frequency and T and ΔT are the design energy and energy difference. Fig. 13 shows the phase slip per MeV as function of the distance.

The required voltage is given by $V_0 = \Delta E/\sin f_{slip}$. The energy jitter after the corrector cavity 0.2 MeV was achieved which is within the requirement of the ring Momentum correction is accomplished with a 2.6 meter long, 16 cell, 805 MHz rf cavity, operating at a gradient (E_0T) of 3.6 MV/m. This cavity is similar to the last cavity of linac. The cavity is located in the first half-cell before the achromat (100 m from the linac).

SNS accumulator ring also need ±4 MeV energy spread for stability reason. This is achieved by placing another RF cavity after the achromat which frequency is about 100 kHz different than the linac frequency. The linac bunches see different phase as they arrive at this cavity and gain/loss different energies depending on the cavity voltage, hence creating required energy spread without creating energy tails. Results from beam tracking, integrated for the entire injection period, are shown on Fig. 14. The width of the energy spread is controlled by RF amplitude of the cavity. Simulations using a debuncher cavity are shown for comparison. Since the spreader cavity only translates the energy, there is no energy tail in this scheme while the other scheme produces a very long energy tail, which can cause the protons to spill over into the extraction gap.

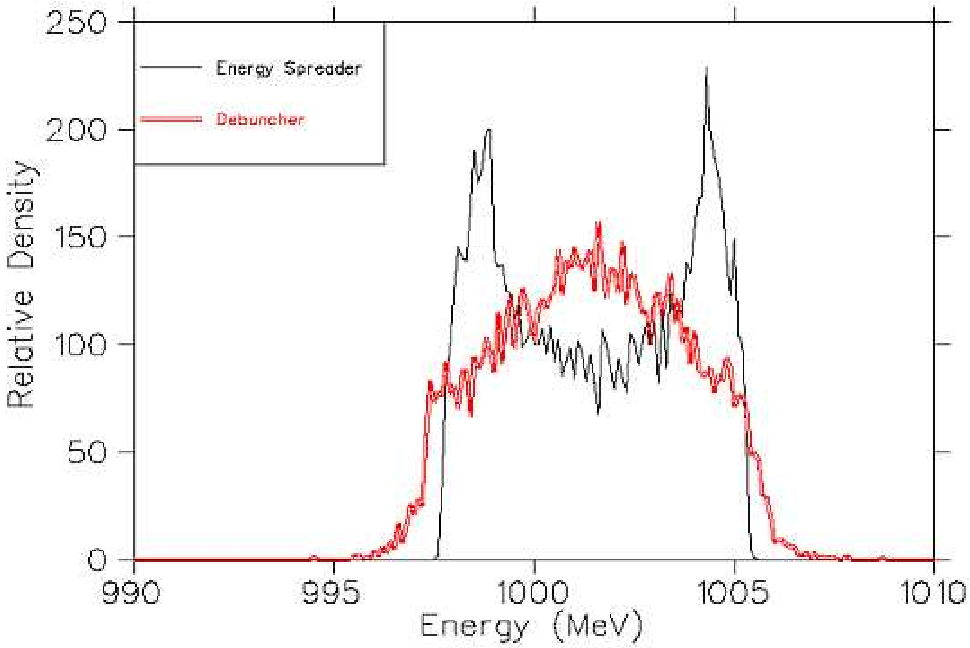

Figure 14: Time integrated energy distribution using constant amplitude energy spreader cavity(black) and debuncher cavity (red).

2.2.1.6 Ring Matching Section

After the achromat, two cells are provided for the diagnostics. At the end of the achromat this line is parallel to the ring straight section, but offset by 10 m, allowing one to have the required "dog leg" for injection into the ring. These bends are necessary to allow the dispersion and its derivative to be zero at the injection stripper foil. The dispersion has a minimum and maximum of similar amplitude but opposite sign through the "dog leg". This section has enough "knobs" (quadrupoles) to match six variables (four amplitude functions and two dispersion functions). There is no vertical bend and no vertical dispersion. The locations of the dipoles are determined by the injection scheme Fig. 15 shows the amplitude function (β_x, β_y) and the dispersion function (η_x) along the HEBT.

2.2.2 Ring optics

The ring optics file is included in Section 6.2.2.

2.2.3 RTBT optics

2.2.3.1 Introduction

Ring to Target Beam Transfer (RTBT) line is about 150 meter long and carry the beam from the ring extraction region to the target and provide the desired footprint for the accelerator complex. The general features of this line are, the line is immune to one kicker failure

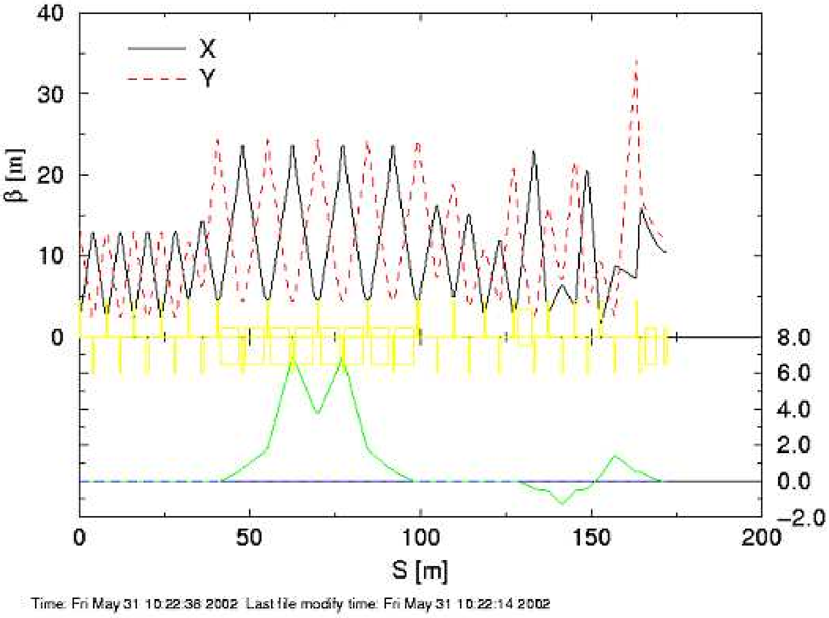

Figure 15: The lattice function β_x, β_y, and η_x along the HEBT.

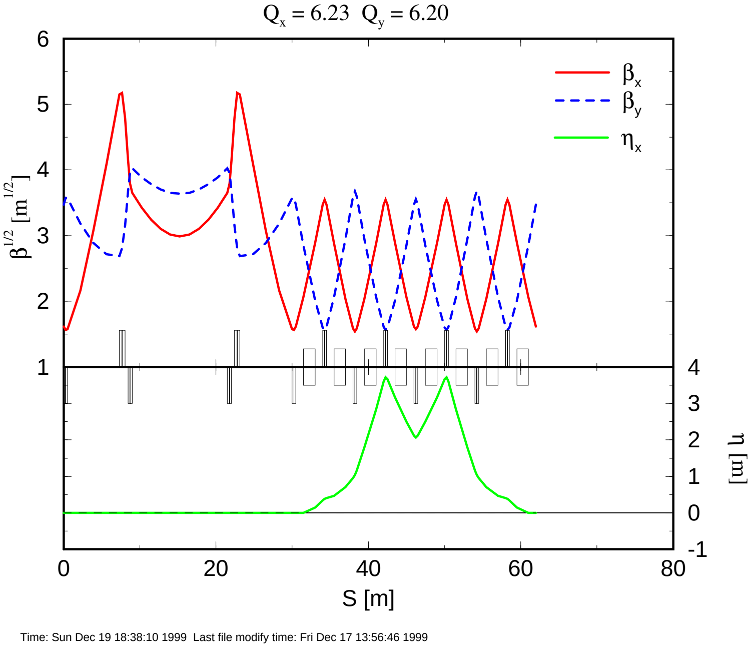

Figure 16: SNS ring lattice superperiod of FODO/doublet structure. The lattice periodicity is 4. Along the indicated beam line are dipoles (centered square boxes), focusing quadrupoles (upper bars), and defocusing quadrupoles (lower bars).

and the ratio of acceptance to rms emittance is more than 20.

2.2.3.2 Design Requirements

The beam requirements at the target are given in Table 15. Table 16 gives the Courant-Snyder parameters of the beam at the beginning of the extraction kicker magnet and at the target.

Table 15: Beam requirements at the target.

Beam width	200 mm
Beam height	70 mm
Time-average beam current density, over beam footprint	≤ 0.147 A/m^2
Beam power within target and outside nominal spot	¡ 10%
Peak time-average beam current density, over 1 cm2	≤ 0.25 A/m^2

Table 16: Courant-Snyder parameters at the ring extraction magnet and at the target for a 1.4 MW beam.

Quantity	Output of Ring	Target	Units
α_x	-0.3180	0.0	
β_x	11.468	83.0	π mm/mrad
ϵ_x	120	120	mm mrad (5 rms, unnorm.)
α_y	-0.2729	0.0	
β_y	13.002	10.2	mm/mrad
ϵ_y	120	120	π mm mrad (5 rms, unnorm.)

2.2.3.3 Design Description and Functions of the RTBT Line

The RTBT uses a FODO lattice up to the beam spreading section. The line has following elements: (a) extraction, (b) beam dump, (c) halo collimation, (d) beam spreader, and (e) diagnostics. The first four functions have essentially been decoupled in the RTBT. The extraction system starts in the ring with a kicker magnet and continues through four cells in the RTBT. Following the extraction system, the beam can be dumped straight through a 16.8° dipole magnet. After this 16.8° bend, two cells are used for the halo collimation. Following another 6 cells of transport, the last five quadrupoles in the line are used for final beam spreading to produce the beam size required at the target. Every quadrupole in the RTBT is followed by a small dipole corrector magnet for steering of the beam in the quadrupole focusing plane. To reduce the probability of uncontrolled beam losses and define the beam size precisely on the target, RTBT is equipped with four transverse beam halo scrapers and several types of diagnostic devices. To keep uncontrolled beam losses low, a study of the required alignment tolerances [5], has led to the requirements given in Table 3.

Fig. 17 shows the amplitude functions (β_x, β_y) and the dispersion function (η) along the RTBT. This line is designed such that it can accommodate the beam current required for the upgrade to 2 MW.

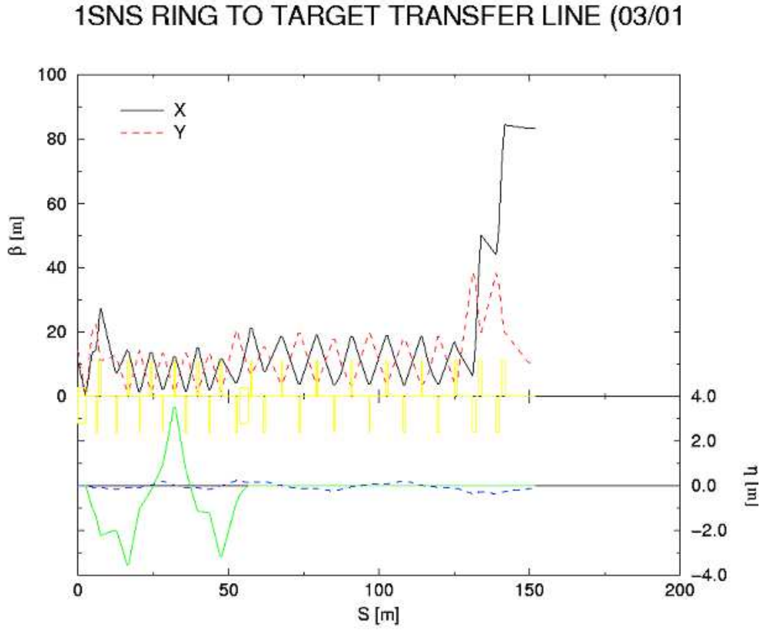

Figure 17: The lattice functions along the RTBT. The phase advance between kickers and target is an integral multiple of π, so that in event of a kicker failure beam will not move at the target.Fig. 18 shows the closed orbit for different kickers failure.

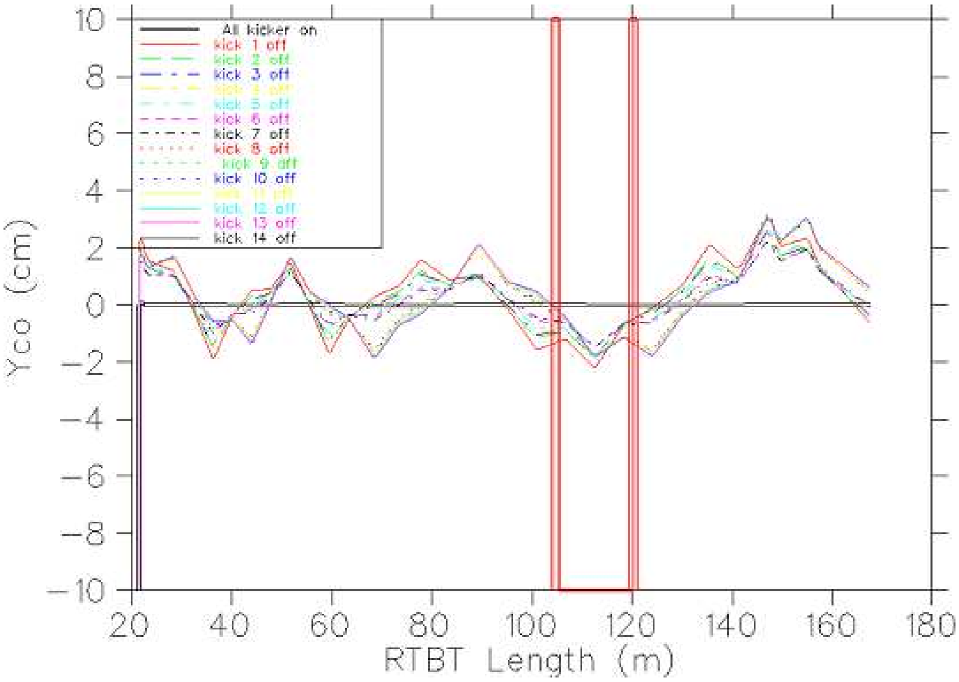

Figure 18: Close orbit due to kickers failure.

Table 17: Expected misalignment for the RTBT magnets.

Translation (x and y)	±0.1 mm
Pitch and yaw	±1 mrad
Rotation	±0.5 deg

2.2.3.4 Extraction

The extraction of the beam is done in a single turn with full aperture at a pulse repetition frequency of 60 Hz. The extraction system consists of two sets (seven each) kicker magnets and a Lambertson magnet septum and a dipole magnet. The Lambertson septum magnet will receive the vertically kicked down beam and will provide large deflection angle (16.8°) to enable ejection horizontally from the accumulator ring. A dipole, which is 540° phase advance away from the Lamberton magnet, bends the beam horizontally in the same direction by 16.8°, making the extraction system achromatic. The Lambertson magnet is rotated 2.55° anti-clock wise to neutralize the vertical kick from the kickers and making the beam about 9 inches difference between the ring and RTBT beam height.

2.2.3.5 Beam spreader

The beam spreader consists of five radiation hard quadrupoles near the end of the RTBT. These five 36 cm diameter aperture quadrupoles provide the desired beam size at the target. Due to thermal considerations of the target, the beam current density on the target must remain below 0.25 A/m^2. This requirement results in a non-Gaussian beam distribution in space (with un-normalized rms emittance of 24 π mm mrad). The required current density distribution is achieved using painting scheme described elsewhere [6].

2.2.4 Ring optics tuning

Detailed studies of the SNS ring lattice optics have been conducted using the MAD Computer Code [7]. The horizontal and vertical tuning ranges for matched solutions with well-behaved lattice functions were determined and the power supply margin verified. Using stability criteria, potential working points have been identified. For these working points, the behavior of the lattice functions was examined with increasingly complex assumptions, including chromatic effects and sextupoles, lattice perturbations due to injection chicane and to dynamic bumps for painting, and magnet field and alignment errors. The results have been used to guide beam dynamics calculations to determine injection painting schemes, dynamic apertures, orbit and resonance correction schemes, collimator settings, and to resolve other design issues.

Determination of the accessible region of tune space involves a number of degrees of freedom and some constraints. Constraints include the necessity of matched solutions, beta functions within aperture-dictated limits, magnet field strengths within specifications, and achromatic arcs. Degrees of freedom include the phase advances in the straight sections and the vertical phase advance in the arcs. The horizontal phase advance in the arcs is restricted to 2π by the achromaticity constraint. The accessible region of tune space for the SNS ring lattice is $6 < \nu_x < 7$ and $4 < \nu_y < 7$. Figure 19 shows the behavior of the maxima of the lattice functions β_x, β_y, D_x and of the doublet focusing quadrupole strength as a function of ν_y for different values of ν_x. Considerations of these and other parameters aided in our definition of the accessible tune space.

For tunes above 7, some magnet strengths exceed specifications and beta functions exceed limits. For tunes below the specified ranges, there is insufficient focusing for solutions to be obtained. Even within the specified range there are inaccessible gaps due to structure resonances. These occur around $\nu_x, \nu_y = 6$ which is a second order structure resonance and also as ν_y approaches 4, which is a first order structure resonance. As a tune approaches one of these structure resonance values, the corresponding beta functions become excessive, and sufficiently close to the resonance no solutions exist. Particularly severe is the case of ν_x approaching 6. Because of the achromatic constraint, the horizontal phase advance is fixed in the arcs, and an excessive change in the rate of phase advance between arc and straight sections causes β_x to become too large at the injection foil by the time $\nu_x = 6.15$. Because the rate of vertical phase advance can be kept more uniform throughout the ring, the effect when ν_y is in the vicinity of the vertical resonant regions is more localized. However, we follow the practice of keeping both ν_x and ν_y well removed from these integer values.

Selection of potential operating points from this large region in tune space becomes simpler with the aid of a resonance analysis. To start, we consider the most dangerous resonances: first and second order resonances, third order structure resonances, and fourth order structure sum resonances. In horizontal tune space, there is a second order resonance at $\nu_x = 6.5$ and a third order structure resonance at $\nu_x = 6.67$. Given the tune spread of the intense SNS beam ($\Delta\nu_x = 0.2$), avoidance of these resonances requires choosing $6.15 < \nu_x < 6.5$. For the same reason, we must also choose $\nu_y < 6.5$. Analysis of the vertical tune space reveals only two regions with working space between resonances at this level: $4 < \nu_y < 4.5$ and $6 < \nu_y < 6.5$. Of these, the stronger vertical focusing yields better behaved vertical beta functions in the

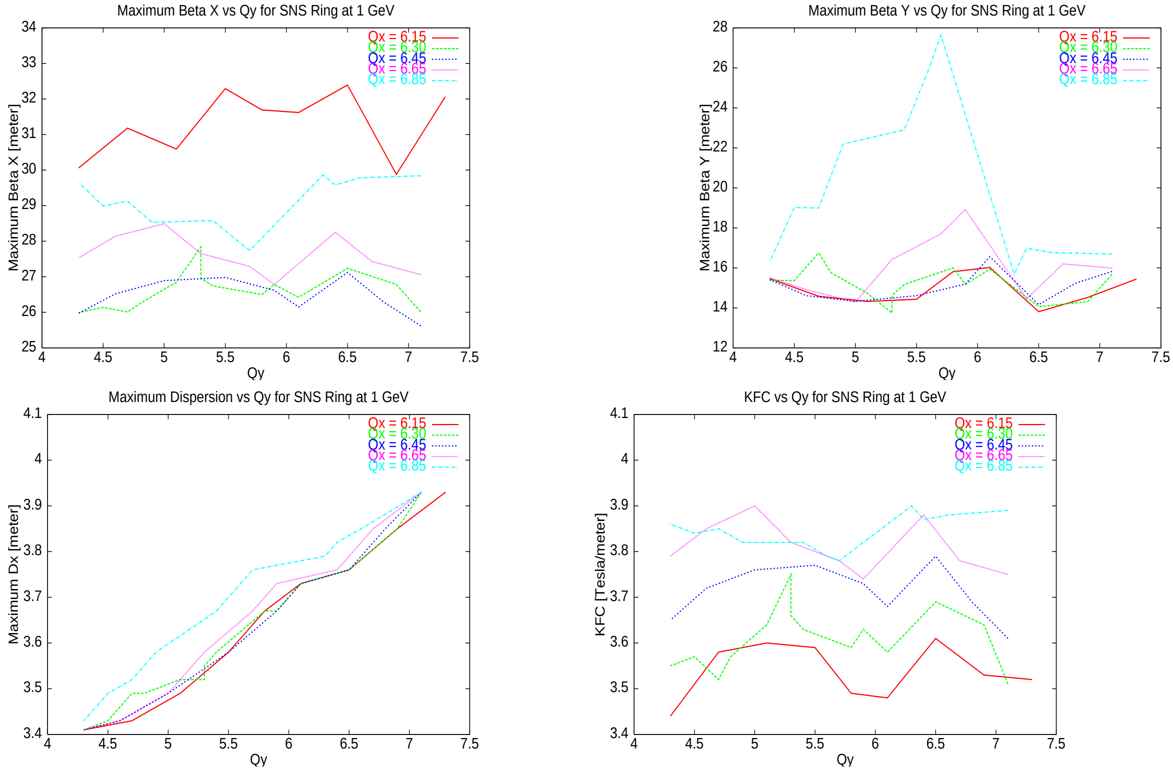

Figure 19: Parameters found in tune space survey.

second region, so we concentrate on operating points in the region $6.15 < \nu_x, \nu_y < 6.5$. Figure 20 shows this region, including all resonance lines to fourth order and two potential operating points. Of these, the point at $(\nu_x, \nu_y) = (6.4, 6.3)$ is further removed from the second order structure resonance at 6.0, but nearby third and fourth order sum resonances will require correction to prevent beam loss. The point at $(\nu_x, \nu_y) = (6.23, 6.2)$ avoids the higher order resonances, but at high intensities the tune spread may excite the structure resonance at 6.0. Both of these operating points have been subjected to full beam dynamic studies [8, 9, 10].

Because these two operating points are reasonably close in tune space, their lattice functions are quite similar. The horizontal and vertical beta functions both peak at the doublets in the straight sections, at approximately $\beta_x = 27m$ and $\beta_y = 15m$, respectively; and the dispersion in the arcs peaks at about $D_x = 3.7m$. At the injection foil, however, the beta values are $\beta_x = 7.2m$ and $\beta_y = 11.0m$ for the $(\nu_x, \nu_y) = (6.4, 6.3)$ operating point and $\beta_x = 10.4m$ and $\beta_y = 12.2m$ for the $(\nu_x, \nu_y) = (6.23, 6.2)$ operating point. Thus, the injection painting scheme must be optimized independently for each operating point. The horizontal and vertical chromaticities are about $\xi_x = -8$ and $\xi_y = -7$, respectively. Consequently, for $\Delta p/p_0 = \pm 0.01$, which corresponds to $\Delta E = 15MeV$ for $1GeV$ protons, the closed orbit deviation reaches $37mm$ in the arcs and about $1 - 2mm$ in the straight sections, and the horizontal and vertical tunes are shifted by about $\Delta\nu_x = -0.08$ and $\Delta\nu_x = -0.07$, respectively.

The injection chicane consists of four static horizontal dipole magnets in one of the $12.5m$ straight section drifts and eight dynamic bump magnets (four horizontal, four vertical) arrayed symmetrically in the corresponding $6.85m$ drifts. When the static injection dipoles are

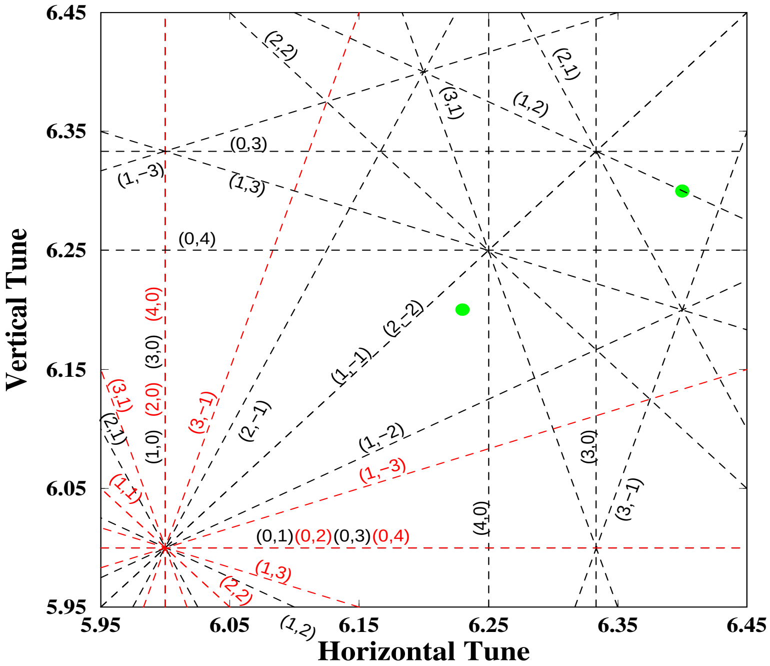

Figure 20: Potential operating points in tune space. All resonance lines through fourth order are shown.

included in the ring lattice, the horizontal closed orbit is bumped about $10cm$ in the injection region. This bump leads to a local blip, also of $10cm$, in the dispersion function and to beta-beating of about 5% in β_y at the doublets. When the dynamic bump magnets are activated, the beta-beating is not strongly affected, but they do generate a residual dispersion function around the ring. In the case of a large bump ($40mm$ in x and $46mm$ in y - sufficient to direct the closed orbit through the foil), the residual horizontal dispersion peaks at $D_x = 25cm$ in the straight section doublets, and there is a vertical dispersion function of up to $D_y = 15cm$ distributed around the ring. For $\Delta p/p_0 = \pm 0.01$ the horizontal closed orbit deviation peaks at about $6mm$ and the vertical closed orbit deviation reaches about $1.5mm$ in the straight sections.

Among the corrector magnets are four sets of chromatic sextupoles in the arc sections. With these sextupoles activated and set to eliminate the first order chromaticities and reduce the variation of the beta functions with energy, the main effect is the reduction of the chromaticities to near zero. The tunes remain essentially constant ($\Delta\nu < 0.01$) for particles with $\Delta p/p_0 = \pm 0.01$. The effect of eliminating the variation of the beta functions with energy is to make the ring maximum beta function values at $\Delta p/p_0 = 0$ minima when plotted versus energy. In spite of eliminating the first order energy variation, the maximum beta function values at $\Delta p/p_0 = \pm 0.01$ typically exceed those at $\Delta p/p_0 = 0$ by a few percent, and for one case, the $(\nu_x, \nu_y) = (6.23, 6.20)$ operating point, the increase in maximum β_x is 20%.

The effects of magnet errors have also been studied. One example involves the large arc quadrupoles, which are located at the maxima in the dispersion function and which accordingly have $26cm$, rather than $21cm$, bore radii. Introducing random magnetic field errors, using a Gaussian distribution of 0.4% width and truncated at 1% maximum error, into these magnets results in beta-beating of about 4% in β_x and in an increase in the maximum of the horizontal disperion function D_x from $4.00m$ to $4.35m$ for the $(\nu_x, \nu_y) = (6.23, 6.20)$ operating point. Because these are focusing quadrupoles, the vertical lattice functions are little affected by the errors. To avoid these errors, the large arc quadrupoles will be placed on their own separate power supply.

Another possible source of error would be a dynamic mismatch of the injection kicker strengths. We considered an extreme worst case situation of 1% errors in the kicker field strengths at the large kick size of $40mm$ in x and $46mm$ in y. The errors were assigned systematically to maximize their effect. The result was a mild closed orbit distortion of $1.6mm$ distributed around the ring. Thus, the control of the beam painting afforded by the kickers will be good.

The results of these optical ring lattice studies have been and are continuing to be used to guide beam dynamic investigations such as determination of injection painting schemes, dynamic aperture and loss calculations, determining collimator settings, and other design issues.

2.2.5 Acceptance

2.3 Beam Loss

In this section, we will calculate the total loss budget expected under nominal conditions and assuming no cleaning systems in both the accumulator ring and transfer lines. Cleanig systems described in section 3.7 are then introduced to concentrate these losses in special areas where restricted acces and special safety procedures will be put in place. The design and layout of the cleaning sections is based on this loss budget and the collimators are required to whitstand the heat load and deformations produced by the losses.

After the various cleaning systems are introduced, a large percentage of these losses will in this way become "controlled losses" and only a small fraction will attain the machine becoming what we call "uncontrolled" loss. These uncontrolled losses are mainly due to the inefficiency of the cleaning systems or to loss mechanism itself. The estimations of the prompt and remanent radiation levels and the calculaions of the required shielding are based in the distribution and intensity of uncontrolled losses. This will be presented after the introduction description of the cleaning systems in section 3.7.

2.3.1 HEBT beam-loss budget

Along the HEBT, the sources of uncontrolled loss are scattering with the residual gas and magnetic H^- stripping.

At 1 GeV the cross sections of H^- stripping for Nitrogen and Hydrogen are

$$\sigma_N = 9.14 \cdot 10^{-19}\ cm^2$$

$$\sigma_H = 1.30 \cdot 10^{-19}\ cm^2.$$

With a vacuum of $5 \cdot 10^{-8}$, the fractional stripping losses account for $\approx 2.8 \cdot 10^{-5}$ along 170 meters or $1.6 \cdot 10^{-7}$ per meter. The scattering produces a flux of neutraly charged halo particles that are homogeneously distributed along the line and inside the magnetic fields. Most of then will thus become uncontrolled loss. These losses take place continuously during normal operation. We may expect though variations if the vacuum pressure or the composition of the residual gas changes unexpectedly.

For magnetic stripping losses, magnet strength is chosen so that the magnetic stripping is at the 10^{-8}per meter level much lower than the vacuum stripping loss.

Steady losses happenning in the HEBT are mostly linked to tails coming from the LINAC. The rms emittance of the beam coming from the linac is expected to be small ($\epsilon_{rms} = 0.5\ \pi$mm·mrad normalised) but large tails in the distribution may contain a fraction of the beam larger than 10^{-4}. Fig. 21 shows the beam fraction contained in the tails of a gaussian beam depending on the beam rms emittance. A factor of two in the beam emittance coming from the linac yields an increase of three orders of magnitude in the halo population. These losses are suceptible of being removed by collimators placed on the path of the beam before the achromat. This collimation system is described in section 3.7.

Longitudinal loses may ocurr if the energy jitter or the energy spread of the beam are larger than expected. No quantification has been done of this effect as it will depend in a large measure of operating conditions. A cleaning device has been foreseen to catch this longitudinal tails before the achromat.

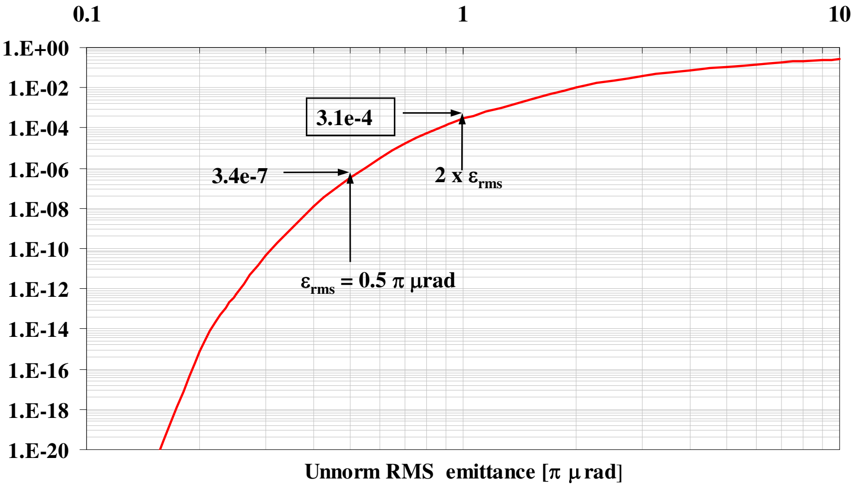

Figure 21: Fraction of the beam exceeding a fixed aperture in the HEBT line. The aperture is chosen to match 13πmm·mrad, half of the HEBT acceptance and equal to the collimator acceptance.

2.3.2 Ring beam-loss budget

During the process of injection and accumulation, space-charge and resonance crossing are expected to make the protons diffuse outwards frm the beam center. Following tracking studies and an optimization of the painting schemes, a fraction of $2.0 \cdot 10^{-3}$ of the beam is assumed to be in the tails of the beam...

Special attention is required at the injection as extraction sections

Injection area The main source of loss in the injection section is the nuclear scattering of the beam in the Carbon foil. Besides, we also need to consider the magnetic stripping of the H^- beam in the second dipole of the injection chicane INJB2 where the H^- beam traverses an area close to the magnet coil and of high megnetic field.

The losses produced at the injection foil are dominated by nuclear scattering. Once the energy and foil thickness have been defined, the loss is determined by the size of the incoming beam and the painting scheme. The maximum number of foil crossings has been estimated by simulation. The average number of foil crossings per proton is ≈ 7 in nominal conditions. Yet, if the beam emittance increases or deviates from a Gaussian distribution, this number increases up to 12 crossings per proton. For a carbon foil of 300 μg/cm^2, the fractional loss at the foil due to nuclear scattering will be $\approx 3.7 \cdot 10^{-5}$ under nominal conditions and up to $\approx 6.3 \cdot 10^{-5}$ for an exceptional large beam.

The fractional loss per meter due to magnetic stripping of H^- is given by the formula

$$\frac{N_{loss}}{NL} = \frac{B}{K_1} e^{-\frac{K_2}{\beta\gamma c B}}$$

$$K_1 = 8 \cdot 10^{-6}; K_2 = 4.3 \cdot 10^9$$

V/m where B is the magnetic field in Tesla and β and γ are the relativistic parameters.

We assume a magnetic field of 0.3 Tesla. For this magnetic field, $1.3 \cdot 10^{-7}$ of the beam will be lost along the effective magnetic length of the dipole ($\approx$ 1 meter) at 1 GeV. For a momentum of 1.3 GeV, the magnet should be replaced with a longer version and the magnetic field reduced to 0.25 to keep the same level of stripping losses.

2.3.3 RTBT beam-loss budget

The beam reaching the RTBT line is assumed to be well inside tha aperture thanks to careful painting and collimation in the ring. No steady losses are expected from halo development or partial cleaning.

In addition to that, the optics of the RTBT has been calculated such that a failure of one of the fourteen extraction kickers will produce an orbit deviation along the RTBT line but no beam hits the vacuum pipe and the beam impacts the target at the nominal location. In the event of a failure of two kickers, approximately 10% of the beam would be lost in the transfer line. Figure 18 shows the trayectory of the beam along the RTBT when any one of the fourteen kickers fail to work. Also maximum deviation of the closed orbit along the line in the case f two kicker failures is indicatedas an envelope by the black line. Form this plot is it clear the losses would be localized inside a range of 10 to 20 meters. In the rare case of more than two kicker failures, the whole pulse would be lost. The average beam losses will be given by the probability of kicker failure. Nevertheless, we have to draw attention to the fact that prompt losses would be high and very localized. The RTBT collimators are essential to prevent transient losses and protect the target vessel from the extraction misfunction. The design of the collimators has been done to resist two whole consecutive pulses after which the machine should be stopped and the kickers fixed.

One should include in this section the losses in the target window due to nuclear scattering.

2.4 Single-particle Effects

Typical values for the tune spread due to different mechanisms in the SNS ring are given in Table 18.

Table 18: Tune spread produced by various mechanisms on a 2 MW beam with transverse emittance of 480 π mm mrad and momentum spread of ±1%.

Mechanism	Full tune spread
Space charge	0.15-0.2 (2 MW beam)
Chromaticity	±0.08 (1% $\Delta\ p/p$)
Kinematic nonlinearity (480π)	0.001
Fringe field (480π)	0.025
Uncompensated ring magnet error (480π)	±0.02
Compensated ring magnet error (480π)	±0.002
Fixed injection chicane	0.004
Injection painting bump	0.001

2.4.1 Kinematic nonlinearity

Note that, even in the absence of any field, the motion of a relativistic particle in free space is a non-linear function of the canonical momentum $\mathbf{p}$. The "kinematic non-linearity" refers to these high-order terms in the expansion of the classical relativistic Hamiltonian which contain only the transverse momenta, p_x and p_y. This non-linearity is negligible in high-energy colliders (*e.g.* RHIC, LHC), where $p_{x,y} \ll p_z$ but it becomes noticeable in low-energy high-intensity rings. In fact, a measure of the impact of this non-linearity is given by the first-order tune-shift. By keeping all the kinematic terms in the expansion of the Hamiltonian, one can obtain a general expression for the first-order tune-shift they induce [47]. The first, usually dominant, term in the series gives an octupole-like tune-shift, *i.e.* linear in the actions. For a high-intensity rings, where the emittance is large and the gamma functions in the straight sections exceed unity, the kinematic terms give a non-negligible tune-shift. For the SNS accumulator ring it is about 10^{-3} at 480 π mm mrad.

2.4.2 Sextupole Effects

The most common magnet non-linearity encountered in small rings arises from high-field sextupoles introduced for chromaticity control. The SNS ring contains twenty chromatic sextupoles, placed in the arcs in high β and dispersion areas [46]. Their non-linear effect has been quantified and found small. Sextupole-like contributions also come from the leading-order fringe-field effect of the thirty-two arc dipoles. These sextupole effects, also small, can easily be corrected by the eight dedicated sextupole correctors.

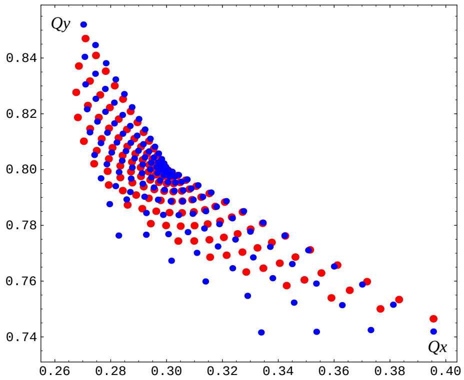

Figure 22: Tune footprints of the SNS ring with a dodecapole error in the quadrupoles of $b_6 = 60$units; results are from tracking data (blue) or the analytic result (2) (red).

2.4.3 Magnet imperfection and nonlinearities

In a magnet with normal quadrupole symmetry the first allowed multipole error is the normal dodecapole, b_6. In the absence of pole-tip shaping, this error can be exceedingly large: for the SNS 21 cm quadrupole [47], an OPERA-3d [62] simulation (with un-shaped ends) gives a dodecapole component of about 120 (in units of 10^{-4}, normalized with respect to the main, quadrupole, component).

Because the dodecapole error is quite localized, its effect can be computed using a thin-element approximation. Applying first-order perturbation theory, one finds the tune-spread induced by dodecapole errors is given by

$$\begin{pmatrix} \delta\nu_x \\ \delta\nu_y \end{pmatrix} = \sum_i \frac{b_{6i} Q_i}{8\pi B\rho} \mathcal{D}_i \begin{pmatrix} J_x^2 \\ J_x J_y \\ J_y^2 \end{pmatrix} , \tag{2a}$$

where $\mathcal{D}_i$ denotes the 3 × 2 matrix

$$\begin{pmatrix} \beta_{xi}^3 & -6\beta_{xi}^2\beta_{yi} & 3\beta_{xi}\beta_{yi}^2 \\ -3\beta_{xi}^2\beta_{yi} & 6\beta_{xi}\beta_{yi}^2 & -\beta_{yi}^3 \end{pmatrix} . \tag{2b}$$

Here the index i runs over all dodecapole kicks in the ring, *i.e.* over the entrances and exits of all quadrupoles. Note that this effect depends linearly on the error strength, but quadratically on the amplitude. A comparison of this analytic result with MaryLie tracking data has shown a striking agreement [47]. In addition, it was made put in evidence that the very large uncorrected dodecapole error gives a tune-spread roughly twice that caused by the quadrupole fringe fields. By shaping the ends of the quadrupoles, one can reduce the b_6 error to 1 unit or less [63]. This constitutes *local* compensation. One might also correct the b_6 error by adding a small negative dodecapole component through the body of the magnet. In Fig. 23 we compare the tune-spreads (2) after local and body compensation. In this example, the compensation works well in both cases, with local compensation being slightly better. But, in fact, it is essential to use local compensation: because the tune-spreads (2) depend cubically on the β functions, the results of body compensation will be very sensitive to the ring optics.

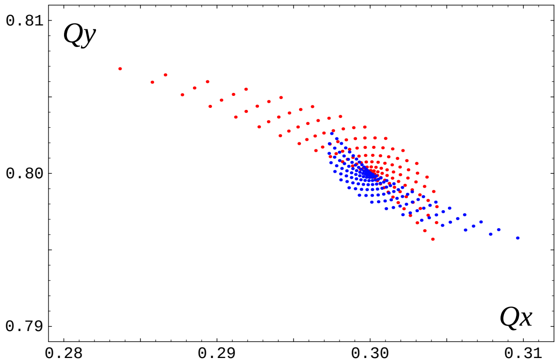

Figure 23: Comparison of tune-shift plots using body (red) and local (blue) compensation of the dodecapole component in the SNS ring quadrupoles [47].

2.4.4 Magnet fringe fields

The relative impact of a longitudinal fringe field on a particle's transverse momentum is proportional to the ratio of transverse emittance to magnetic length [56]. Hence, the effect of quadrupole fringe-fields is usually small in low-emittance, low aspect-ratio machines (*e.g.* RHIC, LHC) but is very important for high-emittance, high aspect-ratio machines such as the SNS. For a quadrupole one can evaluate the fringe-field contribution in the limit of zero fringe length. The corresponding Hamiltonian for a single fringe (to leading order) is [57, 58]

$$H_f = \frac{\pm Q}{12B\rho(1+\frac{\delta p}{p})}(y^3p_y - x^3p_x + 3x^2yp_y - 3y^2xp_x), \tag{3}$$

where Q_i is the quad strength, and the + and − signs are used at, respectively, the entrance and exit of the magnet. It follows, as Lee-Whiting showed many years ago [59], that a quadrupole fringe-field induces an octupole-like transverse kick. Using MaryLie [48], one can build quadrupole maps that include fringe fields based on either (3) or an exact representation [60]. We created tune footprints by applying Laskar's frequency analysis [61] to 1200 turns of MaryLie tracking data. Particles were launched in different directions out to 1000π mm mrad, and the only non-linearities included were those caused by thick elements and magnet fringe fields. Figure 24 shows that quadrupole fringe fields have an important impact on the dynamics of the SNS ring, giving tune spreads of about (0.04,0.03) at 1000π mm mrad, roughly one-third the space-charge tune spread [55]. In addition, Fig. 24 shows that the hard-edge model slightly overestimates the fringe-field effect and therefore represents a conservative estimate.

In our case the tune spread can be accurately represented by the results of first-order perturbation theory [57, 58]:

$$\begin{pmatrix}\delta\nu_x\\ \delta\nu_y\end{pmatrix} = \begin{pmatrix}a_{hh} & a_{hv}\\ a_{hv} & a_{vv}\end{pmatrix}\begin{pmatrix}2J_x\\ 2J_y\end{pmatrix}, \tag{4}$$

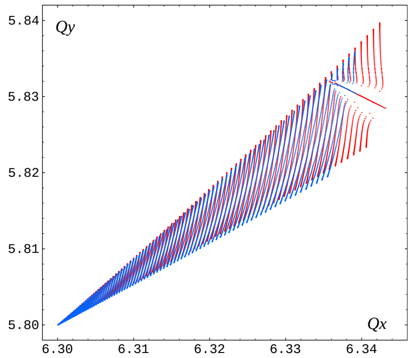

Figure 24: Tune footprints of the SNS ring, based on realistic (blue) and hard-edge (red) quadrupole fringe fields.

where the normalized anharmonicities are given by

$$\begin{aligned} a_{hh} &= \frac{-1}{16\pi B\rho} \sum_i \pm Q_i \beta_{xi} \alpha_{xi}, \\ a_{hv} &= \frac{1}{16\pi B\rho} \sum_i \pm Q_i (\beta_{xi}\alpha_{yi} - \beta_{yi}\alpha_{xi}), \\ a_{vv} &= \frac{1}{16\pi B\rho} \sum_i \pm Q_i \beta_{yi} \alpha_{yi}. \end{aligned} \tag{5}$$

Here the index i runs over the entrances and exits of all quadrupoles in the ring, and the $+$ and $-$ signs are as in (3). Note that the entrance and exit fringe fields do *not* cancel one another: even if the β functions are equal at the entrance and exit, the α functions usually change sign, leading to an additive effect. For the SNS lattice we find $(a_{hh}, a_{hv}, a_{vv}) \approx (49, 22, 42)\ m^{-1}$, and these values closely match (apart from the obvious resonance) the results shown in Fig. 24.

2.4.5 Resonances analysis and frequency maps

We used frequency maps to study the impact of different resonances to the single-particle dynamics of the SNS [52]. In particular, the efficiency of different working points was studied regarding single particle dynamics considerations. In order to compare the performance of each working point, we used the tune diffusion indicator, which is computed by the average of the tune differences used for the construction of the diffusion maps and normalized by the initial emittances, for all the integrated orbits [61]. This indicator is correlated with other global chaos indicators, as the resonances driving terms norm and the dynamic aperture [51]. We plot the value of the tune diffusion coefficient versus the $\delta p/p$ for all w.p., on the top of Fig. 25. The pick values on the diffusion indicators, for all w.p., correspond to areas of the phase space that are perturbed due to 4th order resonances, showing once more the destructive effect of quadrupole fringe fields. The doted lines on the plots represent the average values of the diffusion indicators for all tracked momentum spreads. It is clear that (6.23,6.20) is the best w.p. choice, followed by (6.4,6.3). Their performance can be further improved by using the available multi-pole correctors [53], for correcting the normal and skew 3rd order resonances, in the case of (6.4,6.3), and the 4th order normal resonances in the case of (6.23,6.20). The other two w.p. have the disadvantage of crossing major structural coupling and 4th order resonances, which are very difficult to correct.

In the center of Fig. 25, we plot the tune diffusion coefficient when using the 4 families of chromaticity sextupoles [46] in order to set the chromaticity to 0. In that case, the chromatic tune-shift is completely canceled and all the particles with different $\delta p/p$ are located in the same area of the tune diagram. This is reflected in the very weak dependence of the tune diffusion coefficient with respect to the momentum spread. Furthermore, the values of the average diffusion coefficient are almost equal to the ones for $\delta p/p = 0$, when the chromatic sextupoles are switched-off. This proves the very small non-linear effect introduced by the chromaticity sextupoles. Finally, note that, in this case, (6.3,5.8) seems to be the best w.p. choice. Nevertheless, this is not a fair comparison, as the space-charge force depresses the tunes. A better picture of the w.p. performance can be estimated by the average tune diffusion coefficient of all particles with positive momentum spread and non-zero chromaticity (at the bottom of Fig. 25). The results are pretty much the same as in the case of natural chromaticity.

2.4.6 Dynamic aperture

In Figs. 26, we plot the maximum survival amplitude (in terms of total emittance) of particles launched in 5 different initial ratios of the transverse emittances, with three different momentum spreads ($\delta p/p = 0, \pm 0.2$). The momentum spread of ± 0.2 is indeed higher than the actual RF bucket size of ± 0.7. Nevertheless, it corresponds to the momentum acceptance of the ring and halo particles can reach this level before they are “cleaned” by the Beam-In-Gap kicker. By Figs. 26, one may observe the unacceptable reduction in the dynamic aperture of the SNS ring below the physical aperture of 180 π mm mrad for a momentum spreads of -0.2 (green curve on the left). This is attributed to the fact that the chromaticity pushes the particles' vertical tune towards the very dangerous integer resonance, at $Q_y = 6$ and the particles get rapidly lost. A less pronounced reduction of the dynamic aperture can be attributed to the half-integer resonance at $2Q_y = 11$ for particles with momentum spread of 0.2 (red curve on the left). Finally, the on momentum particles have very similar dynamic aperture (blue curves).

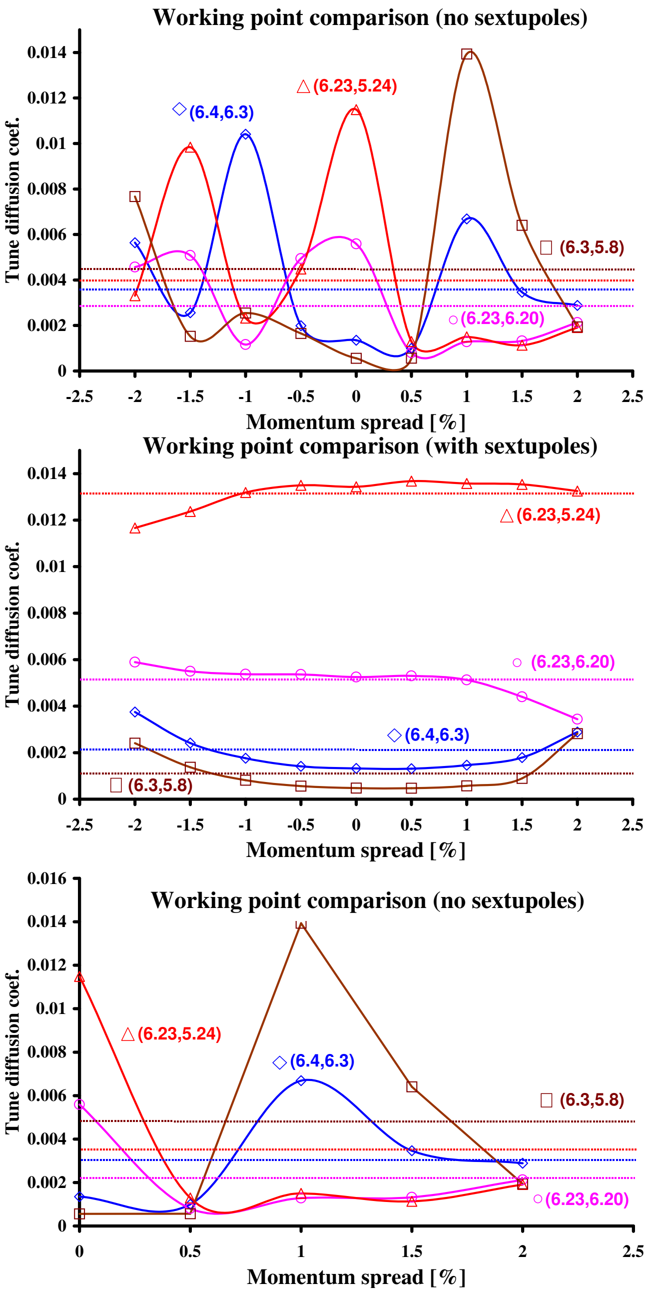

Figure 25: Tune diffusion coefficients for all working points versus the different momentum spreads, for natural chromaticity (top), for zero chromaticity (center) and for natural chromaticity and only positive momentum spread (bottom). The dashed lines are the average of the coefficient over all momentum spreads.

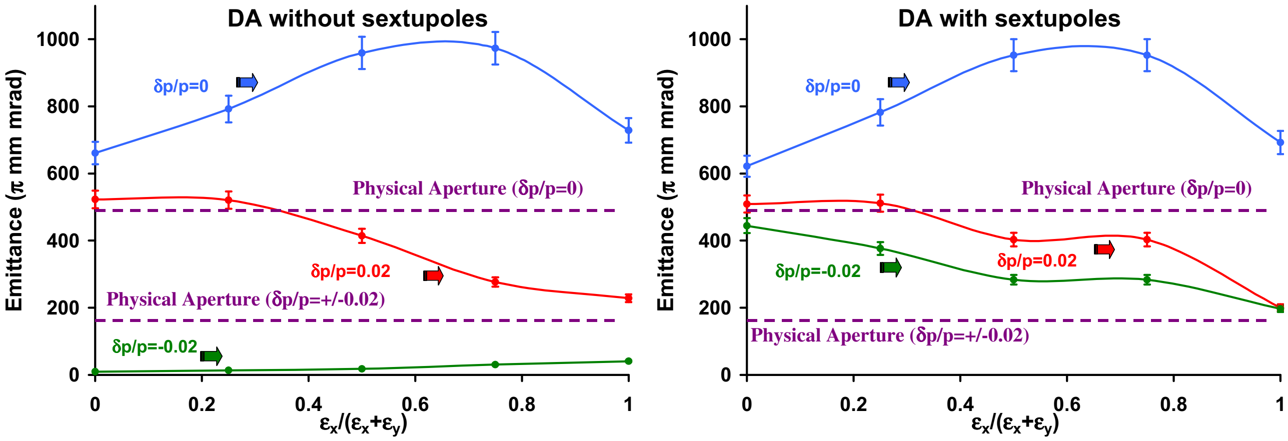
DA without sextupoles

DA with sextupoles

Figure 26: Dynamic aperture for the working point (6.3,5.8), without (left) and with (right) sextupoles.

2.5 Multi-particle Effects

One of the primary tasks in the design of the SNS ring is to control collective effects. Dominant collective effects include space charge, impedance driven instabilities and electron cloud. Transverse painting is used to alleviate space charge force. The variety of space-charge induced halo growth mechanisms and space-charge limit for the SNS ring were explored both analytically and numerically [17]-[24]. Estimates of the coupling impedance and its effect on beam stability are performed through the design stage of the project. The key impedance contributions are identified and benchmeasured with the instability thresholds being estimated [26]- [33]. The cures to prevent instabilities are implemented and feedback system is being evaluated [31], [34].

2.5.1 Space-charge effects

In the longitudinal direction, space charge contributes a defocusing force below transition energy. The corresponding potential is

$$V_{sc} = -IZ_{sc};\ Z_{sc} = -j\frac{nZ_0g_0}{2\beta\gamma^2};\ g_0 = 1 + 2\ln\frac{b}{a}, \tag{6}$$

where I is the peak current, $n = \omega/\omega_0$ is the frequency harmonic, $Z_0 = 377\Omega$, a and b are the average radii of the beam and vacuum chamber, respectively. The bunch spread may cause particle leakage from the RF bucket requiring of enhanced RF field focusing. The SNS ring will have a dual harmonic RF system with peak amplitudes of 40 kV for harmonic $h = 1$ and 20 kV for $h = 2$ which brings the bunch leakage to a negligible level.

In the transverse direction, the space-charge tune shift sets space-charge limit due to the excessive beam loss associated with the low order machine resonances. The maximum incoherent tune shift for the particles near the center of beam distribution can be estimated by

$$\Delta\nu_{inc} = -\frac{N_0r_0R_0}{\pi\nu_0\beta^2\gamma}\left[\frac{\gamma^{-2}-\eta_e}{2\sigma_{x,y}(\sigma_x+\sigma_y)}\frac{F_{sc}}{B_f} + \left(\beta^2 + \frac{\gamma^{-2}-\eta_e}{B_f}\right)\frac{\epsilon_1}{b^2} + \kappa\beta^2\frac{\epsilon_2}{g^2}\right], \tag{7}$$

where r_0 is the classical radius of protons, R_0 is the average radius of ring circumference, ν_0 is the zero-current betatron tune, $\sigma_{x,y}$ is the rms beam size, b is the radius of vacuum chamber, g is the distance to magnetic poles from the beam pipe center, B_f is the bunching factor, η_e is the neutralization factor, κ is a factor showing portion of ring circumference covered with the magnetic poles and F_{sc} is a form factor depending on beam distribution changing from $F_{sc} = 1/2$ for the uniform density beam to $F_{sc} = 1$ for the Gaussian beam. The coherent tune shift of a dipole transverse oscillation of a beam with penetrating magnetic fields is given by

$$\Delta\nu^p_{coh} = -\frac{N_0r_0R_0}{\pi\nu_0\beta^2\gamma}\left[\left(\frac{\gamma^{-2}-\eta_e}{B_f} + \beta^2\right)\frac{\xi_1}{b^2} + \kappa\beta^2\frac{\xi_2}{g^2}\right], \tag{8}$$

and, with non-penetrating magnetic fields, by

$$\Delta\nu^{non-p}_{coh} = -\frac{N_0r_0R_0}{\pi\nu_0\beta^2\gamma}\left[\left(\frac{\gamma^{-2}-\eta_e}{B_f}\right)\frac{\xi_1}{b^2} + \beta^2\frac{\epsilon_1}{b^2} + \kappa\beta^2\frac{\epsilon_2}{g^2}\right]. \tag{9}$$

The Laslett image coefficients $\epsilon_{1,2}$, $\xi_{1,2}$ depend on the geometry of beam pipe, with the subscripts $1, 2$ referring to the electric and magnetic problems, respectively.

Other high-order coherent beam modes are also depressed by a direct space-charge force similar to a single particle depression (which is different from the first order dipole mode not effected by a direct space-charge force with the dipole coherent tune shift $\Delta\nu_{coh}$ in Eqs. 8-9 caused by the image effects). The accurate treatment of beam response to machine resonances should include collective beam behaviour. As a result, the space-charge limit associated with the crossing of the half-integer resonance may be significantly altered when the quadrupole oscillation of beam envelope is taken into account [24].

For the SNS ring, space-charge tune shifts for a realistic distribution based on multi-turn injection painting were calculated using the simulation program UAL/ORBIT [25]. The transverse painting and dual harmonic rf system are used to control the direct incoherent space-charge tune shift with the goal not to exceed $\Delta\nu = 0.2$. The choice of the working tune is then based on consideration of the space-charge induced resonances and the avoidance of dangerous nonlinear resonances excited by magnet imperfections in the presence of the space-charge induced tune spread.

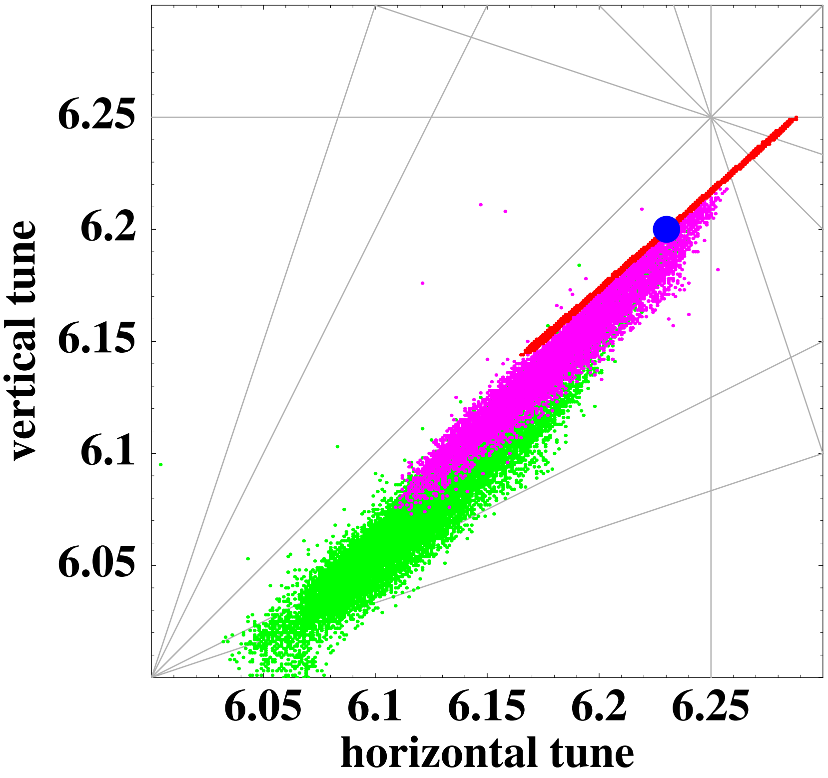

Figure 27: Tune spread at the end 1060-turn injection due to space charge and $\Delta p/p = 0.6\%$ for three final intensities 1)$N = 1 \cdot 10^{13}$ (red), 2) $N = 1 \cdot 10^{14}$ (pink), 3) $N = 2 \cdot 10^{14}$ (green).

For the base line working point, the tune spread for three beam intensities is shown in

Fig. 27. Figure 28 shows combined tune spread of a 2MW beam due to the space charge and $\Delta p/p$. The variety of the space-charge effects and associated beam halo were explored and the space-charge limit for the base line working point was found to be around $N = 2 \cdot 10^{14}$ protons.

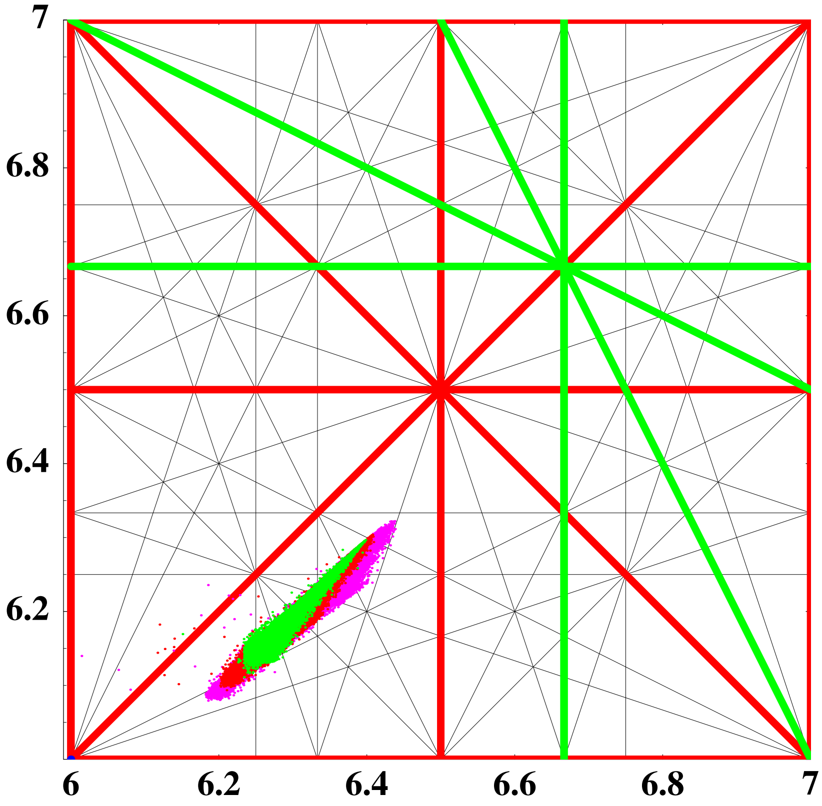

Figure 28: Tune spread of a 2 MW beam for 1)space-charge alone (green), 2) space charge and $\Delta p/p = 0.6\%$ (red), 3) space charge and $\Delta p/p = 1.0\%$ (pink).

The most effective approach to resolve space-charge problems is to rise the injection energy. Other ways of space-charge compensation can be considered but they should be carefully evaluated. For example, space-charge compensation with inductive inserts can lead to a microwave instability if ferrite material have significant losses.

2.5.2 Impedance budget

The longitudinal coupling impedance is defined as

$$Z_{\|}(\omega) = \frac{\int E_z exp(jkz)dz}{I}, \tag{10}$$

assuming a harmonic excitation current of amplitude $I(\omega)$ which excites a harmonic field with complex amplitude $E_z(\omega)$. The transverse coupling impedance is defined as the integral of the deflecting fields over one turn normalised by the dipole moment of the excitation beam current

$$Z_\perp(\omega) = j\frac{\int \Big[E_r + \beta c B_\theta\Big] exp(j\omega z/v)dz}{I\Delta y}, \tag{11}$$

where Δy is the horizontal or vertical offset of the beam from the axis.

At low frequency the impedance is dominated by the skin effect of the vacuum chamber; at medium and higher frequencies the impedance behaves as that of a broad band resonator - thus the word "broadband" impedance. At certain high frequencies there will be strong local resonances, for example, from cavities.

The impedance budget of the SNS ring is being constantly evaluated with the key contributors benchmeasured. The low-frequency contribution is shown in Table 19, for frequencies below 10MHz. Table 20 shows the impedance contribution at an arbitrary chosen frequency of 50MHz.

Some formulas and methods which were used for impedance budget estimates are summarized below:

Space charge The longitudinal space-charge impedance is calculated using

$$Z_\| = -j\frac{Z_0}{2\beta\gamma^2}\frac{\omega}{\omega_0}\left(1 + 2\ln\frac{b}{a}\right). \tag{12}$$

The transverse space-charge impedance is given by

$$Z_\perp = -j\frac{RZ_0}{\beta^2\gamma^2}\left(\frac{1}{a^2} - \frac{1}{b^2}\right). \tag{13}$$

Extraction kicker A prototype of the SNS extraction kicker was measured [33]. The impedance for all 14 kickers was then obtained using the scaling formula [12].

RF cavity The RF cavity impedance was measured [13]. The contribution from the high-order modes to the longitudinal impedance is negligible. For the transverse impedance, a resonant mode at 17.6 MHz was measureed when the cavity was in the first harmonic configuration. The second harmonic configuration did not give that mode. This resonant impedance was strongly decreased by placing four 40Ω carborundum rods (glow-bars) on top and bottom of each gap [15].

Injection foil assembly The impedance of the foil assembly was calculated with the MAFIA code and is expected to be negligible. A possible resonant impedance at 170 MHz can be damped with a lossy material. This impedance will be measured when the device will be built.

Resistive wall Assuming a smooth cylindrical beam pipe of radius b, the longitudinal and transverse impedances are

$$Z_{\|} = \left(sgn(\omega) + j\right)\frac{\beta Z_0 \delta_s}{2b}\frac{\omega}{\omega_0}, \tag{14}$$

$$Z_{\perp} = \left(sgn(\omega) + j\right)\frac{R Z_0 \delta_s}{b^3}, \tag{15}$$

where δ_s is the skin depth at the frequency ω.

BPM, Beam-in-Gap kicker and Tune kikers All these devices are based on the dual plane striplines. For one strip plate

$$Z_{\|} = Z_c\left(\frac{\phi_0}{2\pi}\right)^2\left(\sin^2\frac{\omega l}{c} + j\sin\frac{\omega l}{c}\cos\frac{\omega l}{c}\right), \tag{16}$$

where Z_c is the characteristic impedance of the stripline. Each stripline has a length l and subtends an angle ϕ_0 to the beam pipe axis. For a pair of striplines

$$Z_{\perp} = \frac{c}{b^2}\left(\frac{4}{\phi_0}\right)^2\sin^2\frac{\phi_0}{2}\left(\frac{Z_{\|,2}}{\omega}\right), \tag{17}$$

where $Z_{\|,2}$ is the longitudinal coupling impedance for a pair of striplines.

Broadband impedance The broadband impedance is caused by the bellows, steps, vacuum ports, valves and collimators. The impedance of these components is estimated using the low-frequency approximation formulas for the longitudinal impedance [26]. The transverse impedance is then obtained using an approximate relation

$$Z_{\perp} \approx \frac{2R}{\beta b^2}\left(\frac{Z_{\|}}{n}\right). \tag{18}$$

The impedance of the collimators was estimated using calculations with the MAFIA code, which was found to be in a good agreement with the estimates given by the simple analytic formulas [14].

2.5.3 Impedance minimization

Impedance budget estimates and its minimization is an important measure to prevent collective instabilities.

The imaginary part of the impedance leads to the frequency tune shift while the real part directly contributes to the instability growth rates. The largest contribution to impedance budget in high-intensity rings is typically due to the space-charge, as can be seen in the Tables. However, space-charge contribution is purely imaginary and thus should not be directly used in the stability estimates. On the other hand, large space-charge impedance should not be forgotten, since, in combination with the real part of the impedances coming from other sources, it can strongly influence beam stability as discussed in the following sections.

Table 19: SNS impedance budget below 10MHz

	$\mathbf{Z}_{\parallel}/\mathbf{n}$ $[\Omega]$	$\mathbf{Z}_{\perp}$ $[k\Omega/m]$
Space charge	-j196	j(-5.8+0.45)$\times10^3$
Extraction kicker (25 Ω termination)	0.6n+j50	33+j125 (measured)
RF cavity (measured)	per cavity: 0.6 $(f = 7.49MHz,\ Q = 88)$ 0.2 $(f = 11.37MHz,\ Q = 59)$ 0.1 $(f = 35MHz,\ Q = 1)$ 0.9 $(f = 87MHz,\ Q = 20)$	total: 18 at 17.6MHz (damped by glow-bar)
Injection foil assembly (MAFIA calculation)	j0.05	j4.5
Resistive wall	(j+1)0.71, at ω_0	(1+j)8.5, at ω_0
Broadband		
BPM	j4.0	j18.0
BIG and TK	j1.1	j7
Bellows	j1.3	j11
Steps	j1.9	j16
Ports	j0.49	j4.4
Valves	j0.15	j1.4
Collimator	j0.22	j2.0
Total BB	j9	j60

Table 20: SNS impedance budget at 50MHz

	$\mathbf{Z}_{\parallel}/\mathbf{n}$ $[\Omega]$	$\mathbf{Z}_{\perp}$ $[k\Omega/m]$
Space charge	-j196	j(-5.8+0.45)$\times10^3$
Extraction kicker (25 Ω termination, measured)	19.4+j12	12.5+j65
RF cavity (measured)	per cavity: see before	total: 0 (at 17.6MHz)
Injection foil assembly (MAFIA calculation)	j0.05	j4.5
BPM	2.0+j3.5	9+j16
BeamInGap and TuneKicker	0.7+j0	5.0+j0
Broadband		
Bellows	j1.3	j11
Steps	j1.9	j16
Ports	j0.49	j4.4
Valves	j0.15	j1.4
Collimator	j0.22	j2.0
Total BB	j4.1	j35

As can be seen from the impedance budget table, the largest contribution to the real part of the impedance is from the extraction kickers. The presented measured values for the extraction kickers contribution is a result of significant minimization efforts with the largest reduction achieved by low termination impedance (25 Ω) of the pulse forming network (PFN) circuits [33].

Except for the injection kicker and some beam diagnostics sections, stainless steel vacuum chamber is used. Ceramic vacuum pipes are used to avoid eddy-current heating corresponding to an injection bump risetime of about 200 μs. Their coupling impedance is reduced by an internal 1 μm copper-film coating (much thinner than the skin depth of 0.9 mm). A second, 0.1 μm thin TiN coating is applied to supress the secondary yeild of electron generation.

The steps in vacuum pipe are designed with the tapering length at least three time longer than the step height to avoid sharp discontinuities and resonances. Vacuum ports and valves are shielded. The bellows are not shielded to avoid mechanical complications.

2.5.4 Measurements of coupling impedance

Although good estimates for simple accelerator components can be obtained from theoretical formulas, it is mandatory to determine the major impedance contributions in bench measurements. The validity of these measurements in which the beam is simulated by a single wire for longitudinal or a twin-wire for transverse impedance measurements has been documented by theoretical studies and experience at various machines.

The longitudinal coupling impedance of a component is conveniently measured by inserting a wire in the center of the beam pipe to form a coaxial transmission line. The forward scattering coefficient $s_{21}$is measured both for the device under test and a reference tube of the same length. The ratio,$S_{21} = s_{21}^{DUT}/s_{21}^{REF}$, yields the coupling impedance by an appropriate expression, either the conventional hp-formula or the log-formula [37].

In the typical situation, the characteristic impedance,R_c, of the line is different from the standard impedance of the network analyzer, R_0. Consequently a matching network, such as an impedance transformer, needs to be inserted. Often, for simplicity's sake, a resistive matching is applied. On the input side, forward and backward matching is achieved with a series and parallel resister,

$$R_p = G_p^{-1} = \frac{R_0}{\sqrt{1-\eta}} \sim R_0\left(1 + \frac{1}{2}\eta\right)$$

$$R_{in} = R_c \frac{\eta - \left(1 - \sqrt{1-\eta}\right)}{1 - \sqrt{1-\eta}} \sim R_c\left(1 - \frac{1}{2}\eta\right)$$

with $\eta = R_0/R_c$. Furthermore, on the output side, forward matching is achieved with a series resistor

$$R_{out} = R_c\left(1 - \eta\right)$$

As example for the SNS rf cavity measurement, the characteristic impedance of the 1.25 mm $\emptyset$ wire in the ~15 cm beam tube is
$R_c = \frac{Z_0}{2\pi}\ln\frac{r_o}{r_i} \approx 288\Omega$(vs. 265 Ω measured)

requiring the matching resistors, $R_p \approx 54\ \Omega$, $R_{in} \approx 263\ \Omega$, and $R_{out} \approx 213\ \Omega$.

At sufficiently low frequencies, the component is considered as a lumped element and the forward scattering coefficient follows as

$$s_{21} = \frac{2R_0}{R_0 + \left(R_{in} + R_c + Z_{||}\right)\left(1 + G_p R_0\right)}$$

The expression for the longitudinal coupling impedance is obtained from the ratio of the scattering coefficients,

$$Z_{||} = \left(R_c + R_{in} + \frac{R_0}{1 + G_p R_0}\right)\left(\frac{1}{S_{21}} - 1\right) = 2R_c\left(\frac{1}{S_{21}} - 1\right)$$

in full analogy to the well known hp-formula.

The numerical results for the coupling impedance are preferably presented as real and imaginary part, with the real part of direct interest to the beam stability analysis,

$$R_{||} = 2R_c\left(\frac{\Re(S_{21})}{\| S_{21} \|^2} - 1\right)$$

where $\| S_{21} \|$is the magnitude of the scattering coefficient ratio. Typically, this ratio is stored in the network analyzer as data/memory. By using the conversion from scattering to impedance format, the instrument can produce directly the real and imaginary part of the coupling impedance.

Alternatively, the measurements can be interpreted using the log formula,

$$Z_{||} = -2R_c \log_e S_{21}$$

This expression is derived as approximation for the case $Z_{||} \ll R_c$and is not suited for the wire measurement of the cavity shunt impedance. However, in contrast to the hp-formula, which is derived for a lumped, localized structure, the log formula sums correctly the small values of separate impedances by taking into account the phase shift between different locations. Apart from the fundamental resonance, the real part of the coupling impedance is given by

$$R_{||} = -2R_c \log_e \| S_{21} \|$$

with $\| S_{21} \|$ being downloaded in text format from the instrument.

The transverse coupling impedance of kickers can be measured on the bench by using the standard method in which a twin-wire "Lecher" line, simulating the beam, is inserted into the "Device Under Test". The forward transmission coefficients S_{21}^{DUT} of the kicker is compared with the S_{21}^{REF} obtained in a reference tube of at least equal length and is interpreted according to the HP-formula for lumped units,

$$Z^{DUT} \approx 2Z_L\left(1 - S_{21}^{DUT}/S_{21}^{REF}\right) / \left(S_{21}^{DUT}/S_{21}^{REF}\right),$$

or alternatively the log-formula,

$$Z^{DUT} = -2Z_L \log\left(S_{21}^{DUT}/S_{21}^{REF}\right)$$

with Z_L the characteristic impedance of the line. Finally, one obtains the transverse impedance as [38]

$$Z_\perp = \frac{c}{\omega}\frac{Z^{DUT}}{\Delta^2},$$

with Δ being the spacing of the two wires. This relation requires the knowledge of essentially three quantities: the measured impedance of the device under test, the effective wire spacing and the characteristic impedance. In the typical case of the wire diameter much smaller than the wire spacing, the effective Δ is given by the center-to-center distance of the wires. For wires of diameter d, with center to center spacing D, the effective spacing is known to be

$$\Delta = D\sqrt{1-(d/D)^2}.$$

In all other practical cases, it is necessary to make ad-hoc measurements of the effective spacing, either by a comparison with a line of known properties or by a direct measurement of the mutual inductance. [D. Davino and H.Hahn, to be published in Phys.Rev. S.T. Accel. Beams]

The twin-wire measurements of the SNS extraction kicker were performed by using a line, home-made from 5 × 7.5 mm rectangular tubes, shown in Fig. 29. The center-to center spacing is 45.6 mm, which in good approximation can be taken as Δ for the interpretation of the measurements based on the HP-formula. The other value required in the formula, the characteristic impedance of the line, was measured with a communication network analyzer, Tektronix CSA803, to be 260 Ω. Matching of the line characteristic impedance to the 50 Ω cables of the network analyzer, Agilent 8753ES, is achieved by means of 300 Ω transformers (North Hills 0501BB) with a center-tapped secondary winding, serving as 180° hybrid. The transformer covers the frequencies from 30 kHz up to 100 MHz. The network analyzer was set for a logarithmic frequency range from 100 kHz to 100 MHz, with 1601 points, and a 100 Hz bandwidth. In view of the various measuring errors, a 10-20% uncertainty in the quoted transverse impedances is expected.

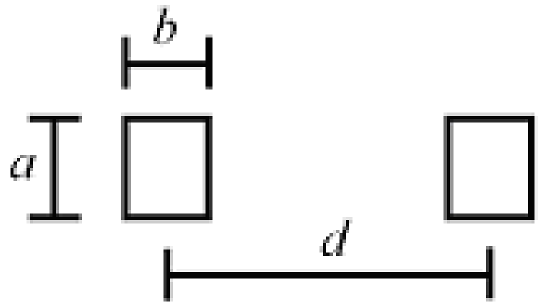

Figure 29: The homemade cable for the twin-wire measurements. The dimensions are: a= 7.5 mm, b=5 mm and d=45.6 mm.

A direct relation exists between the input impedance, Z_{in}, measured at the bus bar port and the external source contribution to the transverse impedance seen by the beam, and measured by the twin-wire method. Ignoring the smaller ferrite contribution for the sake of a simple approximation, a coupling impedance estimate follows by scaling the input impedance according to

$$Z_{\perp}^{in} = \frac{c}{\omega h^2} Z_{in}$$

where h is the aperture in kick direction. This points to the possibility of getting a reasonable idea of the coupling impedance by measuringZ_{in}, especially for kickers mounted in accelerators, provided that an access to the bus-bar is available. The possibility of obtaining the coupling impedance of an installed magnet by combining external impedance measurements at the kicker terminals with an analytical formula is obviously tempting. However, it must be emphasized that only the coupled flux contribution is accessible and the coupling impedance perpendicular to the kick direction is not seen. The comparison of results for the SNS extraction kicker demonstrated that an estimation of the real part is possible, whereas the imaginary part can differ.

2.5.5 Longitudinal instabilities

Disregarding the effect of space charge, the Boussard-Keil-Schnell criterion for longitudinal beam stability is

$$\mid Z_{\|}/n \mid \leq F_{\|} \frac{\mid \eta \mid B_f E_s}{e\beta^2 I_0} \left(\frac{\Delta E}{E_s} \right)^2_{FWHM}, \tag{19}$$

where I_0 is the average bunch current, η is the slip factor, and $F_{\|}$ is the distribution dependent form factor. One can see that large values of energy or momentum spread can help to damp the instability. Such a damping mechanism is known as Landau damping.

The largest resistive contribution to $Z_{\|}$ in the SNS ring come from the extraction kickers and high-order modes of the RF cavities. The space-charge effect plays a stabilizing role in the longitudinal beam stability, significantly raising the instability threshold. For the present impedance budget, the instability threshold with space charge is above $N = 3 \cdot 10^{14}$ [28].

2.5.6 Transverse instabilities

The transverse stability condition is given by

$$\mid Z_{\perp x,y}/n \mid \leq F_{\perp} \frac{4 B_f E_s}{e\beta\beta_{x,y} I_0} \left(\frac{\Delta E}{E_s} \right) \mid (n - \nu_{x,y,0})\eta + \xi_{x,y} \mid, \tag{20}$$

where $F_{\perp}$ is a form factor which depends on the transverse beam distribution, n is an arbitrary integer and $\xi_{x,y}$ is the chromaticity. Instability occurs only for slow waves with $n > \nu_{x,y}$.

The space charge plays destibilizing role for the transverse microwave instability. Minimization of the tranverse impedance significantly increased the intstability threshold. With the present impedance budget the growth rate for the intensity $N = 2 \cdot 10^{14}$ is expected to be only about $1ms^{-1}$ which is negligible [32], [35]. An additional Landau damping can be introduced by means of the chromatic sextupoles.

For the working point below the integer, such as $(\nu_x, \nu_y) = (6.3, 5.8)$ one can have a resistive wall instability (at 200KHz) with the growth rate of $5ms^{-1}$. This instability can be damped by introducing Landau damping with the chromatic sextupoles.

2.5.7 Electron-cloud effects

Beam-induced multipacting is believed to be the leading source of sustained electron production. Depending on beam parameters, one of the two multipacting models usually apply: multi-bunch passage multipacting or single-bunch trailing-edge multipacting. The electron-cloud buildup is sensitive to the intensity, spacing and length of proton bunches, and on the secondary electron yield (SEY) of the beam pipe surface.

The elecrton cloud can in turn lead to e-p instability. This effect was extensively studied for the SNS ring [64]-[66]. For the SNS baseline intensity of $N = 1.5 \cdot 10^{14}$, the electron line density threshold is about $5nC/m$ [36]. Also, the first harmonic voltage of the SNS is designed to have 40kV which is estimates to be sufficient to stabilize the beam for the high-intensity operation of the SNS.

2.5.8 Cures and Feedback

Landau damping with sextupoles The design of the SNS ring has chromatic sextupoles which allows to introduce a relatively large frequency spread. For the resistive wall instability at 0.2 MHz the chromaticity provides strong Landau damping, with $\xi = -7$ completely damping the instability.

For the instability associated with the extraction kicker impedance at frequencies 2-20 MHz the chromaticity has only partial effect, with $\xi = -7$ leading to a 20% thershold increase in the presence of space charge.

For the elecrton cloud instability at frequencies 100-200 MHz, the chromaticity has little effect on the thresholds.

Effect of octupoles The purpose of correction octupoles it to correct imperfection machines resonances. With a maximum coil current in correctors not to exceed 17A the introduced tune spread was found to be unsufficient to introduce effective Landau damping.

Effect of b/a The spread of coherent tunes along the bunch length due to longitudinal current distribution plays effective role in trasnverse beam stability. Increasing the b/a ratio decreases such detuning thus making beam more unstable.

E-cloud cures All internal surfaces, including ferrite are coated with TiN to suppress electron multipacting. The 100 nm thickness is expected to sustain proton-halo bombardment without eddy-current heating.

Injection stripped electrons are guided to the collectors with a low backscattering yield.

A voltage up to ±1 kV can be applied to 42 BPMs to clear electrons. In addition, dedicated electrodes will be placed in the injection region. Also, solenoids can be wound in straight sections to reduce multipacting.

Feedback system A wide-band feedback system can be implemented to damp the instabilities. Three frequency ranges are of interest: 1. 0.2-0.8 MHz (depending on working point) with the growth rates of about $5ms^{-1}$ due to resistive wall impedance, 2. 2-20 MHz with the growth rates of about 1-3 ms^{-1} due to the extraction kicker impedance, 3. 100-200 MHz with growth rates of about 50 ms^{-1} due to the electron cloud instability.

Only for the electron cloud instability this results in a significant power requirements.

The feedback system will be developed using the three tune measurement kickers each of 50 cm length to cover the range of frequncies up to 200 MHz [34].

3 Accelerator Physics and Technical Engineering

3.1 Magnet System

3.1.1 Magnet system requirements

Table 21: Magnet requirements for the HEBT and Linac dump.

	Type	Location	No.	Field	Aperture	Length
Dipoles	8D533	Achromat	8	0.21 T	8 cm gap	5.43m
	8D406	ARMS	1	0.21 T	8 cm gap	4.13m
	16CDH20	LAMS,ARMS,LDUMP	7	0.03 T	12 cm × 12 cm	0.2 m
	16CDV20		7			
	27CDH20	Achromat	2	0.03 T	20 cm × 20 cm	0.3m
	27CDV20		2			
Quadrupoles	12Q45	LAMS,ARMS	26	4.5 T/m	12 cm ϕ	0.5 m
	21Q40	Achromat	8	2.5 T/m	20 cm ϕ	0.505m
	12Q45	LDUMP	6	3.0 T/m	12 cm ϕ	0.505m

Table 22: Magnet requirements for the RTBT.

	Type	Number	Field	Aperture	Length
Dipoles	17D244	1	0.67 T	17 cm × 45 cm	2.64 m
	27CD30	15	0.02 T	20 cm × 20 cm	0.3 m
	36CDR30	4	0.02 T	36 cm × 36 cm	0.3
Quadrupoles	21Q45, 36Q85, 30Q44, 30Q58	23	4.7 T/m	20 cm ϕ	0.5 m
		4	2.5 T/m	36 cm ϕ	1.0 m
		3	4.5	30 cm ϕ	0.55 m
		2	4.2	30 cm ϕ	0.70

3.1.2 HEBT magnets

3.1.3 Ring magnets

3.1.4 RTBT magnets

3.1.5 Magnet measurements and tests

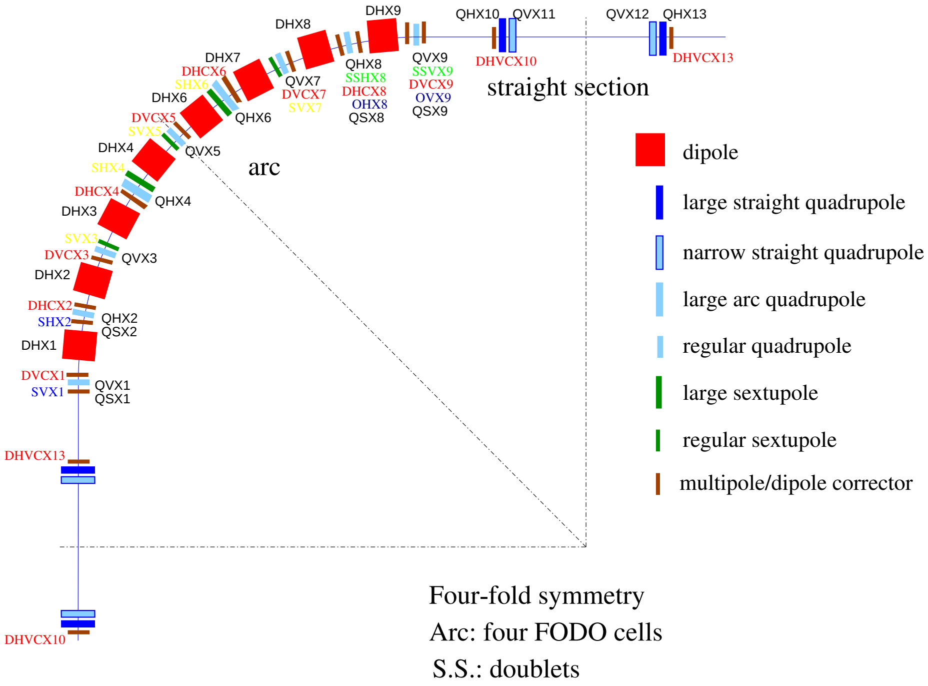

Figure 30: Schematic layout of dipole, quadrupole, sextupole, and correctors in one superperiod of the SNS accumulator ring.

3.2 Power-Supply System (WBS 1.5.4)

3.2.1 Power supply overview

The main ring power supplies are conventional for an accumulator/synchrotron type machine. All main ring elements are operated essentially in dc fashion except for the injection and extraction processes. However, even the dc units are provided with adjustability to enable machine tuning for optimization of ring parameters and operating points.

The ratings and distribution of the power supplies in the main ring and transport lines are shown in Table 23. There are three power levels of DC power supplies, and pulsed power supplies for injection into the ring, and extraction from the ring. With the exception of the extraction kickers, all units are rated for operation at 1.3 GeV.

Table 23: Power supply overview.

PS Function / Technology	Current [A]	Voltage [V]	Power [kW]	HEBT & linac dump	Ring & inj. dump	RTBT & ext. dump	Total
Low field	20	35	0.7	18	98	15	131
corrector /	20	75	1.5		8		8
Switchmode -	40	35	1.4		8		8
linear	40	75	3.0		8		8
	120	35	4.2			4	4
			Total	18	122	19	159
Medium range PS /	185	27	5.0			4	4
	390	24	9.4	15			15
12 pulse phase	700	18	12.6	9		5	14
controlled	900	51	45.9	4		8	12
	1300	95	123.5	1		8	9
	1405	390	548.0	1		6	7
	2400	50	120.0		1	1	2
	4000	18	72.0		6		6
			Total	30	11	28	69
Main dipole PS /	6000	440	2640		1		1
12 pulse phase controlled			**Total**	0	1	0	1
Injection bump PS	1400	800	pulsed		8		8
Switchmode			**Total**	0	8	0	8
Extraction kicker PS	2500	35000	pulsed		14		14
Blumlein PFN			**Total**	0	14	0	14
			Grand total	48	156	47	251

3.2.1.1 Low field corrector power supplies

All configurations of the low field corrector power supplies are built from a common 20 Amp module. The basic module has a switch mode front-end converter and a linear H-bridge output stage for four-quadrant operation. This unit is powered with three phase, 208 VAC, and it's maximum output voltage rating is selectable at either 35 Volts or 75 Volts. This unit is built in $5\frac{1}{4}''$ high rack mounted chassis, with slides.

Up to seven of these basic modules may be put in parallel. When this is done, a ganging cable is used to provide a common reference, common readbacks, and common controls. The entire assembly is controlled and monitored by a single Power Supply Interface. The total current is displayed on the front panel of the uppermost module, and the other module displays are blanked. A fault in any of the modules will shut down all the modules in a unit. Up to seven of these basic modules may be put in parallel. When this is done, a ganging cable is used to provide a common reference, common readbacks, and common controls. The entire assembly is controlled and monitored by a single Power-Supply Interface (PSI). The total current is displayed on the front panel of the uppermost module, and the other module displays are blanked. A fault in any of the modules will shut down all the modules in a unit.

These versatile units are used throughout the ring and transport lines, as well as in the Linac. Stability of the low-field corrector is 10^{-3}.

3.2.1.2 Medium range power supplies

The medium range power supplies are used to power all of the large dipoles, quadrupoles, and sextupoles in the ring and transport system, with the exception of the main ring dipoles. While these operate at varying current and voltage levels, all 69 units are grouped into eight models to minimize spares unit requirements. All units are built as 12-pulse phase controlled power supplies with passive ripple filters, and are powered from three-phase 460 VAC.

The requirement for stability on these power supplies is 2×10^{-4} of the full scale. The specification for the units is 10^{-4}, so that full stability is achieved even when operating at half the output rating of the supply. To extend the voltage range of the power supplies, all units have a 50% tap on the rectifier transformer. This allows the units to operate at lower voltages, without the ripple voltage becoming excessive.

3.2.1.3 Main ring dipole power supply

For the main ring dipoles, a set of 33 magnets will be required in series, 32 within the ring enclosure and one in the ring support building as a reference magnet. In the lattice, Hall-effect probes will be mounted in the gap to measure the magnetic field intensity, and hence the ring energy in a reproducible manner. This will act as the primary standard for the SNS ring. The interconnection of the main dipoles will be by a fold-back, high-current, water-cooled, copper-bus system.

This unit is built as 12-pulse phase controlled power supplies with a passive ripple filter, and is powered from three-phase 13.8 kVAC. The two phase shifting rectifier transformers will located external to the ring service building, while the SCRs, filters, and controls, are inside the building.

3.2.2 Power Supply Interconnection

Figures 31-50 are power supply interconnection diagrams. They shows the power supplies and the magnet loads they energize. The boxes representing the power supplies have the operating current and voltage for 1.3 GeV inside. Just outside the boxes are the full-scale voltage and current rating of those units. The boxes representing the magnets have the magnet model number inside.

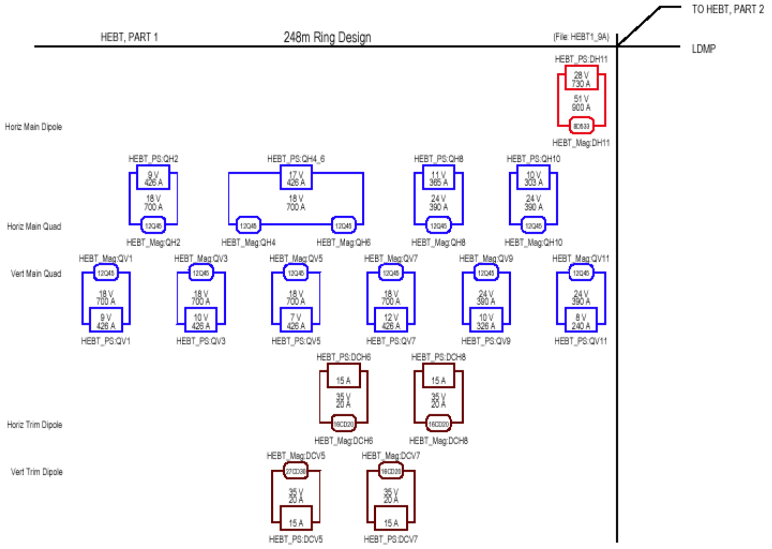

Figure 31: Power supply interconnection (part 1).

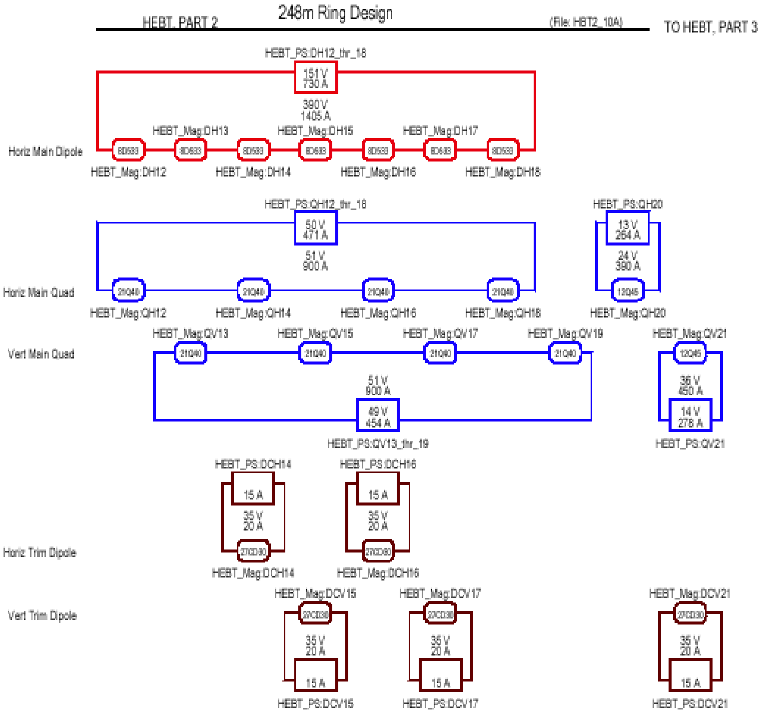

Figure 32: Power supply interconnection (part 2).

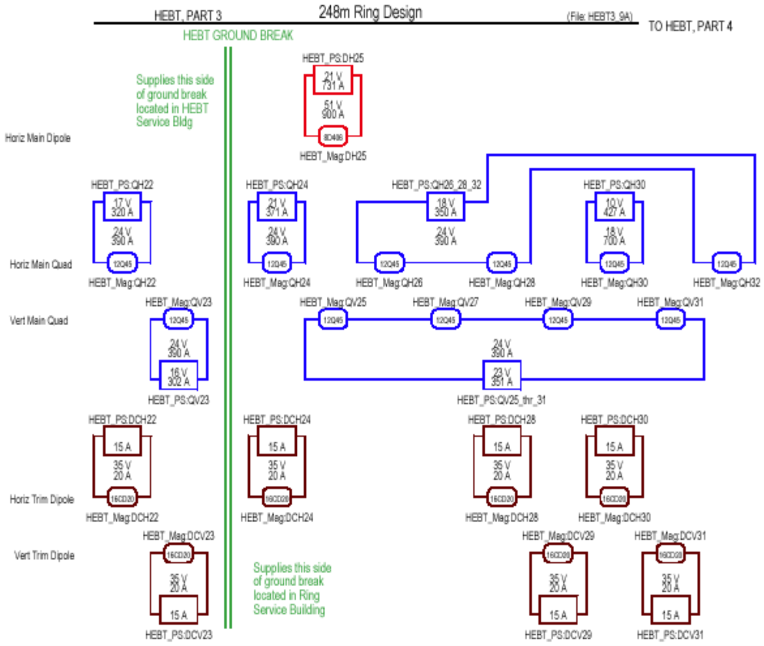

Figure 33: Power supply interconnection (part 3).

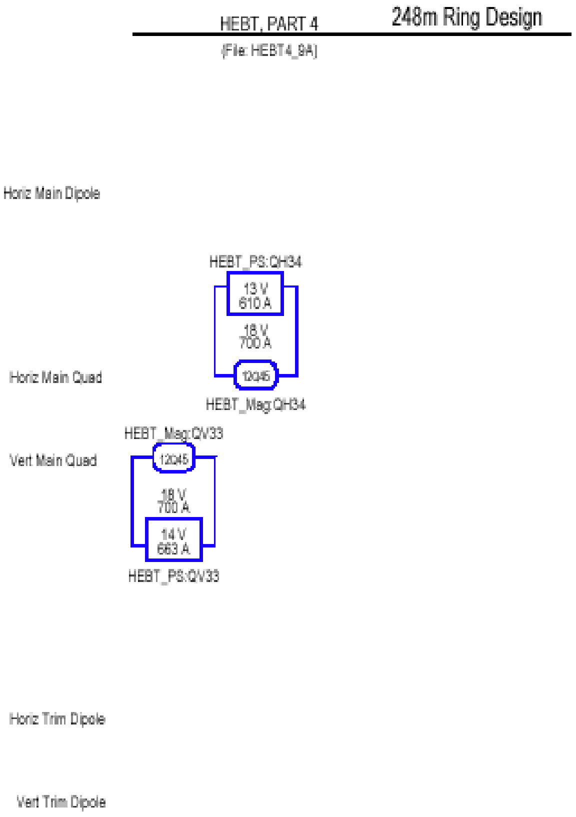

Figure 34: Power supply interconnection (part 4).

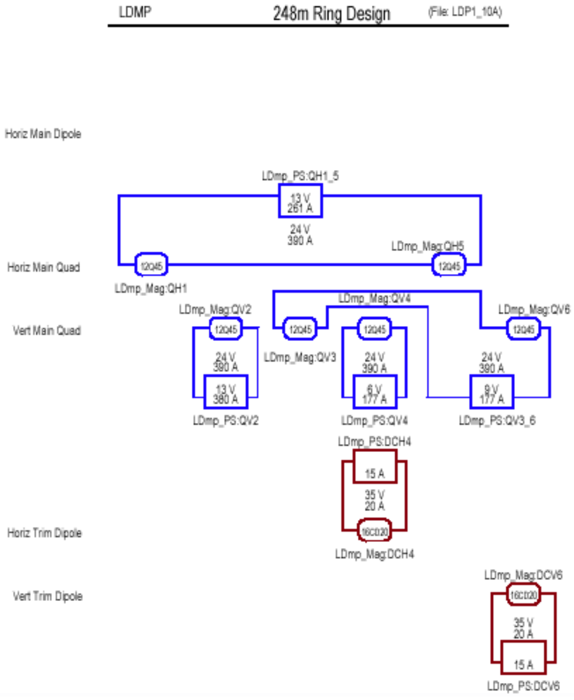

Figure 35: Power supply interconnection (part 5).

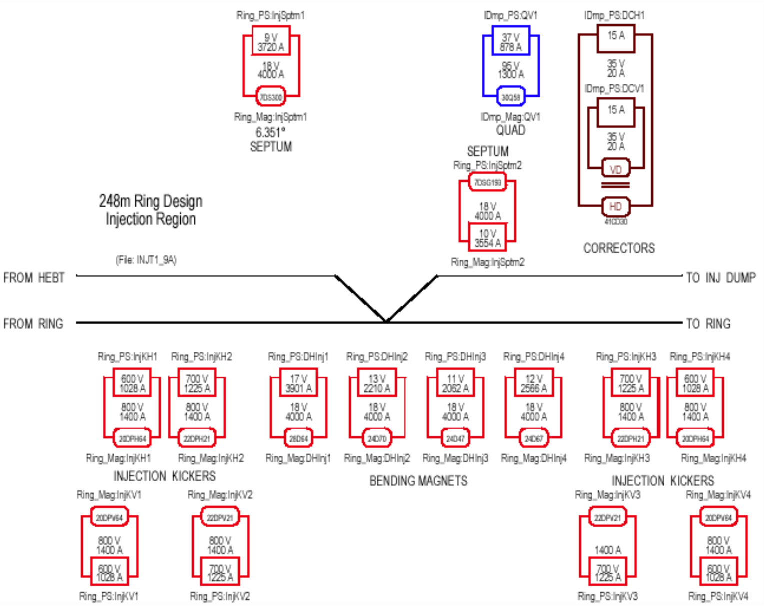

Figure 36: Power supply interconnection (part 6).

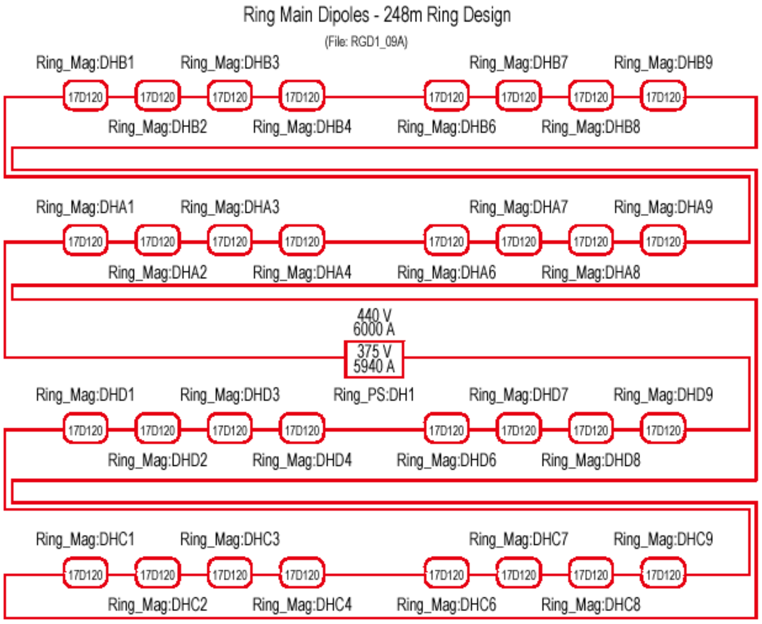

Figure 37: Power supply interconnection (part 7).

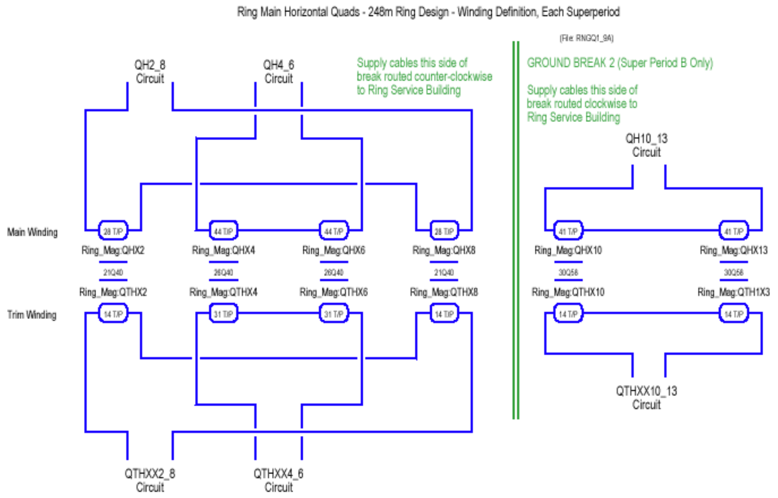

Figure 38: Power supply interconnection (part 8).

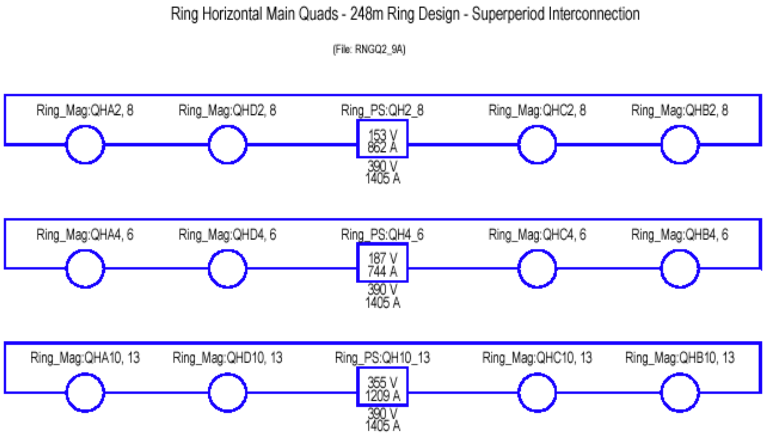

Figure 39: Power supply interconnection (part 9).

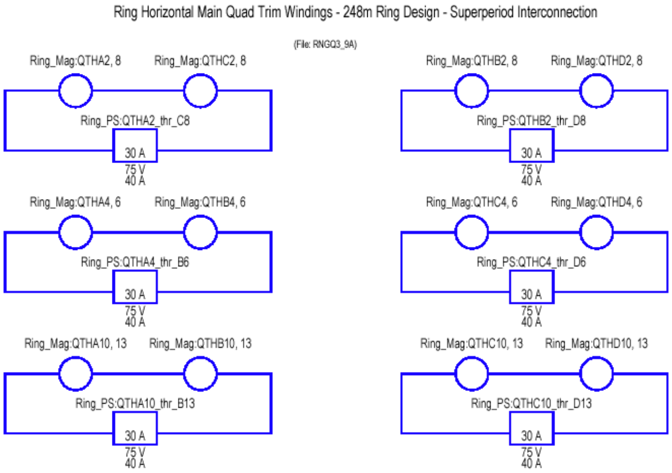

Figure 40: Power supply interconnection (part 10).

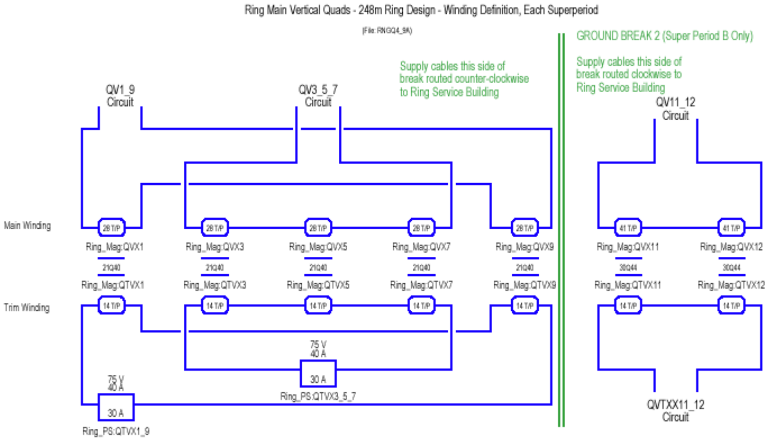

Figure 41: Power supply interconnection (part 11).

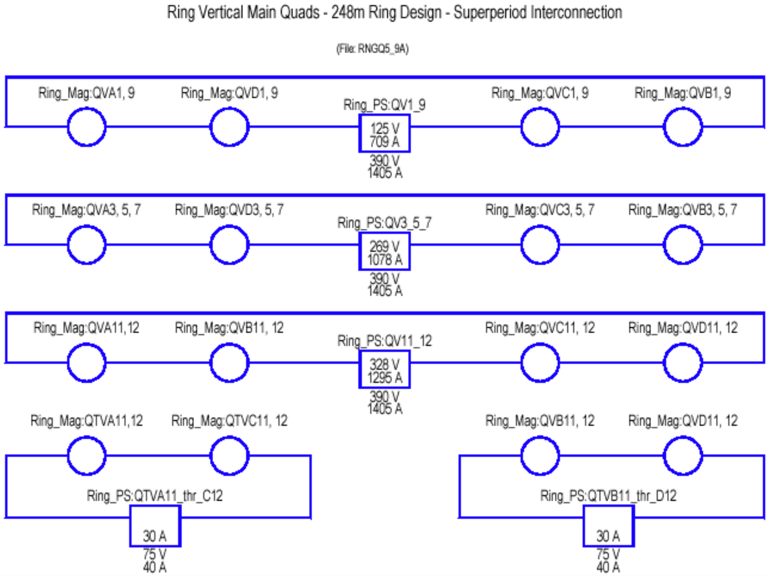

Figure 42: Power supply interconnection (part 12).

In addition, the figure also shows the location of three ground breaks – one in the HEBT, one in the main ring, and one in the RTBT. The power supplies for magnets downstream of the HEBT ground break will be located in the ring service building, as are the power supplies for magnets upstream of the RTBT ground break.

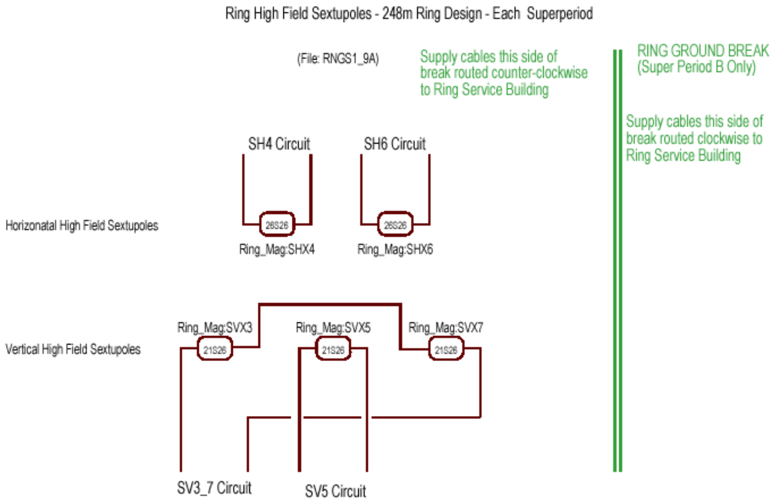

Figure 43: Power supply interconnection (part 13).

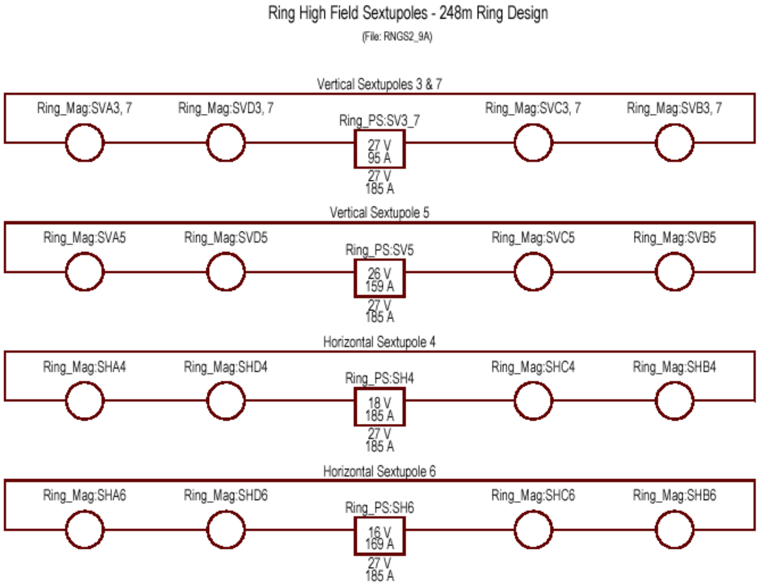

Figure 44: Power supply interconnection (part 14).

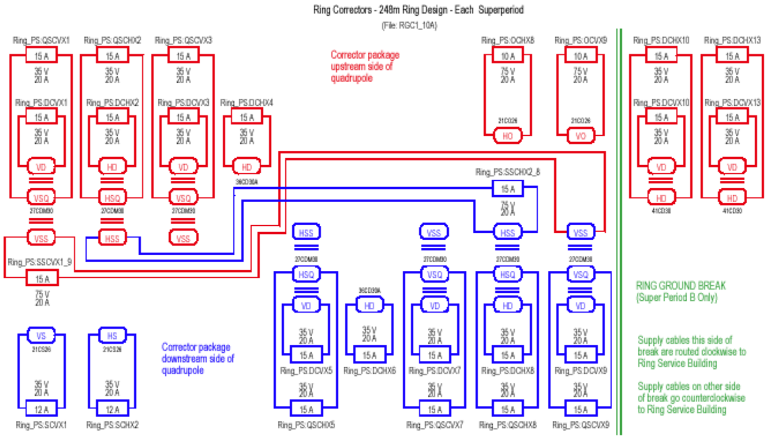

Figure 45: Power supply interconnection (part 15).

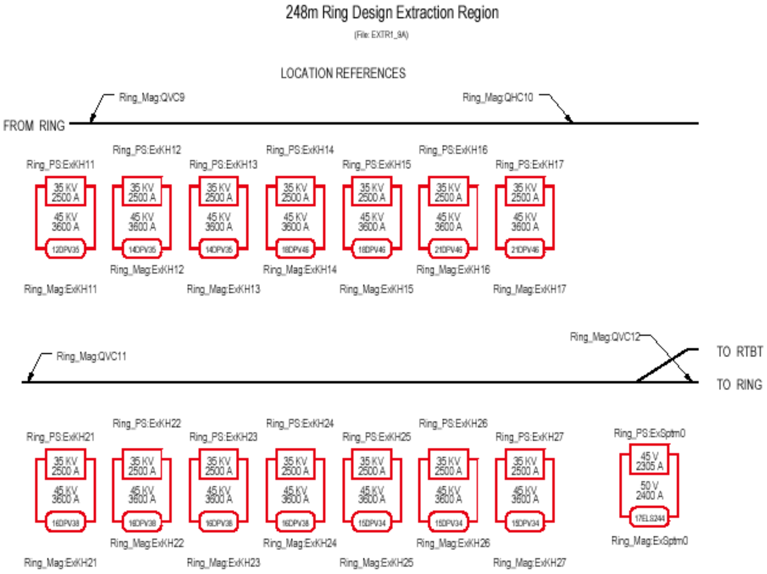

Figure 46: Power supply interconnection (part 16).

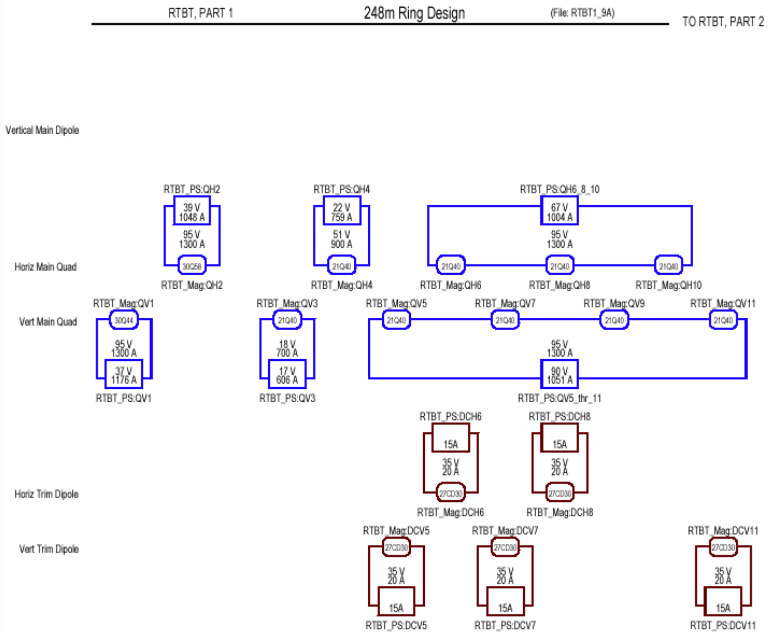

Figure 47: Power supply interconnection (part 17).

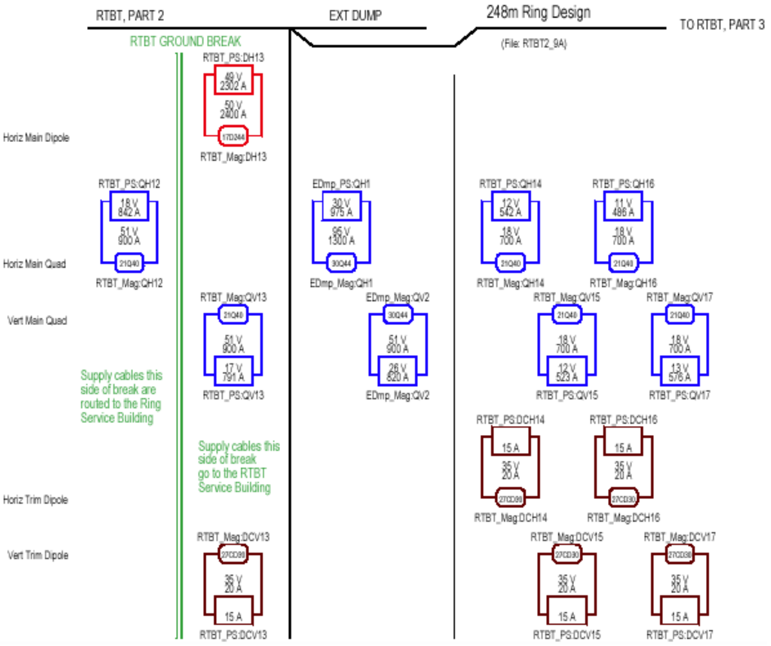

Figure 48: Power supply interconnection (part 18).

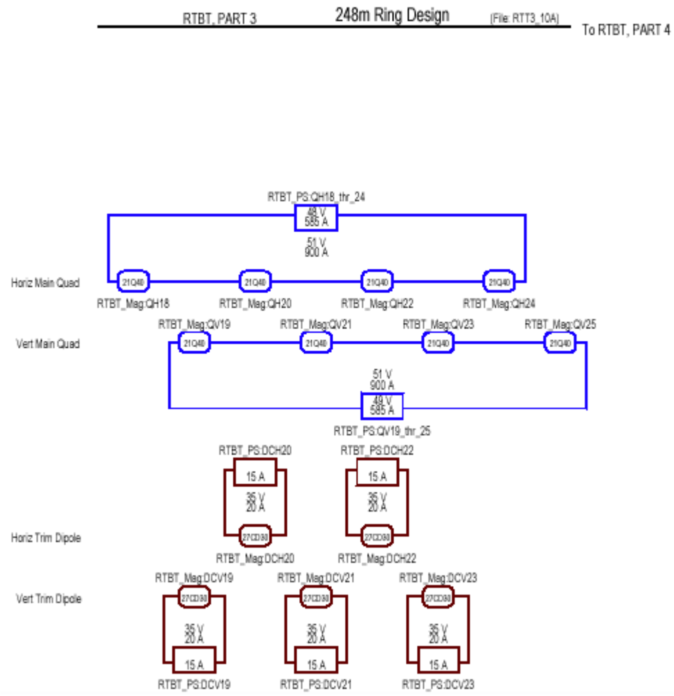

Figure 49: Power supply interconnection (part 19).

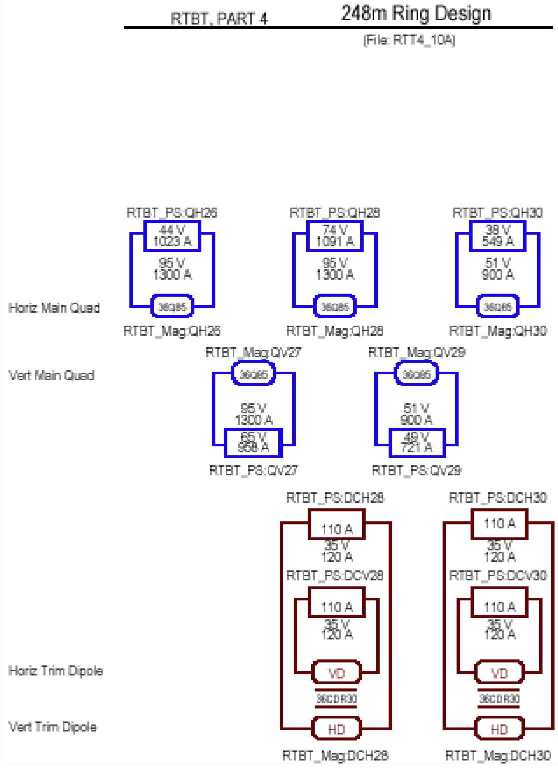

Figure 50: Power supply interconnection (part 20).

3.2.3 Controls Interface

All power supplies will be interfaced to the SNS computer control system. The typical ps interface will be accomplished by its tie-in to the local intelligent operations computer or IOC. The interface for all DC power supplies from the smallest to the largest, will be by Power Supply Interface (PSI) / Power Supply Controller (PSC) link.

A PSI provides one analog reference and up to fifteen digital commands. It also reads four analog readbacks, and sixteen digital status bits. It is electrically at the same potential as the power supply, and is isolated from all other electrical elements by the fiber optic link it uses to communicate with the PSC.

The PSC resides in the IOC on the VME bus, and each PSC can control up to six PSIs. The PSC controls the PSI and has circular buffers for each channel to store up to about 5000 sets of readbacks. For testing purposes, the PSC has a RS-232 port, to allow power supply testing without an IOC.

The pulsed power supplies also use PSIs, but these are supplemented by high-speed components. The injection bumps use the PSI for digital commands and digital status, but requires a high-speed waveform generator for a current reference, and a high-speed digitizer for analog readbacks. The extraction kickers use a trigger pulse and a high-speed digitizer for analog readbacks.

As a system, the PSI/PSC combination has several important features:

- Timed setpoints and readbacks
- Glitch detection
- Waveform monitoring (up to 5 kHz sampling rate)
- Electrical isolation

In addition, since each power supply has its own PSI, this can be integrated at the power supply vendor's facility. It also provides the hardware for continuous monitoring during test and burn in. When the unit is installed at SNS, power supply hardware integration consists of plugging in two fibers.

Table 24: Summary of corrector elements for the Ring system

agnet	Mechanical Nomenclature	Numb
orizontal or Vertical Dipole + Skew Quadrupole + Skew Sextupole (arc)	27CDM30	28
orizontal Dipole (arc wide aperture)	36CD30	8
orizontal and Vertical Dipole (straight section + linac dump)	41CD30	8 + 1
uadrupole TRIM Winding	21QT40, 26QT38, 30QT58, 30QT44	52
extupole	21CS26	8
ctupole	21CO26	8
otal number of elements	121	
otal number of functions	178	

3.3 Correction System

A summary of the correction packages for the ring are described in Table 24. The correction winding elements either share a common magnet frame (dipole, skew quadrupole, skew sextupole), are wound on an main magnetic element (TRIM quadrupole) or stand alone as an individual magnet (dipole, sextupole, octupole). In the following paragraphs, we describe each system in more details.

3.3.1 Closed-orbit correction

The total number of dipole corrector magnets in the SNS ring is 44. They are represented in Fig. 51 as brown rectangles. Due to the aperture change in the middle of the arc there are two types of dipole correctors in these areas: 28 of them have a 27 cm gap (27CDM30 in the magnet nomenclature corresponding to DVCX1, DHCX2, DVCX3, DVCX5, DVCX7, DHCX8 and DVCX9 of Fig. 51 and 8 are designed wider, with a 36cm gap (36CD30 corresponding to DHCX4 and DHCX6). The remaining 8 correctors (41CD30 or DHVCX10 and DHVCX13) are located in the straight sections, adjacent to the doublets (upstream and downstream) and their gap is even larger (41 cm).

Correctors in the arc produce either a horizontal or a vertical dipole kick and the determination of their positioning is imposed by the FODO structure: horizontal dipole correctors are placed near horizontal beta function maxima, adjacent to focusing quads and vertical dipole correctors are placed near vertical beta function maxima, adjacent to defocusing quads. On the other hand, the dipole correctors in the straight sections are designed as combined function magnets able to produce both horizontal and vertical dipole kicks. This will enable the necessary beam steering to any direction in the straight sections: in these areas, the beam envelope becomes wider and the closed orbit control is critical for injection, collimation, extraction and the RF system.

The dipole correction package allows the correction of closed orbit distortion during the accumulation period. This perturbation can be attributed to random quadrupole misalignments and dipole displacements (around 0.5 mm), variation of the dipole field (of the order of a few 10^{-4}), or random tilt of the dipoles (of about 0.5mrad) [39]. In order to achieve

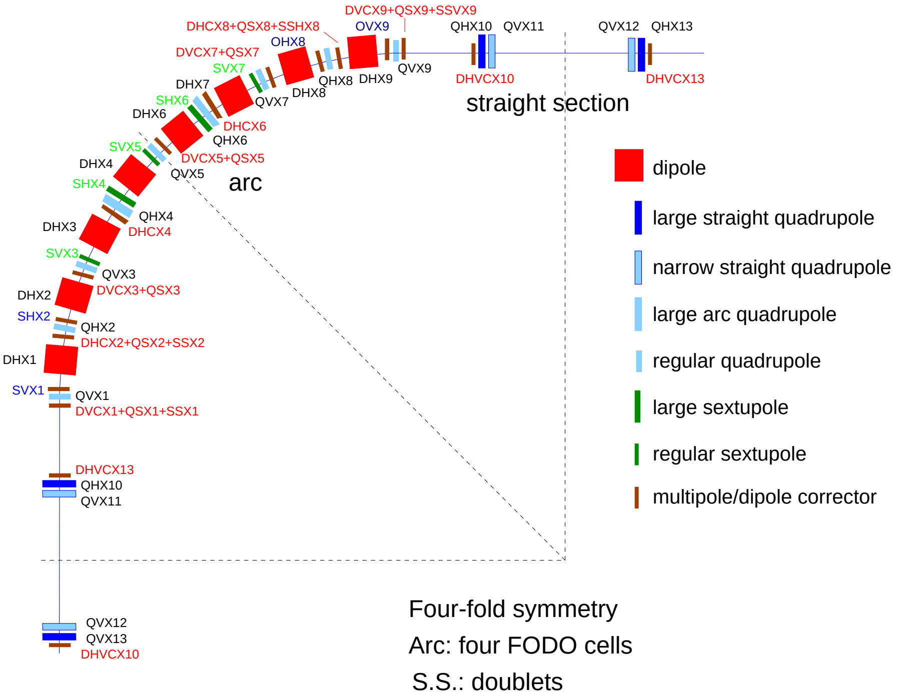

Figure 51: Schematic layout showing dipole, quadrupole, sextupole, and corrector magnets of one lattice super-period.

this, the dipole correctors are powered independently. The integrated dipole field of the arc correctors under design is around 6.7×10^{-4} T m which gives the capability of 1.2 mrad kicks for each corrector, at 1GeV. The dipole correctors in the straight sections are able to produce approximately twice this integrated field and kick, both in the horizontal and vertical direction.

The total number of power supplies needed is 52, one for each arc dipole corrector and 2 for every combined function dipole corrector in the straight sections. The specified field can be given by running the power supplies at 11 A.

3.3.2 Lattice distortion and beta wave

The preservation of the lattice super-periodicity is essential for the good performance of high-intensity rings. Based on first order perturbation theory, a lattice with perfect symmetry does not allow the excitation of resonances other than "structural", given by the condition: $k_xQ_x + k_yQ_y = mN$ where m is the super-periodicity of the lattice (4 for the SNS ring) and k_x, k_y and N integers. On the other hand, when the super-periodicity is broken, e.g. by random errors in the magnets, "non-structural" resonances can be excited as well (m can be any integer number). The combination of lattice perturbation in the presence of large space-charge forces in a high-intensity ring, can lead to excessive beam loss. This effect was already observed [40] and analyzed theoretically [41] in the KEK PS, where a 4th order "non-structure" space-charge induced resonance was excited, as the super-periodicity was broken due to errors in the quadrupole strengths.

The direct observable for a broken super-periodicity is the distortion of the linear optics functions. In the case of the SNS, random and systematic errors in the quadrupole strengths can create significant beta beating and dispersion distortion. Another perturbation comes from the injection chicane and bump which break the four-fold symmetry of the lattice and introduce additional beta wave [42]. In order to compensate these effects and allow a fine tuning of the SNS lattice, every magnet is equipped with TRIM windings able to produce 1% of the magnet quadrupole strength. The quadrupole gradient produced by the TRIMs is of the order of 5×10^{-2} T/m, for 1GeV operation.

Since the early stage of the project, correction schemes have been proposed for the linear optics distortions and quadrupole resonance compensation, by connecting appropriately in strings the quadrupole windings [43]. The total number of quadrupole string families proposed for the original FODO lattice was seven. With the evolution to the 228m hybrid lattice and later to the 248m 1.3 GeV compatible ring, it became apparent that the number of families will be not enough for correcting all optics distortion. An individual powering scheme was proposed to give flexibility in the correction schemes, to assist the orbit correction in the early commissioning stage and to allow the beam-based alignment of the beam position monitors. A Preliminary Change Request (PCR) [44] was submitted requesting for individual powering of the quadrupole TRIM windings with 52 power supplies with an additional power supply for regulating the transfer function variation in the arc focusing quads which are powered in series but have different gap diameter due to the aperture increase in the middle of the arc. Due to the de-scoping of the SNS project, the original PCR was not approved. Finaly, we proposed a more restrictive correction scheme using 16 families of TRIM strings. In order to achieve the required 1% quadrupole gradient in each winding, for all five different types of quadrupoles, the power supplies should be able to give currents of 15 to 30 A.

3.3.3 Transverse coupling

The skew quadrupole correctors are used for the linear decoupling of the horizontal and vertical motion of the beam. Coupling can be mainly attributed to random rolls in the quadrupoles of the SNS ring lattice, whose rms values can be as large as 1mrad. A smaller contribution comes from random and systematic skew quadrupole errors in the magnetic elements.

Apart from the linear optics perturbations such as beta and dispersion beating, skew quadrupole errors can excite the coupling resonances $Q_x \pm Q_y = N$. Especially for the nominal working point $(Q_x, Q_y) = (6.3, 5.8)$ which was close to a structural coupling resonance $Q_x + Q_y = 12$, it was found essential that a very careful correction has to be applied in order to compensate the effect of random quadrupole rolls [45]. In a quite similar way as for quadrupole errors, the large space-charge tune-shift pushes the particles in the resonance and the result is a quite steep increase of beam loss to the 10% level. Moreover, it was shown that the global coupling correction would not be enough to cancel the effect and a local coupling scheme should be employed.

In the SNS ring there are no individual skew quadrupole magnets, but on the cores of the arc dipole correctors (27CDM30) separate windings are mounted that can create a skew quadrupole integrated gradient of about 2.25×10^{-2} T at 10.9 A. They are denoted as QSX1, QSX2, QSX3, QSX5, QSX7, QSX8, and QSX9 in Fig. 51. In the baseline scheme, it was foreseen to power only 16 of these windings, 4 per super-period, i.e. the ones at the beginning and the end of the arcs (QSX1, QSX2, QSX8, and QSX9). Due to the results mentioned above [45], it was apparent that this would not be sufficient. For this, we decided to power the skew quadrupole windings in every 27CDM30 correctors, which gives a total of 28.

In order to achieve the required skew quadrupole gradient in each winding the power supplies should be able to give currents of 11 A, for 1GeV operation.

3.3.4 Chromaticity

One of the design aspects that will help avoiding beam resonances and/or beam instabilities, thereby minimizing the beam losses in the accumulator ring, is the chromaticity control. Without this control, the tune spread produced by the natural chromaticity is about ±0.08, similar to the spread produced by the space-charge. The adjustment of the chromaticity and the optical compensation can be achieved by using chromaticity sextupoles. The SNS lattice contains five 15 cm long chromatic sextupoles per super-period.

Two families of sextupoles, placed at high-beta and high-dispersion regions, can control the linear chromaticity of the ring. The sextupoles however may strongly affect the first and second order of the beta and dispersion functions dependence on the momentum spread, introducing strong "beta/dispersion waves" and, thereby, reducing the dynamic aperture. In addition, this beta/dispersion variation will increase the first and higher order terms of the chromaticity. This is clearly shown in figure 52: with a two-family scheme, the optical distortion in β-function is as large as 30% for off-momentum orbits.

In order to minimize the dependence of the beta, the dispersion functions and the chromaticity on $\delta p/p$, additional families of sextupoles are required. In the proposed chromaticity correction scheme, three of the sextupoles are powered independently and two of them in

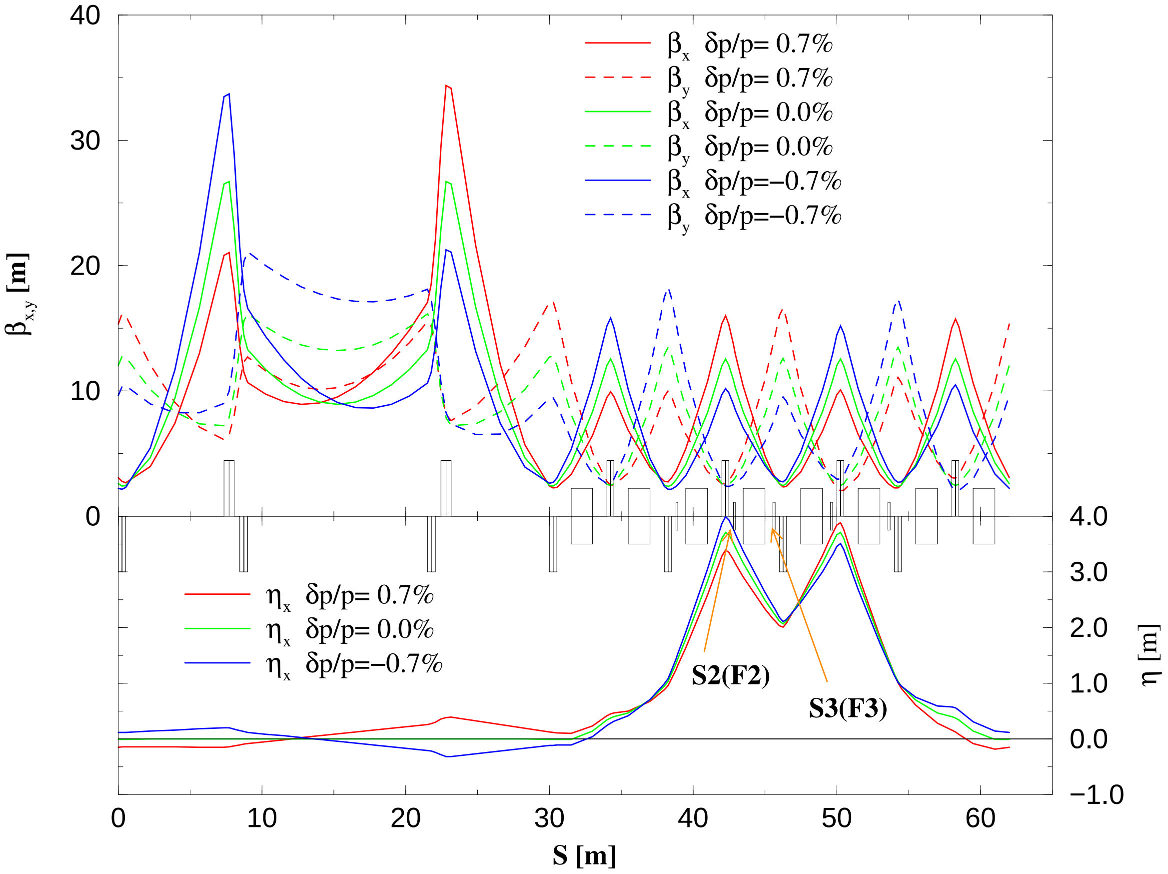

Figure 52: Lattice functions of the SNS accumulator ring for the nominal tunes (6.23,6.20) using two families of sextupoles. The beta and dispersion functions are strongly perturbed for off-momentum cases.

series, forming a total of four families. With a four-family scheme, the off-momentum optics is greatly improved, and the β-wave is minimal (Fig. 53).

3.3.5 Nonlinear multipoles

Skew sextupole correction The excitation of skew sextupole resonances was found to be one of the most important limitations of the AGS booster. Skew sextupole resonances of the type $2Q_x \pm Q_y = N$ and $3Q_y = N$ can be excited by skew sextupole errors coming from rolls in the main dipoles or other geometrical errors in the magnet elements of the SNS ring. In order to correct this effect skew sextupole windings are mounted on the 27CDM30 dipole correctors along with the main dipole coils and the skew quadrupole components. The only one powered are the ones at the beginning an the end of the arc (SSX8 and SSX9). The integrated gradient is 6.6×10^{-2} T/m equivalent to the one of the correctors in the AGS booster.

In the initial scheme, the skew sextupole were powered in 2 families. This would have not been enough for correcting any skew sextupole resonance without changing the connection between correctors. Moreover it would necessitate power supplies producing higher voltage

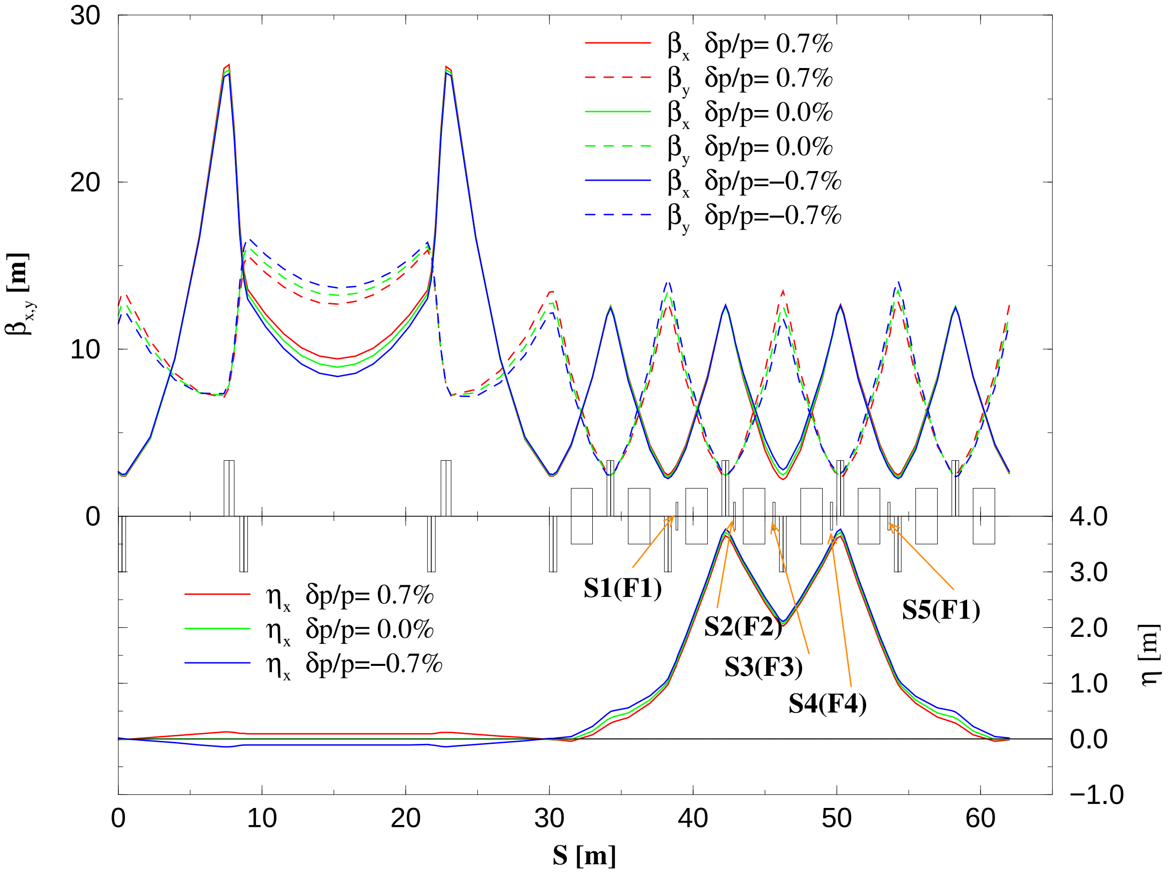

Figure 53: Lattice functions of the SNS accumulator ring for the nominal tunes (6.23,6.20) using 4 families of sextupoles. The beta and dispersion wave has been minimized by the introduction of the 2 supplementary sextupole families.

and power with an increased cost. Thus, it is required the additional powering of the skew sextupole windings in the 27CDM30 correctors at the beginning of the arc (SSX1 and SSX2) and the connection of the correctors in families of two: the first of the arc with the last and the second of the arc with the third are connected in series (the SSX1 with the SSX9 and the SSX2 with the SSX8, see Fig. 51), forming 8 families. The total number of power supplies proposed is 8. In order to achieve the required skew sextupole field in each corrector, the power supplies should be able to give currents of 13 A, for 1GeV operation. The total number of power supplies needed is 8. In order to achieve the required sextupole field in each corrector, the power supplies should be able to give currents of 8.4 A, for 1 GeV operation.

Sextupole correction The main functionality of the sextupole correctors is the correction of erect sextupole resonances of the type $3Q_x = N$ and $Q_x \pm 2Q_y = N$, which can be excited by sextupole errors in the dipoles, dipole fringe-fields at leading order and the small non-linear effect of the chromaticity sextupoles [46]. In the SNS ring, the sextupole correctors are 8 in total and are located at the beginning of the arc in non-dispersive areas in order to avoid "feed-downs" due to closed-orbit displacements giving a quadrupole effect at first order. The correctors are also taking advantage of the high horizontal or vertical beta function maximum in the respective locations. The names of these correctors in Fig. 51 are SVX1 and SHX1 and their mechanical name is 21CS20. The integrated sextupole gradient produced by the correctors is about 2.6 T/m.

For the same reason as for the skew sextupole correctors, it was decided to proceed with an individual powering scheme, with 8 power supplies instead of 2 as it was initially proposed. It will allow the possibility of correction of all resonant lines independently of the selected working point [46].

Octupole correction The octupole correctors are designated to compensate any octupole type of perturbation in the SNS ring. The main "octupole-like" contribution comes from the quadrupole fringe-fields to leading order, which are producing a tune-shift of the order of 0.025 at an amplitude of 480 π mm mrad [47]. This is the third most important contribution in tune spread after space-charge and chromaticity.

The octupole correctors in the SNS ring are located at the end of the arc in non-dispersive areas in order to avoid sextupole "feed-downs" due to closed orbit displacements. They are 8 in total and as the other correctors, their position is determined by the maxima of the beta functions near the arc focusing and defocusing quadrupoles. The names of these correctors in Fig. 51 are OHX1 and OVX1 and their mechanical name is 21OC20.

In order to eliminate completely the large tune-shift coming from quadrupole fringe-fields, a third octupole family is necessary in areas where the horizontal and vertical beta functions are approximately equal, in the short straight sections, just next to the doublet [47]. Unfortunately, this is not possible to a first stage due to the tight space of the ring in these areas and budget issues.

On the other hand, it would be impossible to correct all octupole type resonances of the form $4Q_x = N$, $2Q_x \pm 2Q_y = N$ and $4Q_y = N$ with the initial two-family scheme. For this reason, we proposed individual powering, in much the same way as for the other non-linear correctors. The integrated octupole gradient given by the correctors is 2.9 T/m^2, which will enhance the efficiency of resonance corrections.

The total number of power supplies needed is 8. In order to achieve the required octupole field in each corrector, the power supplies should be able to give currents of 8.4 A, for 1 GeV operation.

3.4 Vacuum System

The operating pressure of the HEBT vacuum is $\sim$5x10^{-8} Torr to minimize the H^- stripping. The accumulator ring vacuum system is to be $<10^{-8}$ Torr to minimize the beam-residual gas ionization. The various beam-residual gas interactions are described in the first section. The layout of the ring vacuum systems, the design of the vacuum chambers, vacuum pumps and other hardware are detailed in the second section. The coating of the ring vacuum chambers and other ring components is described in the third section.

3.4.1 Vacuum requirements

The following beam-residual gas interactions are considered in assessing the required vacuum levels in HEBT; the H^- stripping, the nuclear scattering, the multi Coulomb scattering and the residual gas ionization. As illustrated below, the contribution from the later three is not significant due to the single-pass nature of beam through HEBT. The stripping of the extra electrons from H^- by the residual gas molecules will cause the immediate beam loss and hardware activation. The H^-stripping cross section [1] is proportional to $1/\beta^2$ and is $\sim$1*10^{-18} cm^2 for 1 GeV H^- with a residual gas composition of 40%H_2/40%H_2O/20%CO. At the design pressure of $\sim$5x10^{-8} Torr, the beam loss will be 1.5x10^{-6}/m or 0.3nA/m for a 2mA beam. The residual radiation dosage 30cm from the beam centerline will be $\sim$30mR/hr, 4 hours after shutdown following a 100 consecutive-day run. This level of residual radiation is acceptable for hands-on maintenance. Of course, the level at a few critical spots, such as collimators, momentum scrapers etc., could be much higher and requires shielding or longer cool-down period.

Pressure of 1x10^{-8} Torr or less is needed in the accumulator ring mainly to minimize the residual gas ionization by the protons. The nuclear scattering cross sections σ_n for the protons are proportional to the geometrical cross section of the target nucleus and are $\sim$ 7*10^{-25} cm^2, $\sim$ 5*10^{-26} cm^2 and $\sim$ 1*10^{-25} cm^2 for CO, H_2O and H_2, respectively, which are the most common residual gases in a clean ultrahigh vacuum system. The beam loss due to nuclear scattering is given by $\Delta I \,/\, I = \int \beta\, c\, \sigma_n\, N\, dt$, with N being the residual gas density in the vacuum system. At the designed pressure of 1x10^{-8} Torr, N will be $\sim$7x10^{+8}atoms/cm^3. The resultant beam loss $\Delta I \,/\, I$ will be $\leq$ 3x10^{-9} averaged over one msec.

The multi-Coulomb scattering causes the growth of the RMS beam size. The fractional increase in beam size can be calculated by [2] $\Delta\sigma_y \,/\, \sigma_y = \int k\, \beta_y\, N/\, (p^2\, \varepsilon)\, dt$, with σ_y the transverse beam dimension, k = 1.085x10^{-23} $(GeV/c)^2$ m^3 sec^{-1}, β_y the betatron amplitude (¡20m), p the momentum (= 1.696 GeV/c) and ε the transverse emittance (=120π mm.mrad). The fraction of beam growth over one msec will be ¡1x10^{-7} at a vacuum of 1x10^{-8} Torr.

The residual gas ionization sets the most stringent requirement on the ring vacuum level. The ionization cross sections of 1 GeV protons on H_2, H_2O and CO can be calculated using Bethe formula [3] and are 2x10^{-19} cm^2, 6x10^{-19} cm^2 and 9x10^{-19} cm^2, respectively. The electron-ion pairs generated by the beam will be $\sim$3x10^{-3} per proton over one-msec period. The newly created ions repelled by the beam-wall potential will bombard the chamber wall and desorb gas molecules. The ionized electrons could be trapped in the potential well of the beam causing partial neutralization of the beam, or they could bombard the chamber wall and liberate secondary electrons, and create the electron cloud as observed in a few high intensity proton rings.

3.4.1.1. Pressure Increase due to Ion Desorption

The ions will receive an energy corresponding to the potential at where they are created. For the accumulator ring with a bunched current I $\sim$ 20 A at the end of one msec, the ions hitting the wall will have energy up to a few KeV. For stainless steel, the ion desorption coefficient η, the number of gas molecules desorbed per incident ion, ranges from less than one for a baked and glow discharge cleaned surface to $\sim$5 for an unbaked surface. If the rate of desorption is higher than the rate of removal, the pressure will rise gradually and leads to pressure instability. This could happen if η is large, the conductance C of the chamber is small, the pumping speed S is not sufficient or the distance L between pumps is too large. For each set of S, L and C, there exists a critical value of I*η when the pressure will increase exponentially and becomes unstable. The practical limit of η is decided by the allowable pressure rise in the presence of the beam, i.e., P(I,x)/P(0,x). In the accumulator ring design, a pressure increase of 50% is thought as not excessive and was used to calculate [4] the allowable η. Owing to the large cross section (Φ ¿20cm) and high linear conductance of the ring chambers, and the short accumulation period of 1 msec, the allowable η for CO and H_2 are 10 and 50, respectively, well above that of the clean stainless steel surface. No pressure instability due to ion desorption is expected in the ring vacuum chambers.

3.4.1.2. The Effect of the Ionized Electron

The initial energy of the newly ionized electrons will be a few eV. These primary electrons, heated by the oscillating beam-wall potential generated by the passing bunches, liberate more secondary electrons when bombarding the vacuum chamber wall. These electrons will be attracted by the next bunches and hit the wall liberating more electrons, the so called multi-pacting and electron cloud effects. The electron multi-pacting and resulting e-p instability can limit the achievable proton intensity when excessive electrons are generated and trapped. One major contributing factor to e-p instability is the SEY of the vacuum chamber wall. Most SNS ring chambers are made of stainless steel, which has a peak SEY of $\sim$ 2.5 and can be reduced to 1.9 or lower if the surface is coated with TiN. Simulation of electron cloud effect, as described elsewhere in this design report, has shown that no e-p instability is expected if the SEY is below 2.0.

3.4.2 Vacuum layout

The ring vacuum systems consist of the HEBT, the ring and the RTBT as well as the four beam dump lines, with a total length over 600m. The vacuum systems interface with superconducting linac (SCL) at the pneumatic gate valve upstream the first HEBT quadrupole magnet and with the dump lines and the Target at their respective windows.

3.4.2.1 HEBT Vacuum

The main HEBT line is divided into three sections, the linac matching section, the acromat bend section and the injection section. The linac matching section interfaces with the high-energy differential pumping (HEDP) section of the SCL at the gate valve upstream of the 1^{st} HEBT quadrupole. This section has 12cm beam aperture and consists of two HEBT collimators, their foil strippers, energy corrector cavity and beam diagnostic equipments. The vacuum chambers in this section will be made of 12cm diameter stainless steel tubes. The acromat bend section has eight 21cm quadrupoles/chambers and 8 long dipole magnets/chambers of 6m in length. Three of the dipole chambers have extraction ports to accommodate the linac dump line, the momentum dump line and the Beam-In-Gap monitoring line. A typical dipole chamber with extraction port is shown in Fig. 3.4.1. The ring injection section starts at acromat bend and ends at ring injection septum. The chambers are made of 12cm diameter stainless steel, similar to those of linac matching section. The pressure distribution in HEBT based on an outgassing rate of 5x10^{-11} Torr.l/s.cm^2 48 hours after pump down is shown in Fig 3.4.2, with average pressure ∼3x10^{-8} Torr. Due to the limited space available in the bend section, the spacing between ion pumps in this section is approximately 15m, resulted in higher pressure compared to the rest of HEBT.

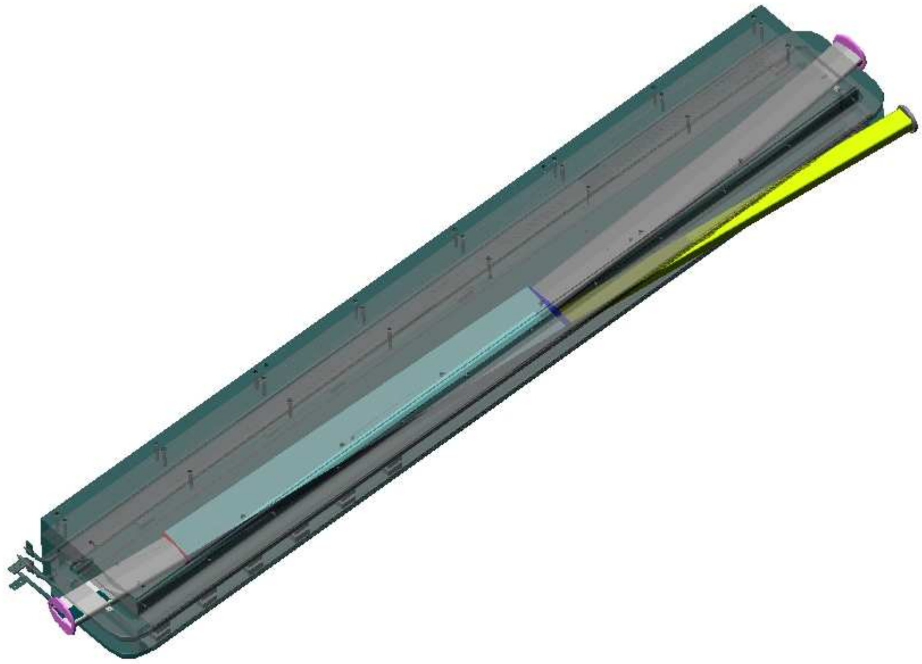

Figure 54: HEBT dipole chamber in the magnet with extraction port for linac dump.

The windows of the three dump lines in HEBT will be configured differently based on the power rating of the dumps. The linac dump window will be edge-cooled with water and be made of inconel 718. The flight tube downstream of this window to the dump will be filled with helium. The momentum dump window will be made of stainless steel with a small air gap between window and the dump. Both windows will be located in the HEBT tunnel. The injection dump, located in the injection dump building, has to handle up to 200 kW power and will be water-cooled. The impact of dump window leaks to HEBT, ring and SCL vacuum systems have been analyzed for two leak rates, 10^{-5} Torr.l/s and 10^{-3} Torr.l/s of air, water or helium. The results are plotted in Fig. 3.4.3, with the pressure profiles starting from the windows. Due to small helium pumping speed provided by the sputter ion pumps, even

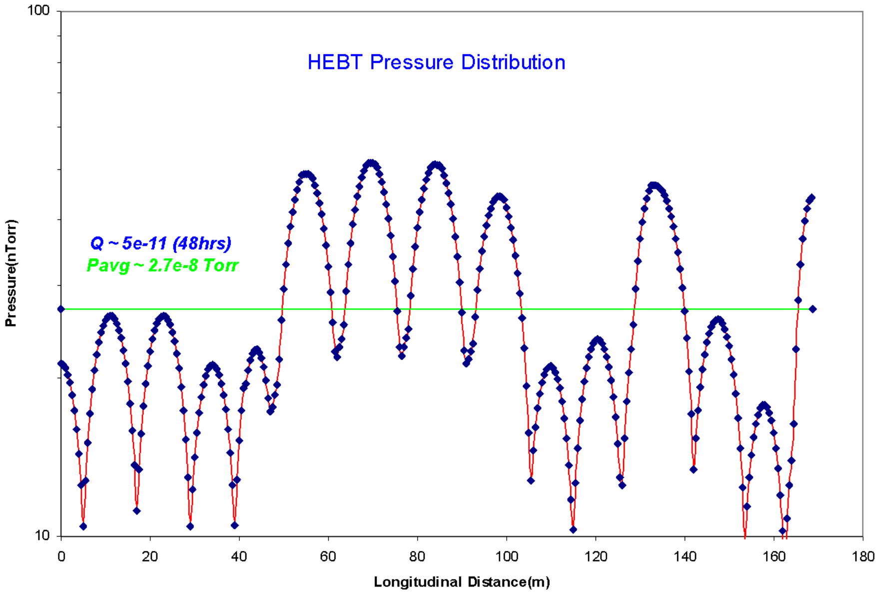

Figure 55: Pressure profile in HEBT, 48 hours after pump down, with ion pumps spaced every 10 to 15 m.

small helium leaks at linac window will have significant impact on the SCL vacuum and have to be repaired immediately. Air and water leaks up to 10^{-4} Torr.l/s from the injection and momentum dump windows can be handled with the existing pumps.

3.4.2.2 Ring Vacuum Layout

The accumulator ring has four arc regions; and four straight sections for injection, collimators, extraction, and RF & diagnostics. The vacuum systems are conveniently divided into eight vacuum sectors isolatable with all-metal electro-pneumatic gate valves located at the interface of the arc sections and the straight sections. One additional large gate valve will isolate the extraction kickers from Lambertson and RTBT vacuum, thus preserving the conditioned ferrite kickers in the event of bleeding up those two sections. The arc vacuum sectors are ∼34 m in length and the straight vacuum sectors, ∼28 m in length. A list of ring vacuum components and their parameters are given in Table 25.

Only UHV compatible metals and ceramics will be used in the construction of the ring vacuum system for their vacuum properties and radiation resistance. No organic materials are allowed. To minimize the RF impedance, the chambers will have tapered transitions wherever significant changes in cross-sections. All the pump ports will be shielded with RF screens. To reduce the secondary electron yield, the inner wall of the chambers will be coated with titanium nitride. Conflat type flanges and seals, for their cost and reliability, will be used to join the arc chambers. Quick-disconnect chain clamps, flanges and metal seals will be used at the straight sections where the expected beam loss will be higher, therefore minimizing the personnel radiation exposure during vacuum maintenance and repair. All the chambers will

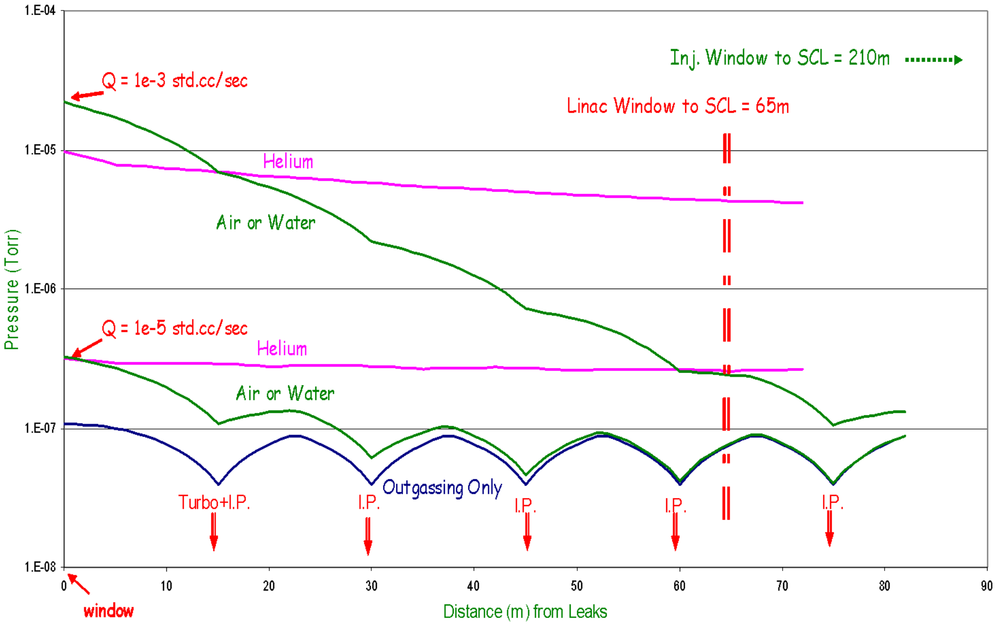

Figure 56: HEBT pressure profile with window leaks, indicating that helium leaks at linac window will impact SCL and have to be repaired.

be chemically cleaned and assembled in a clean environment to minimize contamination. To achieve the low outgassing rates and the designed pressure, all the vacuum chambers and the components within are to be vacuum degassed at the highest allowable temperatures in an in-house vacuum furnace. To preserve the conditioning and prevent high voltage breakdown, the extraction kickers will be in-situ baked to 200 C.

3.4.2.2.1 Arc Vacuum Chambers

Each ring arc section has 8 halfcell chambers and one quartercell chamber. The vacuum chambers and the magnets are grouped symmetrical to the middle quadrupole, such that they are mirror images to each other with quartercell located in the middle of the arc. This strategy reduces the individual chamber components into two types, thus reduce the fabrication and assembly cost. Each halfcell chamber, as shown in Fig. 3.4.4, consists of a dipole chamber section, pump ports, quadrupole section, BPM and bellows. The 2 m long dipole chamber has an elliptical cross section of 23cm (H) x 17cm (V) curved with a bending angle of 11.25^o. There will be a tapered transition from the dipole chamber to the end flanges and to the round pump/quadrupole chamber. The overall length of the halfcell chambers is 4m and will be made of stainless steel 316L or 316LN. To avoid radiation induced stress corrosion, the bellows are made of inconel 625. In all, there are four types of halfcell chambers, three with 20cm quadrupole pipe and one with 25cm quadrupole pipe.

3.4.2.2.2 Straight Section Doublet Chambers

There are eight doublet chambers in the four straight sections. Each consists of a straight pipe of 29cm OD fed through the two 30cm quadrupole doublets, then welded to the 30cm BPM. The length of the doublet chambers ranges from 3m to 5m. Typical doublet chambers

Table 25: Accumulator Ring Vacuum System Parameters

Description	Unit number	Length
Design Vacuum Level	$< 1\text{x}10^{-8}$	Torr
Arc Half Cell Chamber w/ BPM	32	4 m
Arc Quarter Cell Chamber w/ BPM	4	2 m
Straight Region Doublet Chamber with BPM	8	$>$ 3 m
Straight Region Special Chambers	16	0.5 - 4 m
All Metal Gate Valves, 20cm Φ	8	0.14 m
Gate Valve w/ EPDM seal, 30cm Φ	1	0.12 m
Sputter Ion Pumps, 200 l/s	50	
Cold Cathode and Pirani Gauge Set	18	
Residual Gas Analyzers	9	
Turbopump/dry pump stations, 200 l/s	9	
Insitu bake temperature for ext. kickers	200C	

are shown in Fig. 3.4.5. In the injection and RF straight sections, the doublet chambers are tapered down to NW250 quick disconnect flanges once the aperture requirement decreases away from the quadrupoles. In the collimation section, the doublet chambers have aperture of 29cm throughout, which is needed to minimize the capture of secondary particles from the primary scrapers and collimators. Large quick disconnect flanges with Helicoflex Delta seals will be used here for ease of assembly and reliability. In the extraction section, flange/seal design similar to the collimation section will be employed. To minimize the radiation induced stress corrosion, all the bellows in the straight sections will be made of inconel 625.

3.4.2.2.3 Other Ring Vacuum Chambers and Flange Assemblies

In addition to doublet chambers, the balance of the straight sections is occupied by special chambers housing the injection, collimators, rf, extraction and diagnostic equipments. The design of the special chambers will follow closely with the design of the special components to ensure that both the vacuum and the beam impedance budget requirement are met. Large all-metal quick demountable flanges and seals such as the Helicoflex type will be adopted for these chambers. Approximately 10% of the straight section pipes will be wound with axial-field solenoids of $<$ 50 gauss, mostly in the injection and collimation sections, to minimize the potential impact of electron accumulation and multi-pacting.

3.4.2.3 RTBT Vacuum Layout

The pressure of $\sim 10^{-8}$ Torr is required for the RTBT section adjacent to ring extraction so not to disturb the ring vacuum level, and of $\sim 10^{-6}$ Torr near the target and the dump for the reliable operation of Harp units. Most RTBT vacuum chambers have 21cm aperture and will be made of stainless steel. The beam pipes in the last 30m of RTBT inside the Target building will have 35cm aperture. No vacuum pumps will be installed near Target due to the intense radiation and the lack of access. Remote-operable quick-disconnect type flange assemblies will be designed and employed for the quadrupole doublet chambers adjacent to the Target. The pressure profiles from the last turbopump/ion pump to the target are shown in Fig. 3.4.6 in the presence of leaks at various locations in that region. Due to the large conductance of the

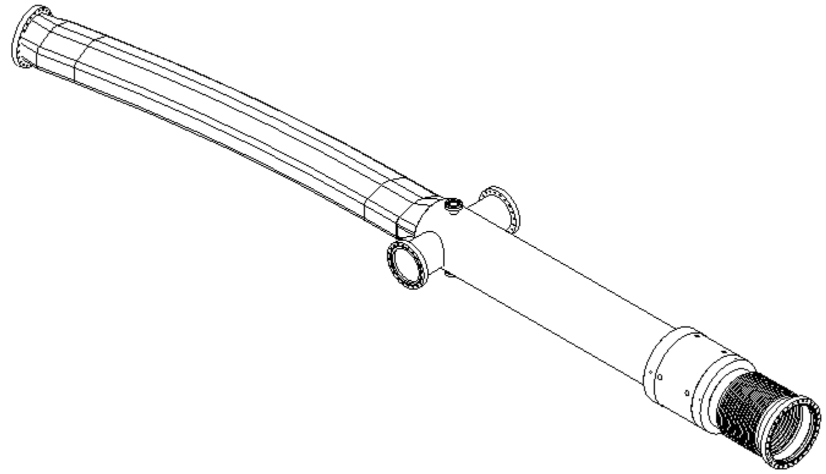

Figure 57: Typical ring arc halfcell vacuum chamber with an overall length of 4m and consisting of a dipole section, pump ports, quadrupole pipe, BPM and bellows.

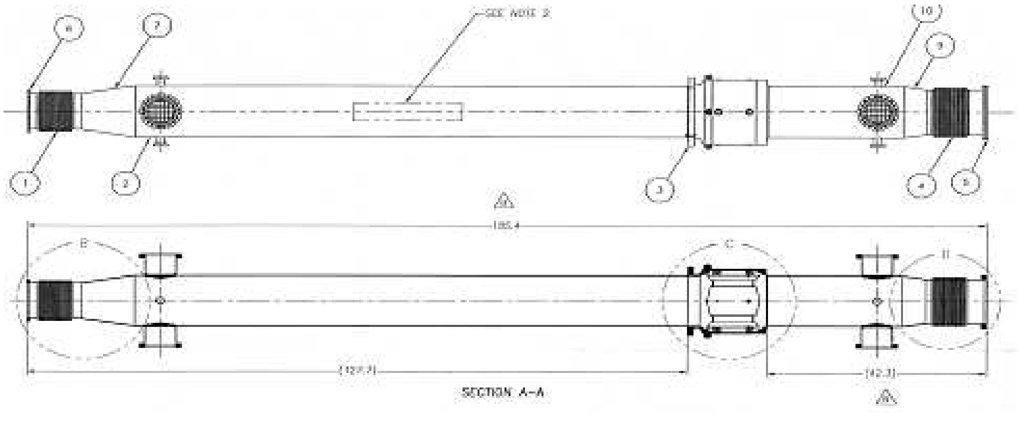

Figure 58: The RF straight section doublet chamber with overall length of 4.7m and aperture of 29cm.

35cm diameter beam pipe, the pressure differentials along the line are within the uncertainty of the vacuum gauge readings, therefore can't be used to identify the leak locations. Remote operable helium lines with nozzles mounted at periodical interval to spray helium at various joints may provide indication of leak locations to a leak detector further upstream. A fast valve and residual gas analyzers will also be employed to monitor and protect RTBT vacuum from catastrophic failure of target or dump windows.

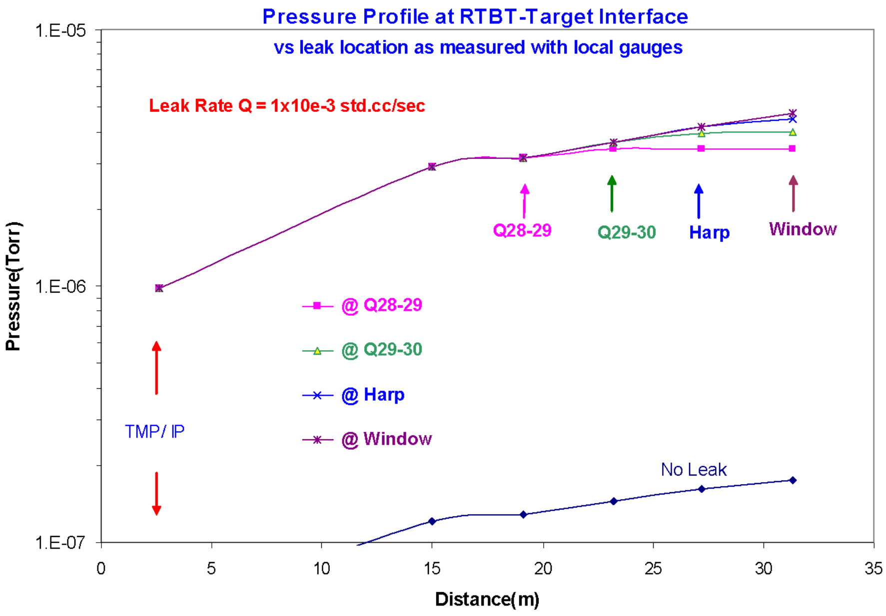

Figure 59: Pressure profiles at RTBT-target interface in the presence of leaks.

3.4.2.4 Vacuum Pumps

Two types of vacuum pumps will be employed in the three vacuum systems. The turbopump/dry pump carts for initial pump down and to supplement the high vacuum sputter ion pumps. One turbopump cart will be installed at each vacuum section preferably near high outgassing sources and potential leaks but away from high radiation areas. A number of sputter ion pumps will be installed in each vacuum section as the main high vacuum pumps for their cleanliness, reliability and cost. A few noble-diode type ion pumps with tantalum cathodes will be placed at strategic locations to pump potential leaks without the ill effect of Ar instability. No linearly distributed pumps are needed due to the large aperture and the large conductance of vacuum chambers.

3.4.2.5. Vacuum Instrumentation and Control

Two sets of Pirani and cold cathode gauges will be installed at each vacuum sector as primary vacuum gauges. The sputter ion pump current, proportional to pressure, will give a more detailed pressure profile around the ring. One residual gas analyzer will also be installed at each vacuum sector and provide a quick analysis of the partial pressures. Due to the high radiation levels in the tunnel, all the vacuum electronic devices will be located at the service buildings. These devices with local and remote capabilities can be operated through front panel switches and will communicate with the Control system through multi-drop serial communication network drops for remote monitoring and control. The PLCs will provide the logic for the operation of the sector gate valves and other machine subsystems. Ethernet network will connect the PLC to the VME front end computer for monitoring, logging and control of the vacuum devices. The PLC will also provide inputs to the beam permit link to abort the beam in the event of a vacuum fault. The layout of the vacuum instrumentation and control system is shown in Fig. 60.

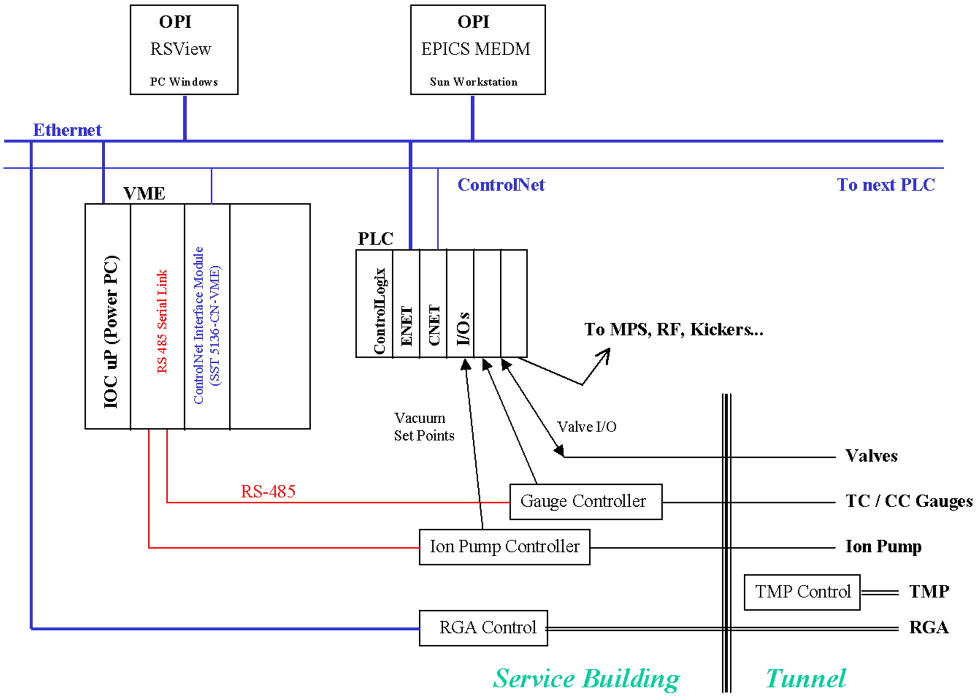

Figure 60: Control System for VME/PLC-based SNS Vacuum Instrumentation.

3.4.3 Coating of Ring Vacuum Chambers

The inner surface of the ring vacuum chambers is to be coated with ∼100nm of titanium nitride (TiN) to reduce the secondary electron yield (SEY), and thus avoid the electron cloud and the e-p instability caused by electron multi-pacting as observed in a few high-intensity proton storage rings. In the extraction kickers, the ferrite surfaces facing the beam will also be coated with TiN. The injection kicker ceramic chambers will first be coated with a layer of copper, to carry the image current, then with 100nm of TiN. The coatings are deposited using DC magnetron sputtering which produces films with correct stoichiometry, good adhesion and reasonable deposition rates.

3.4.3.1 TiN Coating of Ring Vacuum Chambers

DC magnetron sputtering is used to coat the inner wall of the ring vacuum chambers with TiN. A schematic view of the coating set up is shown in Fig. 61.

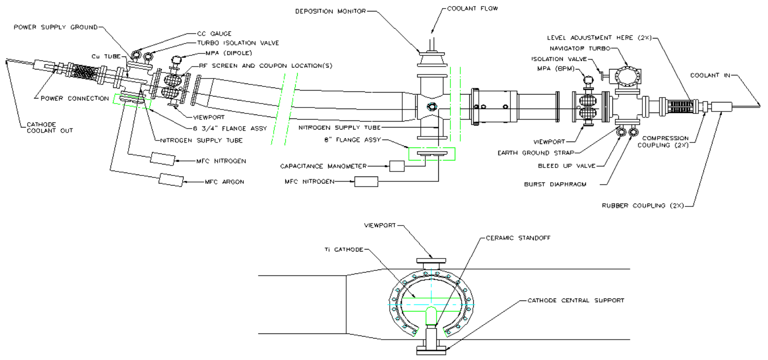

Figure 61: Schematic of TiN coating setup for ring vacuum chambers using DC magnetron sputtering.

A titanium tube centered in the ring chamber is used as the cathode. Commercially available *Alnico* magnets 1.25" diameter and 2" in length are inserted in the 1.5" diameter Ti tube. A 0.5" hole in the center of the magnets allows for the flow of cooling fluid during sputtering. The magnets are stacked with opposing poles using non-ferrous 0.5" spacers, resulting in a looping magnetic field of sufficient strength to project from the cathode surface. This "low cost" cathode works in conjunction with a 10 KW DC power supply to produce the satisfactory field and discharge plasma. Mixture of argon (Ar) and nitrogen (N_2) gases introduced through the mass flow controllers is used as sputtering media. The reactive process is controlled using partial pressure feedback of nitrogen gas as monitored with high-pressure residual gas analyzers. The dense plasma generated and confined by the electro-magnetic field increases the ion density thus the sputtering rate by a factor of ten or more as compared with that of pure DC sputtering, allowing the coating of 100 nm TiN in a few hours. Additionally, DC magnetron sputtering improves the stoichiometry and uniformity over those of DC sputtering. A comparison of coating parameters between DC and DC magnetron is given in Table 3.4.2 while Fig. 63 shows the various operating regions as a function of target nitriding.

To reduce contamination, all chambers are baked at 250^oC for 40 hours or longer prior to the start of sputtering. Coatings done at total pressure ($Ar + N_2$) of 5 mTorr are found to have rougher surface than those done at a total pressure of 1.5 mTorr. The rougher surface also has higher outgassing due to larger surface area and more grain boundary diffusion. However, it is adopted for ring chamber coating due to lower SEY, probably due to the re-entry of the secondary electrons back into the wall of the craters.

Note: Coatings by magnetron sputtering exhibited significantly lower oxygen content partly due to the high plasma density, resulting in an increased presence of atomic nitrogen competing over oxygen for available sites.

Auger Electron Spectroscopy analysis and Rutherford Backscattering analysis will be used to measure the thickness, the composition and the stoichiometry of the coating coupons. In addition, the coupons will be analyzed for SEY by colleagues at CERN and KEK, to ensure

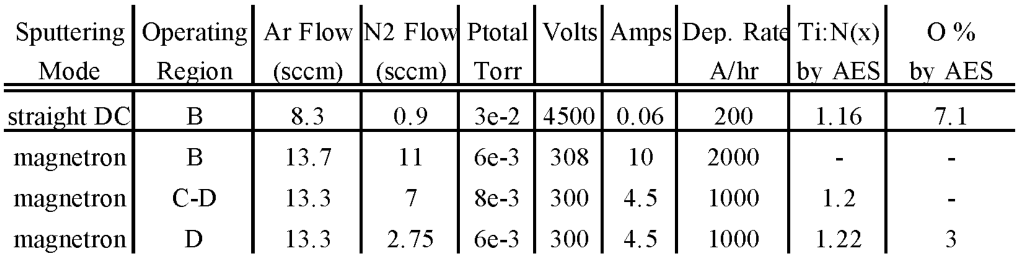

Sputtering Mode	Operating Region	Ar Flow (sccm)	N2 Flow (sccm)	Ptotal Torr	Volts	Amps	Dep. Rate A/hr	Ti:N(x) by AES	O % by AES
straight DC	B	8.3	0.9	3e-2	4500	0.06	200	1.16	7.1
magnetron	B	13.7	11	6e-3	308	10	2000	-	-
magnetron	C-D	13.3	7	8e-3	300	4.5	1000	1.2	-
magnetron	D	13.3	2.75	6e-3	300	4.5	1000	1.22	3

Figure 62: Comparison of coating parameters between DC and DC magnetron sputtering.

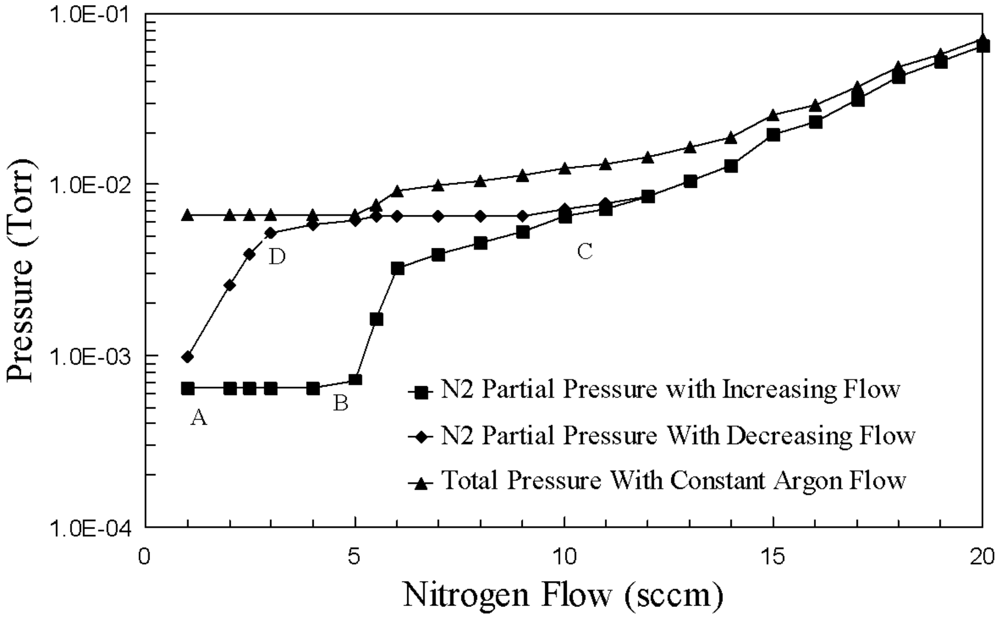

Figure 63: Nitrogen hysteresis with constant Ar flow showing the effects of target nitriding on N_2 consumption.

that the as-received SEY is below the instability thresholds. Typical SEY data for bare and TiN coated stainless steel coupons are plotted in Fig. 64 with electron beam energy between 60 and 3000eV at normal incidence angle. Compared to the bare stainless steel, TiN layer has a significantly lower SEY. The outgassing of the chambers before and after coating will also be measured to ensure the appropriate level of vacuum can be achieved.

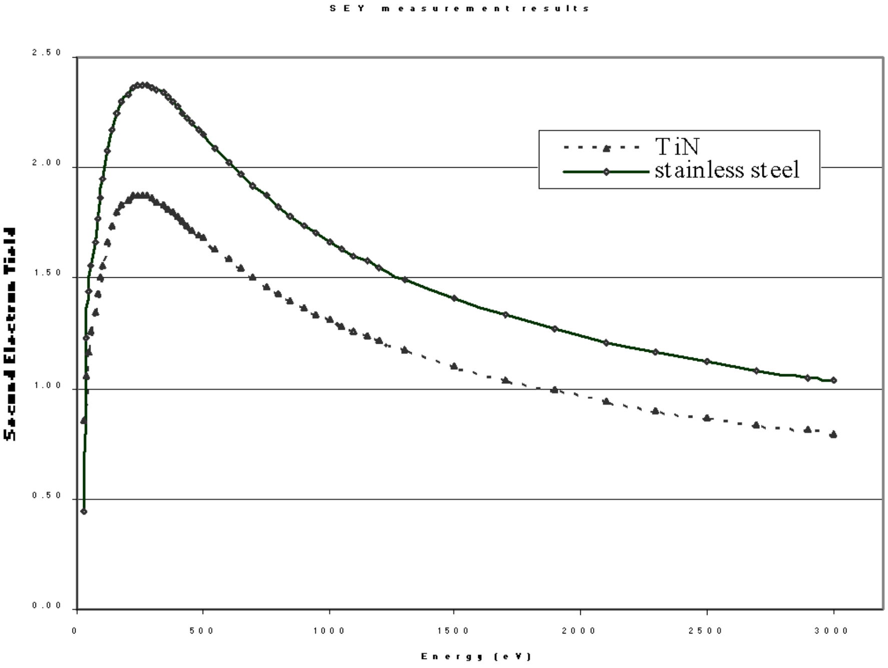

Figure 64: SEY as a function of incidence electron energy for bare and TiN coated stainless steel. The coating reduces the SEY by about 30%.

3.4.3.2 Coating of Injection Kicker Ceramic Chambers and Extraction Kicker Ferrites

To reduce the impedance, the six injection kicker ceramic chambers are to be coated with internal conductive thin films with sheet resistance 0.024 Ohms/square, giving a flange-to-flange DC resistance of 0.04 Ohms.[5] The coating should have a very good adhesion, be azimuthally and longitudinally *uniform* to ±20%, and make good electrical contact to the metal end flanges. The coating material may be any vacuum-compatible metal. The following table gives thicknesses of gold, titanium, copper, and TiN, which achieve the required sheet resistance. Copper is selected as the material for the conductive layer for its ease of sputtering and high conductivity. A copper cathode with similar geometry to the Ti cathode is used to lay down the required 0.7 μm film. An anode screen is needed to smooth out the electrical field during the initial coating of the ceramic tubes to which the charges tend to build up and neutralize the cathode potential. After the coating of the conductive layer, the surface is then coated with 100 nm TiN, as required for all other SNS ring vacuum chambers, for the reduction of SEY.

Material	Resistivity ($\mu\Omega$ cm)	Thickness (μm)
Gold	2.40	1.0
Titanium	90	37.5
Copper	1.70	0.71
TiN	42	17.5

Extraction kickers have large surface of ferrite directly exposed to the beam and ferrite is known to have large SEY. The surface facing the beam must be treated to reduce SEY. It would be attractive to use the same TiN coating, as on the rest of the vacuum chamber, but TiN film is a good conductor and can affect the kicker performance due to eddy currents in the coating layer. Therefore the coating will be divided into long strips of 1-2 cm width with mm gaps in between, parallel to the beam direction and terminated at end of each kicker module.[6]

References

[1] G. Gillespie, Phys. Review, A16, 943 (1977)
[2] G. Guignard, **CERN 77-10**, p33, June, 1977.
[3] Y. Baconnier, Proceeding CERN Accel. School, **CERN 85-19**, pp267-300, Nov. 1985.
[4] H.C. Hseuh, BNL/NSNS Tech Note No. **15**, Feb., 1997.
[5] S. Henderson and S. Danilov, Oct. 15, 2001 (private communication).
[6] A.V. Aleksandrov, Dec., 2000, SNS Tech Note #

3.5 Injection

3.5.1 Injection System

3.5.1.1 Scope

In this section, the design and implementation of the injection and accumulation processes into the main ring are presented. Injection into the accumulator ring is an H^- charge exchange process that allows beam to accumulate in already occupied phase space. As described earlier, the beam from the linac is chopped in the revolution frequency of the ring, ensuring there will be a gap in the circulating proton beam. The following sections describe the process, the choice of the stripping foil, the different loss mechanisms, the disposal of non-captured ions, the dc and dynamic injection orbit bumps, and the hardware needed to implement the process. Figures 65 66 show schematics of the injection area.

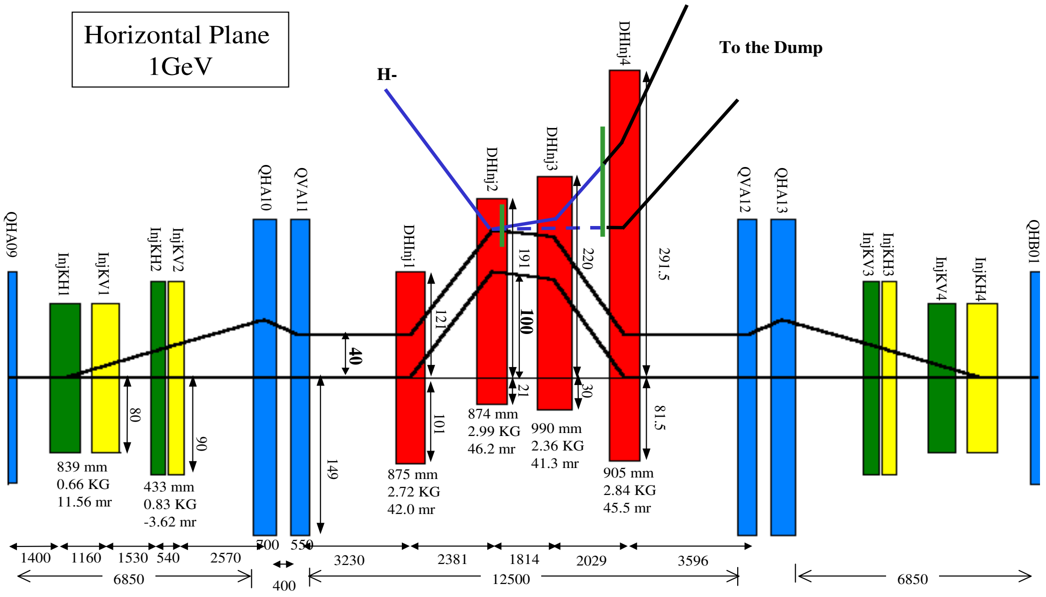

N. Catalan Lasheras 12/04/2002

Figure 65: Injection schematics (horizontal layout).

3.5.1.2 Injection Process

Injection takes place in one of the near-dispersion-free regions (straight section A) of the ring. The process is controlled by a large, especially designed, fixed orbit bump. The fixed orbit bump is a chicane consisting of four dipole magnets in the long straight section. The schematic plan view of the injection straight section is shown in the figure. To facilitate the clean dumping of the Ho atoms excited by the stripping foil, injection takes place in the downstream fringe field of second of this chicane dipole. This dipole, which is a C-type magnet, has a central magnetic field of 3 kG. However the stripping foil is located at the edge of the magnet in a 2.5-kG field region. The magnetic field value is important because the electric field felt by the moving excited H^0 is such that the principal quantum numbers of n=4 or less survive the field, whereas those of n=5 or higher strip immediately The life time of the excited H^0 vs the magnetic field is shown in Figure 65, where hand drawn line is the path of the excited H^0.

The spatially decreasing nature of the fringe field assures that the excited H^0's that are not stripped immediately will probably not be stripped at all because the field is decreasing, and hence the electric field felt by the H^0's will be too low. The third chicane magnet field is 2.4 KG which is lower than the field which the H^- are stripped The uncontrolled loss by the Stark stripping of the excited H^0's is estimated to be on the order of 10^-6 of the injected H^- beam. Even if the energy gap between the $n = 4$ and $n = 5$ states is completely miscalculated, the uncontrolled loss rate would be 10^{-5} .

At the upstream end of the chicane, in the HEBT injection line, a 3 meter long septum magnet with a 2.03 KG field to bring the beam from the HEBT line to the foil, while avoiding the upstream quadrupole and the circulating beam. In front of the last chicane magnet relatively thick stripping foil is placed to strip the electrons of unstripped Ho and H^- to protons At the downstream of the last chicane magnet, there is a 2-meter long septum magnet with a field of 5 kG to take the unstripped H^- and H^0 ions to the external injection dump. This septum is a combined function magnet to manipulate two beams originated from the unstripped H^- and H^0 ions. A water cooled carbon-carbon block at the lower surface of the vacuum chamber under the stripping foil to intercept the stripped electrons from the H^- injected beam. Two sets of kickers (pulsed dipoles), a set of four (4) for each plane, are used to create dynamic orbit bumps in order to paint the optimum phase space of the injected proton population. The kickers are located in the two shorter straight space of the straight section. The kicker magnets are programmable with time constant as fast as 200 μ-sec.The optimum distribution will be determined by computer simulation and by experimentation.

The injection loss and subsequent beam loss due to all injection mechanisms has to be kept manageable. There are several injection loss mechanisms. These are: 1) the linac beam missing the stripping foil, 2) H^0's emerging from the foil, which is a function of the thickness of the foil, 3) H^- 's emerging from the foil, which is calculated to be negligible, and 4) circulating beam loss due to Coulomb and nuclear scattering on the foil. Loss mechanism 1) is related to the stripping foil size and this loss should be kept to less than a few percent. This beam loss along with loss due to mechanism 3) is well known and a controlled dumping of the waste beam is planned. Loss mechanism 4) is directly related to the thickness of the foil and the amount of circulating beam hitting it, which is proportional to the foil size. The foil size is chosen such that it provides a compromise between mechanisms 1) and 4). The thickness of the foil is determined by mechanisms 2), 4) and the foil heating problem described later. Present plans call for a carbon foil of size of 8 mm × 4 mm and a thickness of 300 mg/cm^2.

3.5.1.3 Disposal of Unstored Protons

The H^- ions that miss the stripping foil and the H^0's emerging from the foil should be disposed of in a proper beam dump. The size of the stripping foil is chosen such that a distribution tail of about 2% of the incoming linac beam misses the foil. This is a compromise

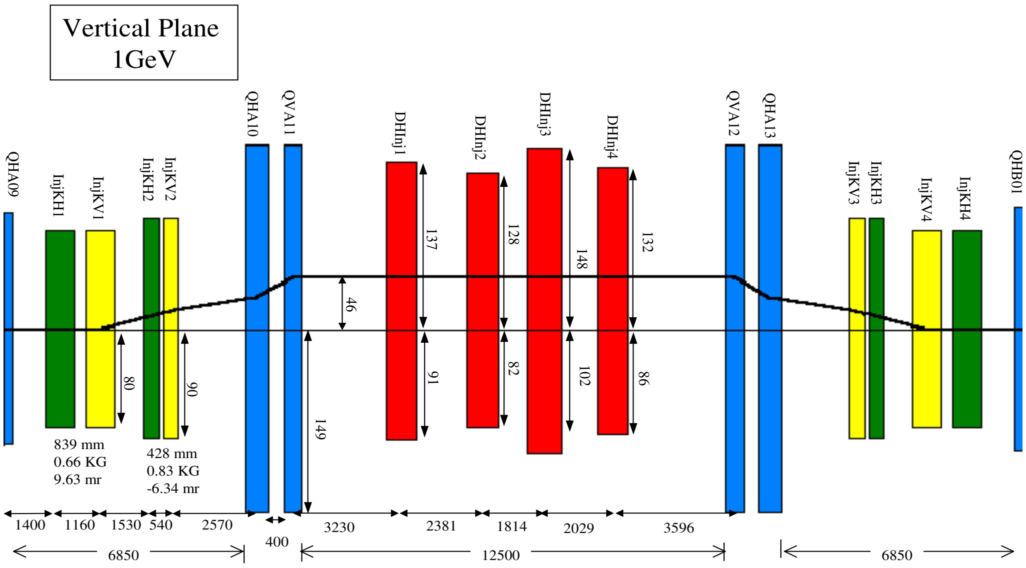

N. Catalan Lasheras 12/04/2002

Figure 66: Injection schematics (vertical layout).

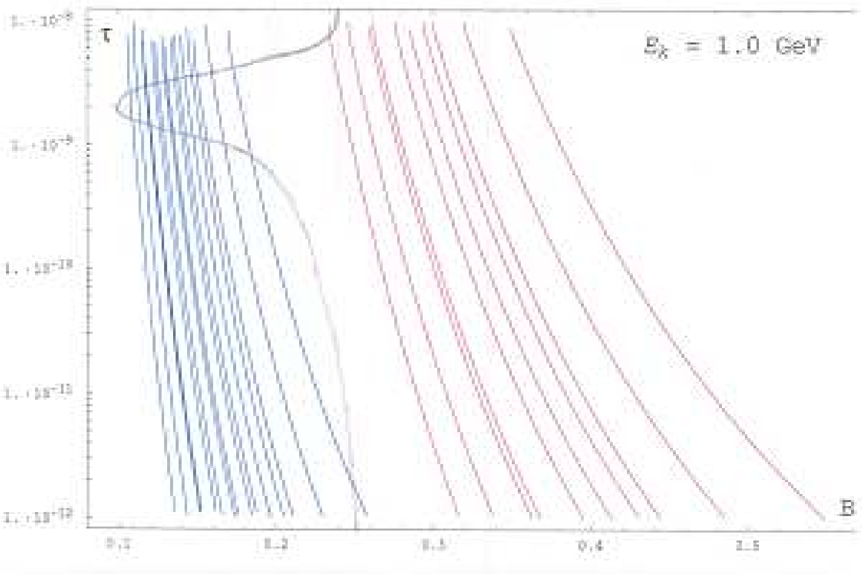

Figure 67: Excited H^0 Lifetime.

between this loss and the loss due to Coulomb and nuclear scattering of the stored protons. Recently very precise measurements of the cross-sections for H^- in carbon have been obtained by Gulley (1996) as follows:

$$\sigma_{-1,0} = (6.76 \pm 0.09)10^{-19}\mathrm{cm}^2 \sigma_{0,1} = (2.64 \pm 0.05)10^{-19}\mathrm{cm}^2 \sigma_{-1,1} = (0.12 \pm 0.06)10^{-19}\mathrm{cm}^2 \quad (21)$$

For a 400-μg/cm^2 thick foil, about 0.82% and for a 300-μg/cm^2 foil about 2% of the incoming H^- ions will emerge as H^0. The population of their quantum of H^0 states is measured to be $n^{-2.8}$, where n is the principal quantum number. The H^0's that emerge from the foil are converted to protons by a thick foil placed in their path. The downstream magnets will separate those protons from the circulating protons. The septum magnet downstream is to be combined function magnet and together with the quadrupole placed downstream shapes the image of the dumped proton beam on to the 200 kW beam dump.

3.5.1.4 Stripped Electron Sweeping and Collection

For 1 GeV SNS injection the stripped electrons from the incoming H^- beam have a momentum of 0.923 MeV/c and a magnetic rigidity of 0.003 T-m. Inside the 2.5 kG magnetic field, the electrons will curve with a 1.2-cm radius. The power of the electrons is about one thousandth of the proton power and is 1 kW at 1 MW SNS, which is formidable electron power. It is essential to dump these electron proper way.

The second and third chicane magnets are specially designed to accommodate the dumping of these electrons. The flux line of the chicane magnet at the foil is 200 m-rad from the vertical, thus the stripped electron spirals downward avoiding lower part of the foil. The path of the electron is shown in Figure 68. In the figure x, y and z projection of the path is shown Aconceptual shape of a electron catcher is shown in Figure 69. The electrons should be caught in underside of the saw tooth to minimize the secondary to re-enter the vacuum space. The material to be used is chosen to be carbon-carbon material for its high melting point and low charge state to minimize the secondary.

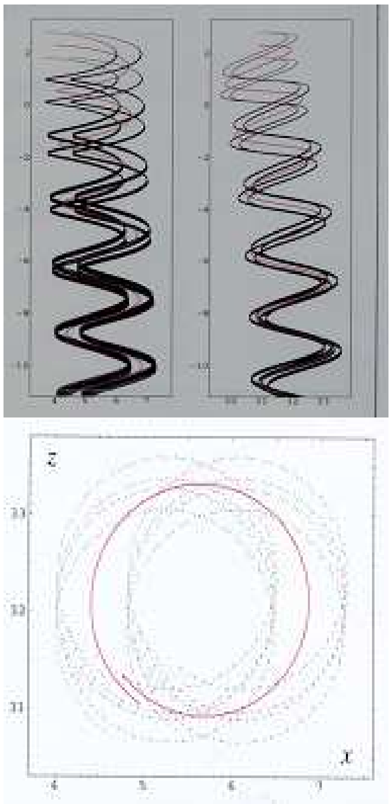

Figure 68: Stripped electron path.

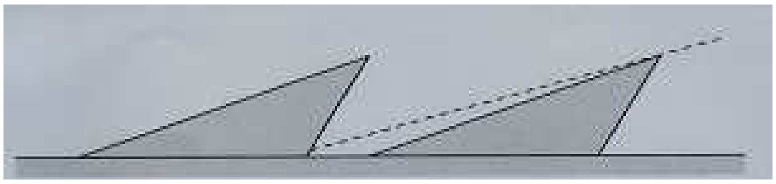

Figure 69: Conceptual shape of the electron catcher.

3.5.1.5 Carbon Foil Heating Considerations

A carbon foil is used to strip the electrons of the H$^-$ beam because of the resiliency and high sublimation temperature of the material. The sublimation temperature of carbon is above 3500°C. The foil is heated by the energy deposited by the proton and the two accompanying electrons. Since they all have the same velocity, they should have approximately same energy loss in a given material. There is no data available for what fraction of the energy lost by the beam contributes toward heating of the material. At higher energies, the efficiency is estimated to be as low as 30%. However, for our calculations we assume that all the energy loss contributes to the heating of the material.

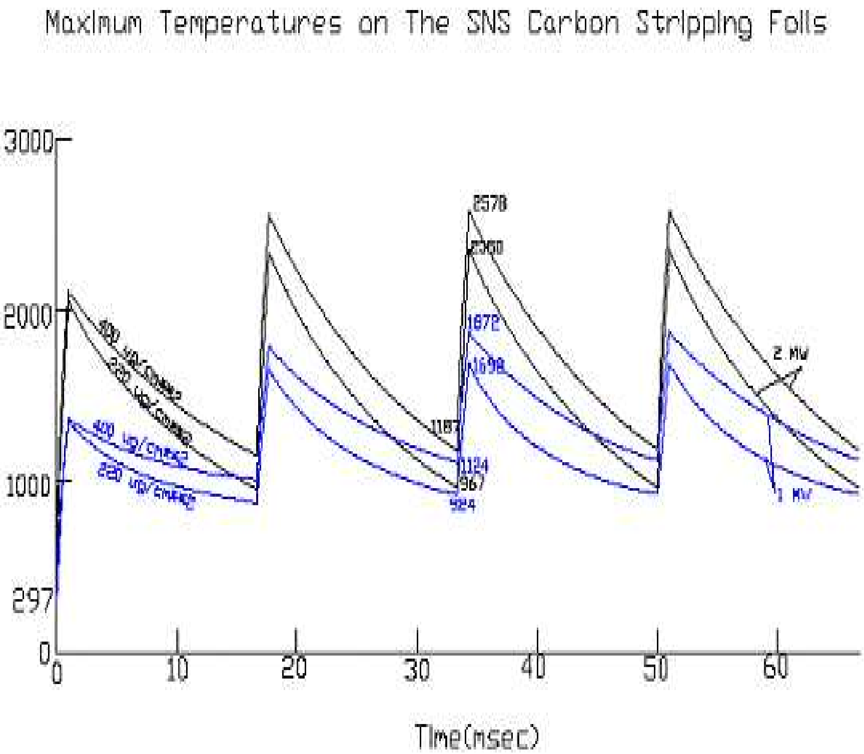

Figure 70: Time evolution of the stripping foil temperature.

For a 1 MW SNS injection, the linac has the following parameters. The effective average current over a macropulse at the injection point is 16.7 mA within the un-normalized rms emittances of 0.14 π mm-mr in both planes. The peak current density at the foil, where the horizontal and vertical beta functions are 16 m and 5 m, is about 2000 A/m^2. The temperature at the spot will rise very quickly toward equilibrium where the heat input and the black body radiation become equal. A ANSYS calculation of the temperature rise at the beam spot for 2 MW SNS is shown in Figure 69. Since the heat input is proportional to the thickness of the foil, while the black body radiation is proportional to the surface area, a thicker foil results in a higher resultant temperature. For the linac current assumed for the SNS injection, a carbon foil of up to 400-mg/cm^2 thickness can survive for 2 MW of beam power, whereas thicker foils may reach their sublimation temperature. However, the mechanism of foil breakage is more complicated than just simple foil evaporation. A experimental result of the foil life time test at the AGS pre-injector beam of 750 keV beam with equivalent to 2MW SNS energy loss is shown in the figure below.

A 1 μm thick CVD diamond foil seem to have long life for the foil stripper. However, a free standing diamond foil has to be produced to use for the purpose. There is on going program of produce such a diamond is in progress.

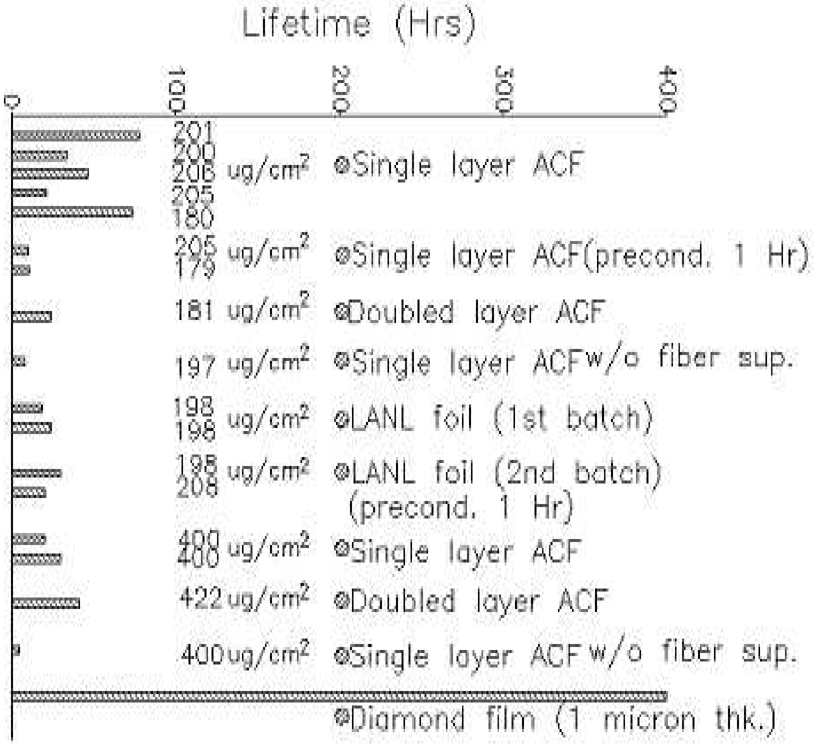

Figure 71: Lifetime of stripping foil measured at 750 keV beam energy at the BNL linac.

3.5.1.6 Foil Changer and the vacuum chambers

As seen, the life time of the stripping foil is not as long as one want to be. One need to be able to change the foil during the operation of the machine without breaking the vacuum. Such a system has been designed and be able to hold over 24 foils which can last for a two week running period. A conceptual picture of the devise is shown in Figure 71.

The vacuum chamber around the injection area are complicated, and shown in Figure 73, 74, 75, and 76.

3.5.1.7 DC Orbit Chicane Magnets

A 10 cm fixed orbit bump is needed to inject the HEBT beam through the injection septum. The septum field is limited to 2.5 KG field at 1.3 GeV injection because of the Lorenz stripping of the H^- ions. For 1 GeV beam energy the septum field is 2.03 kG. The function of the chicane is to shift the closed orbit 10 cm from the nominal and to make the

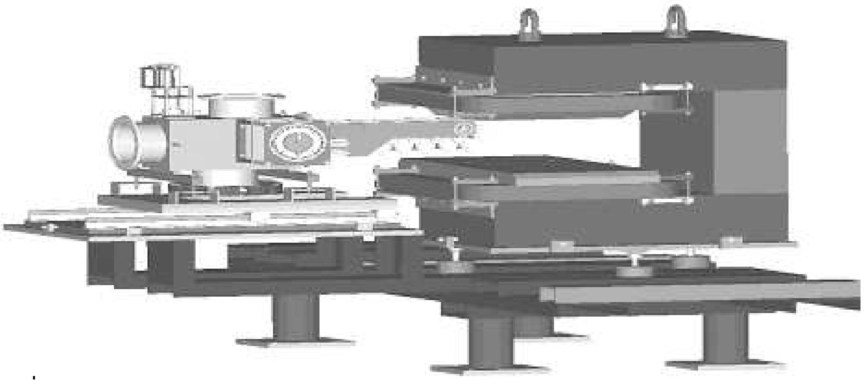

Figure 72: The stripping foil changer in the chicane magnet 2.

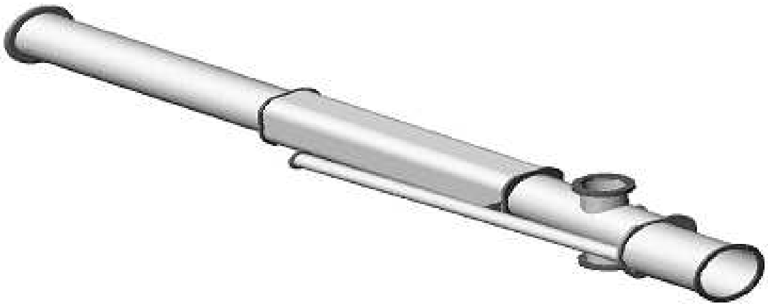

Figure 73: Upstream chamber showing circulating and injected beam pipe.

Figure 74: Chicane 2 chamber with foil changer and viewing port.

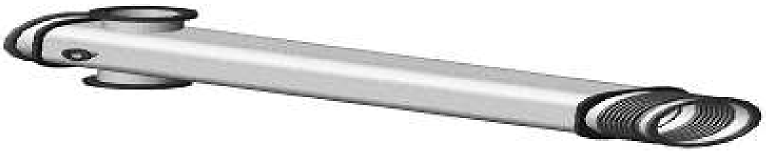

Figure 75: Chicane 3 chamber.

shifted orbit parallel to the nominal orbit. The injection septum is to bring the linac beam tangential to the shifted orbit at the stripping foil. The chicane is consists of four dipoles, and two center magnet needs special attention. Because of aforementioned excited H^0 and of proper dumping of the stripped electron, field direction and strength at the foil must be certain value. The table below defines the requirements for 1 GeV beam energy.

Table 26: Requirement for Chicane Magnets 2 and 3.

Central field	3.0 kG / 2.4 kG
Magnet gap	23.5 cm
Distance between magnet centers	181.4 cm
Magnetic field at the stripping foil	2.5 kG
Field direction at the foil	$\tan^{-1}(Bz/By) >> 65$ mrd
Field integral fefore the foil (chicane #1)	($-\infty$ to foil) 237.6 kG-cm
Field integral after the foil (chicane # 4)	(Foil to ∞) 261.4 kG-cm
Integrated Field Uniformity	$< 5 \times 10^{-4}$

The designed magnets supersedes these requirement and the picture of the magnet and central field plot is shown in the following figure Fig. 75. And the B-field is shown in Fig. 77. The field shown is the result of the TOSCA calculations and we are expected to have the manually shimmed to satisfy the field uniformity.

3.5.1.8 The dynamic orbit bumps

The function of the dynamic orbit bump is to create additional orbit bumps on top of the DC chicane of the injection. The bump shall be fast enough to be able to paint the injected beam density in the phase space in the way minimizes the space charge effects and to minimize a possibilities of any transverse instabilities. The power supplies are programmable and has time constants as fast as 200 μsec. The bump consists of four, two short and two long, magnets in each of the x, y direction located short free spaces of the injection straight section. The picture of the magnets are shown in Figure 79 and the specification of the bump dipoles are in the table.

Figure 76: Injection chamber 4, showing circulating and injection dump port.

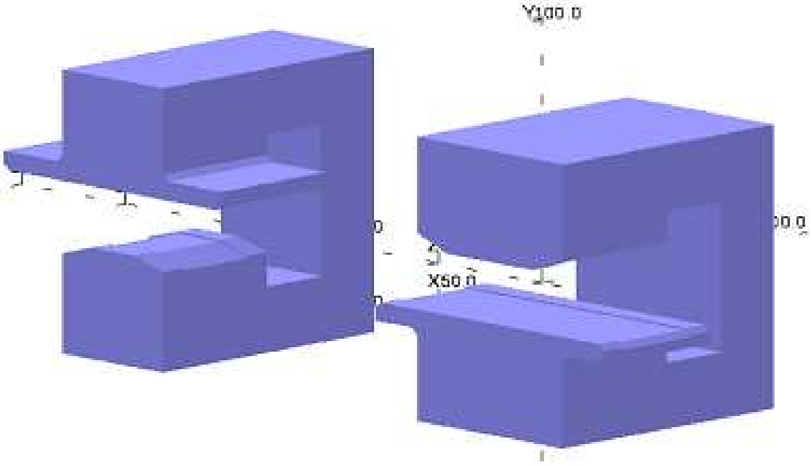

Figure 77: The chicane 2 and 3 magnet core.

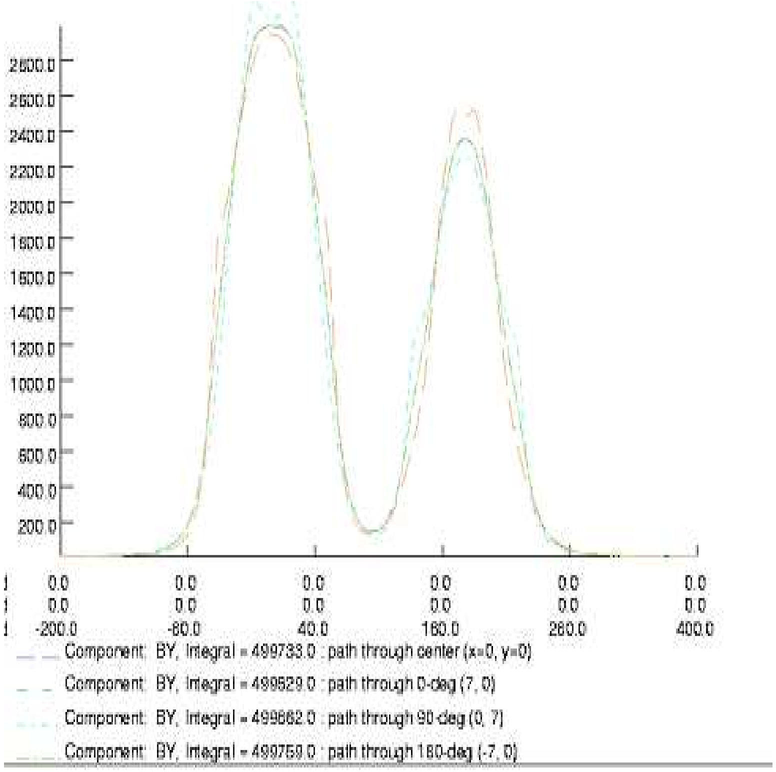

Figure 78: Combined field distribution of the chicanes 2 and 3.

Table 27: Requirement for Chicane Magnets 2 and 3.

	Long	Short
Number	4	4
Core length	64 cm	21 cm
Aperture	19.55×22.48 cm	21.55×24.48 cm
Number of turns	10	12
Max. current	1230 A	1400 A
Max. field	0.079 T	0.1 T
Ceramic vacuum chamber ID	16 cm	18 cm

3.5.2 Transverse phase-space painting

3.5.3 Longitudinal phase-space painting

3.5.4 H^0 and H^- stripping control

3.5.5 Stripped-electron collection

3.5.6 Injection chicane perturbation

3.5.7 Stripping foil assembly

3.5.8 Injection magnets

3.5.9 Ring injection-magnet power supply

3.6 Extraction

3.6.1 Extraction requirements

3.6.2 Extraction layout

3.6.3 Extraction magnets

3.6.4 Extraction-magnet power supply

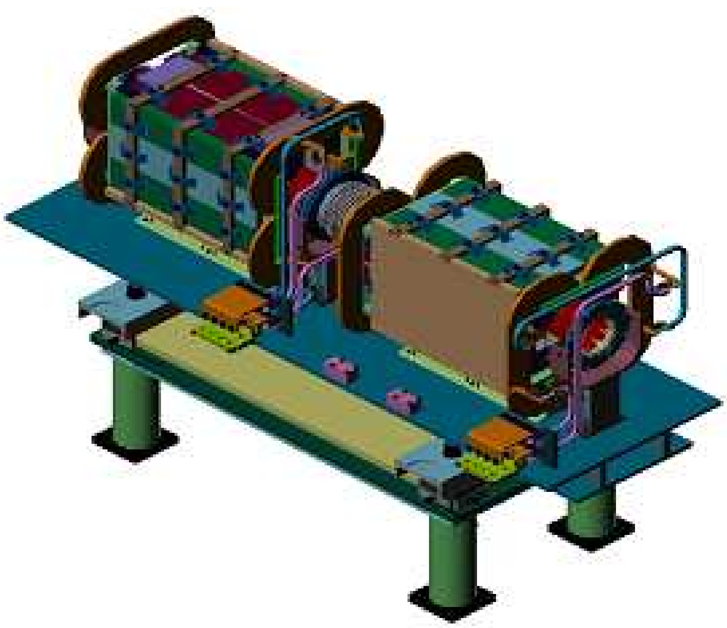

Figure 79: Injection fast kicker.

3.6.5 Extraction Kicker Coupling Impedance Reduction

The success of the SNS (Spallation Neutron Source) will largely depend on reducing the transverse coupling impedance of the accumulator ring. Next to the resistive wall impedance, the largest contribution is made by the fourteen ferrite extraction kicker magnets. Thus, an extensive experimental and theoretical program was carried out to minimize their impedance contribution

The coupling impedance is primarily dependent on the geometric dimensions of the magnet and the impedance presented by the power supply. The power supply impedance is chosen as 25 Ω in view of standard electrical equipment. The minimum apertures of the extraction kickers were determined with the betatron function to yield the overall SNS ring acceptance, although adjustments were made to limit the number of different magnet types to 6. A significant reduction of the impedance was obtained by increasing the vertical aperture, beyond the acceptance limit, while respecting the basic electrical design requirements as to kick strength and pulse rise time.

The magnets will be individually energized by 14 BPFN type (Blumlein Pulse Forming Network) high voltage modulators. Two 50 Ω coaxial cables connected in parallel transfer the current pulse from BPFN to the ferrite magnet and are terminated with a 25 Ω resistor to satisfy the impedance requirement. The BPFN operation voltage was limited to 35 kV, in order to increase the system operational reliability and to be optimal as to the PFN cost. At this voltage, the magnet operating current pulse will be less than 2.5 kA and the magnetic field B is estimated to be from 142 to 251 Gauss, depending on the magnet aperture horizontal dimensions.

The current pulse rise time from 1 to 95% is set at around 200 ns to guarantee clean extraction of the beam. The total magnet plus feed-through inductance is limited at 1.1 μH to meet the pulse rise time constraint thereby limiting the otherwise desirable increase in vertical aperture.

The analysis of the bench measurements performed on the SNS extraction kicker prototype led to an improved model for ferrite lumped kickers. The improved kicker model analyzes the total coupling impedance in terms of contributions from the uncoupled flux and the flux coupled to the external circuit. The coupled impedance represents the dominant part and is given by a general formula that states a more accurate correlation between the coupling impedance of a window frame magnet and its parameters, such as geometric dimensions, external circuit impedance, and ferrite characteristics. It can be used as a guide to the design of kickers in high intensity machines where the coupling impedance budget is a concern.

One of the most interesting property of the model is the scaling law for the contribution to the impedance, coupled to the external circuit, with kicker height, h, :

$$Z_{y\,2} = Z_{y\,1} \cdot \left(\frac{h_1}{h_2}\right)^2$$

This scaling law neglects the fact that the aperture height changes the magnet inductance too and therefore the resonant peak frequency, but it can be considered as an upper limit for the impedances.

For the uncoupled contribution to the impedance, here identified with measurements with shorted bus-bar, one can consider a scaling law that goes, in first approximation, with the square of the aperture gaps, w, namely:

$$Z_{y2}^{sh} = Z_{y1}^{sh} \cdot \left(\frac{w_1}{w_2}\right)^2$$

Combining the impedance reduction from the aperture increase with the various constraints on peak voltage/ current, magnet inductance, and acceptance, resulted in the final extraction kicker dimensions as listed in the following table.

Kicker	Horiz.	Vert.	Length	Kick	I	B/sect	$L = \mu_0 hl/w$
	w [m]	h [m]	l [m]	[mrad]	[kA]	B/sect	[μ H]
K11	0.120	0.166	0.40	1.78	2.40	251	0.695
K12	0.145	0.200	0.40	1.47	2.39	208	0.693
K13	0.145	0.200	0.40	1.47	2.39	208	0.693
K14	0.178	0.195	0.51	1.52	2.40	170	0.702
K15	0.178	0.195	0.51	1.52	2.40	170	0.702
K16	0.211	0.233	0.51	1.28	2.40	143	0.708
K17	0.211	0.233	0.51	1.28	2.40	143	0.708
K21	0.162	0.233	0.43	1.43	2.44	189	0.777
K22	0.162	0.233	0.43	1.43	2.44	189	0.777
K23	0.162	0.233	0.43	1.43	2.44	189	0.777
K24	0.162	0.233	0.43	1.43	2.44	189	0.777
K25	0.151	0.243	0.39	1.40	2.44	203	0.789
K26	0.151	0.243	0.39	1.40	2.44	203	0.789
K27	0.151	0.243	0.39	1.40	2.44	203	0.789

The total coupling impedance for the 14 magnets has been obtained by scaling from the fully measured prototype, for which h = 24.8 cm, w = 15.9 cm and l = 36 cm, as follows. The impedance scales linearly with its length. The transverse impedance of a ferrite lumped kicker in the kick direction has two contributions: one is coupled with the external circuit whereas the other one is not. The coupled impedance scales with the square of the height and the uncoupled impedance with the width of the gap.

The simplest way to represent the coupled contribution of one magnet is by means of a RLC resonator model:

$$Z_y^c = \frac{c}{\omega} R^c \left[1 + jQ(f_r/f - f/f_r)\right]^{-1},$$

where f_r = 27.1 MHz, Q= 0.199, R^c =387 $\Omega/\mathrm{m}^2$for the prototype in operational condition, i.e. connected to the 25 Ω of the PFN. The coupled transverse impedance of the six kicker types, scaled with the vertical aperture and taking into account the resonance change with inductance, are shown in the Fig. 80.

The sum total of the fully scaled impedance values for all 14 magnets is compared in Fig. 81 to the total impedance obtained by applying only the vertical scaling law and keeping the resonance frequency constant. The error made by considering the sum total impedance as due to only one resonator is relatively small, and a good approximation is obtained by multiplying the prototype values with 18.2. Thus, for the sake of simplicity, one can consider the total impedance as generated by one resonator model in numerical beam-instability codes.

The uncoupled contribution to the transverse impedance, which is obtained from the measurement with shorted bus-bar, can be modeled with a lossy inductor and the losses are proportional with the frequency, giving 1kΩ/m at 100MHz. For instability codes purposes, it is still possible to model this contribution with a fictitious resonator,

$$Z_y^{sh} = \frac{c}{\omega} R^{sh} \left[1 + jQ^{sh}(f_r^{sh}/f - f/f_r^{sh})\right]^{-1}$$

where $f_r^{sh} = 400$ MHz, $Q^{sh} = 1.325$, R^{sh} =50 kΩ/m^{2}for the prototype. In the frequency range of interest, this resonator gives an almost-constant imaginary part and a real part, linear with frequency, in good agreement with measurements. The uncoupled impedance is scaled with the aperture width at constant resonance frequency, leading to a factor of about 14 times the prototype result (only by coincidence equal to the number of magnets).

Finally, the total impedance of 14 SNS kickers can be modeled for the purpose of instability codes as:

$$Z_y^{14} \approx \frac{c}{\omega} R_{14}^c \left[1 + jQ^c(f_r^c/f - f/f_r^c)\right]^{-1} + \frac{c}{\omega} R_{14}^{sh} \left[1 + jQ^{sh}(f_r^{sh}/f - f/f_r^{sh})\right]^{-1}$$

with the shunt resistances summed to be R_{14}^c =7.043 kΩ/m^{2}and R_{14}^{sh} =700 kΩ/m^2 , and the quality factors and resonance frequencies approximately taken as unchanged from the prototype.

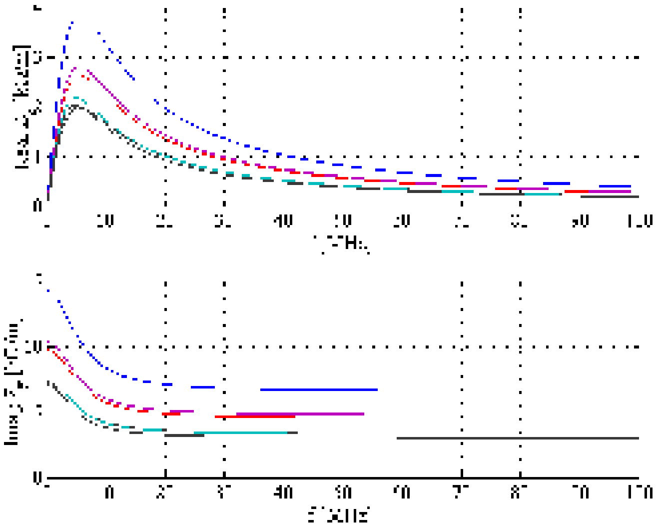

Figure 80: Coupled transverse impedance of the extraction kicker types.

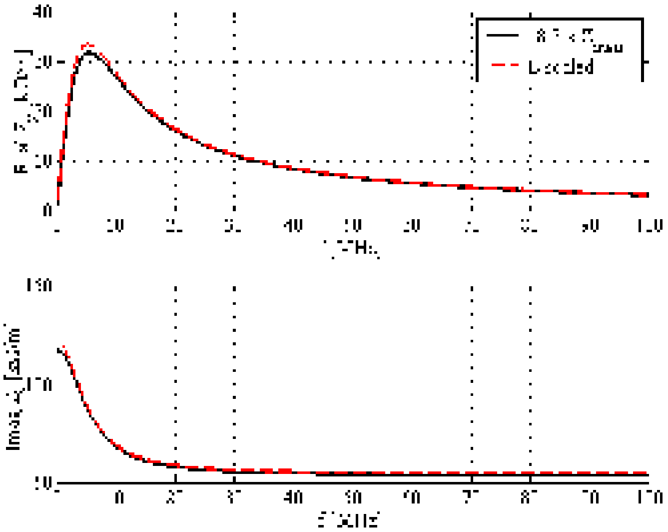

Figure 81: The sum total of 14 extraction kickers, fully scaled. (The solid curve is for constant resonance frequency)

3.7 Beam Scraping and Collimation

In high intensity rings, the size of the beam is enhanced to avoid excessive space-charge forces. The beam thus occupies the highly nonlinear region of the magnetic field near the bore and most of the RF bucket. Large fringe fields are inherent to short and wide magnets and further decrease the beam stability [78]. Rapid acceleration produces non-adiabatic trapping on the longitudinal plane. All these effects pump protons from the core of the beam into the tails in all three dimensions. On the other hand, the relative aperture is dramatically small. While in a high energy collider the aperture of the accelerator is around 10 σ – 15σ (where σ is the rms beam size), in a high intensity ring the aperture is typically less than 4σ.

In the following sections the collimation strategy in the ring and transfer lines will be described, and the mechanical design of the scrapers and absorbers will be outlined.

3.7.1 HEBT Transverse Collimation

The rms emittance of the beam coming from the linear accelerator is expected to be small ($\epsilon_{rms} = 0.5\pi$mm-mrad un-normalized) but large tails in the distribution may contain a fraction of the beam larger than $10^(- 4)$. With a beam power of up to 2MW and beam losses spread along a small number of meters, the residual radiation dose does not satisfy the hands-on maintenance criteria. We need to provide a transverse collimation system upstream in the transfer line HEBT) to prevent losses on the achromat, cavities and injection in the ring.

The minimum aperture in the HEBT line is given by the two RF cavities used for spreading the beam momentum and correcting the central energy [5]. The cavities acceptance is $A_x = 26\pi$mm-mrad. With a small number of collimators in each plane, the main function is to prevent the transport along the transfer line of H^- ions with emittances larger than the line acceptance. Collimators provide little additional shaping capability.

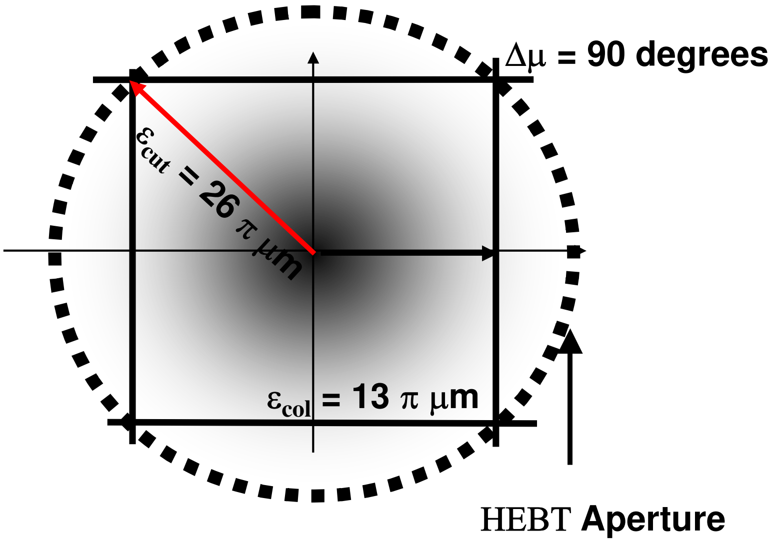

Figure 82: Cuts induced by the striper foils in normalized phase-space.

The layout of the system will be described below. To remove the transverse halo from the beam, we introduce adjustable carbon foils in the path of the beam to intercept the tails. After the passage of the H^- ion through the foil, the two electrons are removed and the H^- focusing lattice moves the proton tails into absorbers where they are stopped and most of the secondary particles also stopped. The aperture of the foils is given by the acceptance of the HEBT line. For transverse collimation of the halo, we have two pair of facing foils in each horizontal and vertical plane.

We locate the foils with a phase advance of 90° between them to achieve the most efficient cut of the phase space. To protect the cavities, the final emittance of any escaping particle must be less than $A_{HEBT} = 26\pi$mm-mrad. Hence, the nominal foil aperture is set to $A_{foil} = 13\pi$mm-mrad (Fig. 82). The horizontal and vertical stripping foils are located at the maximum of the beta function in each plane to enhance the resolution of the system. Once the position

Table 28: Aperture, impact parameter and simulated efficiency for every pair foil/absorber. The initial acceptance at the foils correspond to 13 - mm-mrad. The efficiency has been calculated for 1 GeV energy protons.

Name	Aperture [mm]	Impact [mm]	para. [mrad]	Efficiency [%]	Absorber
Scr 1 U/D	13	12.3	-5.9	94.3	1
Scr 1 L/R	17	4.3	6.7	91.1	1
Scr 2 U/D	13	15.0	-4.1	95.9	2
Scr 2 L/R	17	3.3	6.1	88.7	2

and acceptance of the foils is fixed, the aperture and position of the absorber is decided by the focusing lattice and the required impact parameter. We transported a proton beam created at each foil with any emittance value in the vertical plane. The beam clears the quadrupole aperture and hits the absorber with a large impact parameter. The minimal impact parameters on the absorbers of the proton beam produced in each of the stripers is shown in Table 28. The performance of this arrangement of charge exchange foils and absorbers is outlined below. For H^- collimation by charge exchange the interception of the secondary halo by the absorber is 100% efficient. Still, due to small impact parameters, the protons have a finite probability of escaping the absorber without being removed. Using the values for the impact parameter on Table 28, we simulate the passage of the protons through the material of the absorber with a Monte Carlo code [79]. The absorption efficiency for the secondary H^+ beam generated at each foil is given in Table 28. For efficiency simulations we used a simplified model of the absorbers with a geometry consistent with an equivalent mass of stainless steel. A more realistic model is used for secondary particle production and radiation using the Monte Carlo code MCNPX [80].

The particles escaping the collimator lose a significant fraction of their total momentum by ionization with the absorber material. They are lost along the achromat or captured by the longitudinal collimation system. These values of efficiency are calculated for the nominal aperture of the foils. Opening or closing them produces a different impact parameter at the absorber and changes the final efficiency. In the same way, the absorption efficiency was

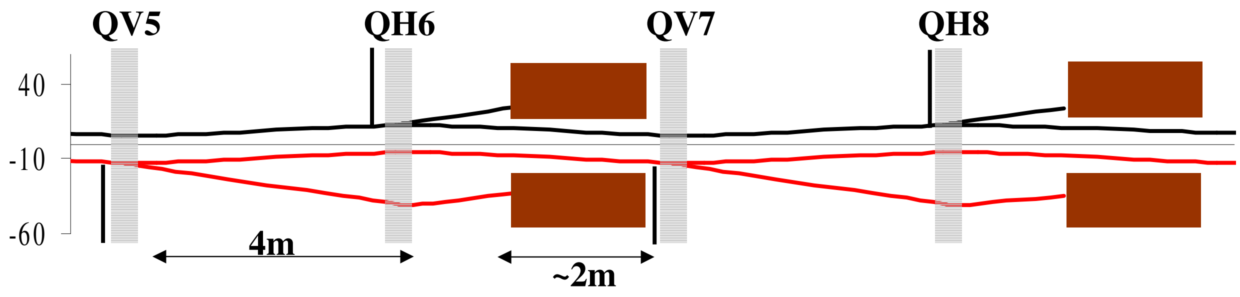

Figure 83: Layout of the HEBT collimation system and proton beam trajectories. Top half corresponds to the horizontal plane while the vertical is represented by the bottom half.

calculated for an energy of 1 GeV. Higher proton energies result in slightly better efficiencies and a different loss pattern downstream from the collimator.

3.7.2 HEBT longitudinal collimation

The tightest requirements for the longitudinal extent of the H- beam are set by the RF cavity in the ring. Previous studies of longitudinal dynamics have concluded that any beam beyond 4 MeV ends up in the gap between consecutive bunches inducing intolerable losses during extraction. A less stringent limit is found in the momentum acceptance of the HEBT achromat where the dispersion is non-zero. We thus locate a charge exchange foil in a high dispersion region in the HEBT achromat to remove the longitudinal tails of the beam before entering in the ring. The losses expected in this collimator are much larger than in the transverse case due to the tighter longitudinal acceptance. Also the uncertainty regarding the energy jitter and momentum spread coming from the super-conducting linear accelerator translate into a larger beam loss budget. In addition, because the one-pass condition in a transfer line, only particles with the incorrect betatron phase are intercepted by the foil and striped even if they have large momentum deviation and emittance. The adjustable foil shaves the beam halo when the following condition is fulfilled

$$x = \sqrt{\epsilon_x \beta} \sin\phi + D\Delta p/p_0 \geq x_{cut} \tag{22}$$

where x_{cut} is the foil horizontal position and $D = 6.9$ m and $\beta = 20$ m are the dispersion and beta function at the foil. A acceptance plot is shown in Fig. 84 where the variables are the horizontal emittance and relative momentum deviation of the H^- ion. The escaping halo clears the HEBT aperture for the emittance range of interest.

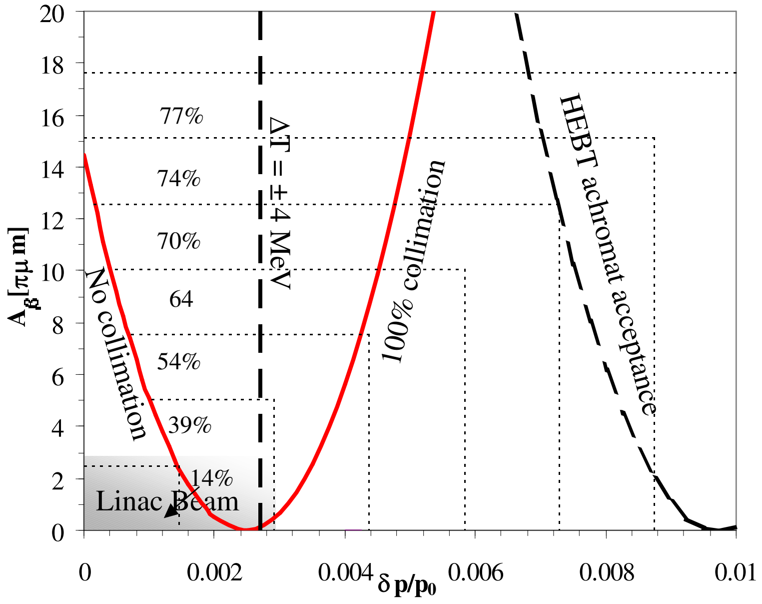

Figure 84: Collimator acceptance in terms of betatron amplitude vs. $\Delta p/p_0$. The geometry acceptance of the HEBT achromat and the momentum spread limit at ±4 MeV are represented by dashed lines.

However, some particles escape with energy deviation above 4 MeV which contribute to the beam in the gap inside the ring. Assuming gaussian distributions, a nominal beam coming from the linac with a transverse emittance of $\epsilon_{rms} = 0.28\pi$mm-mrad and a energy spread of $\Delta T_{rms} = 0.72$MeV will have a less than a fraction 10^{-4} above the limit determined by the foil. A Monte Carlo integration predicts an interception efficiency of the gaussian tails only of 14%. For a beam with an emittance and momentum deviation twice the nominal values area predicts an efficiency of 39%. However, large momentum tails are removed more efficiently than large emittance particles. The interception efficiency for particles with momentum deviation larger than 4 MeV is better than 90% ensuring that the population of the gap in the ring is less than approximately $10^(- 5)$ of the total beam.

After being striped the proton beam is deflected by the dipole field into a large absorber outside the circulating beam trajectory. The vacuum pipe geometry after the foil has been adjusted to clear the dipoles and the H+ beam passes through it to the absorber. In this case the absorber efficiency in the collimator is 100%, since the protons are swept out of the main beam path and impact the absorber located outside the accelerating structure.

3.7.3 Ring transverse collimation

Collimation in the ring is accomplished by passing the beam through a set of jaws, where it undergoes Coulomb scattering, losses energy, and subsequently gets captured in strategically placed absorbers. An important process taking place in the collimator jaws is energy loss by ionization. The mean rate of energy loss is given by the Bethe-Bloch equation. We have not included the density correction term in this analysis, which is important only at very high energies. The energy loss of protons has a shallow minimum at p = 3GeV/c. It is nearly constant toward higher energies but rises rapidly below 1 GeV/c. At an energy level of approximately 1 GeV the relative energy loss by ionization is considerable. Protons out-scattered from the jaws, and those traversing the full collimator may end outside the RF bucket acceptance or the momentum acceptance of the ring given by the maximum dispersion. Energy loss may help increasing inelastic scattering cross section as well as completely stopping the proton in the collimator. It does not help however against out-scattering in the front of the jaw. If we adjust the thickness of the scraper/jaw to have a constant relative momentum loss of $\Delta p/p_0 = 1\%$, the rms angle given by Coulomb scattering increases with the atomic number of the target as shown in Fig. 4. High Z materials are preferred in order to increase the impact parameters in the secondary collimators with minimum energy loss.

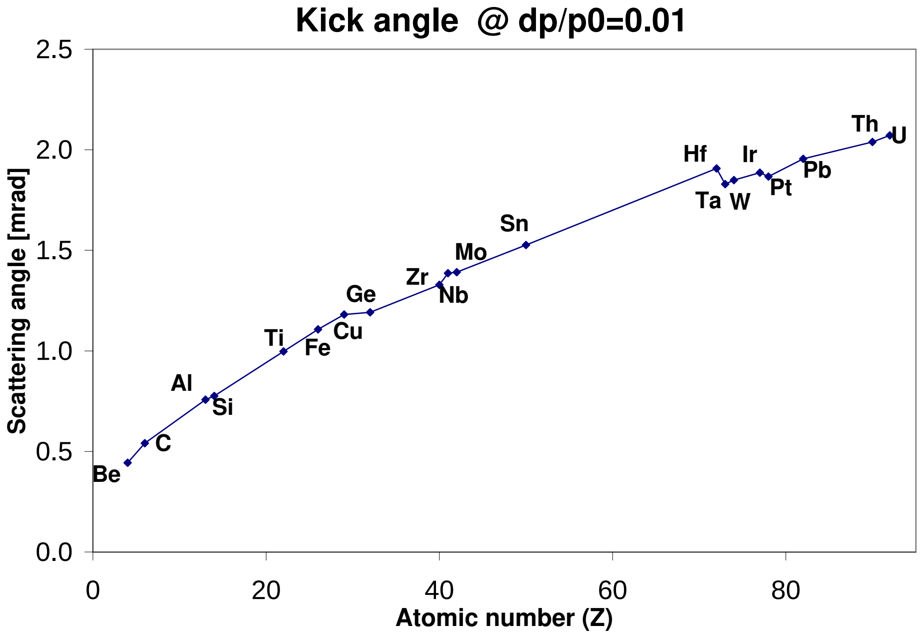

Figure 85: Scattering angle produced by mCs for different materials. The thickness of the scraper has been adjusted to lose 1% of the initial momentum according to Bethe-Bloch equation.

Special care has to be taken when designing momentum collimation with scrapers. The energy loss in the target adds up to negative momentum and prevents multi-turn collimation.

In addition, the betatron oscillation of negative momentum deviation protons may be damped. Different machines take different approaches depending not only on requirements but also available space, energy or expertise. Two existing high intensity proton machines, namely ISIS in Rutherford Appleton Laboratory and Proton Storage Ring (PSR) at Los Alamos, have completely different approaches in dealing with beam losses and collimation. On one hand, ISIS [81], a rapid cycling synchrotron with 0.16 MW of beam power uses a multi-stage collimation system consisting of thin graphite/copper scrapers to absorb mainly trapping losses at low energy (up to 10% at 70 MeV). The measured efficiency reaches 80%. After acceleration, losses become much less important but do not vanish. An upgrade has taken place in the collimator systems to accommodate losses at higher energy. On the other hand, the PSR is an accumulator ring storing 800 MeV protons for a total beam power of 0.8 MW. In this case, no collimators are provided and the total losses are reduced by means of machine conditioning. A new H^- injector, and tight control of instabilities have reduced the beam losses to 0.3% of the total beam [82]. When designing new machines, where both the energy and the power increase considerably, none of these approaches would be sufficient by themselves. Limiting and controlling beam losses will both become necessary to achieve reasonable beam loss levels and low radiation levels. In Table 28, we indicate the main parameters of existing and planned high intensity proton rings.

In the case of the SNS the beam power is projected to be 2 MW and a circumference of 248 m, the beam loss limit of 1 W/m translates into a fractional loss of approximately $10^(-4)$. With an expected halo of about $10^(-3)$ mainly due to space-charge, the collimation system of SNS must have an efficiency larger than 90% [78].

The optimization of a two-dimensional collimation system for SNS operating conditions is achieved by minimizing the extent of the escaping halo, attending to the lattice functions, and collimators geometry. For the present lattice of the SNS accumulator ring, which uses one primary and two secondary collimators, the maximum extent of the residual halo was found to be 480 πmm-mrad. Realistic simulations including scattering in the collimator material show indeed that the residual halo above this amplitude satisfies the tight uncontrolled loss requirements. Our first requirement is to provide an overall aperture equal or bigger than 480 πmm-mrad to maintain the uncontrolled loss under reasonable limits. For momentum cleaning, we require a momentum acceptance of $\Delta p/p_0 = \pm 2\%$ to allow the off-bucket beam to drift between bunches. The condition is easily satisfied along the straight sections. In the arc, the minimum betatron acceptance for this momentum deviation is 220 πmm-mrad, which is still larger than the beam emittance after painting to 160 πmm-mrad.

In the SNS accumulator ring, a straight section 30m long is dedicated to transverse collimation. The lattice functions are common to the entire machine and cannot be modified inside the cleaning section. A set of four movable scrapers made out of 0.45 cm tantalum plates acts as primary collimators increasing the divergence of the halo protons. Two heavy absorbers presenting an equivalent mass of approximately 60 cm of stainless steel are located downstream as fixed aperture secondary collimators. The first secondary collimator is located immediately after the primary scraper. The second secondary collimator is located in at the beginning of the the long straight section between doublets. The last secondary collimator is located at the end of the long straight section between the doublets. Additionally, the second and third secondary collimators are surrounded by approximately 1 meter of solide steel shielding on either side. The layout of the collimators in the straight section is shown schematically in Fig. 86.

Figure 86: Layout of the SNS ring collimators in the collimation staight section. The green ellipses represent the quadrupole magnets, the red rectangle represents the scraper box, the light blue rectangles represent the 300πmm·mrad secondary absorbers, and the dark blue rectangles represent the 480πmm·mrad solid steel shielding. Note: Figure not to scale.

Two painting schemes are planned for the SNS, which provide a circular or square beam in real space. The final size of the beam is likely to be modified during operation. The four tantalum scrapers can move independently to adjust to any beam shape and size as illustrated in Fig. 87. The aperture of the primary collimator is given by the size of the beam and can be set between 120-300 πmm-mrad. The aperture of the secondary collimators is set such so ad to prevent it from becoming a primary collimator under nominal conditions. Nominal scraper apertures are $\epsilon = 220 - 250\pi$mm-mrad. Secondary absorbers have a fixed aperture $\epsilon \geq 300\pi$mm-mrad. The single exception to the constant aperture condition of the secondaries regards the first secondary collimator located just after the primary scraper. This collimator is significantly longer than the other two, and has an aperture shift about two-thirds of the way through. The steel shieldings have apertures that follow the beam pipe with $\epsilon \geq 480\pi$mm-mrad. A summary of the parameters of the ring collimation system is given in Table 29. The positions of the collimators are taken relative the ring injection point. The exact acceptance of each collimator varies over the length of the collimator according the lattice beta function, and must be calculated separately for each lattice working point. The constraint applied to the secondary apertures is that the acceptance is greater than approximately 300πmm·mrad for four of the baseline ring working points: $(\nu_x, \nu_y) = (6.23, 6.20)$, $(\nu_x, \nu_y) = (6.4, 6.3)$, $(\nu_x, \nu_y) = (6.3, 5.8)$, and $(\nu_x, \nu_y) = (6.23, 5.24)$.

The secondary collimators designed for the ring and transfer lines of the SNS consist of a layered structure designed to capture the beam protons and any resulting radioactive isotopes within the structure of the collimator.

The SNS ring collimation system is intended to mitigate beam halo caused by space charge and other collective effects. Additionally, the collimation system will absorb the off-orbit beam resulting from hardware failures and the beam in the gap once it is excited by the kicker fields. Except for a few exceptions, such as the injection and extraction regions, the loss distribution in the SNS ring will be completely controlled by the collimation system.

A complete Monte-Carlo style collimation routine has been implemented into the ORBIT particle-in-cell tracking code [11]. The combined package allows for a realistic assessment of the ability of the collimators to clean the SNS beam halo and to prevent high levels of uncontrolled beam loss in other areas of the machine. Proper handling of magnetic and beam pipe apertures is a must for detailed predictions of loss distributions, and the ORBIT accelerator environment allows the inclusion of these restrictive apertures.

Several ORBIT simulations have been performed for the full ring collimation system. To accurately model loss distributions, the simulations incorporate black absorber apertures for all of the magnets in the ring, and vacuum pipe apertures every few meters in the straight sections. A realistic simulation of the SNS beam incorporates the effect of a slowly drifting beam halo, similar to what might be expected from space charge effects in the beam. In the following simulation, the SNS beam is modeled as a KV distribution with initial maximum emittance $\epsilon = 185\pi$mm·mrad. The four scrapers are again set to 220πmm·mrad. To simulate a realistic halo drift, and small, artificial kick is imparted to beam particles on every turn to induce emittance growth. The rate of growth is chosen such that impact parameters on the scrapers are no more than a few millimeters high. The remainder of the simulation parameters are summarized in Table 30. After several hundred turns around the ring, all of the particles in the beam distribution are lost to either the collimator system or the machine apertures. The loss distribution for the entire ring and the collimation straight section by itself are shown in Figure 88. A summary of the loss distribution is given in Table 31.

Since the exact fraction of beam that will intercept the scrapers is not known a priori (the estimated value is 2×10^{-3}), the collimation results are best described in terms of the percent of the scraped beam. Although in the simulation presented here the entire distribution

Table 29: SNS Ring Collimator Parameters. Positions are measured with respect to the ring injection point.

Element	Position [m]	Length [m]	Material	Aperture [mm]	Acceptace [πmm·mrad]
Primary Collimator Shielding	49.7	0.6	steel	x:100, y:100	≥ 480
Primary Scrapers	50.5	0.0045	tantalum	variable	0-480
Secondary Collimator 1 (Aperture 1)	51.3	1.2	steel/water (65%/35%)	x:68, y:50	≥ 300
Secondary Collimator 1 (Aperture 2)	52.5	0.6	steel	x:74, y:48	≥ 300
Secondary Collimator 1 Shielding	56.7	1.0	steel	x:140, y:140	≥ 480
Secondary Collimator 2	57.7	1.12	steel/water (65%/35%)	x:62.5, y:62.5	≥ 300
Secondary Collimator 2 Shielding	58.8	1.0	steel	x:140, y:140	≥ 480
Secondary Collimator 2 Shielding	64.1	1.0	steel	x:140, y:140	≥ 480
Secondary Collimator 3	65.2	1.12	steel/water (65%/35%)	x:62.5, y:62.5	≥ 300
Secondary Collimator 3 Shielding	66.3	1.0	steel	x:140, y:140	≥ 480

is eventually lost, the scenario is generic for any type of drifting halo beam. The resulting collimation efficiency in the simulation is 91.4%. The trend in the loss distribution to the collimators is for the first collimator in the sequence to absorb the largest fraction of beam, and the last collimator to absorb the smallest fraction. This effect is due to the long tail of the scattered distribution, which intercepts the first restrictive aperture, regardless of the beam phase. An important result not specified in the Table 31 is that although the primary collimator system endures a high fraction of the collimation losses, the vast majority of these losses are within the collimator and not the shielding. Each secondary collimator is designed to handle the entire portion of the anticipated 2×10^{-3} fractional beam intensity; losses on shielding components, however, should be kept to no more than 5-10% of the 2×10^{-3} value.

The uncontrolled beam losses are mostly contained within the second drift of the collimation straight section, between the two quadrupole doublets. In fact, over 98% of the beam is lost within the collimation straight section. Thus, the collimation system meets is baseline efficiency goal of 90% or higher, and moreover it contains almost all uncontrolled losses to a single straight section. The level of residual radiation in this section can be anticipated to be higher than the 1 W/m hands-on maintenance requirement, and therefore very little hands-on access will be allowed in this region, and remote handling of components is expected.

Although only one simulation has been presented here, a large number of simulations using a variety of beam distributions, halo drift velocities, and lattice working points have been performed. These simulations consistently produce collimation efficiencies in the range of 90-92%, and distributions very similar to those shown in this section.

Table 30: Drifting Halo Simulation Parameters

Beam Distribution	KV
Initial Full Beam Emittance	185πmm·mrad
Scraper Aperture	220πmm·mrad
Number of Particles Used	100000
Lattice Working Point	$(\nu_x, \nu_y) = (6.23, 6.20)$

Table 31: Summary of Loss Distribution

Region/Element	% of Scraped Beam Lost
Scrapers	4.5
Primary Collimator and Sheilding	39.7
First Secondary Collimator and Sheilding	28.1
Second Secondary Collimator and Sheilding	19.2
Vacuum Pipe in Collimation Section	5.2
Quadrupoles in Collimation Section	2.0
Ring Outside of Collimation Section	1.3

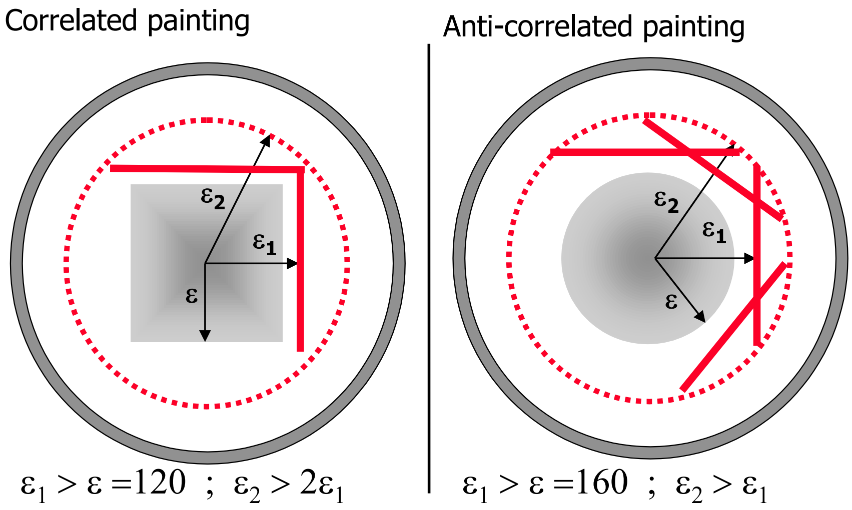

Figure 87: Schematic view of the primary and secondary collimators setup for correlated and anti-correlated painting.

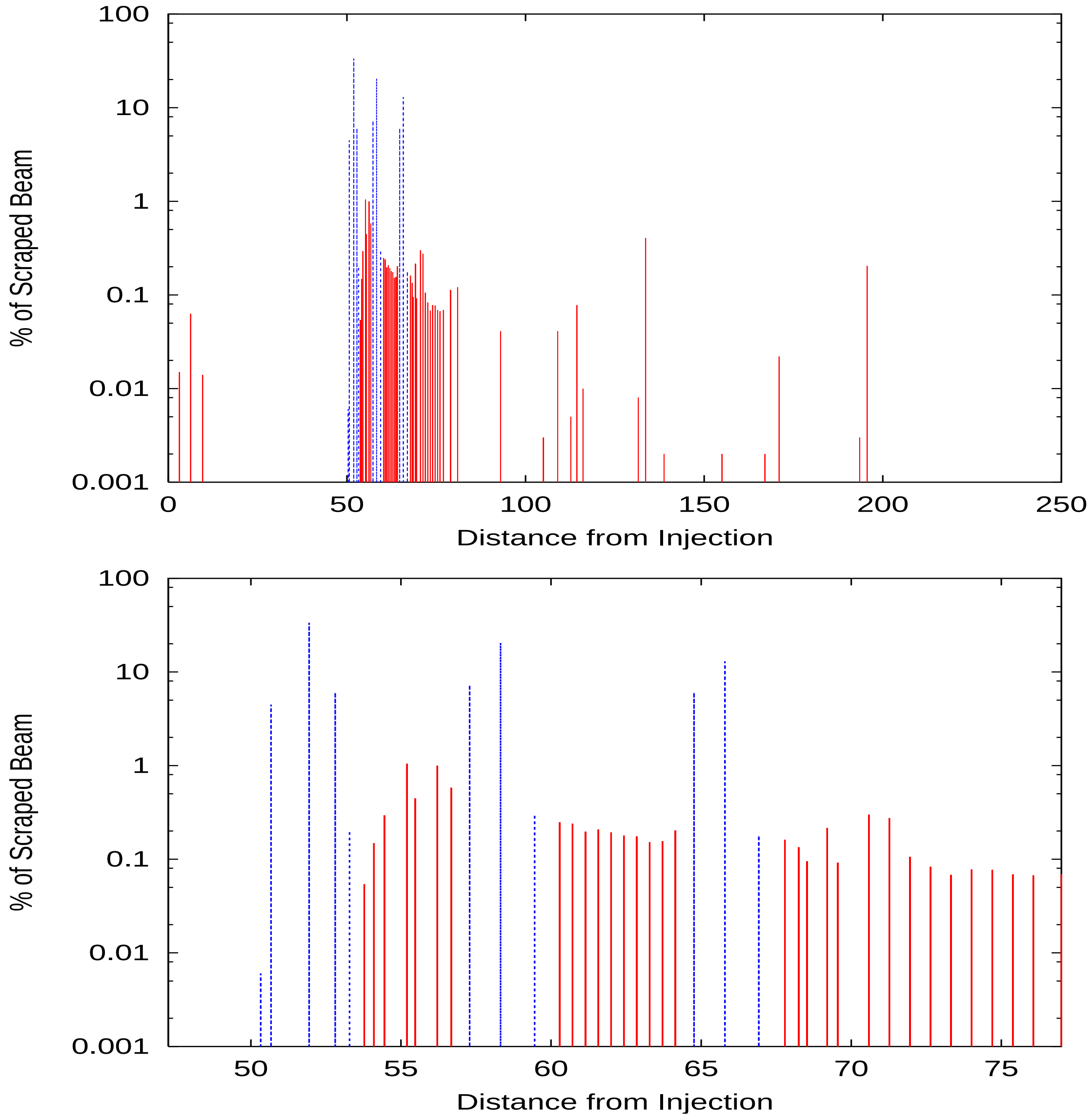

Figure 88: Histogram of predicted particle loss distributions in the SNS accumulator ring, plotted on a logscale. Top: The entire SNS ring. Bottom: The collimation straight section. In both plots, the dashed (blue) lines represents losses to the collimation system, and the solid (red) lines represent losses to magnetic or vacuum pipe apertures.

3.7.4 Ring beam-in-gap cleaning

As the space in the arcs is limited and the straight sections are dispersion free, there is not enough space in the ring to provide a dedicated momentum cleaning section using conventional collimators. A solution is to install a fast rise kicker that fires between bunch passages. The kicker drives the protons to the collimation system in several turns (typically 10-20) where they are eventually removed. The final absorption efficiency of these protons in the collimators is at least as high as for betatron losses because of larger impact parameters. This principle has already been experimentally demonstrated in the National Synchrotron Light Source (NSLS) at Brookhaven and at HERA in DESY. The main difference is that the kicker polarity can be adjusted turn by turn following the betatron oscillation of the beam in gap. The sequence of kicks has to be resonant with the betatron tune to avoid damping of the amplitude.

3.7.5 RTBT transverse collimation

Unlike the HEBT line, where the beam is small and the micro bunch power is reduced, the beam passing through the RTBT line has full beam power, and a considerable size compared to the line aperture. In addition, a full pulse with a large closed orbit deviation may damage the target vessel or the moderators. The main purpose of the RTBT collimation system is to capture the beam in the event of extraction kicker misfire. The optics and aperture have been adjusted so that, if one of the fourteen extraction kickers fails, the beam is transported through the line without scraping, and the deviation on the target is under 2 mm (see Fig. 89). When more than one kicker fails simultaneously, the beam is intercepted by two collimators. The position of the collimators has been chosen between the locations with large orbit deviation and is shown in Fig. 89 superimposed on the closed orbit deviation. The phase advance between them is approximately 135°.

Fig. 9 shows the beam center and extension at the two collimator when two extraction kickers fail simultaneously. Thin lines correspond to one kicker misfire. Bold lines are the maximum and minimum closed orbit deviation when two kickers fail.

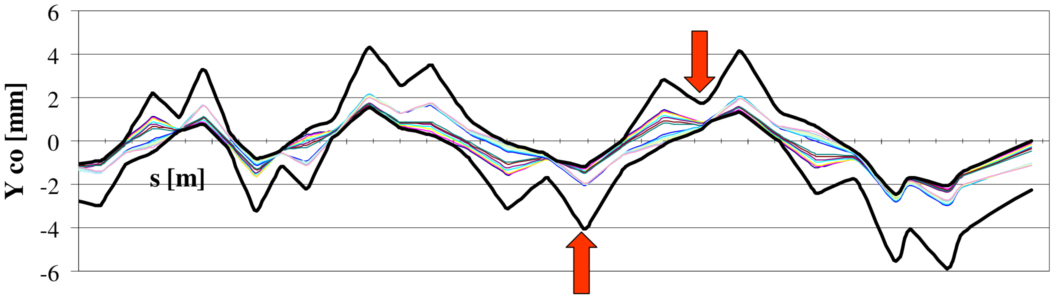

Figure 89: Vertical closed orbit deviation along the RTBT.

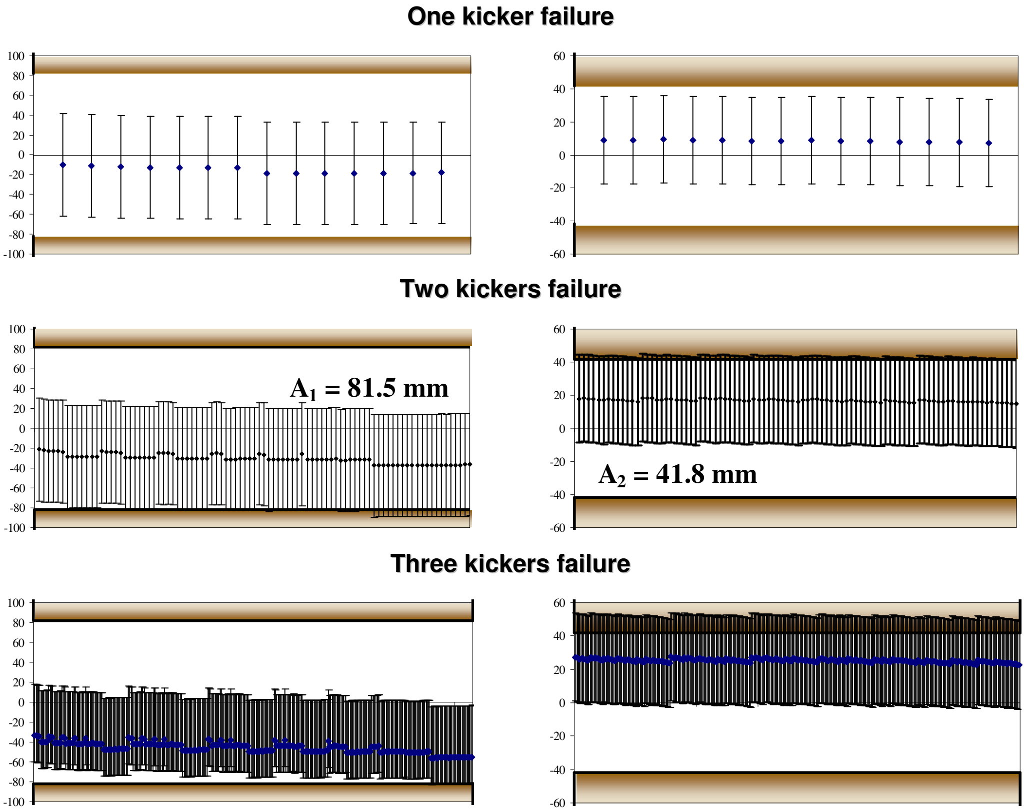

Figure 90: Beam position and size at the two RTBT absorbers after one, two, and three extraction-kicker missfire. The aperture of the collimators corresponds to 400 πmm mrad.

3.7.6 Moveable scrapers design

In this section the mechanical design and thermo-mechanical response of scrapers used in the ring will be described. The perturbation introduced in the halo trajectory by the coulomb scattering in the scrapers is sufficient that it eventually impacts one of the absorbing structures placed in the collimation straight of the ring. It has been determined that 0.55 cm of platinum results in the optimum amount of coulomb scattering, while simultaneously minimizing the energy loss per pass through the scraper. It is thus reasonable to expect that particles that do not immediately impact an absorber will impact one within the next few orbits around the ring. The absorbers are placed at 300πmm-mrad, while the scrapers are at 140πmm-mrad, and the vacuum chamber is at approximately 480πmm-mrad. The scrapers are subjected to periodic thermal loads that increase as the ring accepts particles from the linac, and when the desired intensity has been reached ($\sim$ 1200 turns) it drops off precipitously as the particles are passed to the target. This pattern repeats itself sixty times per second. Thus, fatigue, and possibly thermo-mechanically enhanced stresses will be investigated as possible causes of failure. In addition, material damage due to exposure to the high-energy proton beam will be addressed. The following sections outline the scraper design, method of analysis, and the results.

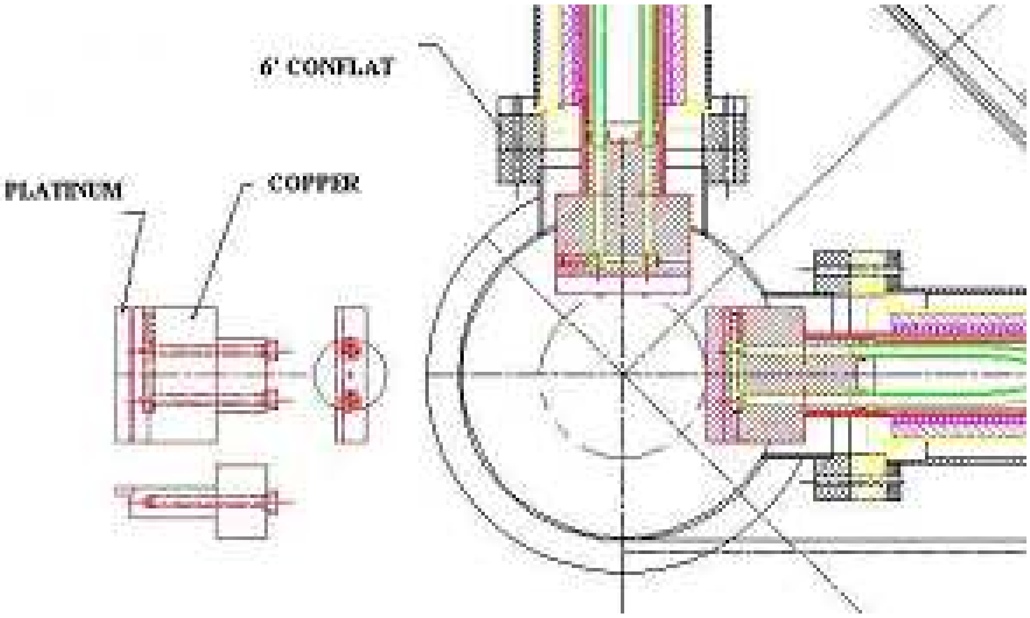

Figure 91: SNS halo intercept layout.

3.7.6.1 Design and analysis

A scraper consists of a platinum piece (mentioned above), 0.55 cm thick, 5.0 cm long, and 1.0 cm wide. This piece is attached to a copper block of similar dimensions, except that its thickness is increased sufficiently to include a water-cooling loop. The copper block is attached to a hollow stainless steel arm, which is support on an appropriate linear bearing. A bellows separates the system vacuum from the environment, and a chain driven linear drive system moves the arm back and forth. The drive motor and its controls are placed far from the scraper to minimize damage to the electronic control mechanism. Additional shielding will be placed between the scraper and the drive motor in the actual installation. The mechanical arrangement of a scraper and its drive system is shown in Fig. 90. Fig. 91 is a schematic of the copper/platinum arrangement that includes the cooling loop. The finite element analysis of the scrapper is based on the discretization of the shown volumes.

The method of analysis employed in this estimate starts by determining the energy deposited in the scraper as a function of position. This result is in the form of Joules/cm^3-p$^+$, and thus the time dependent heat source scales this value during the time dependent pulse. This pulse is in the shape of a tri-angle, building up for 0.0166 seconds and drops off in one micro-second. Fig. 92 depicts the time structure of the micro-pulses in the accumulator ring.

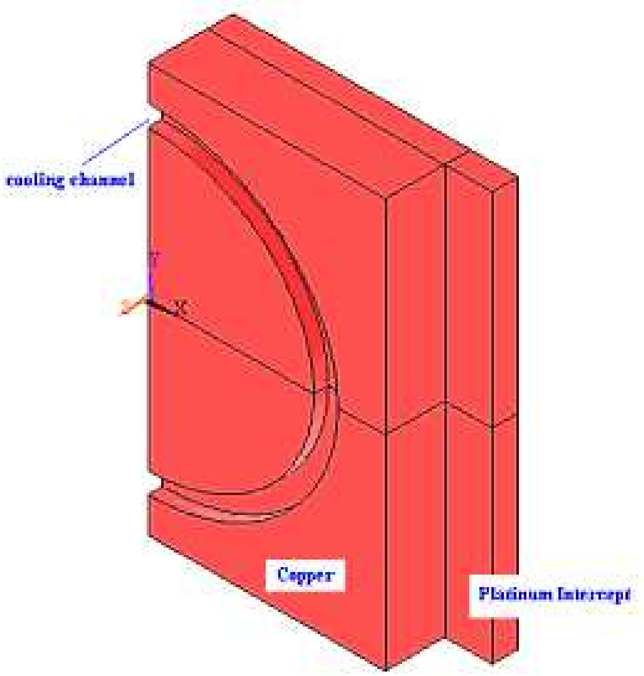

Figure 92: Schematic of the platinum/copper (half) arrangement showing the cooling channel within the copper block.

During this build-up the number of particles increases from zero to 1.5×10^{14} (maximum followed number of particles per pulse), thus simulating the heat deposition rate. A thermal calculation is carried out to determine the temperature distribution. This step is followed by a stress analysis to determine the stresses due to thermal gradients and possible enhancement due to thermo-mechanical effects. The Monte Carlo code MCNPX [80] is used for the first step, and the thermal-stress analysis code system ANSYS [83] is used for the second step.

3.7.6.2 Thermal analysis

The heat deposition rate is determined assuming a parallel beam of 1 GeV protons, with a hollow cylindrical shape. The actual beam is ignored in this calculation, since it is not affected by the scrapers, and only the halo portion is considered. Radially the halo is assumed to be 3 mm thick and it drops off in a step-wise fashion, with 75% in the first millimeter, 20% in the next millimeter, and 5% in the last millimeter. The fraction of the primary beam assumed to be in the halo is 0.001, and thus the maximum number of protons in the halo per pulse is 1.5×10^{11}. However, given that beam may move closer to the scrapper due to instabilities a 1% of the total beam assumed to be intercepted by the scrapper. In the worst-case scenario, the beam may stray excessively toward the scrapper or the scrapper has moved into the beam by accident. In such case the platinum/copper mass will see the full beam with several micro-pulses before the beam is tripped. This accident scenario has not been analyzed.

From the neutronic calculations it is seen that the maximum heat deposited in the platinum scrapper is approximately 0.14 Joules/cc when assuming that only 0.1% of the beam is in the halo. The energy deposited with 1% beam in the halo is 1.4 Joules/cc.

There are two thermal conditions of interest in the interaction of protons with the platinum. First, is the temperature rise that is induced by each micro-pulse and its subsequent diffusion. If such rise is significant then fatigue issues in the material become important. Second, is the steady state that the system reaches after several micro-pulses. The operating temperature profile, given the energy deposited per unit time in the scrapper, will depend on the heat removal capacity that is provided by the coolant in the channel.

By performing a thermal shock analysis on the model it is seen that the temperature rise per micro-pulse is negligible (less than 1° C) indicating that thermal fatigue under normal operating conditions is not an issue. In analyzing the steady state thermal condition that the system can reach with a reasonable choice of heat removal capacity, a peak temperature rise of approximately 42° C was calculated. Shown in Fig. 94 is the temperature profile in the platinum-copper arrangement.

3.7.6.3 Thermal stress shock and fatigue

Following the thermal analyses of the previous section, the temperature profiles for both the steady state and the single micro-pulse interaction were introduced into a steady state and transient stress analyses respectively. As mention earlier, the shock generated by each micro-pulse and its connection to thermal fatigue is not an issue. The steady state thermal stress, on the other hand, is more serious. Shown in Fig. 95 and 96 are the von Mises and axial stress profiles in the scrapper. As anticipated, the critical area is the interface between the two dissimilar materials. From Fig. 96 one deduces a von Mises stress of approximately 30 MPa shared by both materials at the interface. While the stress level may appear to be safe based on the strength of both materials, the way the two are bonded may be an issue. The stress level, however, may be reduced by an increase in the flow rate of the coolant in the channel. This iterative process will guide the final design of the scrapper assembly.

In order to complete the supporting analyses that guide the final design, the accident scenario of full beam intercept need to be carried out.

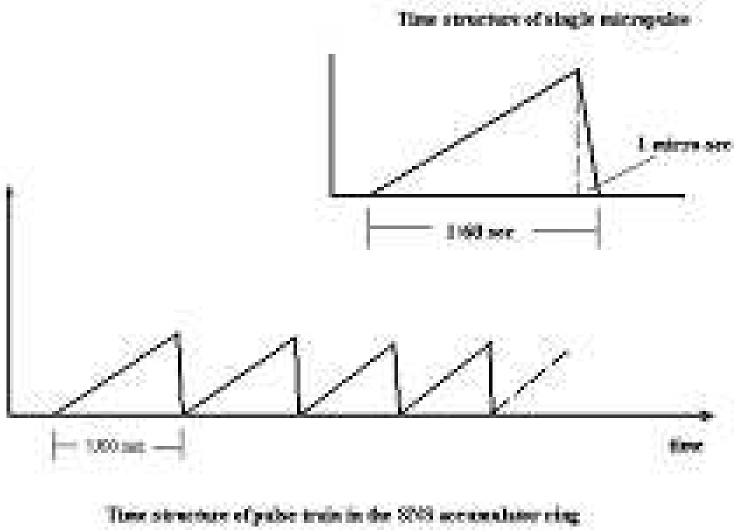

Figure 93: Pulse Time Structure.

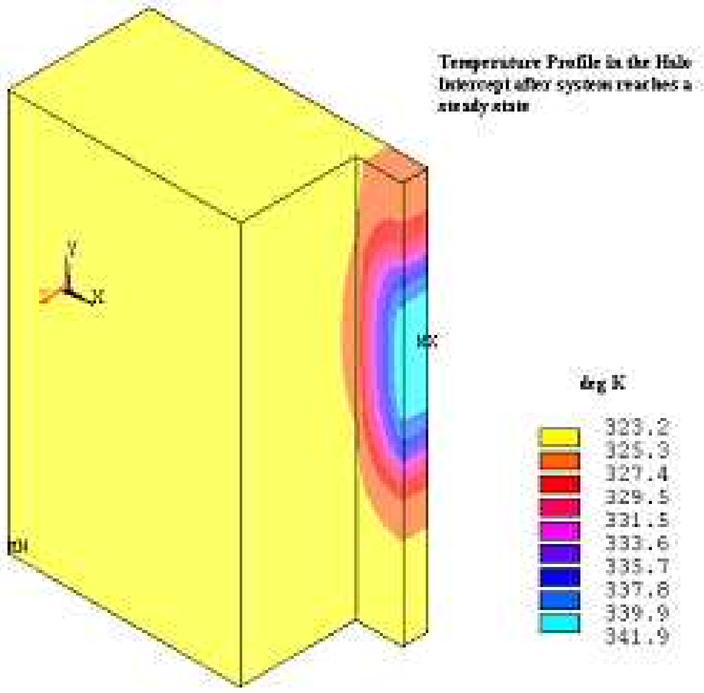

Figure 94: Temperature profile during steady state.

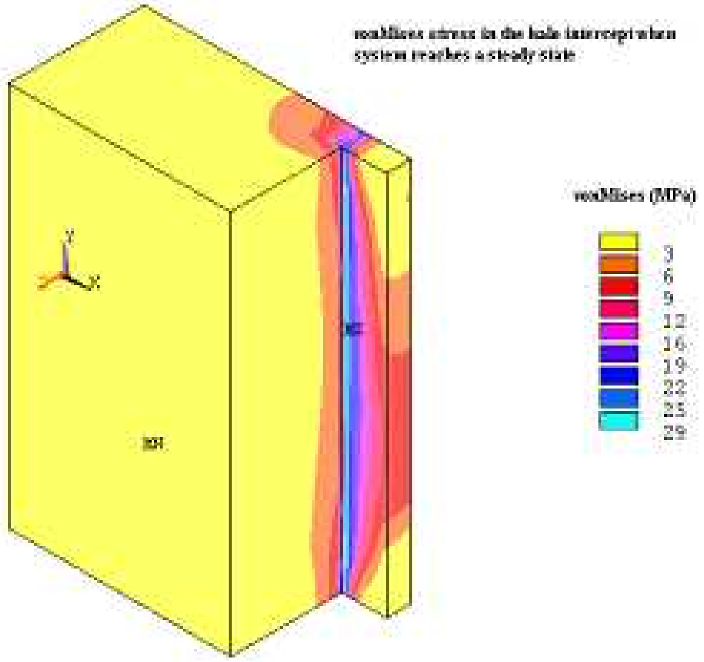

Figure 95: von Mises thermal stress profile under steady-state conditions.

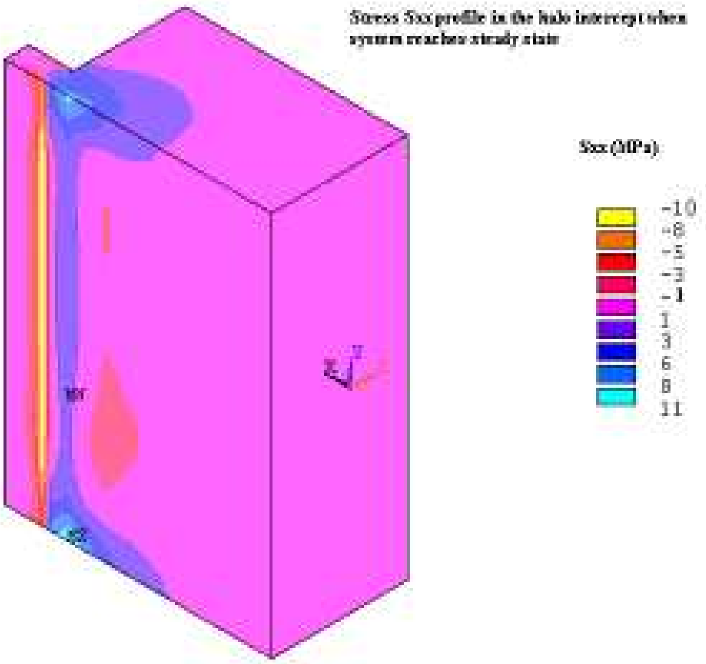

Figure 96: Axial stress profile in the platinum-copper arrangement under steady-state thermal conditions.

3.7.7 Collimator design

It has been assumed that 0.1% of the 2 MW beam will be intercepted by the collimating scheme set at the various sections of the beam transport and accumulation. Shown in Figure 1 is the layout of the generic collimator absorber. It consists of the collimator beam tube, a cooled particle bed that surrounds the beam tube and a ring-shaped shielding that in turn surrounds the particle bed and the collimator tube. All components are enclosed within the space of a stainless steel vessel. Because of its functional importance, particular emphasis is given to the design and performance of the collimator beam tube that represents the first proton-intercepting element of the absorber scheme. The need for the collimator beam tube to minimize beam impedance, and separate the vacuum space from the pressurized flowing light water environment makes its design challenging. Because of lack of experimental data, the long-term behavior of irradiated material that is wetted on the one surface becomes an issue. Such uncertainties prompted a special double-wall design that will enable not only beam halo interception but also the efficient transfer of deposited energy to coolant flow.

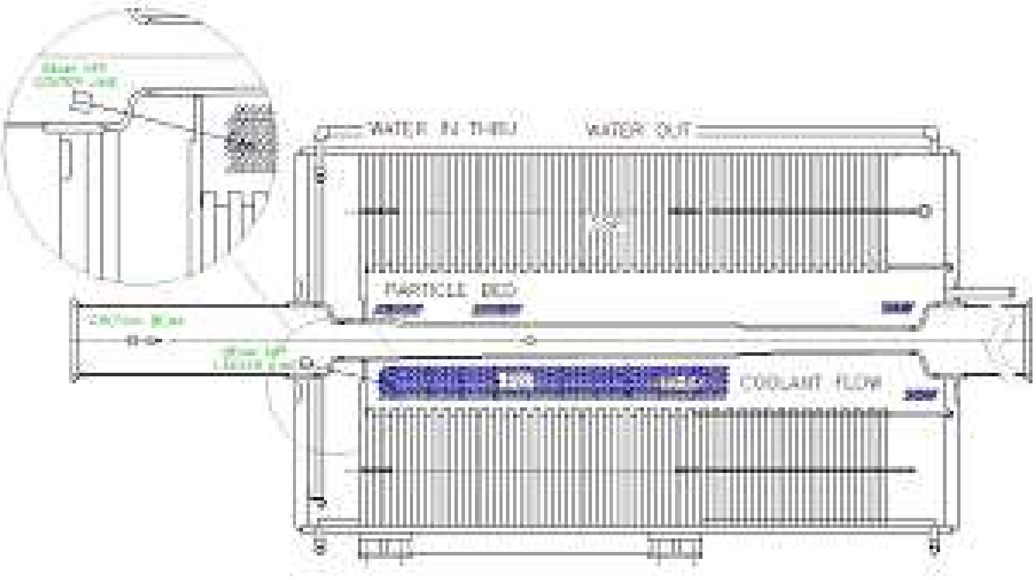

Figure 97: Schematic of the Overall Collimator/Absorber Assembly.

Under normal operating conditions the collimator will intercept 0.1% of the beam. The 2 MW proton beam has a frequency of 60 Hz and pulse duration of 1 μs. In the RTBT line the proton beam bunches have attained peak energies of 1.0 GeV. In the event of beam straying from the designed orbit the full proton beam rather than its halo will penetrate the beam tube and be intercepted by the particle bed. It has been conservatively assumed that two pulses will deposit energy in the bed before the beam is tripped. If such a scenario is anticipated to occur frequently then the integrity of the particle bed or whatever material in its place need to be assessed since it will resemble a target for a couple of pulses.

Given the location and the function of the beam tube within the collimating assembly, a material that exhibits good mechanical strength properties and has good resistance to radiation damage must be selected. The requirements become more stringent due to the fact that there is to be coolant (light water) on the back face of the beam tube. A material that has the required strength and is accompanied by irradiation experience data is Inconel-718. Given that the experience data only involve material free of welds, while in order to satisfy beam impedance requirements a complex transition in the beam tube is introduced that inevitably will contain welds, a double wall concept for the beam tube was introduced. Accordingly, a double Inconel-718 wall separated by a gap filled with pressurized helium has been designed that eases the requirements of no welds in the critical transition region. The purpose of the helium is twofold. On one hand it provides a heat transfer path to the outer wall and on the other hand can be detected in the beam tube vacuum space if a leak in the inner wall occurs. The double wall concept also allows for the separation of the critical inner wall from the light cooling water. In order to help the heat transfer path from the inner wall to the flowing coolant, a cooper wire is introduced within the helium gap. The various elements of the analyses including optimization of the heat transfer path are discussed in the following sections.

3.7.7.1 Engineering analysis

Following the conceptual design of the collimator absorber, thermal and stress analysis of the key elements guided the final absorber configuration. Specifically, based on results of energy deposition generated by the neutronic codes and MCNPX [80] under both normal and off-normal conditions, the thermal response of the beam tube was calculated through a detailed finite element analysis coupled with estimates of heat transfer capacity to the coolant flow.

Following optimization of the thermal problem under normal conditions, the thermal stress response and thermal fatigue problems were addressed using the ANSYS code [83].

3.7.7.2 Thermal analysis

The heat deposition rate for normal conditions is determined assuming a parallel beam of 1 GeV protons. The actual beam for such case is ignored in this calculation (not intercepted by the beam tube) and only the halo portion is considered. Radially the halo is assumed to be 3 mm. thick and drops off in a step-wise fashion, with 75% in the first millimeter, 20% in the next millimeter, and 5% in the last millimeter. The fraction of the primary beam assumed to be in the halo is 0.001, and thus the maximum number of protons in the halo per pulse is 2.0×10^{11}. Due to uncertainties in both the neutronic calculations and the fact that proton beam will be moving around as a result of instabilities, a 1% beam interception has been assumed in the calculations of operating temperatures and stresses.

In the critical section of the double wall beam tube (front transition) where the beam halo is first intercepted, the energy deposited and the subsequent temperature rise experienced by the wall material is maximum. While the entire back surface of the outer wall is wetted by the 50 psi coolant flow as it makes its way though the particle bed, the transition section still operates at much higher temperatures. In an accident condition where the He in the gap has escaped the temperatures could rise dramatically. To circumvent such condition, the heat transfer capacity around the critical section was enhanced. It was achieved by introducing a narrow channel flow that follows the shape of the beam tube transition and increases the velocity of the flowing coolant.

Table 32: Peak temperatures (°C) in beam tube.

	Wire (rad)	Wire (no-rad)	No-wire (rad)
He	374	377	801
No He	388	392	1113

The optimization loop consists of the following steps:

1. Selection of the size of the introduced annular space and the calculation of the velocity of flow U_m that can be achieved based on the mass flow rate of coolant
2. Estimation of the Reynolds number $RE_{DE} = U_m D_E/\nu$ (D_E is the equivalent diameter of the annulus and ν is the dynamic viscosity)
3. Estimation of the Nusselt number
4. $N_{NU} = 0.023(RE_{DE})^{0.8}(N_{PR})^{0.3}$ where $N_{PR} = 5.85$ for water
5. Calculation of heat transfer film coefficient $h_f = N_{NU}\kappa/D_E$ where κ is the conductivity of the coolant

A number of different scenarios were thermally analyzed using the energy depositions calculated by the neutronic codes in order to minimize the operating temperatures. Further, attention was paid to accident conditions that may arise, such as loss of helium in the gap, and the consequences were addressed. Table 32 lists the peak temperatures for different combinations of contributing factors including radiation heat transfer between the surfaces in the helium gap. It is apparent from Table 32 that the copper wire dominates the heat transfer path. Even in an accident condition, the operating temperature will be below critical values for the material.

3.7.7.3 Thermal stress and shock estimation

Following the thermal analysis of the double wall beam tube, steady state and transient stress analyses were performed. Under the "equivalent" steady condition the thermal operating stresses in the beam tube were calculated as a result of the temperature profile that the system stabilized at under normal operations. Shown in Fig. 101 is the axial stress distribution. With peak stresses around 100 MPa, a large safety margin is available. These stresses, however, are to be superimposed onto the stresses generated by the combined effect of pressurized helium in the gap and vacuum inside the beam tube as well as loading from the particle bed onto the beam tube. The combination of all loadings still allows for ample margins on the inconel-718 material that exhibits yield strength of over 1000 MPa. The accident scenario of the beam straying into the collimator is shown in Fig. 102. Two full mis-directed pulses will be allowed before the beam is tripped. The induced shock stresses in the double wall, under such conditions, are still low to be of concern.

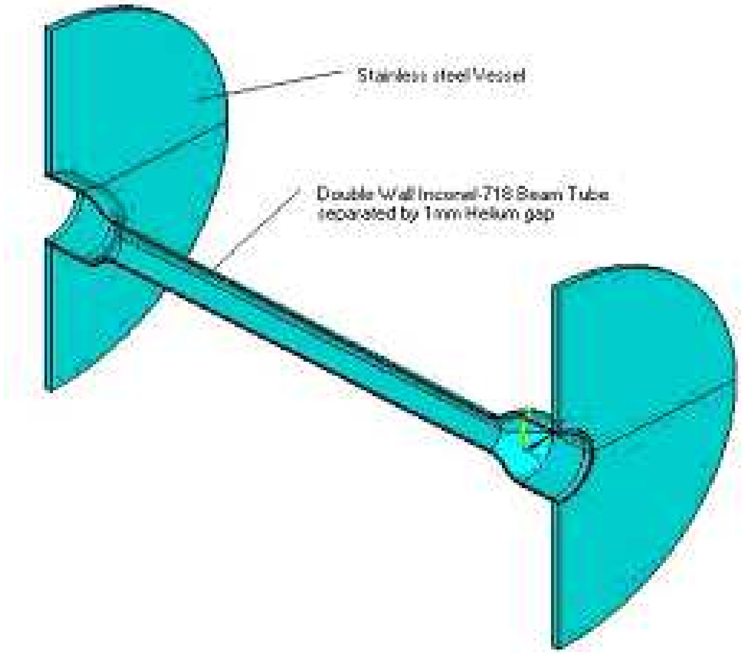

Figure 98: Collimator section used in the thermal and stress analysis using finite elements.

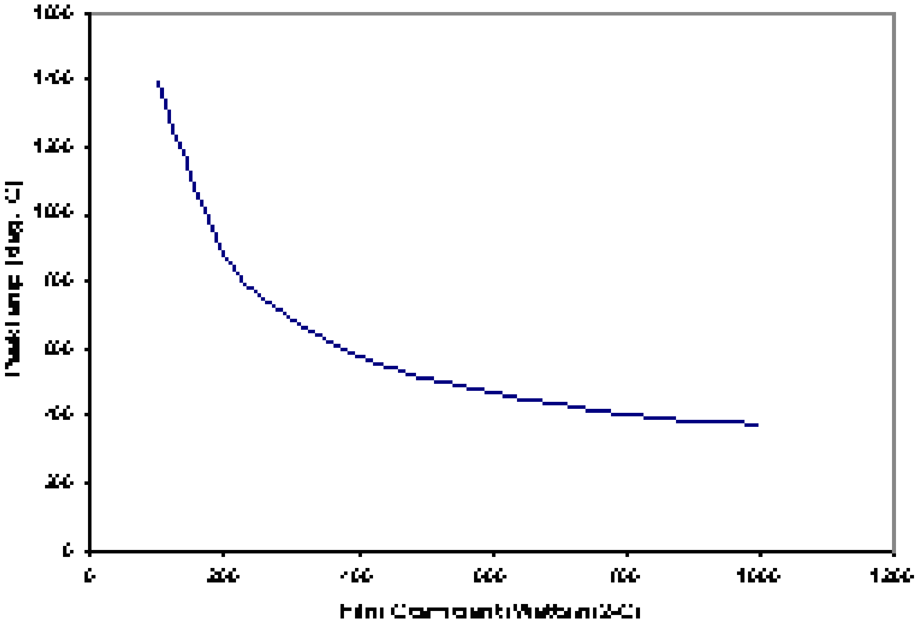

Figure 99: Peak operating temperature as a function of the heat transfer coefficient on the outer Inconel wall.

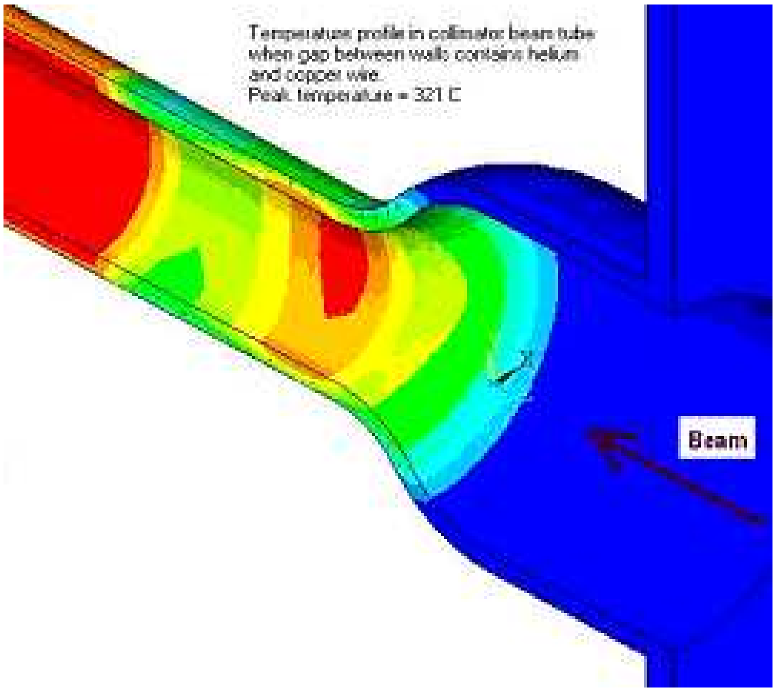

Figure 100: Temperature distribution in the critical section of the beam tube under normal operating conditions.

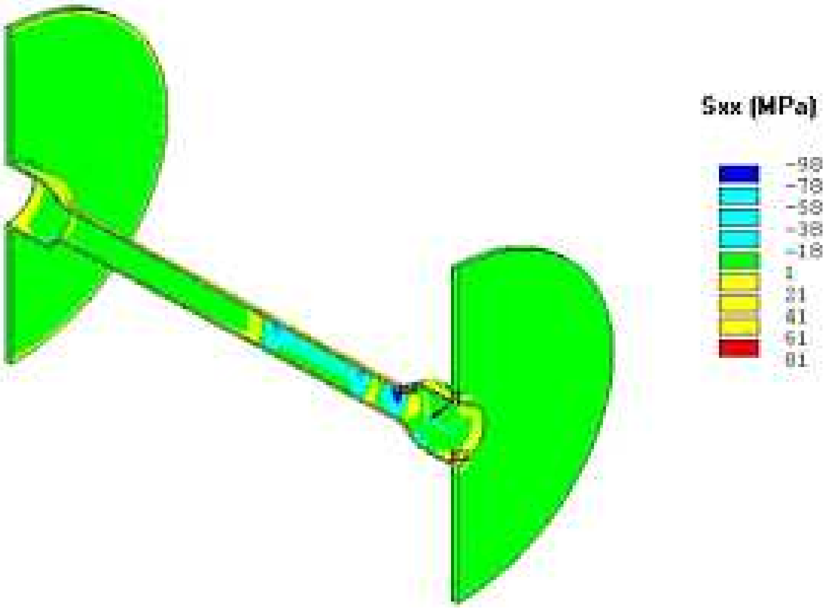

Figure 101: Axial thermal stress for normal conditions.

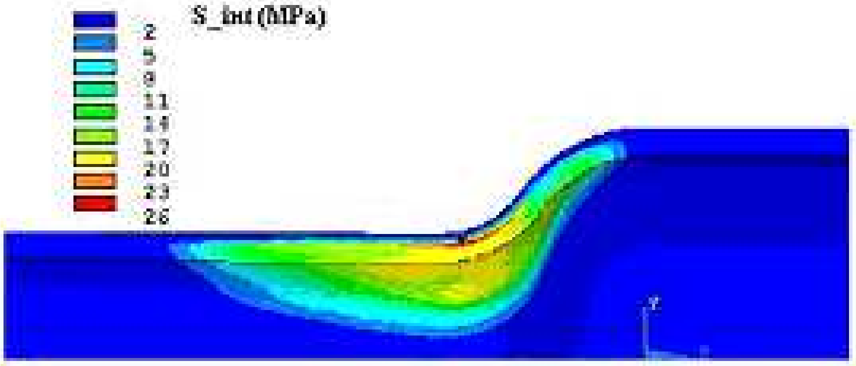

Figure 102: Shock stress generated in the beam tube after full beam strayed into the wall.

3.8 Beam Dump

3.8.1 Linac beam dump

In addition to the 90° bend to the accumulator, there is a 35 m long beam line straight out of the linac for linac beam characterization and beam dumping. Fig. 33 shows the TRANSPORT output for this line. The vacuum window (0.5 mm thick Inconel) located just after the last quad in the dump line. The available aperture for the quadrupoles near window is 55 mm radius. The end to end simulation shows that the beam extant is up to 7 sigma, therefore maximum beam size for 95% beam is 30 mm in diameter. The specification for the beam size at the linac dump beam stop is 120 mm in diameter with a centroid error of ±50 mm and the maximum beam power out side 203.2 mm must be lower than 750 Watts. Table 33 shows constrains for the Linac dump.

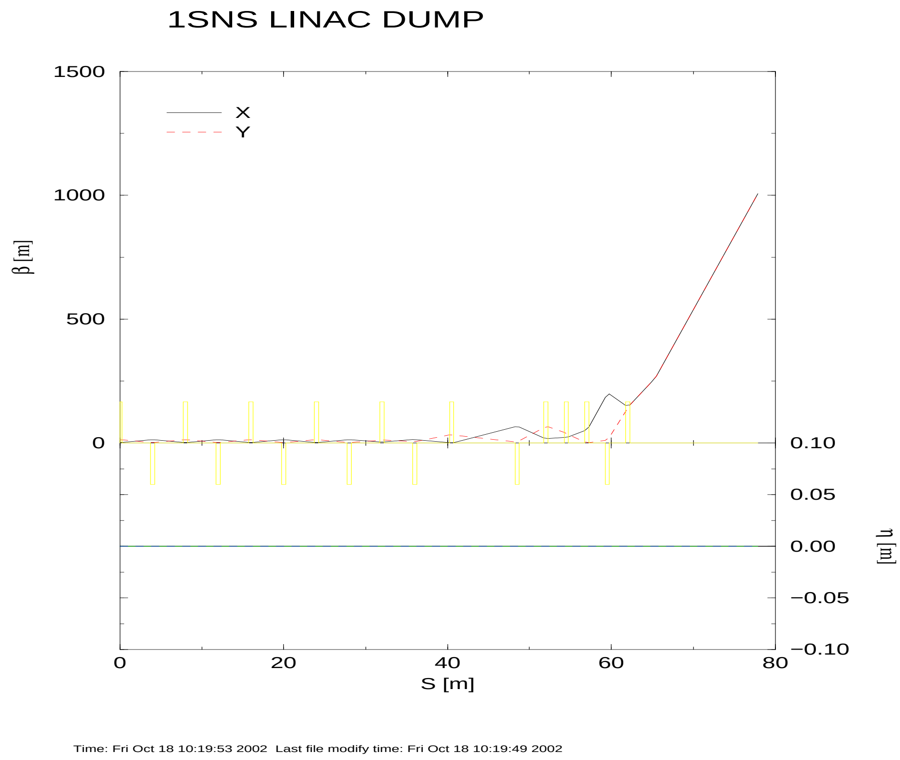

Figure 103: Linac beam dump optics.

Table 33: Linac dump constrains.

Energy [MeV]	Unnormalized rms emittance [mm mrad]	$\beta\gamma$	Beam dia. at window [mm]	Beam dia. at dump stop [mm]	Power [kW]	Beam power [W] outside 203.2 mm dia.
200	0.227	0.69	30	120	??	750
1000	0.595	1.81	30	120	7.5	750

3.8.2 Injection beam dump

The partially stripped H^0 and and missed H^- will be transported to injection dump which can accept up 200 kW of beam power. Figure 104 shows the layout of the injection area. The partially stripped H^0 go straight and missed H^- will be bend 4.2 mrad left due to magnetic field of INJBEND2. The INJBEND 3 further bend the H^- by 42 mrad while H^0 travel in straight line. Just before INJBEND 4 there is second stripper foil thick enough to striped both electrons of H^- and single electron of H^0. THE INJBEND4 bend the protons by 2.65 degrees in the left direction feeding protons to injection dump septum magnet. Figure 105 shows the central orbit for H^- and H^0 (mean of H^- and H^0 trajectories) to the injection dump. Figure 106 shows the closed orbit for H^0 with respect to the central orbit.

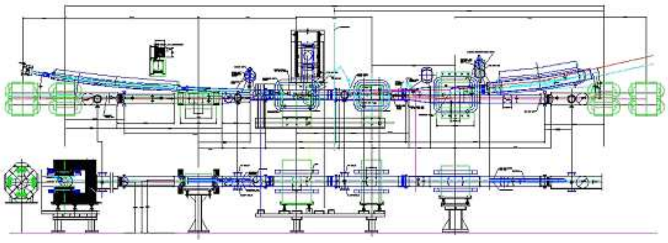

Figure 104: Layout of injection area.

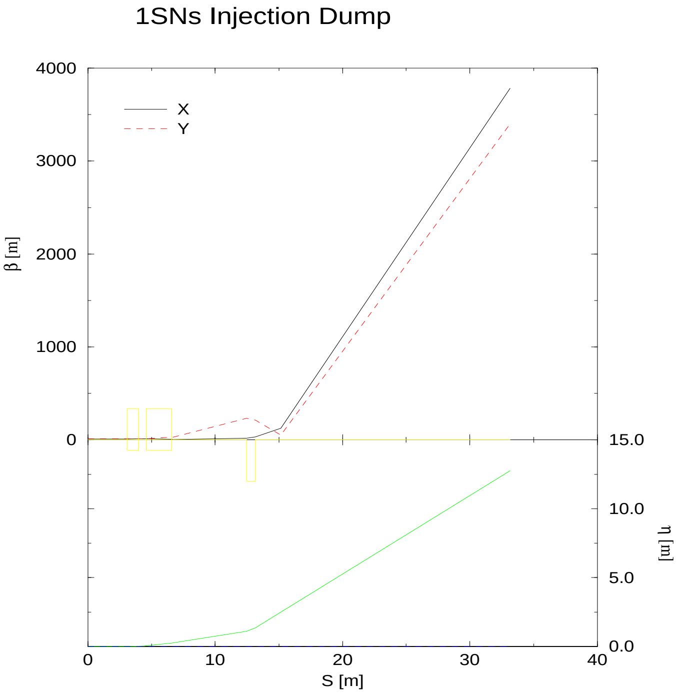

Time: Mon Oct 21 11:11:55 2002 Last file modify time: Mon Oct 21 11:11:51 2002

Figure 105: TRANSPORT out for the Injection dump line.

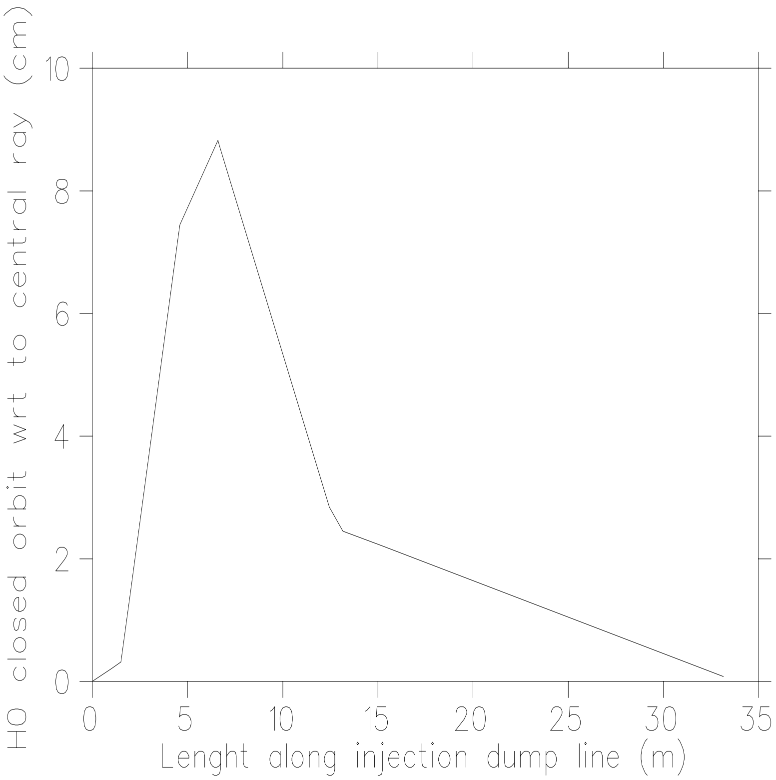

Figure 106: H^0 closed orbit with respect to the central tractory.

3.8.3 Extraction beam dump

In addition to the 16.80 bend to the target, there is a 43 m long beam line straight out of the RTBT for ring beam characterization and beam dumping. Fig. 107 shows the TRANSPORT output for this line. The vacuum window (0.5 mm thick Inconel) is located just after the last quadrupole. The constrains on the beam size at window and the dump is given in Table 34.

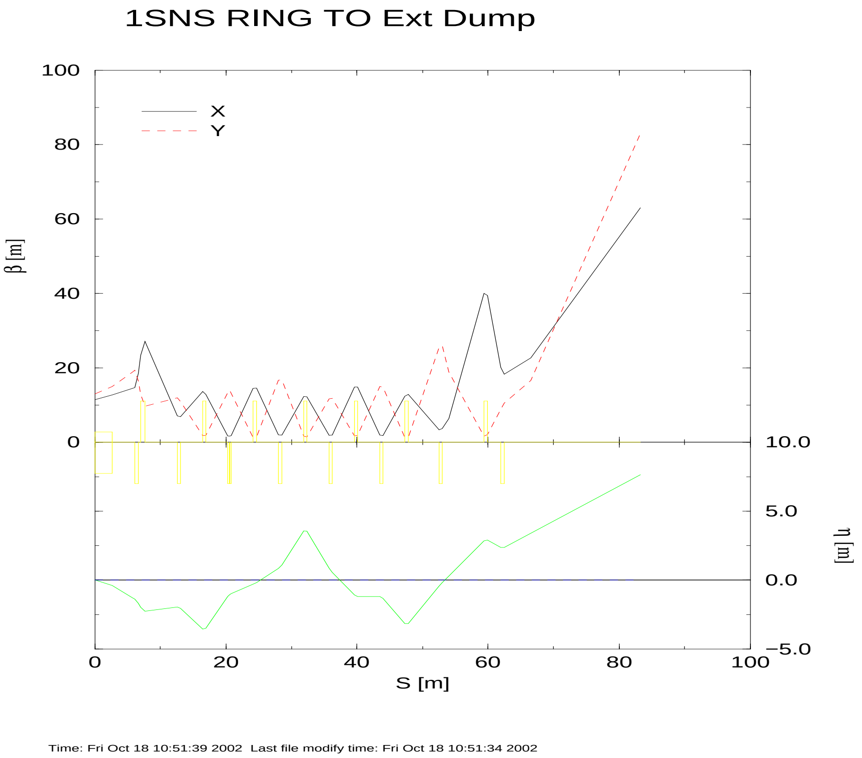

Figure 107: Extraction beam dump optics.

Table 34: Extractionc dump constrains.

Energy [MeV]	Unnormalized emittnace [mm mrad]	β_x, β_y [m]	Beam size at window [mm × mm]	Beam dia. at dump stop [mm]	Power [kW] [kW]	Beam power [W] outside 203.2 mm dia.
1000	240	25, 20	154×128	200	7.5	750

Table 35: RF Machine Parameters for a 2 MW SNS

parameter	value
circumference	248m
transition gamma	5.25
total h=1 voltage	40 kV
h=1 gap capacitance	3 nF
total h=2 voltage	20 kV
h=2 gap capacitance	0.75 nF
space charge Z/n	i200 Ω
proton kinetic energy	1 GeV
injected bunch length	610 ns
injected energy spread	±3.8MeV, full
protons at extraction time	2.08×10^{14}
accumulation time	1100 turns
extraction gap	250ns
repetition rate	60 Hz

3.9 Radio-frequency System

The purpose of the accumulator ring RF system is to maintain a gap for the rise time of the extraction kicker while maintaining low peak beam current and large momentum spread[67, 68, 69, 70]. The latter considerations prevent space charge stopband related losses and coherent instabilities. The system is designed to operate comfortably with 2×10^{14} protons. This has a small impact on system cost and improves reliability with 1.5×10^{14} protons.

With current technology both single and dual harmonic systems are feasible. With its relatively large ratio of extraction gap to bunch length the SNS is a marginal candidate for a barrier bucket RF system, and the technology is unproven. Therefore, the design employs a dual harmonic system operating with harmonic numbers $h = 1$ and $h = 2$. Table 35 summarizes RF related machine parameters.

The choice of 40 kV for harmonic 1 and 20 kV for harmonic 2 was reached by considering beam dynamics and practical constraints. Beam stability associated with transverse and longitudinal coupling impedance issues is discussed in sections 2.5.3 and 2.5.4. The theory of these instabilities has developed over time and estimates can be made with reasonable confidence. For 2 MW the design is close to, but not beyond, acceptable limits. The effect of longitudinal motion on stopband losses as well as the dynamics of the electron-proton instability are less well developed. The studies outlined in sections 2.5.1 and 2.5.5 show that the baseline design should be adequate for 2 MW operation. The momentum spread required to combat instabilities implies good chromatic control as discussed in section 2.4.

Throughout the rest of this section we assume a 2 MW design.

3.9.1 Ring RF system overview

During accumulation the RF beam current in the the Spallation Neutron Source ring rises from 0 to 50 Amperes. Beal loading is a serious concern and we begin our discussion with the high power hardware required to deal with it.

3.9.1.1 Cavity and power amplifier

Harmonic numbers of 1 and 2 imply RF frequencies of $f_1 = 1.05$ MHz and $f_2 = 2.11$ MHz. Each cavity is composed of two RF gaps driven in parallel by the power amplifier. The $h = 1$ cavities are designed for a gap voltage of $V_g = 10$ kV and the $h = 2$ cavities are identical but for less gap capacitance. Inductance is supplied by coaxial stacks of Phillips 4M2 ferrite. There are 21 rings per gap and each ring is 2.72cm thick. The rings have inner and outer diameters of 25 cm and 50 cm, respectively.

A large magnetic field in the ferrite cuts down on the total cavity length. The AGS Booster uses the same ferrite, the same 2 to 1 ratio of outer to inner radius, and a similar frequency range. Assuming the same RF magnetic field, an $h = 1$ gap field of 13kV can be supported without Q losses or similar ferrite problems. Assuming the magnetic field varies as $1/r$ within the ferrite, the magnetic field has a maximum RF amplitude of $B_{rf} = 31$ mT for $V_g = 10$ kV. The cavity resonant frequency is tuned using bias current which flows in opposite directions through the two cells leading to negligible RF voltage across the bias supply. The bias supply allows for sweeping the bias current. We have performed measurements sweeping both the bias current and drive frequency and found that the ferrite tuned well.

The design of the power amplifier is driven by beam loading requirements. During the millisecond of accumulation the average beam current rises from 0 to 34 A. The maximum amplitude of the first harmonic component is $I_1 = 50$ A and the second harmonic component is down by a factor of 7. The philosophy here is to design the power amplifier for $h = 1$ and use the same design for $h = 2$. This reduces EDIA significantly and allows the $h = 2$ system to to be easily modified to $h = 1$ if desired. The base line design requires the power amplifier to fully compensate the beam current while providing the necessary quadrature component to drive the gap voltage. The cavity resonant frequency is fixed, and equal to the RF frequency. In light of the tuning tests this may be pessimistic but the consequences of this assumption to the overall system cost are not great, whereas the benefits for system performance and reliability are very valuable.

A Thompson (TH558) tetrode drives two gaps in parallel while supplying the necessary anode current. With three cavities (6 accelerating gaps) at $h = 1$ and 7 kV/gap the anode dissipation reaches 500 kW at the end of accumulation. The time average dissipation is much smaller, about 50 kW, but very high reliability is required and stressing the tube could lead to shorter life. The $h = 2$ system has one cavity with two gaps and 10 kV/gap. The $h = 2$ beam loading is much smaller than for $h = 1$.

Since the RF system is on for ~ 2 ms every 16.7 ms, the tube will be biased off for most of the time. The grid bias supply can switch between cutoff and quiessant states in $\approx 100\mu$s. An anode power supply consists of two, charging 14 kV, 3 A supplies and capacitor bank. The total capacitance of the bank is 75μF. For a 10 A draw starting at 10 kV, with a charging current of 6 A the anode voltage droops by 3% over 2 ms.

Every effort is being made to reduce surprises during commissioning. Toward this end a full power beam-cavity simulator is planned. This device would use one power amplifier to drive the cavity, and another to simulate the beam. The beam circuit will be attached to the anode of the beam PA and encircle the ferrite stack of the cavity. The low level drive for the simulator will mimick both dipole and quadrupole beam oscillations. In this way we will test the tuning scheme, the high level RF system, and the low level RF system well before installation.

3.9.1.2 Voltage control and beam stability

In analytic models of steady state beam loading [73, 74, 75] the ratio of beam induced voltage to total gap voltage plays an important role. For SNS this beam loading parameter is ~ 4, so the stability if the RF system could be compromised. Unlike typical accelerators, the SNS cycle time is comparble to the synchrotron period, so the transient response of the beam-cavity interaction is very important. Additionally, the dual harmonic system leads to very nonlinear dynamics and analytic results are difficult to obtain. Therefore, simulations of the beam-cavity system have been a primary design tool.

A schematic of the beam, cavity and generator for a single gap cavity is shown in Figure 108. The electric field in the gap, E_g is related to the gap voltage V_g and the equivalent gap length ℓ_g via $E_g \ell_g = -V_g$. The beam current, I_b is positive to the left so a positive value of V_g accelerates the beam. Suppose the system is quiessant for $t < 0$. The anode current I_A, gap voltage and beam current are related via

$$\begin{aligned}\frac{I_A(t) - I_A(0)}{n_{gap}} - I_b(t) &= \frac{V_g(t)}{R_f} + C_g \frac{dV_g(t)}{dt} \\ &+ \frac{1}{L_g} \int_0^t V_g(t')dt', \end{aligned} \tag{23}$$

where C_g and L_g are the equivalent capacitance and inductance of one gap, R_f is the shunt impedance of the ferrite for one gap, and $n_{gap} = 2$ is the number of gaps driven by one power amplifier. The anode voltage V_A, gap voltage, and anode supply voltage B^+ are related via $V_A(t) + V_g(t) = B^+$. With only a few percent droop, the anode supply voltage was assumed constant. The final relation involves the anode current, grid drive voltage V_G and anode voltage. For reasonable parameters the anode voltage depends only on the combination $V_A + \mu V_G$ where the amplification factor μ depends only on the screen voltage, which is held constant during the cycle. Figure 3.9.1 shows $I_A = G(V_A + \mu V_G)$ for the TH558 tetrode with a screen voltage of 2 kV.

The RF control loops directly affect the grid drive voltage so in equation (23) set

$$I_A(t) = G(B^+ - V_g(t) + \mu V_G(t)).$$

The grid drive voltage is taken to be

$$V_G(t) = I_G(t)\sin(\omega_{rf}t) - Q_G(t)\cos(\omega_{rf}t) + \bar{V}_G,$$

where ω_{rf} is the ideal RF frequency, $\bar{V}_G$ is a DC offset and the in phase I_G and quadrature Q_G amplitudes vary slowly. The ideal RF frequency is set before injection begins and the phase is chosen so that extraction can be defined to better than one turn.

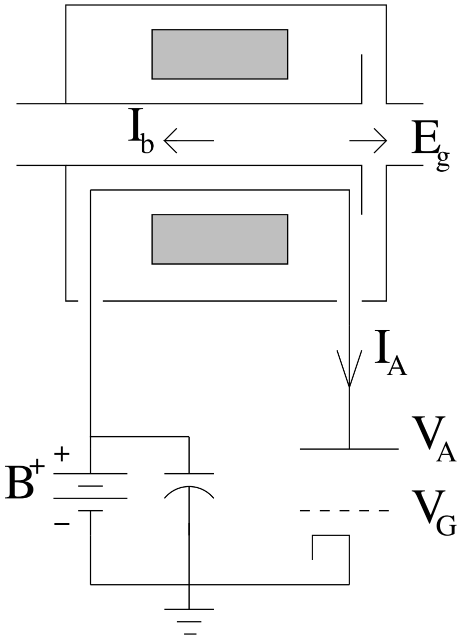

Figure 108: Equivalent beam-cavity circuit.

Since the beam current is not a pure sinusoid, the gap voltage is not a pure sinusoid. However, the in phase I_g and quadrature Q_g components of the gap voltage at ω_{rf} can be defined with respect to a given measurement procedure. The control system will be digital, so a natural unit of time is one turn. Define the raw in phase and quadrature components of the gap voltage on the nth turn to be

$$I_g^0(n) = \frac{2}{T_{rf}} \int_{(n-1)T_{rf}}^{nT_{rf}} \sin(\omega_{rf}t)V_g(t)dt, \tag{24}$$

$$Q_g^0(n) = -\frac{2}{T_{rf}} \int_{(n-1)T_{rf}}^{nT_{rf}} \cos(\omega_{rf}t)V_g(t)dt. \tag{25}$$

In the actual system these might be generated by digital FIR filters but for any reasonable clock rate there will be little difference between the analog and digital quantities. The raw values are then subject to delay and smoothing to create the inputs to the control system. This is modeled as a lagged, auto-regressive filter,

$$I_g(n+1) = \delta I_g(n) + (1-\delta)I_g^0(n-n_g), \tag{26}$$

$$Q_g(n+1) = \delta Q_g(n) + (1-\delta)Q_g^0(n-n_g), \tag{27}$$

where $\delta = \exp(-T_{rf}r_g)$, r_g is the accumulation rate, and n_g is the signal delay in turns. The lower limit on the delay is set by the round trip time between the ring and the RF control room, $n_g T_{rf} \gtrsim 750$ ns.

In general the in phase and quadrature components of the gap voltage will not be equal to their target values $\hat{I}_g(n)$ and $\hat{Q}_g(n)$. The first level of RF control varies the grid drive amplitudes I_G and Q_G to approach the desired values of the gap voltage components I_g and Q_g. To obtain the feedback matrix assume that the error is small and define the error terms $\Delta I_G, \Delta I_g, \Delta Q_G, \Delta Q_g$. Inserting these errors in equation (23) and keeping first order terms yields

$$\begin{pmatrix} \Delta I_G \\ \Delta Q_G \end{pmatrix} = \frac{n_{gap} R_A}{\mu |Z_\ell|} \begin{pmatrix} \cos\phi_z & -\sin\phi_z \\ \sin\phi_z & \cos\phi_z \end{pmatrix} \begin{pmatrix} \Delta I_g \\ \Delta Q_g \end{pmatrix} \tag{28}$$

where R_A is the anode resistance and Z_ℓ is the loaded impedance of the cavity. The phase angle is given by

$$\tan\phi_z = \frac{R_\ell}{\omega_{rf} L_g} - \omega_{rf} C_g R_\ell, \tag{29}$$

where R_ℓ is the loaded shunt impedance of the gap. For feedback loops define a low level gain G_g. The low level loops cause the grid drive signal to change according to

$$\frac{d}{dn}\begin{pmatrix} I_G \\ Q_G \end{pmatrix} = G_g \begin{pmatrix} \cos\phi_z & -\sin\phi_z \\ \sin\phi_z & \cos\phi_z \end{pmatrix} \begin{pmatrix} \hat{I}_g - I_g \\ \hat{Q}_g - Q_g \end{pmatrix}. \tag{30}$$

The phase angle is zero in the baseline design but, anticipating dynamic tuning, take it to be given by equation (29) with R_ℓ replaced by a constant. Assuming that $L_g(n)$ and and C_g are reasonably well known, all the parameters of the voltage feedback loop are defined.

Along with the voltage feedback the design calls for a feed-forward correction using the measured beam current. Assume the in phase I_B and quadrature Q_B components of the beam current are measured using the same algorithm as for the in phase and quadrature components of the gap voltage. Let r_B and n_B be the accumulation rate and delay for the acquisition of the beam current components. The feed forward correction for the beam current is taken to be

$$\begin{pmatrix} I_G^1 \\ Q_G^1 \end{pmatrix} = G_f \frac{n_{gap} R_A}{\mu} \begin{pmatrix} I_B - \hat{I}_B \\ Q_B - \hat{Q}_B \end{pmatrix}, \tag{31}$$

where $\hat{I}_B$ and $\hat{Q}_B$ are the in phase and quadrature components of beam current for which the cavity is tuned. For an accurate value of R_A the ideal feed forward gain is $G_f = 1$. Let I_G^2 and V_G^2 be the solutions to equation (30) then, with the feed forward correction given by equation (31) the high frequency grid drive signal is given by

$$\begin{aligned} V_G(t) = {} & (I_G^1 + I_G^2 + I_G^0)\sin(\omega_{rf} t) \\ & - (Q_G^1 + Q_G^2 + Q_G^0)\cos(\omega_{rf} t) + \bar{V}_G, \end{aligned} \tag{32}$$

where I_G^0 and Q_G^0 are best guess values for the amplitude functions which are based on the behavior during earlier cycles. The in phase and quadrature amplitudes are defined at the beginning of each turn and linearly interpolated between turns.

The RF simulation uses standard techniques[76]. The previous equations are transformed into a set of first order differential equations and discretized. The total RF kick is updated once per particle per turn with 360 time slices per turn. Space charge makes a significant contribution to the longitudinal force. For frequencies below $f_{rf}^2/4\pi h f_s \sim 75$ MHz the space charge forces can be updated once per turn. At the reference azimuth the voltage due to space charge is

$$V_{sc}(t) = \frac{Z_{sc}}{\omega_0}\frac{dI_b(t)}{dt}, \tag{33}$$

where $Z_{sc} \approx 200\Omega$ is the space charge impedance[77]. The space charge kick was obtained by convolving the binned beam current with a differentiated, 50ns pulse. The beam is modeled by $M \sim 10^4$ macro-particles. The beam current on nth turn is a sum over macro-particles and a binning/smoothing function $f(t)$ is used to reduce unphysical high harmonics

$$I_b(t) = \sum_{k=1}^{M} f(t - t_n^k).$$

The change in proton energy depends on arrival time at the gap.

$$E_{n+1}^k = E_n^k + qV_{total}(t_n^k),$$

where the total voltage is $n_{cav}n_{gap}V_{gap}$ plus 2nd harmonic and space charge. Arrival time on the next turn changes depending on the energy deviation

$$t_{n+1}^k = t_n^k + \eta T_{rev}\frac{E_{n+1}^k - E_0}{E_0\beta^2}.$$

The simulations used the parameters in Table 35. Notice that the injected energy spread is ±3.8MeV with a rectangular distribution. This is created by an energy wiggler cavity running at a slightly different frequency from the LINAC RF. The net effect is to broaden the rms width of the energy distribution without creating the tails associated with a debuncher cavity. The simulations assumed 2 turns of delay and the accumulation rates r_g and r_B were taken to be $100/ms$. The low level gain G_g was chosen to give a comparable transient. The target $h = 1$ RF voltage was ramped from 30 to 40 kV over the first 500 turns. To be pessimistic, the best guess values of the in phase and quadrature grid drive voltages were nulled $I_G^0 = Q_G^0 \equiv 0$. Only the voltage error and feed forward signals, via equations (30) and (31), created the grid drive voltage for $h = 1$. With its smaller beam loading, the $h = 2$ voltage was set to half the $h = 1$ target value throughout the cycle.

Figure 3.9.1 shows the longitudinal phase space, the rf bucket, and the edges of the kicker gap just before extraction. Figure 3.9.1 shows the bunch current, the space charge voltage and the total RF voltage just before extraction. The gap is clean and the bunching factor is 0.4.

Figure 3.9.1 illustrates the situation when there is no feed forward. The maximum error in the RF voltage waveform is $\lesssim$5 kV and the bunch is acceptable. However, with the heavy beam loading, feedforward is required for system stability and a small, unstable, oscillation exists without it. Additionally, a feed forward system will reduce the deleterious impact of *e.g.* variations due to aging of the tetrode. In practice, even with marginal feed forward the RF system should easily meet its specifications.

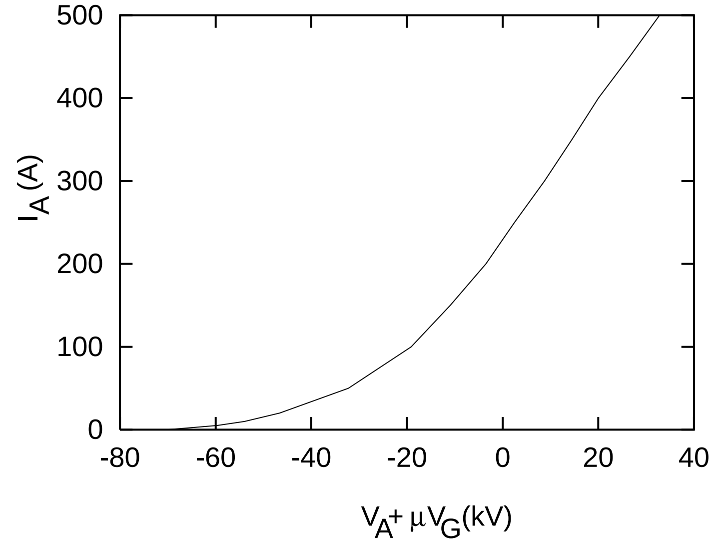

Figure 109: Anode current versus effective voltage for a screen voltage of 2 kV. The amplification factor is $\mu = 132$.

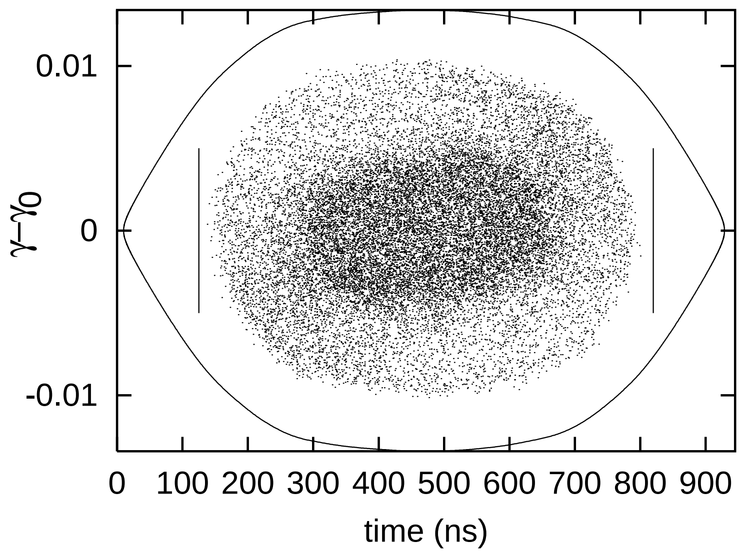

Figure 110: Phase space distribution and bucket at extraction for nominal design.

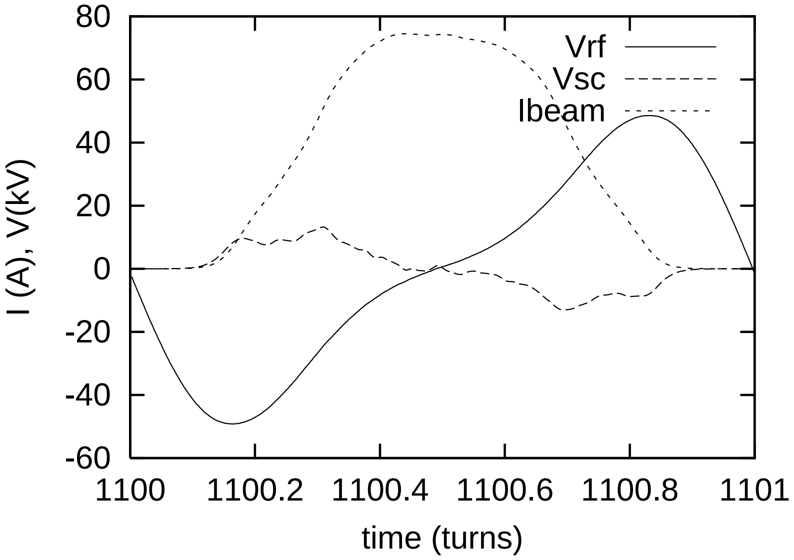

Figure 111: Currents and voltages at extraction for nominal design. The binned current, convolved with a 50ns smoothing pulse, is shown.

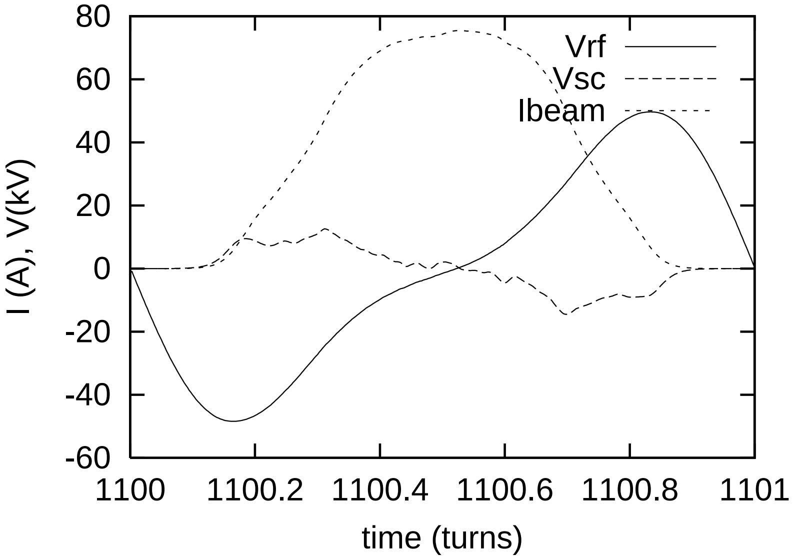

Figure 112: Currents and voltages at extraction for no feed forward.The binned current, convolved with a 50ns smoothing pulse, is shown.

3.9.1.3 Dynamic tuning

By changing the cavity resonant frequency as the beam is stacked the amount of RF drive current can be reduced. Conversely, the $h = 1$ gap voltage can be increased. For a steady state system with beam current $I_b(t) = \hat{I}_b \cos(\omega_{rf} t)$ and gap voltage $V_g(t) = \hat{V}_g \sin(\omega_{rf} t)$, the minumum RF anode current is $I_A(t) = (n_{gap}\hat{V}_g/R_f)\sin(\omega_{rf} t)$ and the cavity resonant frequency is

$$\omega_{res} = \omega_{rf} \left(1 + \frac{\hat{I}_b}{\hat{V}_g C_g \omega_{rf}}\right)^{1/2} . \tag{34}$$

Since $\omega_{res} = 1/\sqrt{L_g C_g}$ the ideal frequency can be obtained by changing the cavity inductance. This is accomplished by changing the bias field within the ferrites and is refered to as tuning the cavity. Dynamic tuning refers to continuously changing the ferrite bias so that equation (34) is satisfied throughout the cycle. For SNS with 2×10^{14} protons and $\hat{V}_g = 6.7$ kV, the inductance per gap needs to drop from 7.5μH to 5.7μH during 1ms. The RF magnetic field will be $\sim$ 300G so the ferrites are changing quickly under high field conditions. Experiments have been done using the first article cavity. The RF drive frequency was swept from 1.06 MHz to 1.22 MHz in 1 ms and the bias current was ramped to keep the cavity in tune. The cavity exhibited no instability and we are confident that dynamic tuning will work. It has been incorporated in the simulations and Figures 3.9.1 and 3.9.1 show its clear benefits.

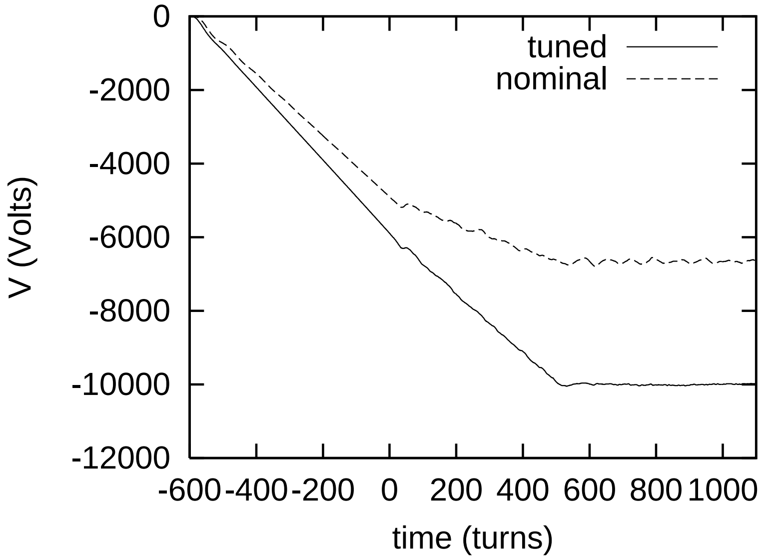

Figure 113: In phase amplitude of gap voltage (I_g) during the cycle for the nominal case and with dynamic tuning.

In both cases, the RF drive starts turning on 600 turns before injection starts (turn 0). For the nominal case the inductance is held constant at 7.5 μH while for the tuned case the inductance varies linearly with time. At turn 0 the tuned inductance is $L_g = 7.5$ μH while at turn 1100 (extraction) it is $L_g = 6.2$ μH. The $h = 1$ gap voltage in the tuned case corresponds

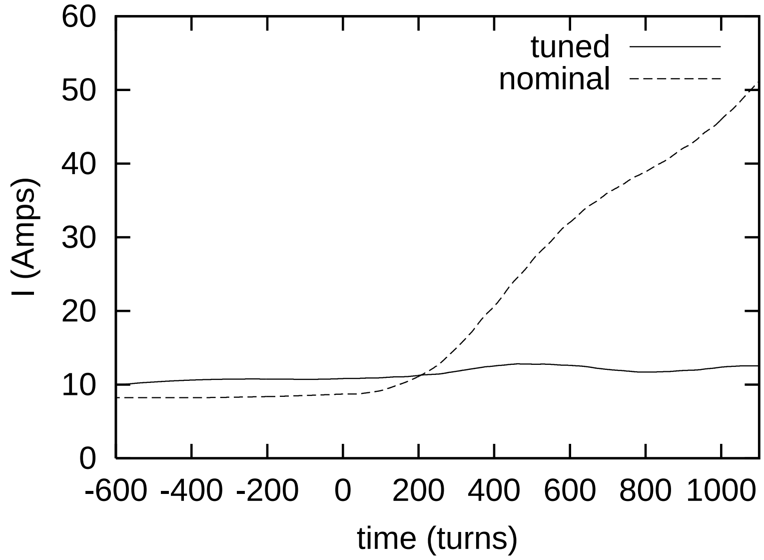

Figure 114: DC anode current during the cycle for the nominal case and with dynamic tuning.

to 60 kV/turn as compared with the nominal 40 kV/turn. The $h = 2$ voltage ramped from 15kV to 20 kV in both cases. The average anode current is significantly smaller for the tuned case. This is true even though the anode power supply voltage is $B^+ = 12$ kV for the tuned case and $B^+ = 10$ kV for the nominal case. Additionally, the total energy deposited in the anode each SNS cycle is significantly smaller for the tuned case.

With operational experience it may be determined that a fully $h = 1$ system is preferable to a dual harmonic system. Conversion to full $h = 1$ is straightforward. Within the tunnel, the only difference between the $h = 1$ and $h = 2$ systems is the number of capacitors loading the gap. Once inside the tunnel, a skilled technicial could convert an $h = 1$ system into an $h = 2$ system in about 10 minutes. Outside the tunnel, new code would be downloaded into the the digital signal processor and end effects associated with tunnel access would dominate the total time.

3.9.2 High Level RF system

3.9.3 Low level RF system

3.9.4 HEBT RF system

3.10 Diagnostics System

3.10.1 Diagnostics requirements

3.10.2 Diagnostics layout

3.10.2.1 HEBT Diagnostics

Table 36 list all the diagnostics in HEBT, Linac dump and Injection dump. Table 36 also shows the responsibility for different diagnostics. Figure 1 show the location for all the diagnostics.

Table 36: Diagnostics in HEBT , linac dump and injection dump.

Detectors	BNL	LANL
BPM	36	0
BPM-phase	(2 TOF systems)	6
BLM	52	0
FBLM	3	0
BCM	5	0
WS	0	11
Foil Video	2	0
HARP	0	2

Figs. 116, 117, and 118 show the diagnostics in the HEBT with respect to the beta functions.

3.10.2.2 Ring Diagnostics

3.10.2.3 RTBT Diagnostics

Table 37 list all the diagnostics in RTBT and extraction dump. Table also shows the responsibility for different diagnostics. Fig. 119 show the location for all the diagnostics in the RTBT.

Table 37: Diagnostics in RTBT and extraction dump line.

Detectors	BNL	LANL
BPM	17	0
BLM	40	0
FBLM	3	0
HARP	0	2
WS	0	5
BCM (FCT)	5	0

Figs. 120 and 121 show the diagnostics in the RTBT with respect to the beta functions.

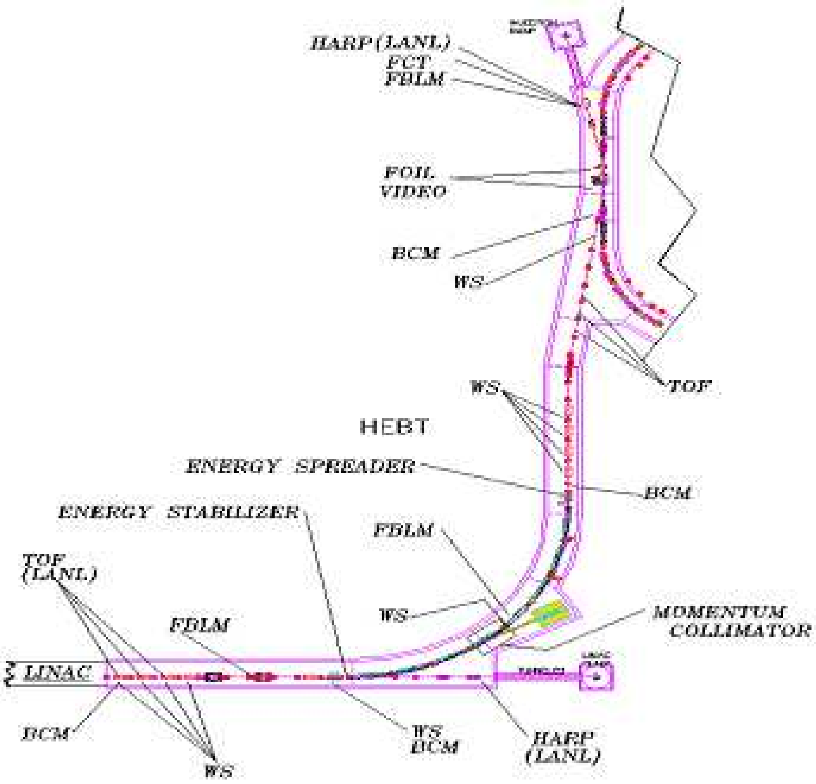

Figure 115: Diagnostics in HEBT, linac and injection dump.

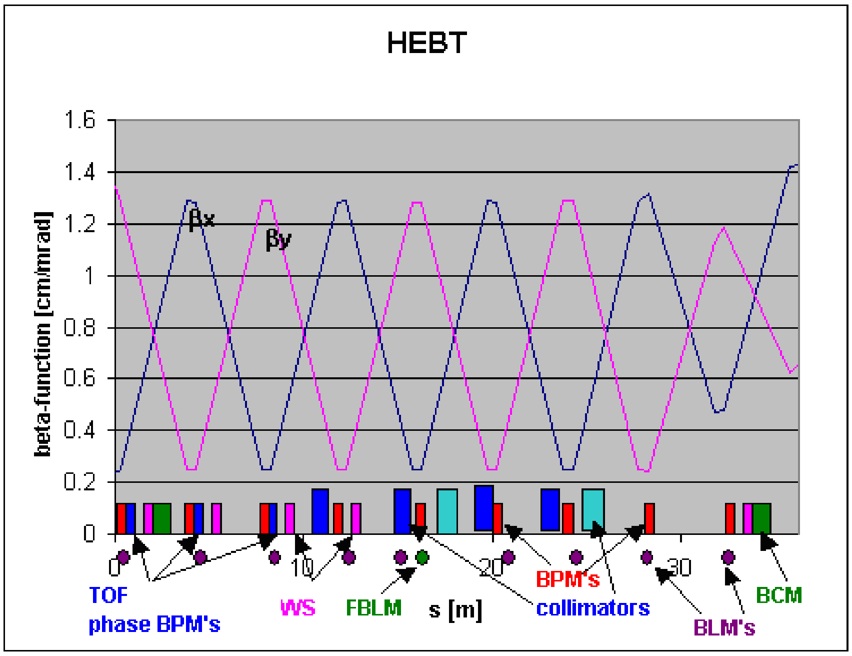

Figure 116: Diagnostic distribution in the linac to achromat matching section(LAMS).

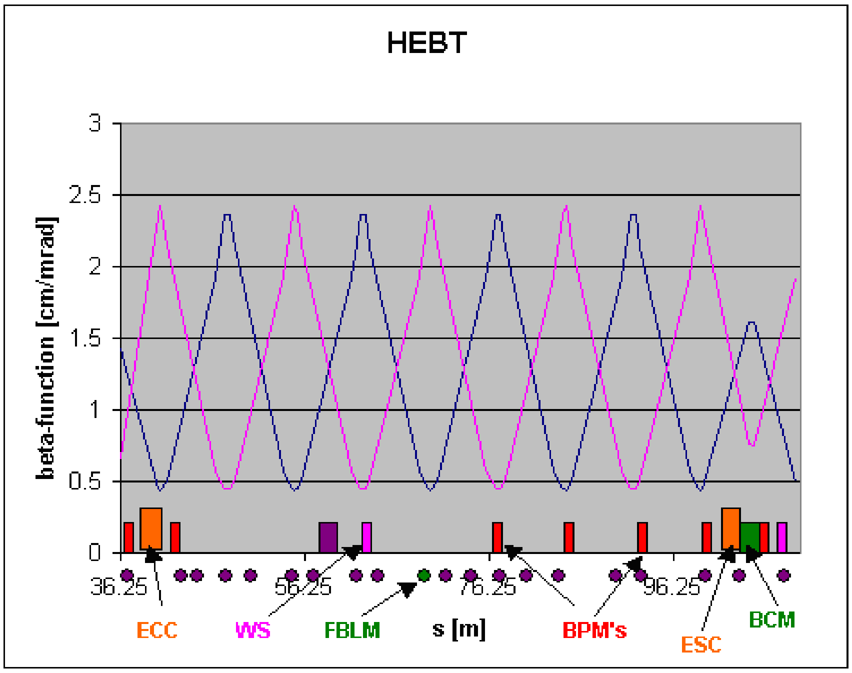

Figure 117: Diagnostics distribution in the achromat.

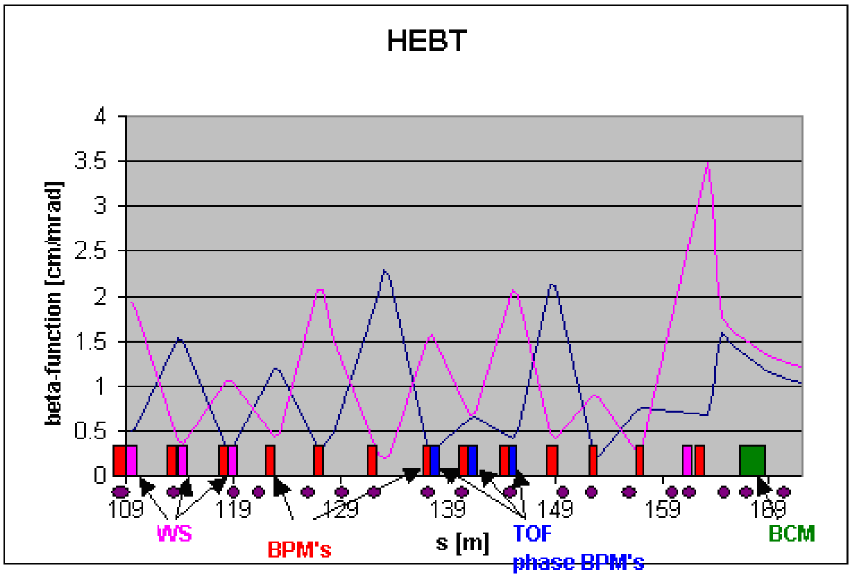

Figure 118: Disgnotics distribution in achromat to ring matching section (ARMS).

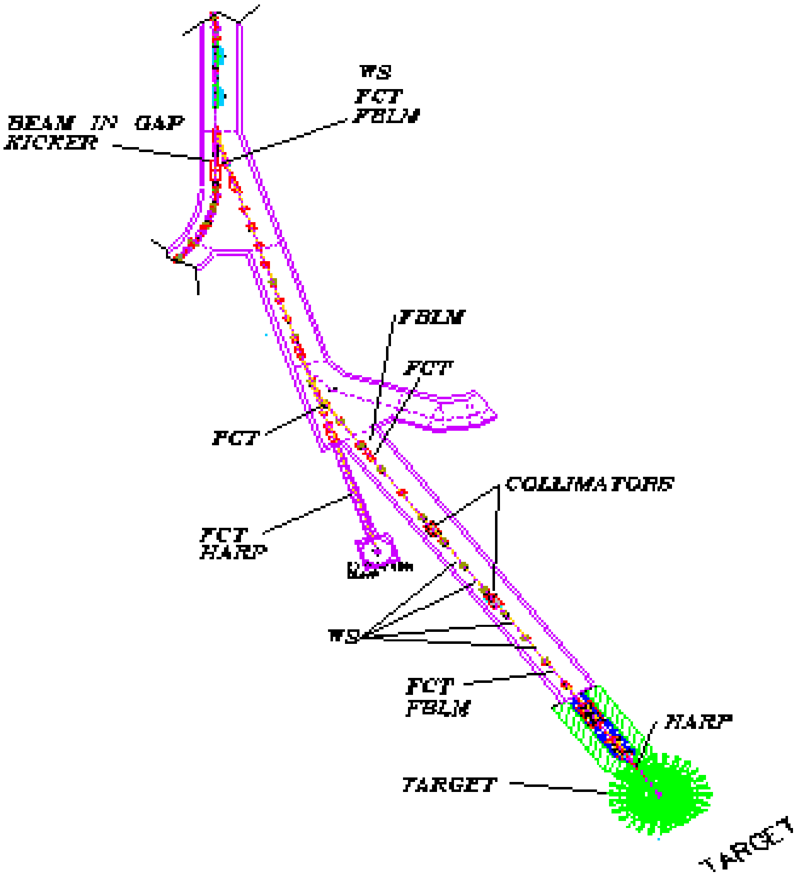

Figure 119: Diagnostics in RTBT and extraction dump.

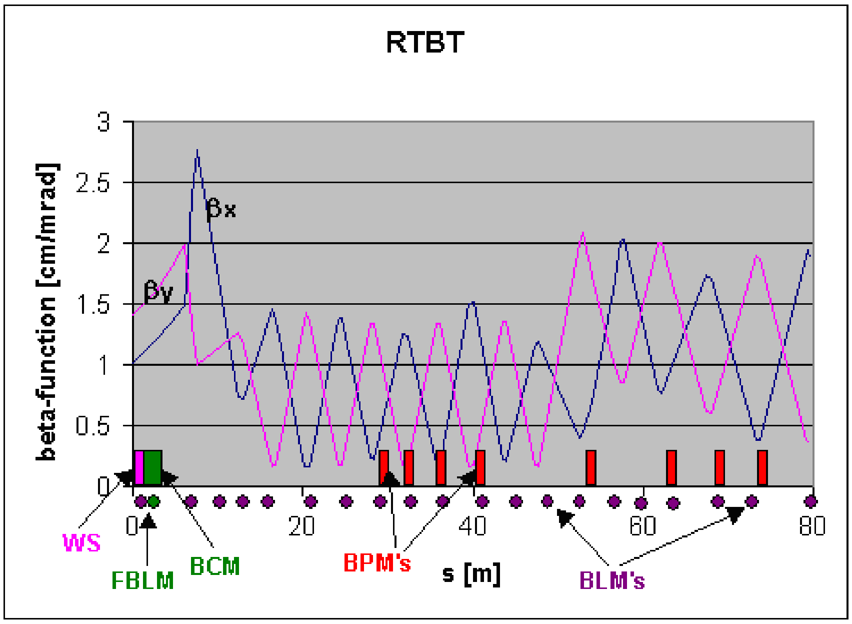

Figure 120: Diagnostic distribution in the RTBT before 16.8 degree magnet.

3.10.3 Beam position monitor

3.10.4 Beam profile monitor

3.10.5 Beam loss monitor

3.10.6 Beam current monitor

3.11 Survey and Installation

3.11.1 Magnet survey

3.11.2 Installation support

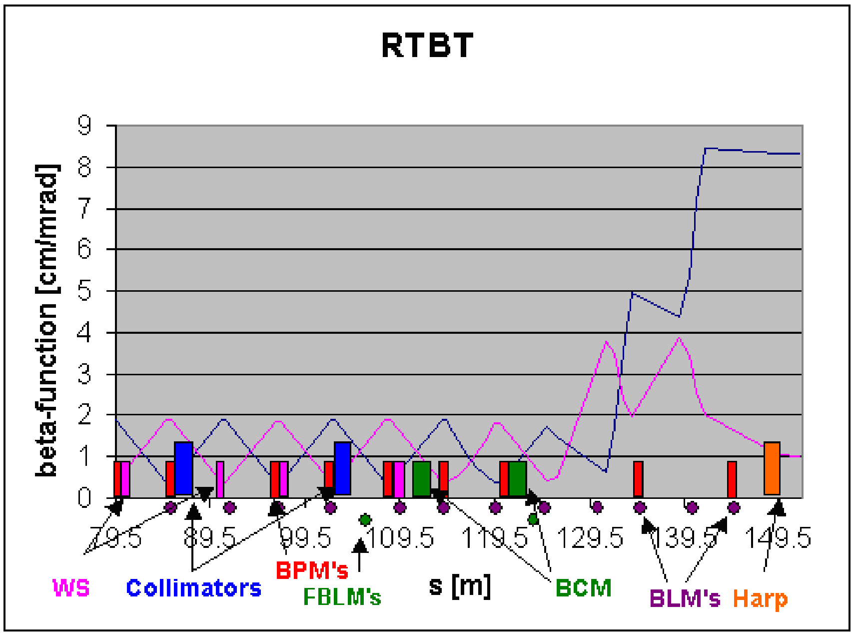

Figure 121: Diagnostics distribution in the RTBT after the 16.8 degree magnet.

4 Integrated Control System

4.1 Overview (WBS 1.9)

4.1.1 Integrated Control System Scope

4.1.1.1 Scope - General

A single, integrated, plant-wide control system will provide control, monitoring, and data acquisition services for SNS. This system is referred to as the "Integrated Control System", or "ICS". The ICS encompasses the high-level controls for all major SNS systems.

The Integrated Control System is divided into two parts. There is a "global" part, which provides common services across the facility. The scope, requirements and design of this part of the ICS is described in section 4.2 (WBS 1.9.1 and 1.9.2) below. In addition, there is a distributed, local part of the ICS which provides for the specific requirements and local I/O for each of the major components and subsystems of SNS, and which makes use of the global facilities. The scope, requirements and design of the HEBT, Ring, and HEBT parts of the ICS are described in sections 4.3 (WBS 1.9.5) below.

Major components of the ICS include:

- Distributed computer systems for equipment interface and control
- Centralized computer systems for operator interface, including main control room equipment
- System and application software
- Local control areas and displays
- Control system local area network
- Timing and synchronization system
- Equipment protection systems
- Other computing systems (e.g. servers) required for the support of control systems
- Control system hardware and software development laboratories

4.1.1.2 Scope - Interface Diagram

Figure 4.1.1 shows the interfaces between the various parts of the Integrated Control System, as well as with the other major components of SNS. Except where noted explicitly, the interface to the ICS is at the front panel of a crate-based I/O system, such as PLC, VME or VXI, or at a transition module where cable break-out and/or signal conditioning takes place. In some cases, where in-house designed VXI modules are used (examples include low-level RF instrumentation and beam diagnostics instrumentation) the interface may be at the crate back plane. Industrial I/O modules may be packaged in an industrial chassis (e.g. PLC) and scanned from a VME crate. By negotiation, the PLC may be a part of the ICS, or of the system with which it was supplied. Instrumentation is described with the systems instrumented.

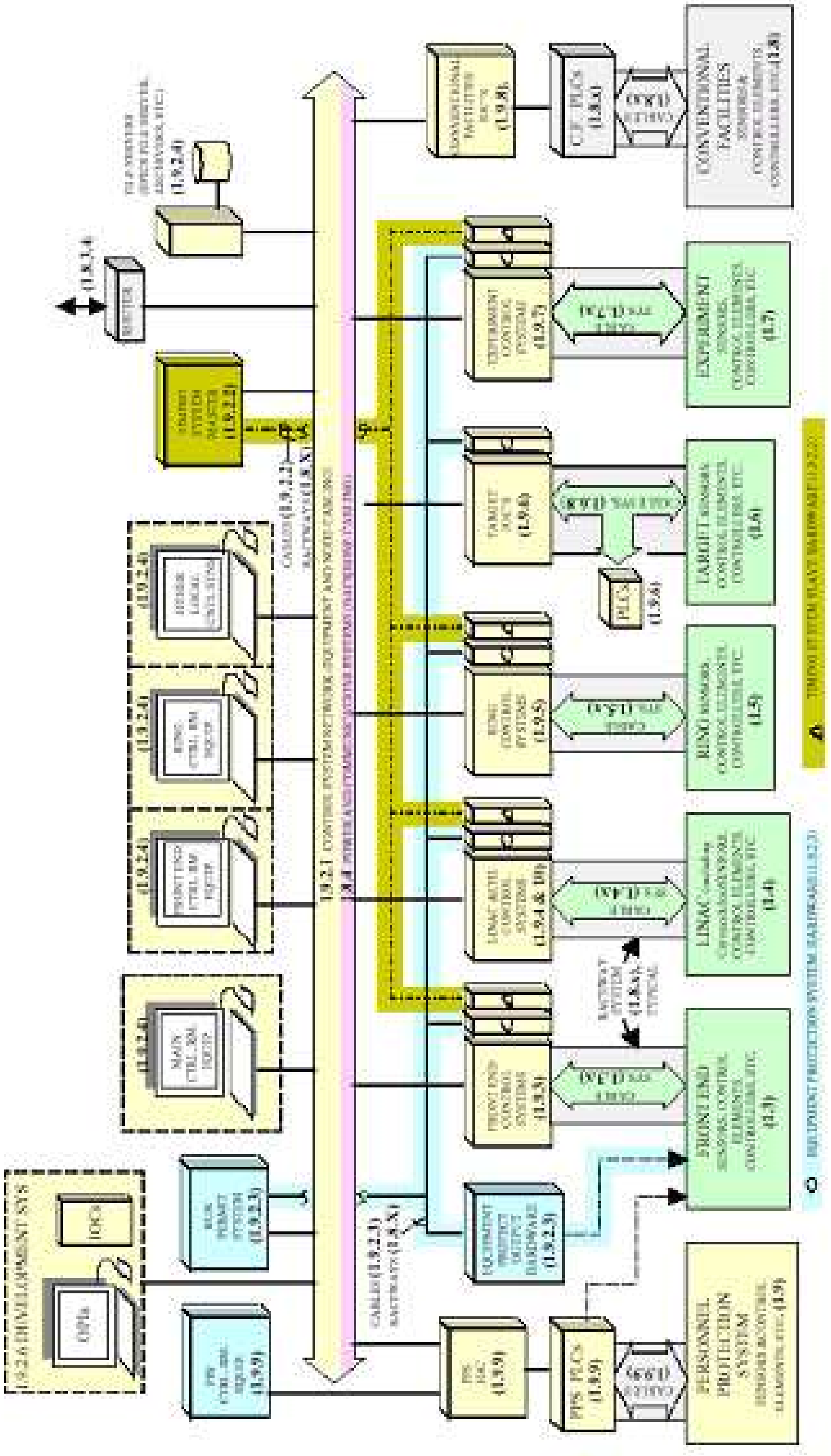

Figure 122: Integrated Control System (ICS) system Diagram.

4.1.2 General Requirements

4.1.2.1 General Functional Requirements

The global system provides hardware and software that is common to all or most systems. The following functionality is provided by application programs developed under WBS 1.9.2.8, which are described in more detail in section 4.2.8 below:

- Operator Monitor and Control.
- Data Acquisition for Accelerator Physics.
- Save and Restore.
- Alarm Management.
- Archiving and Retrieval.
- Automatic Sequencing.
- Closed-Loop Control.
- Mode Control.
- Modeling and Simulation.

In addition, the global system provides a timing and synchronization system (WBS 1.9.2.2) described in section 4.2.2 below, as well as providing for high level (subsystem-spanning) equipment protection (WBS 1.9.2.3 and WBS 1.9.2.4). These systems are described in sections 4.2.3 and 4.2.4 below. (Note that interlock protection of subsystems and components is provided in the distributed systems (WBS 1.9.3 - 1.9.8). Interlock protection for Ring systems is described in sections 4.3 below. These equipment protection systems include:

- Beam Permit Functions:
  - “Run Permit”
  - “Beam Pulse Enable”
- Fast Protect Function

Note that Personnel Safety is *not* a function of the ICS. It is mentioned here only to clarify and emphasize that point. Rather, a personnel protection system, described in the “Conventional Facilities” section of the CDR, will be implemented as a stand-alone system (i.e., with no dependence on the ICS to carry out its safety functions). The personnel protection system will include a personnel access control system to prevent personnel from being exposed to unacceptable levels of radiation and, complementarily, a system of interlocks to prevent beam operation in an area open to personnel. To enhance operation of SNS, the ICS will monitor and annunciate the status of the safety system. Also, outputs from the personnel safety system will be connected to the equipment protection subsystems to provide an additional layer of protection.

4.1.2.2 Requirements by User

The control system is required to serve many different classes of user during many phases of development, from construction to production. It is helpful to view the control system from these different perspectives in order to get a complete understanding of system requirements.

- Equipment Design Engineers. During construction and testing of individual subsystems, design engineers require a stand-alone system that can be located close to the equipment and possibly moved with the equipment from factory floor to its final installation location. To ensure that testing is complete and is relevant to the final system, the control system interface should be the same as planned for operation, both at the hardware and at the operator level. Equipment design engineers require that the control system provide access to all available diagnostic information to assist with commissioning and debugging of the equipment. Equipment should be built with selfdiagnostics, and these should be available to the control system to assist with equipment maintenance.

- Control System Engineers. The control system must provide to its own engineers, both on request and in an archive, data on its own status and behavior. This should include such information as CPU loading, network loading, processor and process heartbeats, connectivity status, and reports of any control system faults or errors. This information is required during all phases of operation but is most important during commissioning and routine operation.

- Accelerator Physicists. Maximum demands are made on the control system by accelerator physicists during the commissioning phase. This phase is when the functional requirements listed earlier under “Data Acquisition” and “Modeling and Simulation” are most heavily used. The control system must be designed for the bandwidth and processor demands anticipated during this time. In addition, the control system must facilitate the rapid implementation of newly conceived diagnostic programs and the interfacing of acquired data with a variety of analysis programs. Application program interfaces must be carefully designed to meet this requirement.

- Operators. The primary users of the control system are the accelerator operators. Where there are conflicting requirements, these should be resolved in favor of ease and safety of routine operation by the operations team. The control system should provide data as predictably, unambiguously, and efficiently as possible. This requirement implies, among other things, a clear, consistent, plantwide naming convention. The system should include an on-line help facility to expedite access to manuals and other documentation when required. Procedures should be automated wherever possible to reduce routine tasks. The system should encourage and facilitate the keeping and passing of operation logs, particularly from shift to shift. Alarm and error messages must be clear and unambiguous (no “Error # 3476221”), and action should be recommended.

- Experimenters. Experimenters making use of neutron beams also require information from the control system. Here the emphasis is on accelerator and target status and performance, as well as on control of each beamline. In addition to information on the status of the machine, some experiments may require timing signals. (The neutron choppers will be an integral part of the timing system. See Sect. 7.3.1.) In addition, the control room may require some data available from experimenters, such as target performance, so two-way communication is required. It is common practice in light sources and other neutron facilities to allow remote access to their experiments and beamlines to off-site experimenters. The Experimental Physics and Industrial Control System (EPICS) system proposed for use by SNS already incorporates a "gateway" capability, allowing safe remote access (with limited performance) for just such applications.
- Maintenance Engineers. The control system must provide useful fault diagnoses to assist with equipment maintenance. It should provide an easy interface to databases of equipment properties, manufacturers, documentation, locations, cabling data, and fault histories. It should also provide access to fault prediction algorithms to allow for scheduled maintenance of components likely to fail.
- Facility Managers and Overseers. The control system should be capable of producing operating reports and statistics in a form required by facility managers, site overseers, and regulating agencies.

4.1.2.3 Performance Requirements

In addition to the functional requirements described in Sect. 4.1.2.1 and the need to satisfy the special needs of users outlined in Sect. 4.1.2.2, the ICS must meet the performance requirements given in Table 38, which provides current estimates of channel counts, system response times, and availability.

4.1.3 Design Overview

4.1.3.1 Design Approach

Like the SNS itself, the Integrated Control System will be designed collaboratively. The distributed parts of the control system (IOCs, distributed database, input - output, local interlocks and system-specific displays and applications - WBS 1.9.3-8) are designed and implemented at the laboratories responsible for the respective subsystems. These systems are built to standards established by the Integrated Control System Working Group (ICSWG) which consists of the lead control system engineer from each participating laboratory. (For example - the ICSWG has published a device naming convention which is in use throughout the collaboration.) The global systems (WBS 1.9.2) will be designed and implemented collaboratively under the guidance of the ICSWG, which will allocate specific subsystems and tasks among the collaborating laboratories. A concerted effort will be made to take advantage of the knowledge base at existing accelerator facilities. CEBAF and APS may offer particularly

Table 38: Control system performance parameters.

Parameter	Value
Total facility I/O channel count[1]	38,700
Front end number of I/O channels[1]	21,500
Linac number of I/O channels[1]	9,000 (Many are wave forms)
Target I/O channels[1]	1,700
Conventional facilities I/O channels[1]	4,300
Console update rate	>5 Hz/channel or 1000 channels/sec
Time to bring up new screen	<1 sec
Time for fast protect to turn off beam	<10us
Maximum use of IOC capacity	50%
Maximum IOC to IOC response	0.1 sec
Time stamp resolution (EPICS)[2]	(<16ms)
Total archive rate[3]	10,000 pts/sec
Total archive capacity	0.5 gigabyte/day
Total network bandwidth[4]	17 Mbits/sec (minimum)
Availability (ICS total)[5]	>99% (see below)

Note: IOC = input-output controller.

1. Channels: In general, a "channel" is a single signal or named measurement or setpoint. Note however that some channels are complex, and in the beam instrumentation case, one channel may represent a complete waveform. The number of channels has been rounded up to reflect the uncertainty of these estimates. Channel counts for front end, linac, ring, targets, and conventional facilities reflect data given in the corresponding design manual sections. Channel estimates at the conceptual stage of similar projects have frequently been low. Larger numbers are assumed where appropriate for conservative design.

2. Time stamp resolution. The time associated by EPICS with acquired data will allow events associated with a given macropulse to be correlated.

3. Archiving rate. Based on a maximum archive rate of 1000 pts at 10 Hz. A background rate of all channels (50,000) every 5 minutes is negligible.

4. Bandwidth. Display: 40 screens @ 100 pts/console @ 10 Hz @ 24 bytes/pt. @ 10bits/byte = 9.6 Mbits/sec Archive: 10K pts/sec @ 24bytes/pt @ 10bits/byte = 2.4 Mbits/sec Total = 9.6Mbits/sec (Display) + 2.4 Mbits/sec (Archive) + 5Mbits/sec (Misc) = 17 Mbits/sec

5. Availability. An availability budget for the SNS control system has not yet been established; however, the RAM budget for most modern accelerators imposes a control system availability in excess of 99% of scheduled operating time. The paragraphs under "Availability" in Sect. 4.1.3.2 describe the strategies to be used in meeting this demanding requirement.

relevant lessons since they use EPICS for controls and are of a similar scale.

4.1.3.2 Design Philosophy

The design of the SNS ICS will be based upon the following underlying principles.

- Economy in operations. The control system and the control room will be designed to require the smallest operating crew consistent with safe operation. Maximum use of automation, consolidation of all operational aspects in one location, and well engineered data visualization will be used to minimize the size of the necessary operating crew.

- Availability. The SNS control system will meet the RAM requirements designated by the project. These requirements are not established yet for SNS. However, most modern accelerators impose a control system availability in excess of 99% of scheduled operating time. This very high reliability requirement imposes a design with a long mean time between failure (MTBF) and short mean time to repair (MTTR). These properties must be built into the system, using proven off-the-shelf hardware where available, using redundancy where required, and derating both components and systems. On-line testability will be designed into all control system modules, processors, and subsystems. The availability requirement also leads to the twin design principles of modularity and distribution. Failures in one part of a distributed, modular system need not adversely affect other parts. Besides being itself reliable, the control system must contribute to the availability of the subsystems it monitors and controls by incorporating fault prediction, automatic fault recovery, and process automation wherever possible.

  Since control system MTTR will directly affect SNS availability, control systems will be designed to minimize the time required to diagnose and fix problems. System module failures will be alarmed. Diagnostic routines will facilitate finding the source of problems. Spare parts will be inventoried strategically. Records will be maintained to aid in the continuous improvement of control system reliability. In order to minimize the time it takes for the control systems to recover after a power failure, uninterruptible power must be supplied to critical equipment. For example, file servers and the control systems network must be supplied with uninterruptible power.

- Scalability. The control system will be designed to be scalable. Small subsystems will be commissioned independently, and their control systems will then be combined into larger and larger systems without performance or reliability degradation. It will be simple to grow the system in this way, and the system should itself recognize and incorporate new components as they are added. This scalability is also important in dealing with new equipment and/or requirements not considered in early designs; and in the case of SNS, it is particularly important to accommodate the eventual power upgrades and addition of a second front end, accumulator ring, and target. The need for scalability leads once again to the two fundamental design approaches of modularity and distribution. The system scales by the addition of new modules.

- Openness. To the extent possible, the control system design will be based upon open standards. The use of open standards will allow for the easy integration of commercial off-the-shelf hardware and software with the special in-house-developed hardware and software required for some applications. The use of open standards is driven also by the need for economy, as network equipment, I/O modules, processors, and some software applications can be provided on a competitive basis by many suppliers; and it allows easier incorporation of new technologies in a timely manner.

- Using open standards, the design can be done early but the actual implementation done ”just-in-time” to make use of the most current technologies in a rapidly changing arena. Combined with modularity, this design principle leads to maximum versatility.
- Integration. The main elements of the SNS facility-accelerators, transfer lines, ring(s), targets, experiments, and conventional facilities-must work together as an integrated facility. It is the control system that is most responsible for effecting this integration. The design of the accelerator control system is based on the assumption that the same design approaches, philosophies, and technologies can be used for each of the subsystems listed. The main control room and the control system communication network together form the operational nexus for this integration. The control system and the control room will provide a uniform environment for the differing tasks of equipment designers, accelerator physicists, and plant operators.
- Toolkit Use. The control system design will be based upon the use of a configurable “toolkit”. Such a toolkit permits rapid system reconfiguration, development of new operator screens, and introduction of new sequences and programs that are required, particularly during the commissioning phase. A toolkit should contain basic functional tools (e.g., archiver, alarm manager, sequencer, display manager, configuration database, communication protocol) as well as a well-defined application program interface for the addition of new capabilities.
- Flatness. The control system will be designed to be as architecturally “flat” as possible. That is, the number of (processor) layers that any message must traverse should be minimized. Flatness improves performance, removes potential bottlenecks, and increases versatility. It is important to note that flatness in the hardware or communications architecture does not necessarily imply flatness in the software architecture. The software architecture will be appropriately “layered” with welldefined software interfaces between the layers.
- Off-line Software Development Capability. During the life of SNS, it will be necessary for software development activities to occur concurrently with construction, start-up, and operation. Since the actual control systems will not be available for software development most of the time, an independent software development system will be provided.
- Configuration Management. A vast amount of control system software will be required to operate SNS, and a system will be in place to ensure that only tested and approved software is used.

4.1.3.3 Choice of EPICS

The SNS control system is based upon the widely used and accepted Experimental Physics and Industrial Control System - EPICS.

Two recently completed large accelerator projects-the Advanced Photon Source (APS) at ANL and the Continuous Electron Beam Accelerator (CEBAF) at the Thomas Jefferson National Accelerator Facility (TJNAF)-have used the EPICS toolkit to implement their control systems. EPICS was developed cooperatively by many collaborators, primarily at LANL, ANL, and TJNAF. In addition to the two large facilities mentioned, EPICS is now in use at nearly 100 institutions worldwide for accelerators, telescopes, detectors, large industrial plants, and a variety of smaller experiments and instruments.

EPICS comes very close to meeting fully the control system requirements outlined in the previous sections. It was designed with the same design approach and philosophy. Because CEBAF and APS are facilities similar to SNS (at least in terms of functional requirements) and of comparable scale, EPICS is demonstrably capable of controlling the SNS accelerators and associated equipment. Technology in this arena changes rapidly, however, and it is not at all clear what EPICS will mean when the SNS is actually constructed. However, the toolkit has a history of keeping up with changes in technology, and EPICS can be expected to continue to be an appropriate choice for SNS controls.

The features and capabilities of EPICS are well documented and are available on the World Wide Web.

4.1.3.4 Elements of the EPICS System

Two components together define EPICS software: the EPICS distributed database; and the protocol used to communicate between clients and servers (see below), known as “Channel Access”, or “CA”. EPICS provides many additional tools and applications, but these two elements form the core of EPICS - with them, it’s EPICS; without them, it’s not.

Many design details are implied by the simple statement that EPICS has been selected as the basis for the SNS control system design. However, one still needs to select the most appropriate EPICS tools to use. Moreover, the specific I/O to be used for each subsystem must be chosen. I/O equipment already supported by EPICS is preferred, and, wherever possible, an industrial control approach will be used. Nonetheless, many requirements cannot be met by commercial systems (synchronous data taking, high data bandwidths, special instrumentation), so the design will involve the integration of commercial and in-house hardware and software. EPICS is based upon the familiar and widely-used client-server model. The following paragraphs describe the common features of the clients and the servers. (Note again that the parts of the control system that are specific to the various accelerator subsystems are described with those subsystems).

- Clients. The operator consoles described earlier are one class of client using data from the accelerator that are ”served” to them by data servers elsewhere on the network. These clients will be selected primarily for their suitability for data visualization. UNIX-based workstations or PCs running Windows-NT are appropriate candidates. Other clients will be selected based upon function. An archiver-client and an alarm manager-client will also be needed. A critical client application will be for modeling of both the accelerator and the entire facility operation.

- Servers. Providing data to the client applications are data servers distributed about the network. These servers, known as I/O controllers (IOCs), communicate directly with I/O devices [e.g., ADCs, DACs, transient recorders, stepping motor controllers, programmable logic controllers (PLCs), binary input gates, and output registers], which in turn are connected to sensors and control elements. It is anticipated that the facility will have between 25,000 and 40,000 of these I/O channels; therefore, the IOCs are widely distributed. An estimate of 100-150 IOCs for the accelerator, transfer lines, ring, target, and conventional facilities is not unreasonable.

Technology changes rapidly, and it is premature to select he CPU to be used. All laboratories will use the same CPU for ease of maintenance. It is likely that by the time SNS is implemented, newer systems with faster CPUs, more memory, and 100Mbit/sec Ethernet will be the standard. Each IOC consists of a VME crate, CPU board, utility module, timing modules, and battery-backed-up memory. In many IOCs a protection system module will be needed. Each IOC will have other modules specific to requirements for its system. (It is conceivable that by the time SNS is implemented, a completely new technology, such as PC/NT-based front end computers, will be the appropriate choice. The present baseline design assumes the use of VME-based hardware).

SNS will use standard VME crates. (Note that the EPICS collaboration is currently developing IOCs which are PC based. This development will be closely followed, and PCs may be used in appropriate applications if they prove sufficiently performant and reliable.) VME specifications will call for a 750-W power supply, cooling air plenum, five DC cooling fans with ball bearings, fan speed sensors, power fail detect sensor, slots for rear-mounted transition modules, and other features. A utility module will monitor and alarm on temperature, voltage, current, fan speed, and possibly control fan speed and issue resets. A power-fail-detect sensor will alert the computer to a pending power failure in sufficient time to take actions such as saving key parameters in battery backed-up memory and stopping motors. Short-term power failures will cause the power-fail-detect circuit to force a restart, thereby preventing the IOC from being left in a "hung" state. To minimize traffic on the network, and thereby optimize performance, the IOCs check acquired data for alarm conditions, passing on only anomalous readings to the appropriate client. Similarly, only changes outside predefined "dead bands" are passed on to consoles for display. Sequences that can be completed locally are executed within an IOC without the intervention of other processors or the need to pass data on the network. All of these features imply a complete descriptive database in each IOC for the channels it is controlling.

Because the IOCs may be running many tasks and may have to react rapidly to unsolicited events, a high-performance real-time kernel is required to run the IOC software. In the spirit of open standards, real-time POSIX would be the preferred choice; however, in the absence of an established standard, a proprietary system with a declared intention of meeting the POSIX standard when it evolves is acceptable. Currently, EPICS uses the proprietary VxWorks kernel.

In addition to this network of processors and processes, some additional subsystems perform important global functions: a beam permit system, a fast protect system, a timing system, and a number of project databases. These systems are all somewhat or completely independent of EPICS; they are described in the subsections of 4.2 below.

4.1.3.5 System Architecture

The main components of the SNS (EPICS) system are illustrated schematically in Figure 4.1.3, which shows the control system from the hardware point of view. Figure 124 shows the same configuration from the software point of view, and Figure 125 shows a typical IOC configuration. Details of specific IOC configurations required for control of the various accelerator subsystems are given in their respective control system subsections.

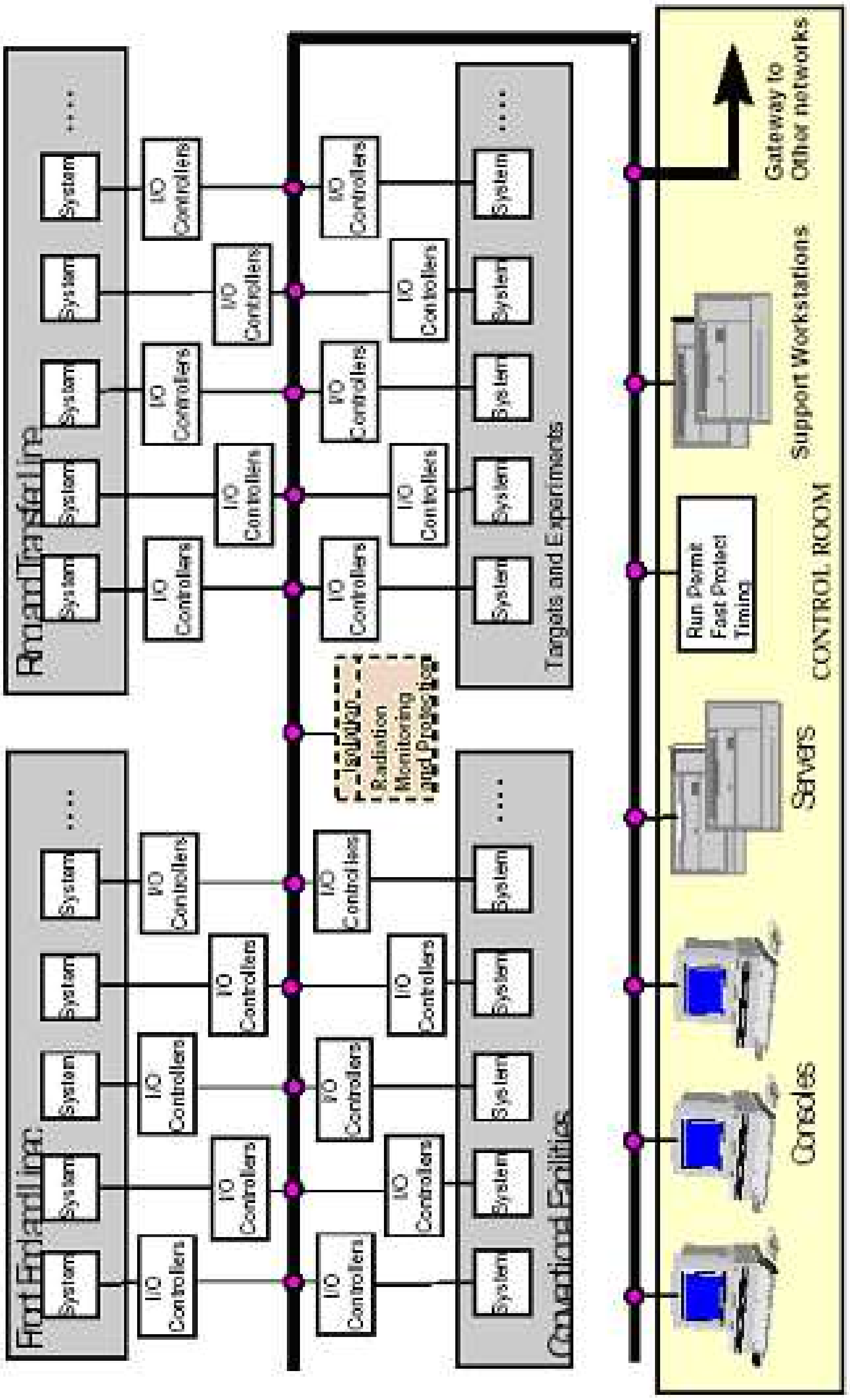
Front End and Linac
Ring and Transfer Line
Conventional Facilities
Targets and Experiments
System
....
I/O Controllers
Isolation - Radiation Monitoring and Protection
Consoles
Servers
Run Permit
Fast Protect
Timing
CONTROL ROOM
Support Workstations
Gateway to Other networks

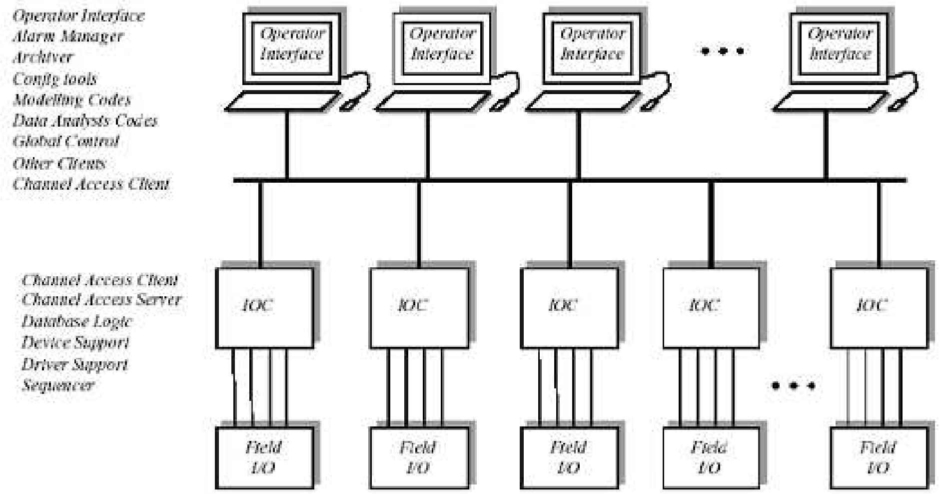

Figure 124: Control system from the software point of view.

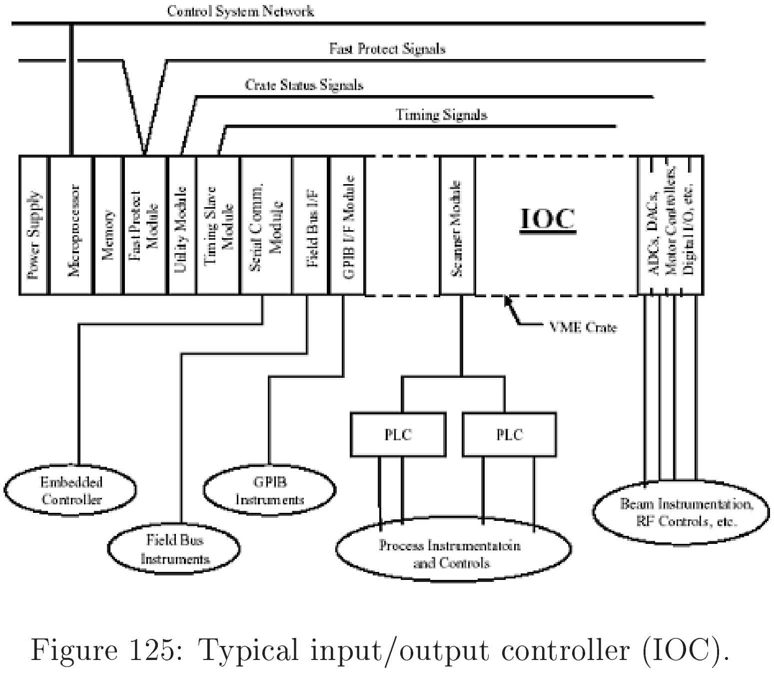

Figure 125: Typical input/output controller (IOC).

4.2 ICS Global Systems (WBS 1.9.1 AND 1.9.2)

WBSs 1.9.1 and 1.9.2 contain the "global" portions of the integrated control system, including:

- ICS integration activities (WBS 1.9.1)
- Control system network (WBS 1.9.2.1)
- Timing system (WBS 1.9.2.2)
- Fast protection system (WBS 1.9.2.3)
- Beam permit system (WBS 1.9.2.4)
- Main control room (WBS 1.9.2.5)
- Software development system (WBS 1.9.2.6)
- Computing systems (WBS 1.9.2.7)
- System and application software (WBS 1.9.2.8)

Each of these is discussed separately in the following sections.

4.2.1 ICS Integration (WBS 1.9.1)

WBS 1.9.1 includes the management and coordination of "instrumentation and control system working group" (ICSWG) activities.

This WBS also includes a controls laboratory, preferably close to the control room, where modules can be repaired and spares can be kept. This laboratory will be equipped with an automatic test facility for rapid testing and debugging of failed control system modules and components and wiring check-out. Similarly, there will be a software development area for the development and maintenance of control system software during the commissioning and operation stages of the project. The equipment in these laboratories will result from the consolidation of development laboratories distributed among the collaborators during earlier stages of the project.

4.2.2 Control System Network (WBS 1.9.2.1)

4.2.2.1 Control System Network Scope

The control system communication network carries all computer communication related to the functions of the SNS Integrated Control System as described in this chapter. This includes the real-time control messages for active running of the plant; general file transfers needed for control system software development, and any needed connections of the control system to external networks (ftp, www). In addition to data packets associated with conventional computer programmatic needs, some amount of voice and video will be divided between the network hardware and conventional audio and video circuitry. General-purpose communication, related for example to business computing or experimental data analysis is not in the scope of the control system network.

4.2.2.2 Control System Network Requirements

The network must meet requirements in the areas of performance, reliability, repairability, scalability, security, and adherence to standards and good engineering practice. Performance and reliability of the network is derived from the performance requirements of the various supported areas within the scope. The control system communication bandwidth requirements, as called out in Table 38, can be summarized as >17Mbits/sec with >99% availability.

The network must connect to the following component types:

- IOCs and Consoles associated with EPICS (generally comprising WBS 1.9.3-8);
- File servers holding setpoint configurations and archival data associated with running the accelerator and analyzing or modeling its performance (also WBS 1.9.3-6);
- File servers holding experimental data produced by the experimental systems (WBS 1.9.7);
- Vendor equipment provided as part of the conventional facilities (WBS 1.9.8);
- Other dedicated computers supplying external needs such as WWW access or gateways to external networks.

The network should have no single point of failure.

4.2.2.3 Control System Network Design Description

Following modern practice, the network will physically be a hierarchy with redundancy. All network media will support the TCP/IP protocol; (Where performance is an issue, UDP will be used.) additional computer protocols required by various operating systems (such as Unix, Windows NT, and business systems); and some audio and video (specific to operating requirements). On top of these standards, EPICS layers its own protocol, known as “Channel Access”, which is optimized for performance.

As suggested earlier, maximum performance and flexibility will be achieved by using a flat network architecture-the only exception being the use of one or more gateways for remote and lower priority access. Although network hardware is undergoing rapid industrial development, some general trends are clear.

Topology. Each end-node will have its own wire connection, with multiple connections joined at “hubs”, which can perform a switching (frame-level) or routing (protocol-level) function. Hubs themselves will be joined at higher level hubs. At the highest level one or more hubs will form the (virtual) backbone. Only at this level will external connections to SNS appear.

Critical nodes will require redundant paths between each other and a minimal set of consoles and servers. IOCs will require dual paths, since each is critical; it is sufficient that roughly one-half of the consoles and servers survive a single component network failure (hub or signal wire). Judicious use of Uninterruptable Power Systems (UPS), hotswappable power supplies on hubs, and alternate cableway routing will ensure that no single external event (loss of power, severing of cableway) compromises the designed-in logical redundancy.

Hardware. Typical IOCs and Consoles will each require 10Mb/s or 100Mb/s connections. Servers and other demanding components will generally demand 100Mb/s, or higher. The obvious choice to satisfy the first two needs is 10Mb/s and 100Mb/s switched Ethernet (although other standards such as Token Ring and FDDI could in principle work). For the third requirement, either 1000Mb/s Ethernet or Asynchronous Transfer Mode (ATM) offer benefits and cost advantages. Generally, Ethernet allows easiest upgrades and direct, frame-level compatibility for data traffic; ATM offers potentially the highest throughput if needs beyond 1000Mb/s are required, and also "constant bit rate" and other quality-of-service features suitable for audio and video. Both 1000Mb/s Ethernet and ATM can be attached directly to end nodes, but will generally be relegated to back-bone service.

Software. It will be necessary to monitor the status and performance of the network to detect incipient failures (high error rates or capacity overloads) and to perform reconfiguration when automatic failover is not available or appropriate; such monitoring will also allow for orderly capacity planning as operating conditions of the facility evolve over time. Monitoring will be provided by a combination of dedicated, non-intrusive, "snooping" hardware with appropriate software, and by added software on existing hubs and nodes.

Security. The requirement for some external access brings with it the requirement for maintaining security. In addition to monitoring for intrusion, routers, firewalls and/or gateways will be used.

4.2.3 Timing System (WBS 1.9.2.2)

4.2.3.1 Timing System Scope

A modern physics facility must synchronize the operations of equipment over a wide area. The primary purpose of the sitewide SNS synchronization and timing system is to synchronize the extraction of the accumulator ring to the neutron choppers and distribute appropriate timing signals to various accelerator systems, including the Injector, the Linac, and the Accumulator Ring. Signals to be distributed by the system include the ring RF clock, real time timing triggers, machine mode and other informational events. Timing triggers and clocks from the SNS synchronization and timing system are used to synchronize hardware operations including the LINAC beam chopper, equipment state changes, and data acquisition for power supplies and beam diagnostics equipment.

The timing system to be developed under WBS 1.9.2.2 consists of a phase locked loop (PLL) to generate a 120 Hz power line locked clock and two master encoding and distribution systems, a timing event system (eventlink) and a real time data distribution system (RTDL). The SNS eventlink is made up of a master encoding chassis including a VME chassis, input modules, timing system encoder, distribution system to all equipment locations, and a general purpose VME receiver module. The VME receiver module shall be configurable to respond to user-selectable timing events and provide TTL electrical pulse outputs and local delay capability. Receivers will be provided for all equipment requiring access to timing system signals. VME chassis to house the receiver modules are not included. An SNS diagnostic

V123S Event encoder	http://www.agsrhichome.bnl.gov/Hardware/snsbeamsync/V123S.htm
V101 Event input	http://www.agsrhichome.bnl.gov/Hardware/timeline/eventsys.htm
V124S Event trigger	http://www.sns.bnl.gov/epics/timing/doc/v124s/v124s-specs.pdf
V205S RTDL encoder	http://www.sns.bnl.gov/epics/timing/doc/RTDL/SNS-RTDL-specs.pdf
V206 RTDL input	http://www.agsrhichome.bnl.gov/Hardware/rtdl/rtdlsyst.htm
V108S Utility(RTDL decoder)	http://www.agsrhichome.bnl.gov/Hardware/util/utilmap.htm

monitor capable of recording and timestamping all events present on the event link will also be provided

The RTDL system distributes real time data and mode information, including time-of-day. The RTDL system includes a central encoding chassis including a VME chassis, input modules, RTDL encoder module, distribution system to all equipment locations, and a VME Utility module. This document is written for a linac operating at 1.0 GeV and an accumulator ring of 248 meters. There will be no design changes necessary if the Linac energy is increased to 1.3 GeV. Each of these timing system components has detailed design descriptions in separate documents.

4.2.3.2 Timing System Requirements

Synchronization of Neutron Choppers

The neutron choppers are very high inertia mechanical rotors with collimators that chop the neutron beam. To prevent modulation of the neutron energy spectrum, the chopper operation must be synchronous with the arrival of protons on the target. Thus the phase of the chopper is fixed with respect to extraction while the phase of a chopper is independent of the operation of the linac. For the several types of choppers, Fermi, T0, and bandwidth limiting choppers, the most stringent desired timing accuracy for the synchronization is about ± 0.5 μs. The required accuracy is still to be determined, but is in the ± 1 μs range.

Synchronization of Linac

In order to inject approximately 1060 turns into the ring, the beam injection into the linac must begin about 896 s before extraction. For a super conducting linac, the klystron modulators must be pulsed about 400 μs earlier than the beam. The reason for this is to fill the rf cavities with field before the injection of beam. Thus the first required timing pulse for a complete beam pulse cycle is required about 1666 μs before the ring extraction time.

Klystons in the linac require synchronization with the power grid. Failure to maintain this synchronization results in non-linear performance and beam losses.

Linac Beam Chopper Synchronization

The beam in the linac injector is chopped by two systems, a gated electrostatic focusing electrode in the LEBT, and a traveling-wave deflector (beam chopper) in the MEBT following the RFQ. Each of these systems, and especially the beam chopper in the MEBT, must be synchronized to the ring period. The reason for chopping the beam is to produce a gap in the beam current that is synchronized to the ring period with a cumulative error of about ± 5 ns for the entire 896 μs accumulation period.

Synchronization of Ring Extraction to Neutron Chopper

The beam occupies about 67% of the ring circumference, and the remainder of the ring (the beam gap) is free of beam (to about 1 part in l05) in order to accommodate “clean” extraction (without unnecessary beam loss). The extraction from the ring must be synchronized to the beam to about ± 5 ns (the beam gap is about 300 ns long).

Variation in the Ring Revolution Period

For a 1 GeV proton circulating in a ring of circumference 248 meters, the revolution period is 945.4 ns. During normal operation, tuning the ring by changing the B field (which changes the orbit radius), or tuning the linac to change the injection energy, or a combination of both, can change the revolution period by up to ± 2 ns. During ring commissioning, the change can in principle be even larger. Although 2 ns is not a large number, the cumulative timing error over a normal accumulation cycle of 1060 turns exceeds 2 μs, more than one complete ring period. This is much larger than the desired cumulative synchronization accuracy of ± 5 ns for accumulating 1060 turns of beam in the ring. Any cumulative error exceeding 10 ns can begin to fill in the beam gap in the ring. Any beam in the gap will activate the extraction septum. A beam synchronous timing system tied to the rotation frequency of the ring will compensate for this variation in fill time and maintain ± 5 ns timing accuracy.

Beam Diagnostics Synchronization

Ring Diagnostics

The beam diagnostics in the ring measure the revolution of the beam during the accumulation cycle. The ring beam diagnostic measurements include global systems such as a beam closed-orbit measurement (BPM) system, and local systems such as the azimuthal distribution of beam charge density (current monitor). Global and local refer respectively to systems that are widely distributed around the ring, or are needed in only one or two azimuthal locations. These systems need to be synchronized to the beam in the ring to within about 5 ns, even though the accumulation period may vary by 1000 ns or more.

Linac Diagnostics

Although the linac RF is not synchronized to the ring, the periodic beam gap in the linac is. Because of the effect of the beam gap on the performance of the linac beam diagnostics, the sampling of the beam diagnostics signals from all the diagnostics needs to be synchronized relative to the beam gap. In particular, beam current, beam position, and beam synchronous phase measurements would benefit from being synchronized relative to the beam gap. Thus the linac diagnostics also need to be synchronized to the beam in the ring. A 60-ns timing granularity (not jitter) of a timing signal relative to the beam gap is adequate (the beam gap is 300 ns long, and the beam mini pulse between beam gaps is 645 ns long).

Beam lines

Diagnostics in the beam line between the linac and ring requires synchronization to the ring period. In addition, RF cavities in this beam line require the 805-MHz reference signal. Diagnostics in the beam line between the ring and the spallation target need only a single

Table 39: Master Timing generator I/O

Cycle Start	output signal generated Ncs ring rf periods prior to ring extraction
Test Input	diagnostic input signal injected into master timing generator in place of zero crossings for the power grid
Grid-coupling	register for the grid-coupling parameter that controls how closely the PLL follows the fluctuations of the power grid
Ncs	register for the number of ring rf cycles that Cycle Start will be generated prior to extraction
Ring period	register loaded from the RTDL system at 120 Hz with current ring period
60-Hz phase difference	register loaded by master timing generator

pretrigger a few 100 ns before extraction.

4.2.3.3 Timing System Design Description

Experience at other spallation sources has shown that the linac, ring, and neutron choppers can synchronize operation with each other and follow trends in the phase fluctuations of the ac power grid. Each subsystem operates as a slave to a master timing generator which smoothes phase fluctuations present in the power grid. At SNS the competing demands of the linac that limits phase differences with respect to the power grid and of the neutron choppers that limit the acceleration or deceleration of high-inertia rotors can be simultaneously satisfied within a “phase” window of ±500 μs measured with respect to the power grid.

To synchronize the accelerator systems and the neutron choppers, a phase-stable timing signal, Cycle Start, is generated and distributed around the facility. This 60 Hz signal shall be used to generate several key timing signals (events) on the event link (see section 4.4). Cycle Start shall be generated some number (Ncs) of ring-rf cycles before extraction. Ncs might vary depending on the number of micropulses injected into the ring. The phase of the ring RF will be resynchronized at Cycle Start while the accelerator is idle and the ring is empty. Once established at Cycle Start, the phase and frequency are held fixed until after the beam is extracted. In addition the frequency is dictated by the tune of the storage ring as discussed in section 4.2.3.2.

Each period of the ring RF is counted so that at ring extraction this count has value zero. All accelerator control functions are keyed to the time as reflected in the count sequence. After ring extraction the ring-RF count sequence will be positive until Ncs ring-rf cycles before the next ring extraction. Cycle Start will force the count sequence to a fixed negative count of Ncs exactly Ncs ring-rf cycles before extraction.

Since ring rf and Cycle Start are critical signals for correct operation of SNS, these signals are monitored in a separate module. Should the master timing generator lose synchronization as indicated by the Cycle Start signal drifting too far from the zero crossing, then a sync lost pulse will be generated for each cycle until synchronization is regained. Conditions for defining lost synchronization are TBD.

PLL

The master timing generator will implement a phase-locked loop (PLL) that will follow the phase fluctuations of the power grid and produce the Cycle Start signal with "smoothed" phase fluctuations. The residual fluctuations should not exceed the ability of the neutron choppers to maintain phase lock with Cycle Start or with signals derived from the timing distribution system. Similarly the residual phase fluctuations must not exceed ± 500 μs to ensure correct operation of the klystrons in the linac.

Grid-coupling Parameter

The ac-line synchronization requirement should be established by an operational parameter varied under computer control. In operational terms The parameter characterizes the balance between the variance of the time interval between the zero crossing and the Cycle Start signal and how quickly this time interval is allowed to change (slew rate).Over its full range this parameter is expected to provide for phase coupling from essentially identical to the power grid through phase coupling with a standard deviation of 125 s. Under this same range of conditions, the slew rate is expected to vary from approximately 3 mHz to 0.3 mHz/sec. An additional operating mode shall be available which explicitly limits the slew rate. This limit shall be adjustable from 0.1 mHz/sec to 3 mHz/sec.

60-Hz Phase Difference

The master timing generator will update the 60-Hz phase difference register for each 60-Hz cycle with the measured time interval between Cycle Start and the zero crossing with positive slope of the power grid. The zero crossing with negative slope will be not update this register.

Relationship to ring RF

To synchronize extraction of the beam from the storage ring with the rotation of neutron choppers, the master timing generator will first determine when beam should be extracted for the next beam pulse. Then the timing generator must schedule generation of the Cycle Start signal allowing for Ncs ring-rf cycles prior to extraction. The Cycle Start signal will reset the phase of the ring rf to zero.

Ring period

To calculate the time to assert Cycle Start the master timing generator must support registers to record the value of Ncs and the ring period. Although the value for Ncs is generally fixed, during tuning this value may change to reflect changes of the pulse width from the linac. The ring period on the other hand is routinely changes due to slow variations in closed-loop ring controls. Consequently the value for the ring period is captured prior to each pulse from the RTDL system defined in section 5.

Test Input

To verify correct operation of the master timing generator, a test input to the PLL may be substituted for the normal input from the zero-crossing detector.

Section 1 Monitor for cycle start signal and ring rf

Since Cycle Start and the ring rf are critical to SNS operation, a separate module shall monitor these signals and substitute placeholder signals in case any problems are detected.

Cycle Start

If the time interval between Cycle Start and the zero crossing exceeds a limit specified by the grid-window register, then the monitor will issue an interrupt and constrain the qualified

Table 40: PLL I/O

Cycle Start	input signal generated by the master timing generator
Qualified Cycle Start	output signal that usually is a delayed version of Cycle Start but may be constrained within a window centered around the zero crossing of the
Ring RF	ring rf input signal
Qualified Ring RF	output signal that is usually a copy of the ring rf but may be generated internally if the input rng rf signal is lost
Grid Sync Lost	output signal asserted when the interval between the Cycle Start and the zero crossing of the power grid exceeds the time specified in the Grid-difference li
Ring RF Lost	output signal asserted when the input ring rf signal is lost
Grid-difference limit	register for the grid-coupling paramter that controls how closely the PLL follows the fluctuations of the power grid

Cycle Start signal to the edge of the specified window.

Note that the qualified Cycle Start signal will necessarily be delayed by one half the width of the specified window.

If the Cycle Start signal does not fall within the specified window, the module will assert Grid Sync Lost.

Ring RF

If the ring rf is lost, the module will issue an interrupt and generate ring rf at the last observed frequency.

If the ring rf is lost, the module will assert Ring RF Lost.

Timing Distribution

The most convenient way to broadcast timing signals to many hundreds of clients distributed over a kilometer or more of accelerator and beam lines is to encode all the timing signals on a carrier frequency (clock), and to distribute this signal to all clients. Encoding the timing signals on the same cable (or fiber) as the clock eliminates the possible timing ambiguity due to non-equal cable lengths. If the carrier frequency on which the events are encoded, is synchronous with the beam in the ring, rather than a fixed frequency, then timing triggers and delays derived from the carrier frequency maintain the proper relationship with the beam revolution period. This eliminates the need to adjust timing delays due to changes in the ring revolution period, even though the total ring accumulation period may vary by as much as ±2 μs.

Each receiver decodes the timing signals and recovers the carrier (clock) frequency. Digital filters in each receiver are configured to recognize specific real-time trigger signals, which are synchronous with the clock cycles. Output signal levels for clock and trigger outputs from the general purpose decoder delay module shall be TTL signal levels with 50 ohm drive capability.

The SNS accumulator ring revolution period is 1.05 MHz for a 248 meter ring operation at 1 GeV. If we operate the SNS timing system on a carrier frequency exactly 16 times the ring revolution frequency, from a clock supplied by the ring low level RF, the carrier frequency will be 16.92 MHz. Choosing a carrier frequency 16 times the revolution period of the ring allows easy recovery of the 1.05 MHz revolution clock at the receivers. Short-term jitter due to encoding, signal distribution and clock recovery can be kept below 2 ns. Drift due to thermal effects of the fiber are 38 ps/km/°C. Based on the requirements outlined above, the specification of the SNS timing and synchronization system is described below.

Timing stability – About $|pm5$ ns (relative to the beam in the ring). This includes long-term drift and pulse-to-pulse jitter. Stability in this range allows use of the timing system for triggering the beam chopper in the linac injector and the extraction kicker in the ring, as well as for all the beam diagnostics. The timing system described here does not need to address the timing (phase) stability of the linac rf systems, which must be stable to ± 0.5 degrees at 805 MHz (about ± 0.002 ns).

Frequency compliance (to variations in ring revolution frequency) – Many systems in the injector, linac, and ring, will have individual downloaded delay settings (integer cycles of a reference clock). Variations of the ring revolution period up to ± 2 ns (± 2000 ns for a complete accumulation period) should not require changing any downloaded preset delay settings in order to maintain the 5 ns timing stability relative to the beam in the ring.

Clock – The distributed clock signal must be CW, independent of whether beam is in the ring.

Real-time event encoding – The SNS timing encoder shall have the ability to encode and transmit 100's of distinct timing signals (”events”) in a real-time fashion (meaning synchronized to a clock). An event prioritizing system is provided to ensure that important timing signals are transmitted on the correct clock cycle. Real-time events include all the preset timing signals, such as for beam choppers, klystron modulators, etc. In addition, triggers are required for synchronizing beam diagnostics measurements (beam position and beam synchronous phase measurements in the linac, closed orbit measurement in the ring, and pretriggers are required for the diagnostics in the ring-to-target beamline).

Number of distinct event (trigger) types – The SNS timing system shall be capable of transmitting 256 different timing signals.

Granularity – This refers to the timing system clock period, which should be short relative to the ring period. This relates to the minimum step size in setting the transmission time of encoded events. Granularity for a 16.92 MHz carrier is 59 ns. Finer delay settings can be achieved by using fixed length cables, or by using delay chips that are remotely programmable with better than 5-ns delay granularity and stability. Granularity does not need to be as good as timing stability (see above).

Transmission method – Broadcast transmission over optical fibers or cables using a self-clocking encoding scheme in which the timing signals are encoded on the clock signal. The receivers each recover the original unmodulated clock signal (carrier), and have individually programmed digital filters to recognize and decode specific encoded timing “events”.

Distribution mechanism – Encoded event (trigger) signals and clock are distributed on the same fiber (or cable) to permit convenient distribution over the entire site. The SNS timing system is distributed via singlemode fiber-optic cable to all equipment buildings where a fiber optic receiver converts it to an electrical signal. Distribution within an area is point to point on twisted pair copper cable.

Distribution area – Sitewide. This means that all receivers will receive all transmitted events, including linac-specific and ring-specific events.

Bit error rate (BER) – Whatever it has to be to ensure an acceptable reliability.

Informational events – The timing system should have the ability to distribute informational events as well as timing events. Informational events might include identifying the accelerator cycle type (e. g., beam to spallation target or to linac beam dump, or Beam Pulse Disable (e.g., ring extraction kicker capacitor bank not completely charged by time CycleStart). The critical timing signals occur in the 6 ms between CycleStart and Text. (see Figure 4.2.3)There are 2 ms between Text and the next CycleStart signal. During the period between Text and CycleStart informational events can be transmitted with a lower priority that can be "bumped" by timing events because their exact timing is not critical. Priority system for event transmission-Critical timing events are given priority for a given time slot to prevent any contention. Non-critical timing signals are delayed (by about 1 μs (a 12-bit word requires about 12 clock cycles or 630 ns to transmit). Informational events have a low (low-time-critical) priority.

4.2.3.4 Real-Time Data Link System Design Description

The RTDL system is a master slave system used to broadcast data over a wide area in real time. The RTDL master consists of an encoder module and input modules. IOCs will have access to RTDL broadcasts through the Utility Module. Each input module provides eight data frames of information. A maximum of 256 data frames can be defined. Each data frame is made up of a 8 bit frame ID, a 24 bit data field and an 8 bit CRC. Data is serially transmitted using a bi-phase mark encoding method on a 10 MHz carrier. At this transmission rate, all 256 frames can be transmitted in less than 1.7 ms. The RTDL encoder contains a list of frames to be transmitted. Upon each occurance of an external trigger, all frames contained in the list are sent out. The RTDL is transmitted synchronous with the accumulation cycle before CycleStart. A list of the defined frames is shown below.

Time of day (IOC timestamps)
Ring revolution period (in ps.)
Operating Mode
60 Hz phase difference
Beam Parameters for LEBT chopper
Previous beam pulse data
Data acquisition mode
Beam profile ID
IOC reset address
Section 1Time stamp

A VME module resident in the RTDL chassis receives time of day information from a GPS receiver. At RTDLStart the time will be updated in the RTDL system for broadcast to all receivers. Thus each machine cycle shall have a unique time of day timestamp. For systems requiring a timestamp with greater resolution within a machine cycle, hardware counting at some multiple of the ring revolution frequency shall provide the additional fractional machine cycle component of the time stamp.

Utility Module-Each IOC will contain a utility module. The utility module provides a number of VME chassis services including receiver circuits for the Eventlink and RTDL links. The utility module can be configured to initiate VMEbus interrupts on the detection of specified events. Data transmitted on the RTDL are stored in local memory. One of the RTDL frames provides remote reset of VME chassis. All Utility modules monitor this frame for their remote reset address. When the reset code matching an IOCs utility modules preprogrammed reset address is received, the Utility module asserts the VMEbus SYSRESET/ signal.

4.2.4 Equipment Protection 1 - Beam Permit System (WBS 1.9.2.4)

Three systems will be provided to protect equipment:

- a run permit system
- a beam pulse permit system,
- and a fast proctect system.

The “run permit” system and the ”beam pulse permit” system (both described in this section) verify the operational status of a specified list of equipment and interlocks before allowing the beam to be enabled. They are sensitive to the operating mode of the facility, as the permit chain is dependent upon that mode. Complementing these permit functions, a ”fast protect” system (described in section 4.2.5) will shut off the beam in a matter of microseconds if an anomalous condition-radiation level or equipment failure-is detected. The fast protect system will serve as an essential tuning aid and will be designed to allow quick restoration of the beam once the anomalous condition is corrected.

4.2.4.1 Beam Permit System Scope

The Beam Permit system is made up of two elements - a “Run Permit” function, and a “Beam Pulse Enable” function. The former is a steady-state function which ensures that the accelerator components are in a proper configuration to allow beam running (or other functions such as rf power) for the desired operational mode. The second is a system tied to the timing system which verifies before delivery of each macropulse that the accelerator chain is ready to accept it.

4.2.4.2 Beam Permit System Requirements

The “run permit” system is designed to provide a signal (permit) that will allow the introduction of beam into the accelerator (linac and/or ring). Beam will be enabled only when the linac, ring, target, and experiment equipment, as well as the personnel safety and fast protect systems, are properly configured and operating correctly for a selected operating mode. The run permit system must be aware of the operating mode of the accelerator, because the logic leading to beam permission varies according to the operating mode-for example, which ring(s) and target(s) are on line, whether the beam is to be directed into a tuning line, or whether beam is stopped somewhere at the lowenergy end of the linac. A careful definition of accelerator operating modes is critical to this system.

Note that the primary function of the run permit system is to prohibit beam from being turned on when inappropriate. When the permit chain is broken, beam will be disabled, but this need not necessarily be quick, and other systems (beam pulse enable and fast protect) must be relied upon for rapid shutdown.

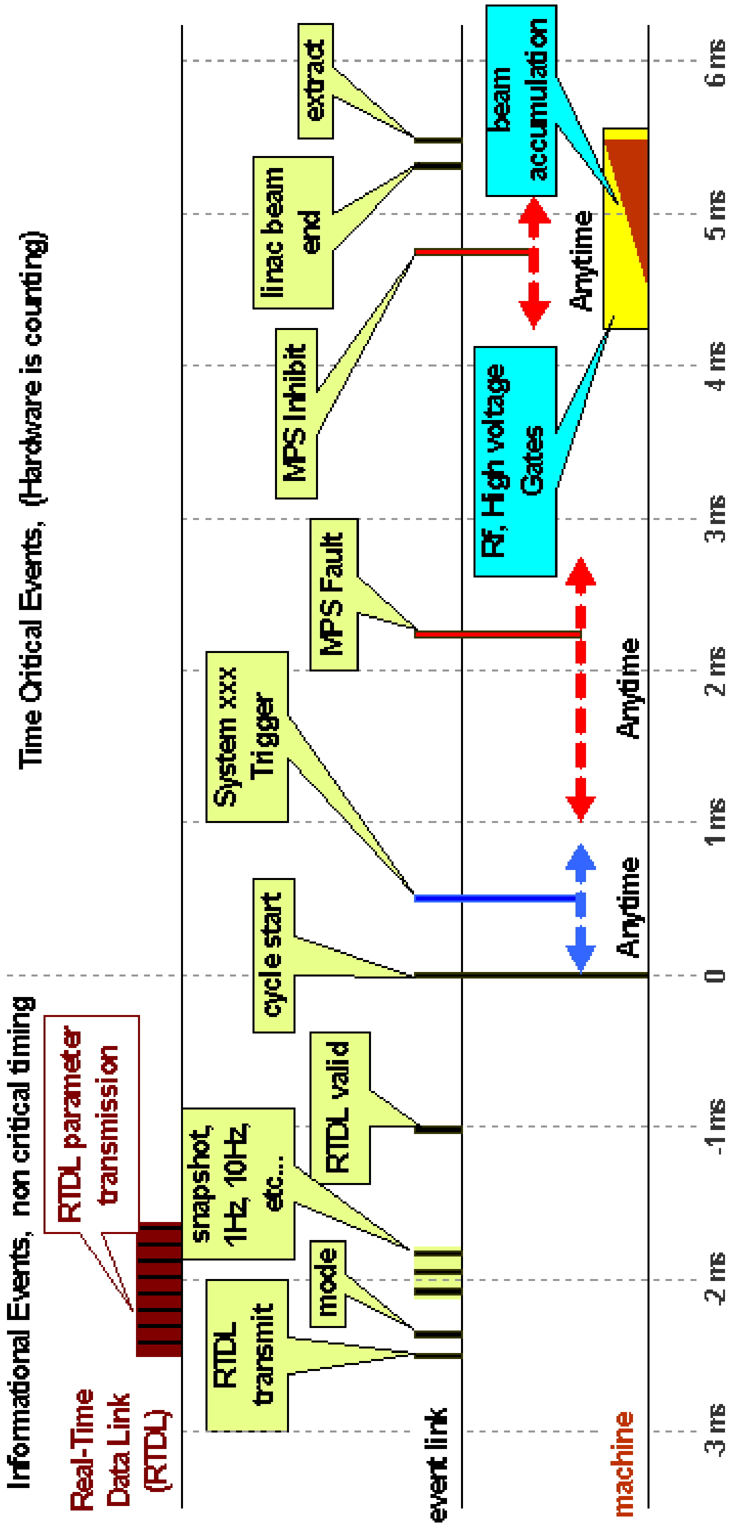

Figure 126: Event Timing.

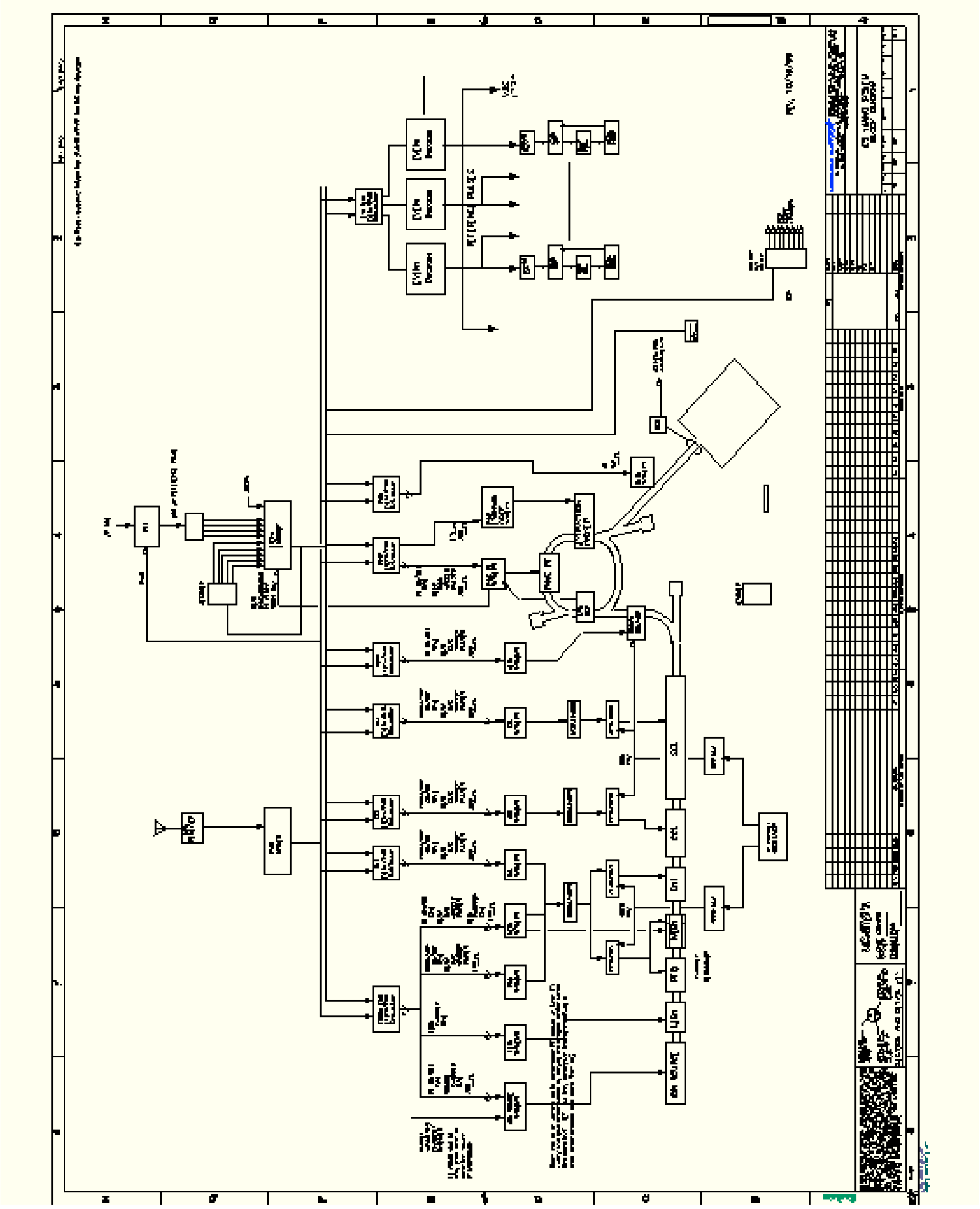

Figure 127: Block Diagram SNS Timing System.

Table 41: Beam Pulse Enable Conditions.

System Monitored	Time BeforeExtraction
Main Ring Magnets	1 msec
Dipole Currents	
Dipole Fields	
Quadrupole Currents	
Ring Injection	
DC Magnets	1 msec
I established in Kickers	500 μs
RF on	100 usecs
Extraction Ready	
Fast Kicker PFN Charged	500 μs
Lambertson Current OK	1 ms
Coupled Injection	Next Pulse
Beam Shape (Quality) delivered to target OK	
RTBT Power Supplies OK	1 ms
Intensity Variation at target	Next Pulse
Vacuum Good	1 ms
Beam Permit System heartbeats	1 msec?
Timing System OK	1 msec?
Damper	
Debuncher	
Loss Monitors NG Signal	Next Pulse
High Loss	Inhibit mid-pulse
Target cooling systems	Next Pulse

The beam pulse enable function verifies that all necessary systems are ready to accept beam before each macropulse. These requirements are given below in Table 41.

4.2.4.3 Beam Permit System Design Description

The logic of the run permit system may be implemented in software and may in fact be a part of the supervisory control system and distributed among the IOCs, although at least some of the logic-that related to personnel access safety-will be implemented independently. The control system will be capable of monitoring and displaying to the operator the status of all signals forming part of the beam permit logic and their logical relationships, so as to show clearly when and why beam is not permitted.

The run permit system is logically distinct from the fast protect system (Sect. 4.2.4), although each may provide an input to the other, and they could in principle use common hardware (although the SNS conceptual design assumes independent systems).

The "Beam Pulse Enable" function is an integral part of the timing system.

4.2.5 Equipment Protection 2 - Fast Protection (WBS 1.9.2.3)

4.2.5.1 Fast Protection System Scope

This system is an independent hardware system which turns off the beam rapidly (~ 10 μsec) when necessary, such as in the case of high radiation levels. It is intended to protect equipment, and is not a personnel safety system.

4.2.5.2 Fast Protection System Requirements

The fast protect system is the complement of the beam permit system. Whereas the beam permit system prevents the beam from being turned on, the purpose of the fast protect system is to turn the beam off. It is designed primarily to protect accelerator equipment by turning off the beam quickly in response to a number of defined events or circumstances. It is also an essential accelerator tuning aid. A response time of a few microseconds is required.

4.2.5.3 Fast Protection System Design Description

This system will be implemented entirely in hardware and will be independent of the main control system, although the main control system must be capable of monitoring the fast protect system, and, in the event of a beam trip, of identifying the originating event or of analyzing a sequence of events. A series of latching registers distributed in IOCs about the plant, designed to fail safe and linked with optical fiber with a carrier frequency, will effect this function. Loss of any input to any one of these registers will result in the carrier's being lost; carrier loss will in turn cause the beam to be turned off because the rf to the ion source and to the RFQ will be turned off in such a way that it can be restored when the offending condition is removed. The carrier and the input latches can be redundant if RAM analysis shows redundancy to be necessary.

In addition to signals from the personnel access safety system and from any equipment whose failure requires rapid beam shutdown, inputs to the fast protect system will include strategically located beam loss monitors (provided by others). Beam loss monitor electronics will interface with the ICS to allow remote setting of operating parameters and to implement testing features. Sensitivity will be automatically adjustable on the basis of accelerator operational parameters. Once operating parameters are downloaded, the monitors will operate independently of the control system. The sources of all of these signals can be redundant if required.

If possible, logic should be excluded from the fast protect system, which, for purposes of reliability, should be as simple as possible. Nonetheless, it may prove necessary to include some simple logic to eliminate spurious trips, which are likely to be frequent.

4.2.6 Control Rooms (WBS 1.9.2.5)

4.2.6.1 Control Room Scope

The control room WBS includes all the equipment - consoles, computers and peripheral devices which are located in the SNS Main Control Room, as well as that equipment located in local control areas.

4.2.6.2 Control Room Requirements

The Main Control Room (MCR) must provide a central location for all SNS operational activities. There must be adequate console space to accommodate commissioning and routine operations of all aspects of the SNS facility. In addition, the capability must be provided for local operations during maintenance and equipment commissioning.

4.2.6.3 Control Room Design Description

Main Control Room (MCR). All major systems will be operated from a single central control room. Personnel safety systems will be monitored from the same room.

The control room will be an open area with a number of consoles distributed around it. Primary consoles will consist of a desktop and several workstation-driven monitors (4- 6) with no more than two keyboards and two interactive devices (mouse or trackball). These consoles will be fully interchangeable. In addition, several secondary consoles (4- 6) consisting of a single workstation and monitor will be available on tables for auxiliary work, development, and monitoring.

If it should be necessary to display analog signals (from oscilloscopes) in the control room, these will be digitized and displayed in ”windows” on the operator screens wherever possible. If needed, accommodation can be made for a small number of racks of analog equipment.

Local Control Rooms. All normal operations will be conducted from the MCR. Nonetheless, during equipment commissioning and maintenance periods, it is frequently necessary to operate equipment and/or subsystems locally, meaning close to the equipment. Both permanent local control rooms and temporary secondary consoles (of the type described in the preceding paragraph) will be available for this purpose. At present it is planned to have permanent local control rooms for the injector, ring, and neutron target areas.

Temporary Consoles. The temporary consoles will be portable and plug into the network as required. There will be no difference in the capability of these remote consoles. Their functionality could be software-limited, but they will appear on the network exactly as main control room consoles, and their users will be in a fully familiar environment. Finally, using a gateway to impose necessary security, permitted external workstations belonging to, for example, off-site physicists, operations managers, beam physicists, or administrators and overseers, will be able to access operator screens and data, again in a familiar environment.

4.2.7 Software Development System (WBS 1.9.2.6)

4.2.7.1 Software Development System Scope

The software development system covers the evolving hardware (computers) and software needed to support software design during design, construction, and operation of SNS. Although some hardware required for operation and construction, such as networking equipment, file servers, and so forth, will be utilized to some extent, this item refers to additional components.

4.2.7.2 Software Development System Requirements

Control hardware will not be available during the initial design and construction phases of SNS. Thus, it will be necessary to have separate and independent systems dedicated to software development at each participating lab. Licenses will be required for some commercial software, such as compilers, operating systems, analysis/design tools, and code management/release tools. The latter has the additional requirement of allowing concurrent, multi-site, shared ("remote") development until the development and maintenance activity is consolidated at the SNS site.

Some type of electronic "groupware" (audio, shared whiteboard, etc) will also greatly enhance the process over and above the use of telephone, travel, and e-mail, particularly for producing design and interface documents.

Software development systems will include the ability to simulate accelerator and conventional facility processes.

4.2.7.3 Software Development System Design Description

Control room equipment may be ordered early and loaned out during this phase. (Although the labs own several types of hardware and software, the requirement for final integration and the need to keep initial maintenance efforts within bounds may preclude use of it.) When software design is completed, the development systems will be consolidated into a single system located at SNS.

The control system portion of the development system will cover operator interfaces, IOCs, and all configuration and archiving services. Although a great deal of functionality is provided with the EPICS tool kit that forms the basis of the control system, some aspects will require new development by SNS.

The simulation hardware will consist of computers (either distributed control system equipment or other types of computers) running dynamic models of plant systems. The actual models will be implemented by specialists from each area; this WBS will supply only the base hardware and software.

4.2.8 Support Computing Systems (WBS 1.9.2.7)

4.2.8.1 Support Computing Systems Scope

This WBS (1.9.2.7) is to support both the hardware and the software for computers which, though not an integral part of the control system, are required to support controls and operational activities.

4.2.8.2 Support Computing Systems Requirements

Support computers should be compatible with control system network protocols and other standards. In general, they will be accessible to the control system through a gateway or router. Some possible examples include:

Data Analysis Engine. A powerful "compute engine" for analysis of beam physics data acquired and possibly archived through the control system.

Database Servers. Several of the databases listed in Section 4.2.8 below (e.g., maintenance database, cable database, machine models) will be in computers not directly connected to the control system network segment, but accessible only through a gateway. These therefore should be considered as separate support systems.

Simulation Engine. Another "compute engine" may be required to support accelerator modeling and simulation. This could become an on-line tool for automation.

4.2.8.3 Support Computing Systems Design Description

The support computers will be commercially available systems generally using commercially available software (e.g. Database management systems) or software available from within the accelerator community (e.g. Accelerator modeling codes). Network connections to these computers are included in WBS 1.9.2.2

4.2.9 Software (System and Application) (WBS 1.9.2.8)

4.2.9.1 Software (System and Application) Scope

System Software. The system software provides the infrastructure into which new devices (at the bottom) and new applications (at the top) can easily be added. This enforces a layered approach to system software design, with the careful design and enforcement of interfaces between the layers. Thus the distributed database described earlier is an essential part of the system software. New devices and their relationships to other devices are implemented at this level.

Application Software. Application software is built onto the infrastructure provided by the system software. Global applications include:

- Operator Monitor and Control.
- Data Acquisition for Accelerator Physics.
- Save and Restore.
- Alarm Management.
- Archiving and Retrieval.
- Automatic Sequencing.
- Closed-Loop Control.
- Mode Control.
- Modeling and Simulation.

Most (but not all) of these applications are available with EPICS. Some - notably modeling and simulation and analysis and display of beam instrumentation data - will be specific to SNS and will have to be developed. Note that while the tools for supervisory operator monitor and control (user interfaces) will be provided by this global WBS (1.9.2.8), specific implementations for individual subsystems belong to the WBS for the control of those subsystems (WBS 1.9.3 - 1.9.8).

4.2.9.2 Software (System and Application) Requirements

Here follows a brief description of the requirements for a number of the globally provided application programs.

- Operator Monitor and Control. The SNS control system will provide the capability for facility operators to monitor and control the status of the facility in a safe and efficient manner. This capability will be available both from a common, central location-the main control room-and, in some circumstances, from locations closer to the subsystems and equipment (local control). In general it will be possible to monitor all facility parameters, but to control only those permitted by the people responsible for the subsystems. Tools will be available to present data in ways that maximize information transfer to the operators (e.g., color, graphics).

- Data Acquisition for Accelerator Physics. The SNS control system will provide a flexible means of acquiring data for analyzing beam behavior to aid understanding of the physics of the accelerator. From provided beam instrumentation, it will be possible to acquire measures of transmission and transverse and longitudinal beam motion, and to correlate these data with each other or with any other machine parameter. It will be possible to acquire these data both synchronously and asynchronously. Tools will be provided for both analysis and visualization of these data and for passing acquired data to off-line programs. A mechanism will be provided to initiate this data acquisition upon operator request and under program control.

- Save and Restore. Both for operational efficiency and for subsequent performance analysis, the SNS control system will provide a facility that saves the operational status of the accelerator and targets and then restores that status on request. As a minimum, this facility will save all relevant (to restoring the beam) set points, although a more sophisticated tool that saves beam properties and tunes the beam to reproduce them may be required. This facility will allow the saving of more than one beam tune and the selection, from a number of possibilities, of the tune to be restored. It will also allow a return to conditions at some marked moment in order to reverse unsuccessful tuning.

- Alarm Management. The SNS control system will provide a sophisticated alarm management system. This system will allow the reporting of various event, alarm, trip, and error conditions, using a severity encoding scheme to ensure appropriate operator response. The alarm system will allow the reporting of alarms hierarchically, to limit the data reported in the (not uncommon) situation of cascading alarms. A method will be provided to determine the root cause of an alarm cascade, and all alarms will be time-stamped to a precision allowing for subsequent event analysis. The system will include a report-generating capability to assist with understanding and analyzing the reliability, availability and maintainability (RAM) performance of the facility. Where possible, the alarm management system will be capable of advising the operator of the appropriate response or of triggering an automated response.

- Archiving and Retrieval. The SNS control system will provide a flexible data archiving and retrieval system. This system will be capable of gathering and storing data either at regular timed intervals, or upon request, or at specified events-possibly simply synchronization events. Data acquisition rates will be variable and operator programmable, with different rates for different parameters as appropriate. The system will be capable of storing large amounts of data for long periods of time. Since the archive is of little use without a sophisticated retrieval system, this system will allow retrieval of archived operational data in time to be useful and will be able to present the retrieved data in several different ways. It will be possible to present retrieved data in formats compatible with on-line visualization and data analysis tools. This archiver is limited to data gathered by the controls system and related to the state and performance of the accelerator, storage ring, and targets. Experimental data are stored by separate experimental data acquisition systems.

- Automatic Sequencing. For increased operational efficiency, and in support of a demanding accelerator availability requirement, the control system will include the capability of automatic sequencing, including decision-making. These sequences could include automatic run-up procedures, automatic fault-recovery sequences, and automatic data-taking routines. The system will provide simple tools for defining sequences as experience is gained and will be capable of monitoring the status of automatic sequences, annunciating problems encountered in sequences, and intervening or overriding sequences if necessary.

- Closed-Loop Control. Autonomous, closed-loop control will be provided for SNS processes. Examples of systems that may require closed loop control include the ion source, various cooling loops, and beam control in the ring and transfer lines. It will be possible to turn these closed loops on and off and to adjust their control parameters.

- Mode Control. SNS will have a number of distinctly different operating modes (e.g. source tuning, linac tuning, ring tuning, neutron production), each with its own set of configuration requirements and permissive conditions. The SNS control system will allow operators to select the desired operating mode, will aid in setting up for operating in this mode, and will automatically apply the proper set of operating permissives for this mode.

- Modeling and Simulation. Accelerators are designed using models. The SNS control system will include the capability for operators to connect with a simulator based on these same accelerator models. The simulator can then be used for exploring “what if” scenarios. The model can also be used to aid understanding of unexpected beam behavior and to suggest corrections. Finally, if required by the operations plan, this simulator could be used to assist with operator training.

In addition to these applications, there will be a number of project databases. Their function is primarily off line, and they are generally linked only loosely to the main control system. Some of the more important of these databases are these:

- Device Database. Sometimes known as the configuration database, this database contains all the information related to the devices and their controllers that are connected to the control system. It includes the location (in control system hardware) of control modules, scanning rates, warning and alarm limits, engineering unit conversions, etc.

This database should be changed as changes to the control system configuration are made, and it should be possible to derive the on-line distributed database automatically from this off-line database. Although there is no such requirement, this database is well-suited to the use of modern object database technology.

- Machine Models. Descriptions of the accelerator used by machine models are contained in databases used during the design phase and need to be accessible to the control system for on-line or off-line modeling.
- Tunes and Archives. The existence of an archiver implies the existence of a database to facilitate accessing of archived data. Those data include machine parameters and beam characteristics as a function of time and of each other. The database must be capable of presenting archived data to control system applications so that the same tools and programs can be used on archived data as on live data. This database is very large, and sophisticated database management tools and retrieval strategies are required to make it useful. The actual size of the on-line retrievable database depends upon operational policy decisions on the amount and frequency of routine data-taking.
- Operations Log. The operations log will be maintained electronically, and the database of log entries must be accessible on-line by date, shift name, operating conditions, and keywords.
- Reliability Statistics. Related to the operations log will be a database of reliability statistics (e.g., trips, errors, beam interruptions, equipment failures) used for analysis of RAM performance of the facility.
- Cable Database. To facilitate maintenance of the control system and other components, a cable database will be maintained. It will contain the physical characteristics, numbers, colors, and routings of all the cables in the installed plant. It needs to be created and used at the time of cable installation and then available online to operators to assist with maintenance and trouble shooting. Many commercial databases are available with this function; their interfaces should be carefully considered for ease of operational integration.
- Maintenance Database. For purposes of increased maintenance efficiency, a database is required which tracks the maintenance history of every electronic module and processor in the control system. Besides manufacturer and serial number, this database will include the maintenance history of each module, its dates of use, where it was installed, failure mode, repair made, etc. The same database should include electronic versions of operator and service manuals for all control system equipment. This database will serve to identify weak components and component types, speed up repair, and anticipate failures. It could also be used as the basis for a preventative maintenance program. It should be available to operators on-line.

An underlying and critical requirement for all of these databases is the existence and use of a common, plantwide naming convention. Such a naming convention for SNS has been established, and is described in the project web page.

4.2.9.3 Software (System and Application) Design Description

System Software. It is at the system software level that the toolkit approach is implemented. The system software for SNS is EPICS. The careful design of interfaces allows the use of tools to construct specific control system applications. Graphical tools are used wherever possible. Tools are available to design and construct operator screens and to connect graphical images of accelerator devices directly and automatically to their corresponding database representations. Likewise, graphical tools are available to construct the hierarchical device database. The operating system on the client side could be such widely-used systems as UNIX or Windows NT. In the IOCs, a real-time kernel (VxWorks) committed to the evolving POSIX standard is used. UNIX is desirable because of its openness. Another possibility is Windows NT, which, though proprietary, is so widely used and broadly supported as to constitute a de facto standard offering the same benefits as openness. The system software also provides a higher-level protocol to connect clients and servers (Channel Access). This protocol provides a fully defined application interface to facilitate the addition of new clients as required, and it will be optimized for performance over the network.

Application Software. In addition to system software, which provides the software infrastructure upon which the control system is built, there is application software, which provides required control system functionality. Two categories of application (client) software can be identified: (1) applications that come with the control system and have been described earlier as required functionality (e.g., the archiver, the alarm manager, the operator interface) and (2) applications that are machine-specific and must be designed and implemented. The latter category includes specific sequences; specific applications of advanced control techniques, such as fuzzy logic or neural networks; closed-loop control implemented either locally in a single IOC or at a higher level; and the use of accelerator models for on- or off-line data analysis. It is the careful design of a uniform, complete, and easy-to-use application program interface (API) that facilitates the implementation of these and other applications. For example, the set of accelerator physics applications (SDDS) and associated tools developed for commissioning the APS at ANL, or the similar applications developed at TJNAF, could be interfaced to the SNS control system for initial commissioning. If required, the well-defined API will permit the interfacing of pre-existing codes written in various computer languages with the control system; however, the use of modern toolkits designed for the purpose will be encouraged.

4.3 Ring Controls

4.3.1 Scope

This section describes the control system for the RING, HEBT and RTBT systems.

4.3.2 Design Requirements

The control system must provide an easy to use operator interface. It must provide data archiving, saving and restoring of setpoints, startup and shutdown sequencing, error handling, notification of alarms and other functions considered standard in a modern control system. It must be able to read and save data at the maximum pulse rate of 60Hz and save the information for analysis on beam dumps. The control system must be able to interface with a variety of equipment to be specified by engineers, collect and analyze large quantities of data and implement control sequences specified by physicists and operators. The control system must provide a suitable environment in which engineers and operators can control the hardware and implement sequencing, monitoring and feedback algorithms. A Beam Permit/Fast Protect system will be used to protect hardware and limit radiation and shutdown the system on serious errors. It will disable injection whenever a hardware error, excess radiation or other unusual conditions are detected. The control system is EPICS based and must meet all the requirements of the ICS in the areas of signal naming, network hardware, timing signals, beam-permit signals, low-level bus and board types, commercial software and workstation types. The control system will be a portion of the Integrated Control System and thus must be compatible with the control software from all labs. The number of IOCs will depend upon several factors: location of hardware, number of channels per IOC, the desire to keep functions separated, or provide redundancy, the development cycle, maintainability and other factors.

4.3.3 Description

This section describes the control system requirements for the Ring, HEBT and RTBT lines. Much of the detailed design and implementation is documented separately in Interface Control Documents (ICDs). Those ICDs will be referenced where applicable rather than repeat the ICD contents in this document. Systems that interface with the control system can be divided into 4 broad categories: Magnet Power Supply systems, Beam Diagnostic Systems, Vacuum systems, and RF systems. Within each broad category exist many subcategories that will each be described in subsequent sections.

4.3.3.1 Magnet Power Supplies

Magnet power supplies for the HEBT, Ring, and RTBT fall into three broad categories. The most common category, called the “standard” power supply, maintains a constant magnetic field during normal operations. Although the setpoint rate is low for the DC supplies, a fast readback rate (>60 Hz) will be needed for the analysis of the cause of beam aborts. The setpoints, state control, and readbacks are all controlled via VMEbus-based Power Supply Controller modules (PSCs), and Power Supply Interface modules (PSIs) which are located near the power supply. The PSC provides 16 bits of resolution for setpoints and readbacks. The second category is the injection ”kicker” magnets, which vary the magnetic field in a controlled fashion during injection (1.2 msecs) in order to paint the beam in phase space for optimal particle distribution. Dedicated function generator and fast readback hardware is needed for this category. The third category is the extraction kickers, which normally have no magnetic field, but which must rise to a predefined level during the 200ns gap in the circulating beam. Unlike the power supplies in the other two categories, power supplies in this category have a voltage setpoint (about 35KV), rather than a current setpoint. The voltage setpoint is accommodated with the PSC/PSI combination of the "standard" configuration. The current in the kicker magnet is determined by characteristics of a Pulse Forming Network (PFN). 200-300 MHz oscilloscopes are needed to monitor the output of the PFNs. The ICD that covers the magnet power supply/controls interface is available as SNS document SNS-10500000-IC0005-R00. Table 42 indicates the number of "standard" power supplies, the number of magnets powered by those supplies and the total number of channels. The number of channels corresponds to the number of process variables in the EPICS database that supports the PSC/PSI combination.

Ramping Power Supplies - The injection "kicker" power supplies use a 10 MHz function generator for the current reference and a 1 MHz ADC to monitor the current and voltage produced by the power supply. Table 43 indicates the number of "ramping" power supplies, the number of channels per supply and the resolution required.

4.3.3.2 Beam Diagnostic Systems

There are many different diagnostic systems. Some systems, such as the Beam Loss Monitor, Beam Profile Monitor, and Beam Current Monitor have a high multiplicity and are spread throughout the facility, including all parts of the LINAC. Other systems, such as the Beam In Gap, Tune, and Ionizing Profile Monitor systems exist as single systems, located only in the ring. Many Diagnostic systems will use an embedded PC, running the Windows operating system, rather than the standard control system VMEbus processor running VxWorks. These embedded PCs are called Network Attached Devices (NADs). The BCM, BPM, laser scanners, and video foil fall in this category. In this case, EPICS will run in a process under Windows, relying on a shared memory interface to provide data, high-resolution timestamps, and synchronization between the Diagnostic software and the EPICS process. The EPICS process is on Windows is referred to as IOC core.

A general-purpose digitizer has been developed for use with a number of diagnostic systems. The digitizer board is in the PCI form factor, compatible with the NAD platform. The digitizer board can host different analog "daughter cards", providing flexible triggering and signal processing capabilities, making the digitizer suitable for a number of different beam-synchronous diagnostic systems.

The control system will provide a number of high-speed (GigaHertz) oscilloscope channels, and multiplexors to provide flexible capability of monitoring a few signals of particular interest remotely, at a higher speed than ordinarily available for those signals. Examples of signals in this category are Beam Position Monitors and Fast Beam Loss Monitors, as well as signals from RF systems. Triggers for these oscilloscopes will be via central timing system trigger modules for beam synchronization.

In addition to the baseline systems listed here, research and development continues on a number of one-of-a-kind diagnostic systems for SNS that could be included in future base-

Table 42: Power Supply Data.

Magnet Type	Polarity	# Supplies	# Magnets	Channels / Supply	Total Channels
HEBT					
Dipole	Unipolar	3	9	55	165
Quadrupole	Unipolar	22	34	55	1210
Corrector	Bipolar	16	16	55	880
Inj. Dump Quadrupole	Unipolar	1	1	55	55
Inj. Dump Corrector	Bipolar	2	2	55	110
Lin. Dump Quadrupole	Unipolar	4	6	55	220
Lin. Dump Corrector	Bipolar	2	2	55	110
Total		50	70		2750
Ring					
Dipole	Unipolar	1	32	55	55
Quadrupole	Unipolar	6	52	55	330
Corrector	Unipolar	104	112	55	5720
Quadrupole	Bipolar	16	52	55	880
Sextupole	Unipolar	4	20	55	220
Chicane	Unipolar	4	4	55	220
Kicker	Unipolar	22	22	55	1210
Septum	Unipolar	3	3	55	165
Total		160	297		8800
RTBT					
Dipole	Unipolar	1	1	55	55
Quadrupole	Unipolar	19	30	55	1045
Corrector	Bipolar	19	19	55	1045
Ext. Dump Quadrupole	Unipolar	2	2	55	110
Total		41	52		2255

Table 43: Ramping Power Supply Data.

Power supply	Bipolar	Resolution bits	Number of magnets	DC	Number of supplies	Channels / supply	Total channels
Ramping supplies	No	13	8	No	8	25	200
Readback waveform (100 kHz digitizer)	No	14	8	No	8	120	192,000 (2 sec)

lines, such as a luminescence monitor, and various schemes for electron cloud detection and mitigation. Every effort will be made to reuse and reconfigure existing infrastructure for such efforts. For instances, a distinct possibility is the use of a solenoid magnet near the injection collimator. The power supply for the solenoid magnet will use the same PSC/PSI interface as other magnet power supplies.

Even among the baseline systems, designs have a tendency to evolve rapidly to embrace new possibilities. Therefore, firm ICDs do not exist for the majority of Diagnostic systems. The following descriptions represent the present designs of the Diagnostic systems.

Laser Scanners - The laser will be stepped into the beam and measurements taken to determine the beam profile. Stepping motors will be used to position the scanners over a range of 5 cm with 0.1 mm resolution. The platform for laser scanner control and monitoring is a NAD. Labview software is used to automate the process of stepping the laser and acquiring the profile. An EPICS interface using the Portable Channel Access Server was used during MEBT commissioning, but an upgrade to IOC core is planned.

Beam Current Monitor - 5 current monitors are planned for HEBT, 1 for the ring, and 5 for RTBT. The platform for the BCM is also a NAD, using the standard PCI digitizer, and a custom analog processing daughter card. Labview software is used for signal processing, and interfacing with EPICS via IOC core.

Beam Position Monitors - 35 position monitors are planned for the HEBT line (and assorted beam dumps). 44 are planned for the ring, and 17 for RTBT. Stripline sensors are used to measure the transverse beam position. Data acquisition and processing are similar to BCM hardware and software, with a somewhat different analog module.

Wall Current Monitors - 2 wall current monitors are planned for the ring, to measure detailed longitudinal structure of the beam. Wall current monitor signals will be digitized using high-speed oscilloscopes.

Collimators - Motor controls are needed to position the movable collimators. The system will have inner and outer limit switches to prevent movement outside of that prescribed, position indicators for error checking, and an ADC to measure position via LVDTs. Accuracy requirements are on the order of 0.1 mm. Four of the collimators will be movable. All collimators will have temperature and water flow monitoring.

The four Ring Collimators will be fixed in position and need no controls except for temperature and flow control monitoring.

Beam Dumps - The Beam Dumps will be instrumented with thermocouples to sense excess heat buildup in the dumps. Each thermocouple channel will have a separate remotely settable temperature threshold. Any thermocouple exceeding the threshold will generate an alarm, and inhibit further beam via the Machine Protect system. The inhibit logic will reside in an Allen-Bradley ControlLogix PLC.

Beam Loss Monitor - The Beam Loss Monitors will monitor beam loss by measuring the radiation at intervals around the ring. There will be about 300 monitors distributed around the ring, in HEBT, and RTBT, and in the LINAC, located at each quad and other points where losses could be high. The Beam Loss Monitors will read the data on each pulse at a 100kHz rate. Digitizers will be synchronized with the pulse via central timing system trigger modules. The IOC will save several seconds worth of data in memory for beam dump analysis when failures occur.

Catastrophic losses, on the order of 1system to inhibit beam production via the Machine Protection System. Thresholds for MPS "trips" will be remotely settable via a DAC module. The IOC will accumulate loss information in order to monitor prolonged beam losses that exceed approximately 1 watt per meter of beamline. Such beam loss might lead to excess activation of beamline components. The sensor high bias voltage will come from either a VMEbus module, or a rack mounted power supply using a DAC output as a reference. BLM gains will be remotely settable, and configuration settings will be remotely readable via TTL I/O signals. Software will be needed to display the beam loss as a function of location around the ring for a particular sample time, the pulse-to-pulse variation in beam loss, and the beam loss versus time.

Fast Beam Loss Monitors - Scintillator-Photomultipliers (12) will be located in critical areas around the ring to give more detailed information on beam loss. Signals from these FBLMs will be captured using the same data acquisition electronics used for BCM and BPM signals. For more detailed information on beam loss, any one of the FBLM signals can be routed through an analog multiplexor to an oscilloscope and sampled at rates up to 1GHZ.

Beam In Gap (BIG) Monitor - Beam is cleaned from the gap during accumulation using kickers that are synchronized to the beam gap. The beam is either collected by the ring collimator, or results in loss throughout the ring. The BIG monitor uses BLMs around the ring to measure the amount of beam cleaned from the gap.

Fractional Tune Measurement - Several techniques are under active investigation for measuring the fractional tune. All involve measuring and analyzing beam motion. Some involve exciting beam motion with a transverse kick. The platform for the analysis is expected to be a DSP or set of DSPs resident on a VMEbus module.

Ionizing Profile Monitoring - This system will determine the horizontal and vertical profile of the beam by measuring the distribution of electrons freed by ionizing collisions of beam with residual gas in the beamline. The electrons are drawn toward a micro-channel plate via a biasing voltage. Electromagnets are used to offset the affect of the electric field. Each sensor measures one plane. A possible future upgrade is a 45-degree sensor. Each plane consists of 72 channels. The signal may be digitized using the standard PCI digitizer, or a VMEbus module to be selected which can measure at least 12 bits at several times per revolution, and be triggered via the central timing system trigger module. A controlled gas leak may be provided to enhance electron production in the early portions of the accumulation cycle, when beam intensity is lowest.

Video Foil - The injection stripping foil will do double-duty as a 2 dimensional profile monitor, or flag. A radiation-hardened video camera will be trained on the stripping foil, and provide image data at 60Hz to a PCI frame grabber. The platform for the video foil will be a NAD, and the controls system interface will be IOC core.

4.3.3.3 Vacuum Systems

The components of the vacuum systems that need controls are given below. Table 44 includes the number of each type of device and an estimate of the number of channels needed per device. The Total Points Logged refers to the number of channels that will be saved to disk periodically. While the configuration for the HEBT, RING and RTBT are different the software and interface hardware is similar for all three systems. An Allen-Bradley ControlLogix

Table 44: Vacuum Data.

Equipment	# Items	# Channels per item	Total channels	Total points logged
HEBT				
Sector Valves	6	3	18	6
Ion Pumps	20	5	100	20
Roughing Pumps	5	8	40	5
Gauges	5	4	20	5
Total	36		188	36
RING				
Sector Valves	8	3	24	8
Ion Pumps	64	5	320	64
RoughingPumps	8	8	64	8
Gauges	16	6	96	16
Total	96		504	96
RTBT				
Sector Valves	6	3	18	6
Ion Pumps	18	5	90	18
Roughing Pumps	5	8	40	0
Gauges	5	6	30	5
Total	34		178	29

5000 PLC is used for valve control. The interface to controls is via Ethernet. The interface to the pumps and gauges will be via multi-drop RS-485. Control screens will display status of vacuum system components as slowly updating comfort displays. The ICD that covers the vacuum/controls interface is available as SNS document SNS-105000000-IC0003-R00.

4.3.3.4 RF Systems

The Ring RF system is used to maintain a well-defined bunch structure with a clean gap to allow for the rise time of the extraction kicker magnet. A dual harmonic system is used. Three of the four cavities operate at the revolution frequency, and one operates at twice the revolution frequency.

The RF system is divided in the low-level system, and the high-level system. The low-level system uses digital electronics to maintain appropriate cavity voltages and frequencies via feedback loops, and provides the reference frequency to the central timing system. The high-level system amplifies these signals to the many kVolt level needed. The low-level system includes DDS modules that produce a reference frequency appropriate for the beam energy and orbit, analog input modules which measure beam position and cavity voltages, analog output modules which correct cavity voltage and frequency, and DSP modules which act as a platform for feedback loops. The control system is used to configure and initialize the modules, as a conduit to download new feedback software to the DSPs, as a conduit to download functions tables, such as turn-by-turn cavity voltage and phase tables, and as a measurement system to allow real-time monitoring of active feedback loops. The controls group will provide application software to edit and download necessary functions to the RF systems DSPs. The control system must also provide mode information to the low-level RF system to support mode-sensitive adaptive learning algorithms. Selected RF signals may be routed to the high-speed oscilloscope used to monitor diagnostic signals. The low-level system also provides a signal to the Machine Protection System to inhibit beam if the RF system is not functioning properly, and provides interlocks to prevent damage to RF equipment, and to minimize power draw. The high-level system consists of tetrode-based power amplifiers (which provide RF gap voltage) and tuning amplifiers (which control the cavity resonant frequency by applying current to the ferrite in the cavity). Control and monitoring of these systems, as well as all necessary interlocks are provided by a single PLC. From this PLC, the control system monitors about 500 I/O points per cavity, and updates control screens at about 1/5 Hz. The ICD that covers the high-level RF/controls interface is available as SNS document SNS-105060100-IC0001-R0A. The ICD for the low-level RF/controls interface is currently under development.

5 Discussions and Options

5.1 Fault Studies

5.2 Operations at a Reduced Beam Energy

5.3 Path to 1.3 GeV Operation

5.4 Upgrades to a Higher Beam Power

6 Appendices

6.1 Parameter Lists

6.1.1 Primary parameters

6.1.2 Magnet parameters

6.1.3 Power-supply parameters

6.1.4 RF system parameters

Table 45: Spallation Neutron Source HEBT, Ring, and RTBT magnet parameters (compiled by M. Hemmer).

Rev. 2002-JUL-29	**Lattice Rev "W2"**		**Fixed magnet parameters**					**1.0 GeV operation**			**1.3 GeV operation**		
Type	**Name**	**No.**	**Core length [cm]**	**Gap** or **aperture [cm]**	**Coils per pole [turns]**	**Magnetic length [cm]**	**Magnet parameter source**	**Dipole int. field [kG*cm]**	**Int. gradient (Note 1)**	**Nominal current [A]**	**Dipole int. field [kG*cm]**	**Int. gradient (Note 1)**	**Nominal current [A]**
DIPOLES	**17D120**	32	124.0	17.0	12	144.1	**Measured**	1115.3		4395	1338.7		5407
	8D406	1	406.4	8.0	12	417.1	CALC	867.6		553	1038.6		666
	8D533	8	532.5	8.0	12	543.2	**Measured**	1108.0		553	1328.0		666
	17D244	1	244.0	17.0	24	267.0	CALC	1788.9		1884	2136.0		2250
Species	*4*	**42**											
CHICANE DIPOLES	**28D74**	1	73.6	28.5	8	102.0	3D Model	244.8		3050	306.0		3800
	24D70	1	70.0	24.8	14	94.0	3D Model	282.0		2168			
	24D48	1	48.0	24.8	14	90.8	3D Model	218.0		1720			
	24D67	1	66.9	24.1	14	91.0	CALC	268.5		2000	327.6		2400
Species	*4*	**4**											
SEPTUMS	**7DS300**	1	300.0	6.8	2	306.4	CALC	622.0		2800	747.6		3420
	7DSG193	1	193.0	7.0	4	200.0	CALC	900.0		2833	1080.0		3400
	17ELS244	1	244.0	16.8	24	267.0	CALC	1788.9		1884	2136.0		2254.7
Species	*3*	**3**											
KICKERS	**20DPH64**	2	64.0	19.6	5	83.0	3D Model	54.8		1028	65.6		1230
	20DPV64	2	64.0	19.6	5	83.0	3D Model	54.8		1028	65.6		1230
	22DPH21	2	21.0	21.5	6	43.0	3D Model	35.7		1225	43.0		1476
	22DPV21	2	21.0	21.5	6	43.0	3D Model	35.7		1225	43.0		1476
	12DPV35	1	35.0	12.0	0.5	40.0	3D Model	10.0		2400	12.0		2400
	14DPV35	2	35.0	14.5	0.5	40.0	3D Model	8.3		2390	10.0		2390
	18DPV46	2	45.5	17.8	0.5	50.5	3D Model	8.6		2400	10.3		2400
	21DPV46	2	45.5	21.1	0.5	50.5	3D Model	7.2		2400	8.7		2400
	16DPV38	4	37.8	16.2	0.5	42.8	3D Model	8.1		2440	9.7		2440
	15DPV34	3	34.0	15.1	0.5	39.0	3D Model	7.9		2440	9.5		2440
Species	*10*	**22**											
QUADRUPOLES	**21Q40**	59	40.0	20.9	28	50.0	**Measured**		23.500	755		28.400	925
	21QT40	–	40.0	20.9	14	50.0	CALC		0.2350	14.0		0.2840	16.5
	26Q40	8	40.0	26.0	44	54.1	3D Model		23.500	705		28.400	909
	26QT40	–	40.0	26.0	31	54.1	CALC		0.5085	20.0		0.5680	25.8
	30Q44	11	44.2	30.0	41	53.3	3D Model		23.985	1025		2.878	1335
	30QT44	–	44.2	30.0	14	53.3	CALC		0.2399	20.5		0.0288	26.7
	30Q58	11	58.0	30.0	41	67.3	3D Model		28.266	950		3.392	1240
	30QT58	–	58.0	30.0	14	67.3	CALC		0.2827	19.0		0.0339	24.8
	12Q45	32	44.5	12.0	20	50.0	**Measured**		30.000	464		36.000	570
	12QT45	–	44.5	12.0	11	50.0	Measured		0.300	4.6		0.3600	5.7
	36Q85	4	85.1	36.2	39	102.0	3D Model		26.204	845		30.994	1025
Species	*6*	**125**											
CORRECTORS	**21CS26**	8	26.0	21.0	300	35.4	**Measured**		0.600	10.00		0.731	12.1
	21CO26	8	26.0	21.0	292	33.0	**Measured**		0.108	8.40		0.129	10.0
	27CDH30	9	30.0	27.0	216	54.5	CALC	8.60		10.4	10.8		13.0
	27CDV30	10	30.0	27.0	216	54.5	CALC	8.60		10.4	10.8		13.0
	27CDHM30	8	30.0	28.0	240	58.5	**Measured**	6.88		10.0	8.60		13.0
	27CDVM30	20	30.0	28.0	240	58.5	**Measured**	6.84		10.0	8.56		13.0
	27CDMSQ30	–	30.0	28.0	183	44.9	**Measured**		0.2220	10.0		0.2770	13.0
	27CDMSS30	–	30.0	28.0	54	44.5	**Measured**		0.00520	10.0		0.00650	13.0
	36CDM30	8	30.0	34.0	245	61.8	CALC	7.20		10.2	9.0		12.7
	36CDMSQ30	–	30.0	34.0	282	47.8	CALC		0.2660	10.2		0.3330	12.7
	41CDM30DS	9	30.0	40.0	335	67.3	CALC	7.50		10.2	9.4		12.7
	41CDM30DD	–	30.0	40.0	335	67.3	CALC	7.50		10.2	9.4		12.7
	41CDMSQ30	–	30.0	40.0	374	50.2	CALC		0.2410	10.2		0.3010	12.7
	16CDH20	7	20.0	16.0	315	33.0	**Measured**	7.00		9.0	8.4		10.8
	16CDV20	7	20.0	16.0	315	33.0	**Measured**	7.00		9.0	8.4		10.8
	36CDHR30	2	29.8	36.5	43	68.0	CALC	7.20		92.0	8.6		110
	36CDVR30	–	29.8	36.5	43	68.0	CALC	7.20		92.0	8.6		110
Species	*11*	**96**											
SEXTUPOLES	**21S26**	12	26.0	21.0	21	31.7	CALC		25.541	121		30.594	145
	26S26	8	26.0	26.2	23	33.0	CALC		17.157	140		20.549	168
Species	*2*	**20**											
Total	40 species	312	Note 1: units are kG, kG/cm, and kG/cm^2 for quadrupole, sextupole, and octupole, respectively										

6.2 Optics Files

6.2.1 HEBT Optics File

```
" SNS High Energy Beam Transport"
0 ;
PRINT, REFER ;
PRINT, BEAM, ON       ;
PRINT, TRANS, ON ;
PRINT, ACCEL, ON ;
PRINT, ONELINE   ;
QL1:=0.2500 ;
QL2:=0.5000 ;
QAR:=10.00 ;
16 16 0.0 ;
16 17 0.0;
16 18 0.0 ;
16 19 0.0 ;
16 20 0.0 ;
-13 12 ;
PLOT, ZFLOOR, XFLOOR ;
BM: BEAM.0000,BETAX=1.3453,ALPHAX=0.0,BETAY=0.2377,ALPHAY=0.000,P0=-1.6960 ;
STORE, BX0=BETAX;
STORE, BY0=BETAY;
STORE, AX0=ALPHAX;
STORE, AY0=ALPHAY;
Q01:  QUAD.00, L=QL1, B=-4.17887, APER=QAR ;
LA4:  DRIFT,   L=3.5 ;
Q02:  QUAD.00, L=QL2, B=4.17887, APER=QAR ;
FLA4:  DRIFT,  L=3.5 ;
Q03:  QUAD.00, L=QL2, B=-4.17887, APER=QAR ;
LA5:  DRIFT,   L=3.5 ;
Q04:  QUAD.00, L=QL2, B=4.17887, APER=QAR ;
LA6:  DRIFT,   L=3.5 ;
Q05:  QUAD.00, L=QL2, B=-3.56650, APER=QAR ;
LA3:  DRIFT,   L=3.5 ;
Q06:  QUAD.00, L=QL2, B=3.13568, APER=QAR ;
LA4:  DRIFT,   L= 3.5;
Q07:  QUAD.00, L=QL2, B=-3.02585, APER=QAR ;
LA5:  DRIFT,   L=3.5;
Q08:  QUAD.00, L=QL1, B=2.85933, APER=QAR ;
Q08:  QUAD.00, L=QL1, B=2.17254, APER=QAR ;
LL3:  DRIFT,   L=1.00,
DR3:  ROTAT,  ANGLE=0.0 ;
DD2:  BEND,   L=5.0, ANGLE=15.0 ;
DR4:  ROTAT,  ANGLE=0.0 ;
LL4:  DRIFT,   L=0.5,
Q09:  QUAD.00, L=QL1, B=-2.19453, APER=QAR ;
Q09:  QUAD.00, L=QL1, B=-2.19453 , APER=QAR ;
LL1:  DRIFT,   L=1.00 ;
DR1:  ROTAT,  ANGLE=0.0 ;
DD1:  BEND,   L=5.0, ANGLE= 15.0 ;
DR2:  ROTAT,  ANGLE=0.0 ;
LL2:  DRIFT,   L=0.50,
Q10:  QUAD.00,  L=QL1, B=2.17254, APER=QAR ;
Q10:  QUAD.00,  L=QL1, B=2.17254, APER=QAR ;
LL3:  DRIFT,   L=1.00,
DR3:  ROTAT,  ANGLE=0.0 ;
DD2:  BEND,   L=5.0, ANGLE=15.0 ;
DR4:  ROTAT,  ANGLE=0.0 ;
LL4:  DRIFT,   L=0.5,
Q11:  QUAD.00, L=QL1, B=-2.23260, APER=QAR ;
Q11:  QUAD.00, L=QL1, B=-2.23260, APER=QAR ;
LL1:  DRIFT,   L=6.50 ;
Q12:  QUAD.00,  L=QL2, B=2.17254, APER=QAR ;
LL3:  DRIFT,   L=1.00,
```

```
DR3:  ROTAT,  ANGLE=0.0 ;
DD2:  BEND,   L=5.0, ANGLE=15.0 ;
DR4:  ROTAT,  ANGLE=0.0 ;
LL4:  DRIFT,   L=0.5,
Q13:  QUAD.00, L=QL1, B=-2.19453, APER=QAR ;
Q13:  QUAD.00, L=QL1, B=-2.19453 , APER=QAR ;
LL1:  DRIFT,   L=1.00 ;
DR1:  ROTAT,  ANGLE=0.0 ;
DD1:  BEND,   L=5.0, ANGLE= 15.0 ;
DR2:  ROTAT,  ANGLE=0.0 ;
LL2:  DRIFT,   L=0.50,
Q14:  QUAD.00,  L=QL2, B=2.17254, APER=QAR ;
LL3:  DRIFT,   L=1.00,
DR3:  ROTAT,  ANGLE=0.0 ;
DD2:  BEND,   L=5.0, ANGLE=15.0 ;
DR4:  ROTAT,  ANGLE=0.0 ;
-10 -1 6 0.0 0.0001;
-10 -2 6 0.0 0.0001;
LL4:  DRIFT,   L=0.5,
Q15:  QUAD.00, L=QL1, B=-2.19453, APER=QAR ;
Q15:  QUAD.00, L=QL1, B=-2.19453, APER=QAR ;
LLQ:  DRIFT.1, L=3.5 ;
Q16:  QUAD.01,  L=QL2, B=3.04737, APER=QAR ;
LLQ:  DRIFT, L=3.5 ;
Q17:  QUAD.01  L=QL2, B=-2.80288,  APER=QAR;
LLR:  DRIFT, L=3.5 ;
Q18:  QUAD.01  L=QL2, B=3.06842,   APER=QAR;
LLS:  DRIFT, L=3.5 ;
Q19:  QUAD.01  L=QL2, B=-3.52617,  APER=QAR;
LBR:  DRIFT.1, L=3.5 ;
Q20:  QUAD.0B  L=QL1, B=2.87258,   APER=QAR;
Q20:  QUAD.0B  L=QL1, B=2.87258,   APER=QAR;
LLU:  DRIFT, L=0.5 ;
DRP:  ROTAT,  ANGLE=0.0 ;
DD7:  BEND, L=2.5, ANGLE=7.5 ;
DRQ:  ROTAT,  ANGLE=0.0 ;
LLV:  DRIFT, L=1.0 ;
Q21:  QUAD.0A, L=QL2, B=-3.53749, APER=QAR;
LLX:  DRIFT, L=3.5 ;
Q22:  QUAD.0B  L=QL2, B=2.87258 , APER=QAR ;
LLY:  DRIFT, L=3.5 ;
Q23:  QUAD.0A, L=QL2, B=-3.53749 , APER=QAR ;
LLZ:  DRIFT, L=3.5 ;
Q24:  QUAD.0B  L=QL2, B=2.87258, APER=QAR ;
LAA:  DRIFT, L=3.5 ;
Q25:  QUAD.01, L=QL2, B=-4.61742 , APER=QAR ;
LAB:  DRIFT, L=3.5 ;
Q26:  QUAD.0B  L=QL2,B=2.87258, APER=QAR ;
LAC:  DRIFT, L=3.5 ;
Q27:  QUAD.0A, L=QL2, B=-3.53749 , APER=QAR ;
LAD:  DRIFT, L=2.224 ;
DRV:  ROTAT,  ANGLE=0.0 ;
DDG:  BEND, L=0.776, ANGLE=+1.983618363 ;
DRW:  ROTAT,  ANGLE=0.0 ;
LAE:  DRIFT, L=0.5 ;
Q28:  QUAD.01 L=QL2, B=5.22345 , APER=QAR;
LAF:  DRIFT, L=0.5 ;
Q29:  QUAD.01 L=QL2, B=-4.78283 , APER=QAR;
LAF:  DRIFT, L=1.25 ;
DRT:  ROTAT,  ANGLE=0.0 ;
DDF:  BEND, L=2.50000, ANGLE=-7.597420363 ;
DRU:  ROTAT,  ANGLE=0.0 ;
LAG:  DRIFT, L=0.3389 ;
DRV:  ROTAT,  ANGLE=0.0 ;
DDG:  BEND, L=0.776, ANGLE=-1.886198 ;
DRW:  ROTAT,  ANGLE=0.0 ;
```

```
L5H:  DRIFT, L=0.0
10 -1 6  .0 0.001;
10 -2 6  .0 0.001 ;
FPBT: FIT, BETAX=0.5350,TOLER=0.001 ;
FPB1: FIT, ALPHAX=0.085, TOLER=0.001 ;
FPB2: FIT, BETAY=0.888,TOLER=0.001 ;
FPB3: FIT, ALPHAY=0.05,TOLER=0.001 ;
SENTINEL
SENTINEL

FPBT: FIT, BETAX=0.4645,TOLER=0.001 ;
FPB1: FIT, ALPHAX=0.0973, TOLER=0.001 ;
FPB2: FIT, BETAY=2.3202,TOLER=0.001 ;
FPB3: FIT, ALPHAY=-0.1216,TOLER=0.001 ;

FPBT: FIT, BETAX=0.5452,TOLER=0.001 ;
FPB1: FIT, ALPHAX=-0.7312, TOLER=0.001 ;
FPB2: FIT, BETAY=1.2456,TOLER=0.001 ;
FPB3: FIT, ALPHAY=1.6109,TOLER=0.001;
DRP:  ROTAT,  ANGLE=0.0 ;
DD7:  BEND, L=2.5, ANGLE=7.5 ;
DRQ:  ROTAT,  ANGLE=0.0 ;
LLV:  DRIFT, L=0.5 ;
Q22:  QUAD.0A, L=QL2, B=-4.17887, APER=QAR;
LLX:  DRIFT, L=3.5 ;
Q23:  QUAD.0B  L=QL2, B=4.17887 , APER=QAR ;
LLY:  DRIFT, L=3.5 ;
Q24:  QUAD.0A, L=QL2, B=-4.17887 , APER=QAR ;
LLZ:  DRIFT, L=3.5 ;
Q25:  QUAD.0B  L=QL2, B=4.17887, APER=QAR ;
LAA:  DRIFT, L=3.5 ;
Q26:  QUAD.01, L=QL2, B=-4.17887 , APER=QAR ;
LAB:  DRIFT, L=3.5 ;
Q27:  QUAD.0B  L=QL2,B=4.17887, APER=QAR ;
LAC:  DRIFT, L=3.5 ;
Q28:  QUAD.0A, L=QL2, B=-4.17887 , APER=QAR ;
LAD:  DRIFT, L=2.224 ;
DRV:  ROTAT,  ANGLE=0.0 ;
DDG:  BEND, L=0.776, ANGLE=+1.983618363 ;
DRW:  ROTAT,  ANGLE=0.0 ;
LAE:  DRIFT, L=0.5 ;
Q29:  QUAD.0B L=QL2, B=4.17887 , APER=QAR;
LAF:  DRIFT, L=0.5 ;
DRT:  ROTAT,  ANGLE=0.0 ;
DDF:  BEND, L=2.50000, ANGLE=-7.597420363 ;
DRU:  ROTAT,  ANGLE=0.0 ;
LAG:  DRIFT, L=0.3389 ;
DRV:  ROTAT,  ANGLE=0.0 ;
DDG:  BEND, L=0.776, ANGLE=-1.886198 ;
DRW:  ROTAT,  ANGLE=0.0 ;
L5H:  DRIFT, L=0.0
10 -1 6  .28137 0.001;
10 -2 6  .02921 0.001 ;
FPBT: FIT, BETAX=1.569,TOLER=0.001 ;
FPB1: FIT, ALPHAX=-1.955, TOLER=0.001 ;
FPB2: FIT, BETAY=0.5162,TOLER=0.001 ;
FPB3: FIT, ALPHAY=0.7762,TOLER=0.001 ;
SENTINEL
SENTINEL

FPX1:FIT, NAME=BETAX-BY0, VALUE=0.0, TOLER=0.001;
FPX2:FIT, NAME=BETAY-BX0, VALUE=0.0, TOLER=0.001;
FPX3:FIT, NAME=ALPHAX-AY0, VALUE=0.0, TOLER=0.001;
FPX4:FIT, NAME=ALPHAY-AX0, VALUE=0.0, TOLER=0.001;
SENTINEL
SENTINEL
```

```
LL5:  DRIFT,   L=0.50 ;
DR5:  ROTAT,  ANGLE=0.0 ;
DD3:  BEND,   L=1.850, ANGLE= 5.625 ;
DR6:  ROTAT,  ANGLE=0.0 ;
LL6:  DRIFT,   L=3.50,
Q11:  QUAD.0B,  L=QL2, B=2.5780, APER=QAR ;
LLD:  DRIFT,   L=0.5 ;
DRD:  ROTAT,  ANGLE=0.0 ;
DD4:  BEND,   L=1.85, ANGLE= 5.625 ;
DRE:  ROTAT,  ANGLE=0.0 ;
LLE:  DRIFT,   L=3.50,
Q15:  QUAD.0A,  L=QL2, B=-2.52872, APER=QAR ;
LLF:  DRIFT,   L=0.50,
DRF:  ROTAT,  ANGLE=0.0 ;
DD5:  BEND,   L=1.85, ANGLE=5.625 ;
DRG:  ROTAT,  ANGLE=0.0 ;
LLG:  DRIFT,   L=3.50,
Q16:  QUAD.0B, L=QL2, B=2.5780, APER=QAR ;
LLH:  DRIFT,   L=0.5 ;
DRH:  ROTAT,  ANGLE=0.0 ;
DD6:  BEND,   L=1.85, ANGLE=5.626;
DRI:  ROTAT,  ANGLE=0.0 ;
LLI:  DRIFT,    L=3.50;
Q15:  QUAD.0A,  L=QL2, B=-2.52872, APER=QAR ;
LLF:  DRIFT,   L=0.50,
DRF:  ROTAT,  ANGLE=0.0 ;
DD5:  BEND,   L=1.85, ANGLE=5.625 ;
DRG:  ROTAT,  ANGLE=0.0 ;
LLG:  DRIFT,   L=3.50,
Q16:  QUAD.0B, L=QL2, B=2.5780, APER=QAR ;
LLH:  DRIFT,   L=0.5 ;
DRH:  ROTAT,  ANGLE=0.0 ;
DD6:  BEND,   L=1.85, ANGLE= 5.625;
DRI:  ROTAT,  ANGLE=0.0 ;
LLI:  DRIFT,   L=3.50,
Q17:  QUAD.0A,  L=QL1, B=-2.52872, APER=QAR ;
10 -1 6 0.0 0.0001;
10 -2 6 0.0 0.0001;
FPX1:FIT, NAME=BETAX-BX0, VALUE=0.0, TOLER=0.001;
FPX2:FIT, NAME=BETAY-BY0, VALUE=0.0, TOLER=0.001;
FPX3:FIT, NAME=ALPHAX-AX0, VALUE=0.0, TOLER=0.001;
FPX4:FIT, NAME=ALPHAY-AY0, VALUE=0.0, TOLER=0.001;
SENTINEL
SENTINEL
Q17:  QUAD.00,  L=QL1, B=3.91019, APER=QAR ;
LLQ:  DRIFT, L=3.5 ;
Q18:  QUAD.01  L=QL2, B=-3.09694,  APER=QAR;
LLR:  DRIFT, L=3.5 ;
Q19:  QUAD.01  L=QL2, B=3.08200,   APER=QAR;
LLS:  DRIFT, L=3.5 ;
Q20:  QUAD.01  L=QL2, B=-3.07567,  APER=QAR;
LBR:  DRIFT, L=3.5 ;
Q21:  QUAD.01  L=QL2, B=3.97382,   APER=QAR;
FPBT: FIT, BETAX=0.4452,TOLER=0.001 ;
FPB1: FIT, ALPHAX=-0.7312, TOLER=0.001 ;
FPB2: FIT, BETAY=1.2456,TOLER=0.001 ;
FPB3: FIT, ALPHAY=1.6109,TOLER=0.001 ;
LLU:  DRIFT, L=0.5 ;
DRP:  ROTAT,  ANGLE=0.0 ;
DD7:  BEND, L=3.5, ANGLE=5.625 ;
DRQ:  ROTAT,  ANGLE=0.0 ;
LLV:  DRIFT, L=0.5 ;
Q22:  QUAD.0A, L=QL2, B=-3.95374, APER=QAR;
LLX:  DRIFT, L=3.5 ;
Q23:  QUAD.0B  L=QL2, B=3.11428 , APER=QAR ;
LLY:  DRIFT, L=3.5 ;
```

```
Q24:  QUAD.0A, L=QL2, B=-3.95374 , APER=QAR ;
LLZ:  DRIFT, L=3.5 ;
Q25:  QUAD.0B  L=QL2, B=3.11428, APER=QAR ;
LAA:  DRIFT, L=3.5 ;
Q26:  QUAD.0A, L=QL2, B=-3.95374 , APER=QAR ;
LAB:  DRIFT, L=3.5 ;
Q27:  QUAD.0B  L=QL2,B=3.11428, APER=QAR ;
LAC:  DRIFT, L=3.5 ;
Q28:  QUAD.0A, L=QL2, B=-3.95374 , APER=QAR ;
LAD:  DRIFT, L=3.224 ;
DRV:  ROTAT,  ANGLE=0.0 ;
DDG:  BEND, L=0.776, ANGLE=+1.983618363 ;
DRW:  ROTAT,  ANGLE=0.0 ;
LAE:  DRIFT, L=0.5 ;
Q29:  QUAD.0B L=QL2, B=3.11428 , APER=QAR;
LAF:  DRIFT, L=0.5 ;
DRT:  ROTAT,  ANGLE=0.0 ;
DDF:  BEND, L=3.50000, ANGLE=-7.597420363 ;
DRU:  ROTAT,  ANGLE=0.0 ;
LAG:  DRIFT, L=0.3389 ;
DRV:  ROTAT,  ANGLE=0.0 ;
DDG:  BEND, L=0.776, ANGLE=-1.886198 ;
DRW:  ROTAT,  ANGLE=0.0 ;
L5H:  DRIFT, L=0.0
10 -1 6  .28137 0.001;
10 -2 6  .02921 0.001 ;
FPBT: FIT, BETAX=1.569,TOLER=0.001 ;
FPB1: FIT, ALPHAX=-1.955, TOLER=0.001 ;
FPB2: FIT, BETAY=0.5162,TOLER=0.001 ;
FPB3: FIT, ALPHAY=0.7762,TOLER=0.001 ;
SENTINEL
SENTINEL

Q11:  QUAD.00,  L=QL1, B=3.95881, APER=QAR ;
LL8:  DRIFT,   L=3.50,
Q12:  QUAD.00, L=QL2, B=-3.96258,, APER=QAR ;
LLA:  DRIFT,   L=3.50;
Q13:  QUAD.00,  L=QL2, B=3.95881,, APER=QAR ;
LLC:  DRIFT,   L=3.50,
Q14:  QUAD.00, L=QL1, B=-3.96258,, APER=QAR ;
Q14:  QUAD.00, L=QL1, B=-3.83355 ,, APER=QAR ;

FIT , NAME=BETAX-BX0, VALUE=0.0, TOLER=0.001 ;
FIT , NAME=BETAY-BY0, VALUE=0.0, TOLER=0.001 ;
FIT , NAME=ALPHAX-AX0, VALUE=0.0, TOLER=0.001 ;
FIT , NAME=ALPHAY-AY0, VALUE=0.0, TOLER=0.001 ;
FPX1: FIT -11 2. 0.25 0.00001 ;
FPY1: FIT -13 4. 0.25 0.00001 ;
SENTINEL
BM: BEAM.0000,BETAX=1.3039,ALPHAX=0.2124,BETAY=0.3889,ALPHAY=-0.2229,P0=-1.6960
linc beam

BM: BEAM.1111,BETAX=0.2377,ALPHAX=0.0,BETAY=1.3453,ALPHAY=0.000,P0=-1.6960 ;
STORE, BX0=BETAX;
STORE, BY0=BETAY;
STORE, AX0=ALPHAX;
STORE, AY0=ALPHAY;
Q01:  QUAD.0A, L=QL1, B=4.17887, APER=QAR ;
FLA4:  DRIFT,  L=3.5 ;
Q02:  QUAD.0B, L=QL2, B=-4.17887, APER=QAR ;
LA5:  DRIFT,   L=3.5 ;
Q03:  QUAD.0A, L=QL1, B=4.17754, APER=QAR ;
FIT , NAME=BETAX-BX0, VALUE=0.0, TOLER=0.001 ;
FIT , NAME=BETAY-BY0, VALUE=0.0, TOLER=0.001 ;
FIT , NAME=ALPHAX-AX0, VALUE=0.0, TOLER=0.001 ;
FIT , NAME=ALPHAY-AY0, VALUE=0.0, TOLER=0.001 ;
```

```
FPX1: FIT -11 2. 0.25 0.00001 ;
FPY1: FIT -13 4. 0.25 0.00001 ;
SENTINEL
SENTINEL

FPBT: FIT, BETAX=0.4256,TOLER=0.001 ;
FPB1: FIT, ALPHAX=-0.0581, TOLER=0.001 ;
FPB2: FIT, BETAY=1.2045,TOLER=0.001 ;
FPB3: FIT, ALPHAY=-0.0571,TOLER=0.001
before dogleg

FPBT: FIT, BETAX=0.4645,TOLER=0.001 ;
FPB1: FIT, ALPHAX=0.0973, TOLER=0.001 ;
FPB2: FIT, BETAY=2.3202,TOLER=0.001 ;
FPB3: FIT, ALPHAY=-0.1216,TOLER=0.001 ;
before achromat
```

6.2.2 Ring Optics File

```
!***********************************************
!*      Spallation Neutron Source
!*      1.3 GeV  Compatible Accumulator Ring Lattice
!*      18 October 2000
!*      Created by Kip GARDNER
!***********************************************
!* Missing elements:
! - Skew quadrupole correctors
! - Skew sextupole correctors
! - Collimators
! - Extraction kickers
! - RF cavities
! - Magnet Errors
!* Elements to be reviewed:
! - Magnetic lengths of all elements, reflecting magnet models/measurements
! - New values for kicks in injection chicane and bumps
!
!* List compiled by Y.Papaphilippou 02/2002
!-----------------------------------------------------------
! Bending Magnets (32, each split into left and right half)
! Magnetic length changed by Y.Papaphilippou 08/2001
!-----------------------------------------------------------
  ANG:= 2*PI/32
  EE := ANG/2
  LBEND := 1.4342
  BL:  Sbend, L=LBEND/2, Angle=EE, E1=0., E2=0.
  BR:  Sbend, L=LBEND/2, Angle=EE, E1=0., E2=0.
  BND: Sbend, L=LBEND, Angle=ANG, E1=0.0, E2=0.0
  RHOB:=LBEND/ANG ; Value RHOB
  BBND:=Brho/RHOB ; Value BBND
!-----------------------------------------------------------
! Initial Quad Strengths (for matching)
!-----------------------------------------------------------
   KF:= 3.882808E+00
   KD:=-4.123195E+00
  KDE:=-2.00
  KDC:=-4.00
  KFC:= 4.00
 KDEE:=0.5*(KDE+KD)
!-----------------------------------------------------------
 KVX1:=KDEE
 KHX2:=KF
 KVX3:=KD
 KHX4:=KF
 KVX5:=KD
 KHX6:=KF
 KVX7:=KD
 KHX8:=KF
 KVX9:=KDEE
 KHX10:=KFC
 KVX11:=KDC
 KVX12:=KDC
 KHX13:=KFC
!-----------------------------------------------------------
! Initial Sextupole and Octupole Strengths
!-----------------------------------------------------------
 CHRM3:=0.0
 CHRM4:=0.0
 CHRM5:=0.0
 CHRM6:=0.0
 CHRM7:=CHRM3
 KSVX1:=0.0
 KSHX2:=0.0
 KSV3:=CHRM3
```

```
 KSH4:=CHRM4
 KSV5:=CHRM5
 KSH6:=CHRM6
 KSV7:=CHRM7
 KOH8:=0.0
 KOV9:=0.0
!-------------------------------------------------------------
! Generic Half-Quads
!-------------------------------------------------------------
   LF:=0.25
   LD:=0.25
  LDE:=0.25
 LDEE:=0.25
!-------------------------------------------------------------
! New quad lengths: Jeff Holmes, 10/2000
!-------------------------------------------------------------
  LDC:=0.275
  LFC:=0.35
!-------------------------------------------------------------
   QF:  Quad,  L=LF,   K1=KF/Brho
   QD:  Quad,  L=LD,   K1=KD/Brho
  QDE:  Quad,  L=LDE,  K1=KDE/Brho
 QDEE:  Quad,  L=LDEE, K1=KDEE/Brho
  QDC:  Quad,  L=LDC,  K1=KDC/Brho
  QFC:  Quad,  L=LFC,  K1=KFC/Brho
!-------------------------------------------------------------
! Generic Whole-Quads
!-------------------------------------------------------------
   LLF:=2.0*LF
   LLD:=2.0*LD
 LLDEE:=2.0*LDEE
  LLDC:=2.0*LDC
  LLFC:=2.0*LFC
   QQF:  Quad,  L=LLF,   K1=KF/Brho
   QQD:  Quad,  L=LLD,   K1=KD/Brho
 QQDEE:  Quad,  L=LLDEE, K1=KDEE/Brho
  QQDC:  Quad,  L=LLDC,  K1=KDC/Brho
  QQFC:  Quad,  L=LLFC,  K1=KFC/Brho
!-------------------------------------------------------------
! Individual Whole-Quads
!-------------------------------------------------------------
  QVX1:  Quad,  L=LLD,   K1=KVX1/Brho
  QHX2:  Quad,  L=LLF,   K1=KHX2/Brho
  QVX3:  Quad,  L=LLD,   K1=KVX3/Brho
  QHX4:  Quad,  L=LLF,   K1=KHX4/Brho
  QVX5:  Quad,  L=LLD,   K1=KVX5/Brho
  QHX6:  Quad,  L=LLF,   K1=KHX6/Brho
  QVX7:  Quad,  L=LLD,   K1=KVX7/Brho
  QHX8:  Quad,  L=LLF,   K1=KHX8/Brho
  QVX9:  Quad,  L=LLDEE, K1=KVX9/Brho
  QHX10: Quad,  L=LLFC,  K1=KHX10/Brho
  QVX11: Quad,  L=LLDC,  K1=KVX11/Brho
  QVX12: Quad,  L=LLDC,  K1=KVX12/Brho
  QHX13: Quad,  L=LLFC,  K1=KHX13/Brho
!
  QVA1:  Quad,  L=LLD,   K1=KVX1/Brho
  QHA2:  Quad,  L=LLF,   K1=KHX2/Brho
  QVA3:  Quad,  L=LLD,   K1=KVX3/Brho
  QHA4:  Quad,  L=LLF,   K1=KHX4/Brho
  QVA5:  Quad,  L=LLD,   K1=KVX5/Brho
  QHA6:  Quad,  L=LLF,   K1=KHX6/Brho
  QVA7:  Quad,  L=LLD,   K1=KVX7/Brho
  QHA8:  Quad,  L=LLF,   K1=KHX8/Brho
  QVA9:  Quad,  L=LLDEE, K1=KVX9/Brho
  QHA10: Quad,  L=LLFC,  K1=KHX10/Brho
  QVA11: Quad,  L=LLDC,  K1=KVX11/Brho
```

```
  QVA12: Quad,  L=LLDC,  K1=KVX12/Brho
  QHA13: Quad,  L=LLFC,  K1=KHX13/Brho
!
  QVB1:  Quad,  L=LLD,   K1=KVX1/Brho
  QHB2:  Quad,  L=LLF,   K1=KHX2/Brho
  QVB3:  Quad,  L=LLD,   K1=KVX3/Brho
  QHB4:  Quad,  L=LLF,   K1=KHX4/Brho
  QVB5:  Quad,  L=LLD,   K1=KVX5/Brho
  QHB6:  Quad,  L=LLF,   K1=KHX6/Brho
  QVB7:  Quad,  L=LLD,   K1=KVX7/Brho
  QHB8:  Quad,  L=LLF,   K1=KHX8/Brho
  QVB9:  Quad,  L=LLDEE, K1=KVX9/Brho
  QHB10: Quad,  L=LLFC,  K1=KHX10/Brho
  QVB11: Quad,  L=LLDC,  K1=KVX11/Brho
  QVB12: Quad,  L=LLDC,  K1=KVX12/Brho
  QHB13: Quad,  L=LLFC,  K1=KHX13/Brho
!
  QVC1:  Quad,  L=LLD,   K1=KVX1/Brho
  QHC2:  Quad,  L=LLF,   K1=KHX2/Brho
  QVC3:  Quad,  L=LLD,   K1=KVX3/Brho
  QHC4:  Quad,  L=LLF,   K1=KHX4/Brho
  QVC5:  Quad,  L=LLD,   K1=KVX5/Brho
  QHC6:  Quad,  L=LLF,   K1=KHX6/Brho
  QVC7:  Quad,  L=LLD,   K1=KVX7/Brho
  QHC8:  Quad,  L=LLF,   K1=KHX8/Brho
  QVC9:  Quad,  L=LLDEE, K1=KVX9/Brho
  QHC10: Quad,  L=LLFC,  K1=KHX10/Brho
  QVC11: Quad,  L=LLDC,  K1=KVX11/Brho
  QVC12: Quad,  L=LLDC,  K1=KVX12/Brho
  QHC13: Quad,  L=LLFC,  K1=KHX13/Brho
!
  QVD1:  Quad,  L=LLD, K1=KVX1/Brho
  QHD2:  Quad,  L=LLF, K1=KHX2/Brho
  QVD3:  Quad,  L=LLD, K1=KVX3/Brho
  QHD4:  Quad,  L=LLF, K1=KHX4/Brho
  QVD5:  Quad,  L=LLD, K1=KVX5/Brho
  QHD6:  Quad,  L=LLF, K1=KHX6/Brho
  QVD7:  Quad,  L=LLD, K1=KVX7/Brho
  QHD8:  Quad,  L=LLF, K1=KHX8/Brho
  QVD9:  Quad,  L=LLDEE, K1=KVX9/Brho
  QHD10: Quad,  L=LLFC, K1=KHX10/Brho
  QVD11: Quad,  L=LLDC, K1=KVX11/Brho
  QVD12: Quad,  L=LLDC, K1=KVX12/Brho
  QHD13: Quad,  L=LLFC, K1=KHX13/Brho
!------------------------------------------------------------------------
! Drifts
! drift lengths between quad and dipole changed by Y.Papaphilippou 08/2001
!------------------------------------------------------------------------
  SO:=1.0329
  SOO:=1.0329
  DSO:=0.0
  DSOO:=0.0
  O: Drift, L=SO+DSO
  OO: Drift, L=SOO+DSOO
  DUU:= 0.0
  LV:=1.025-LFC-LDC
  L4U:=7.45-LDEE-LFC
  LU:=DUU+L4U/4.0
  L4W:=13.05-LDC-LDC
  LW:=L4W/4.0
  UU: Drift, L=LU
  VV: Drift, L=LV
  WW: Drift, L=LW

!-----------------------------------------------------------
! Injection Bends and Drifts:
```

```
! Modified by Jeff Holmes: 10/2000 with parameters from
! BNL Technote 76 with updates from Nuria Catalan-Lasheras
  SCAL:=1.0
!------------------------------------------------------------
! New Bend Angles: From Nuria Catalan-Lasheras
!------------------------------------------------------------
  PHI1:=-42.0E-03*SCAL
  PHI2:= 45.0E-03*SCAL
  PHI3:= 43.6E-03*SCAL
  PHI4:=-46.6E-03*SCAL
!------------------------------------------------------------
! New Bend Lengths (X-Projections): From Technote 76
!------------------------------------------------------------
  LPI1:=0.863
  LPI2:=0.872
  LPI3:=0.990
  LPI4:=0.890
!------------------------------------------------------------
! New Radii of Curvature: From above information
!------------------------------------------------------------
  RHO1:=-LPI1/SIN(PHI1)
  RHO2:= LPI2/(SIN(PHI2+PHI1)-SIN(PHI1))
  RHO3:= LPI3/(SIN(PHI3+PHI2+PHI1)-SIN(PHI2+PHI1))
  RHO4:=-LPI4/(SIN(PHI4+PHI3+PHI2+PHI1)-SIN(PHI3+PHI2+PHI1))
!------------------------------------------------------------
! New Bend Path Lengths: From above information
!------------------------------------------------------------
  LBI1:=-RHO1*PHI1
  LBI2:= RHO2*PHI2
  LBI3:= RHO3*PHI3
  LBI4:=-RHO4*PHI4
!------------------------------------------------------------
! New Bend Fields: From above information
!------------------------------------------------------------
  BBI1:=Brho/RHO1
  BBI2:=Brho/RHO2
  BBI3:=Brho/RHO3
  BBI4:=Brho/RHO4
!------------------------------------------------------------
! New Chicane Bends: From above information
!------------------------------------------------------------
  BMI1: Sbend, L=LBI1, Angle=PHI1, E1=0.0, E2=PHI1
  BMI2: Sbend, L=LBI2, Angle=PHI2, E1=-PHI1, E2=PHI2+PHI1
  BMI3: Sbend, L=LBI3, Angle=PHI3, E1=-(PHI2+PHI1), &
E2=PHI3+PHI2+PHI1
  BMI4: Sbend, L=LBI4, Angle=PHI4, E1=-(PHI3+PHI2+PHI1), &
E2=(PHI4+PHI3+PHI2+PHI1)
!------------------------------------------------------------
! New Inter-Bend Drift Lengths: From Technote 76
!------------------------------------------------------------
  LC12:=2.381-LPI1/2.0-LPI2/2.0
  LB12:=LC12/COS(-PHI1)
  LC23:=1.814-LPI2/2.0-LPI3/2.0
  LB23:=LC23/COS(PHI2+PHI1)
  LC34:=2.029-LPI3/2.0-LPI4/2.0
  LB34:=LC34/COS(PHI3+PHI2+PHI1)
! Chicane Width:
  LSHC:=LPI1+LC12+LPI2+LC23+LPI3+LC34+LPI4
! Quad-to-Bend and Bend-to-Quad Lengths:
  LQTB:=3.230-LDC-LPI1/2.0
  LBTQ:=12.500-LQTB-LSHC
!------------------------------------------------------------
! New Injection Drifts: From above information
!------------------------------------------------------------
  DQTB: Drift, L=LQTB
  DB12: Drift, L=LB12
```

```
  DB23: Drift, L=LB23
  DB34: Drift, L=LB34
  DBTQ: Drift, L=LBTQ
!-----------------------------------------------------------
! New Injection Kickers: From Technote 76
!                        and Nuria Catalan-Lasheras
!-----------------------------------------------------------
!  HKCK1:= 9.39E-03
!  HKCK2:= 0.25E-03
!  HKCK3:= 0.25E-03
!  HKCK4:= 9.39E-03
!  VKCK1:=-8.17E-03
!  VKCK2:= 3.68E-03
!  VKCK3:= 3.68E-03
!  VKCK4:=-8.17E-03
  HKCK1:=0.00E-03
  HKCK2:=0.00E-03
  HKCK3:=0.00E-03
  HKCK4:=0.00E-03
  VKCK1:=0.00E-03
  VKCK2:=0.00E-03
  VKCK3:=0.00E-03
  VKCK4:=0.00E-03
  LHKCK1:=0.839
  LHKCK2:=0.428
  LHKCK3:=0.428
  LHKCK4:=0.839
  LVKCK1:=0.839
  LVKCK2:=0.428
  LVKCK3:=0.428
  LVKCK4:=0.839
  IKDH1: HKICKER, KICK= HKCK1, L= LHKCK1
  IKDH2: HKICKER, KICK= HKCK2, L= LHKCK2
  IKDH3: HKICKER, KICK= HKCK3, L= LHKCK3
  IKDH4: HKICKER, KICK= HKCK4, L= LHKCK4
  IKDV1: VKICKER, KICK= VKCK1, L= LVKCK1
  IKDV2: VKICKER, KICK= VKCK2, L= LVKCK2
  IKDV3: VKICKER, KICK= VKCK3, L= LVKCK3
  IKDV4: VKICKER, KICK= VKCK4, L= LVKCK4
!-----------------------------------------------------------
! Drifts between injection kickers:
! Modified by Jeff Holmes, 10/2000, information from
! BNL Technote 76 and Nuria Catalan-Lasheras
!-----------------------------------------------------------
  DLI1:=1.650-LDEE-LHKCK1/2.0
  DLI2:=1.160-LHKCK1/2.0-LVKCK1/2.0
  DLI3:=1.530-LVKCK1/2.0-LHKCK2/2.0
  DLI4:=0.540-LHKCK2/2.0-LVKCK2/2.0
  DLI5:=2.570-LVKCK2/2.0-LFC
  DKH1: Drift, L=DLI1
  DKV1: Drift, L=DLI2
  DKH2: Drift, L=DLI3
  DKV2: Drift, L=DLI4
  DQFC: Drift, L=DLI5
  DKV3: Drift, L=DLI5
  DKH3: Drift, L=DLI4
  DKV4: Drift, L=DLI3
  DKH4: Drift, L=DLI2
  DQDE: Drift, L=DLI1
!-----------------------------------------------------------
! Bare Four-fold Symmetric Ring:
! Arc Cell (AC); Straight Cell (SC); Superperiod (SP)
!-----------------------------------------------------------
    AC: Line = (QD,OO,BL,BR,O,QF,QF,OO,BL,BR,O,QD)
   ACL: Line = (QDEE,OO,BL,BR,O,QF,QF,OO,BL,BR,O,QD)
   ACR: Line = (QD,OO,BL,BR,O,QF,QF,OO,BL,BR,O,QDEE)
```

```
   ARC: Line = (ACL,AC,AC,ACR)
   SCL: Line = (QDE,UU,UU,UU,UU,QFC,QFC,VV,QDC,QDC,WW,WW)
   SCR: Line = (WW,WW,QDC,QDC,VV,QFC,QFC,UU,UU,UU,UU,QDE)
  SCLL: Line = (QDEE,UU,UU,UU,UU,QFC,QFC,VV,QDC,QDC,WW,WW)
  SCRR: Line = (WW,WW,QDC,QDC,VV,QFC,QFC,UU,UU,UU,UU,QDEE)
    SC: Line = (SCL, SCR)
   SCC: Line = (SCLL, SCRR)
   SPP: Line = (SC,AC,AC,AC,AC)
    SP: Line = (SCC, ARC)
!  RING: Line = (4*SP)
!------------------------------------------------------------
! Bare Ring with Injection Chicane and Kickers:
!------------------------------------------------------------
!  Put in Injection Chicane (CJG 11 Nov 1999):
!  Put in Injection Kickers (CJG 30 Nov 1999):
  INJM1: Marker
  INJM2: Marker
!   SIL: Line = (QDEE,UU,UU,UU,UU,QFC,QFC,VV,QDC,QDC)
  SILA: Line = (QDEE,DKH1,IKDH1,DKV1,IKDV1,DKH2,IKDH2)
  SILB: Line = (DKV2,IKDV2,DQFC,QFC,QFC,VV,QDC,QDC)
   SIL: Line = (SILA,SILB)
  SINJL: Line = (DQTB,BMI1,DB12,BMI2)
  SINJR: Line = (INJM1,DB23,BMI3,DB34,BMI4,DBTQ)
!   SIR: Line = (QDC,QDC,VV,QFC,QFC,UU,UU,UU,UU,QDEE)
  SIRA: Line = (QDC,QDC,VV,QFC,QFC,DKV3,IKDV3,DKH3,IKDH3)
  SIRB: Line = (DKV4,IKDV4,DKH4,IKDH4,DQDE,QDEE,INJM2)
   SIR: Line = (SIRA,SIRB)
  SISINJL: Line = (SIL,SINJL)
  SISINJR: Line = (SINJR,SIR)
  SINJ: Line = (SISINJL,SISINJR)
  SPINJ: Line = (SISINJL,SISINJR,ARC)
  RING: Line = (SPINJ,SP,SP,SP)
!------------------------------------------------------------
! Ring for Beam Dynamics with Injection Foil at Beginning
! Jeff Holmes, 10/2000
!------------------------------------------------------------
  RNGOBT: Line = (SISINJR,ARC,SP,SP,SP,SISINJL)

!------------------------------------------------------------
! Bare lattice with Chromaticity Sextupoles
! Jeff Holmes and Yannis Papaphilippou, 01/2001
!------------------------------------------------------------
  ACLSX1: Line = (QD,Q3D,SVX3,Q3B3,BL,BR,O,QF)
  ACLSX2: Line = (QF,Q4D,SHX4,Q4B4,BL,BR,B4Q5,SVX5,Q5U,QD)
  ACRSX1: Line = (QD,OO,BL,BR,B6Q6,SHX6,Q6U,QF)
  ACRSX2: Line = (QF,OO,BL,BR,B7Q7,SVX7,Q7U,QD)
   ARCSX: Line = (ACL,ACLSX1,ACLSX2,ACRSX1,ACRSX2,ACR)
    SPSX: Line = (SCC,ARCSX)
  RINGSX: Line = (4*SPSX)

!------------------------------------------------------------
!   Assemble Superperiod with PUE's and Correctors:
!------------------------------------------------------------
! value of sextupole and sextupole magnetic length changed,
! Y.Papaphilippou, 01/2001
!
  LSXT:=0.3
  LCNT:=0.1
  LSTQ:=0.01
  LOCT:=0.3
  LOTQ:=0.01
   LSV1:=LSXT
   SQ1U:=LSTQ
   SQ1D:=LCNT
 KDVTX1:=0.0
   SVX1: Sextupole, L=LSV1, K2=KSVX1
```

```
    Q1U: Drift, L=SQ1U
  BPMX1: Monitor
    Q1D: Drift, L=SQ1D
  DVTX1: VKICKER, KICK=KDVTX1
    QX1: Line = (SVX1,Q1U,QVX1,BPMX1,Q1D,DVTX1)
   Q1B1: Drift, L=S00+DS00-SQ1D
!------------------------------------------------------------
   LSH2:=LSXT
   SQ2U:=LSTQ
   SQ2D:=LCNT
 KDHTX2:=0.0
   SHX2: Sextupole, L=LSH2, K2=KSHX2
    Q2U: Drift, L=SQ2U
  BPMX2: Monitor
    Q2D: Drift, L=SQ2D
  DHTX2: HKICKER, KICK=KDHTX2
   B1Q2: Drift, L=S0+DS0-LSH2-SQ2U
    QX2: Line = (SHX2,Q2U,QHX2,BPMX2,Q2D,DHTX2)
   Q2B2: Drift, L=S00+DS00-SQ2D
!------------------------------------------------------------
   SQ3U:=LCNT
   SQ3D:=LSTQ
   LSV3:=LSXT
 KDVTX3:=0.0
  DVTX3: VKICKER, KICK=KDVTX3
    Q3U: Drift, L=SQ3U
  BPMX3: Monitor
    Q3D: Drift, L=SQ3D
   SVX3: Sextupole, L=LSV3, K2=KSV3
   B2Q3: Drift, L=S0+DS0-SQ3U
    QX3: Line = (DVTX3,Q3U,QVX3,BPMX3,Q3D,SVX3)
   Q3B3: Drift, L=S00+DS00-SQ3D-LSV3
!------------------------------------------------------------
   SQ4U:=LCNT
   SQ4D:=LSTQ
   LSH4:=LSXT
 KDHTX4:=0.0
  DHTX4: HKICKER, KICK=KDHTX4
    Q4U: Drift, L=SQ4U
  BPMX4: Monitor
    Q4D: Drift, L=SQ4D
   SHX4: Sextupole, L=LSH4, K2=KSH4
   B3Q4: Drift, L=S0+DS0-SQ4U
    QX4: Line = (DHTX4,Q4U,QHX4,BPMX4,Q4D,SHX4)
   Q4B4: Drift, L=S00+DS00-SQ4D-LSH4
!------------------------------------------------------------
   LSV5:=LSXT
   SQ5U:=LSTQ
   SQ5D:=LCNT
 KDVTX5:=0.0
   SVX5: Sextupole, L=LSV5, K2=KSV5
    Q5U: Drift, L=SQ5U
  BPMX5: Monitor
    Q5D: Drift, L=SQ5D
  DVTX5: VKICKER, KICK=KDVTX5
   B4Q5: Drift, L=S0+DS0-LSV5-SQ5U
    QX5: Line = (SVX5,Q5U,QVX5,BPMX5,Q5D,DVTX5)
   Q5B6: Drift, L=S00+DS00-SQ5D
!------------------------------------------------------------
   LSH6:=LSXT
   SQ6U:=LSTQ
   SQ6D:=LCNT
 KDHTX6:=0.0
   SHX6: Sextupole, L=LSH6, K2=KSH6
    Q6U: Drift, L=SQ6U
  BPMX6: Monitor
```

```
    Q6D: Drift, L=SQ6D
  DHTX6: HKICKER, KICK=KDHTX6
   B6Q6: Drift, L=SO+DSO-LSH6-SQ6U
    QX6: Line = (SHX6,Q6U,QHX6,BPMX6,Q6D,DHTX6)
   Q6B7: Drift, L=SOO+DSOO-SQ6D
!------------------------------------------------------------
   LSV7:=LSXT
   SQ7U:=LSTQ
   SQ7D:=LCNT
 KDVTX7:=0.0
   SVX7: Sextupole, L=LSV7, K2=KSV7
    Q7U: Drift, L=SQ7U
  BPMX7: Monitor
    Q7D: Drift, L=SQ7D
  DVTX7: VKICKER, KICK=KDVTX7
   B7Q7: Drift, L=SO+DSO-LSV7-SQ7U
    QX7: Line = (SVX7,Q7U,QVX7,BPMX7,Q7D,DVTX7)
   Q7B8: Drift, L=SOO+DSOO-SQ7D
!------------------------------------------------------------
   LOH8:=LOCT
   SQ8U:=LOTQ
   SQ8D:=LCNT
 KDHTX8:=0.0
   OHX8: Octupole, L=LOH8, K3=KOH8
    Q8U: Drift, L=SQ8U
  BPMX8: Monitor
    Q8D: Drift, L=SQ8D
  DHTX8: HKICKER, KICK=KDHTX8
   B8Q8: Drift, L=SO+DSO-LOH8-SQ8U
    QX8: Line = (OHX8,Q8U,QHX8,BPMX8,Q8D,DHTX8)
   Q8B9: Drift, L=SOO+DSOO-SQ6D
!------------------------------------------------------------
   LOV9:=LOCT
   SQ9U:=LOTQ
   SQ9D:=LCNT
 KDVTX9:=0.0
   OVX9: Octupole, L=LOV9, K3=KOV9
    Q9U: Drift, L=SQ9U
  BPMX9: Monitor
    Q9D: Drift, L=SQ9D
  DVTX9: VKICKER, KICK=KDVTX9
   B9Q9: Drift, L=SO+DSO-LOV9-SQ9U
    QX9: Line = (OVX9,Q9U,QVX9,BPMX9,Q9D,DVTX9)
!------------------------------------------------------------
  ARCLX: Line = (QX1,Q1B1,BND,B1Q2,QX2,Q2B2,BND,B2Q3,QX3, &
                     Q3B3,BND,B3Q4,QX4,Q4B4,BND,B4Q5,QX5)
  ARCRX: Line = (Q5B6,BND,B6Q6,QX6,Q6B7,BND,B7Q7,QX7,Q7B8, &
                      BND,B8Q8,QX8,Q8B9,BND,B9Q9,QX9)
   ARCX: Line = (ARCLX,ARCRX)
!------------------------------------------------------------
  SQ10U:=LCNT
  SQ13D:=LCNT
    UU9: Drift, L=LU-SQ9D
   UU10: Drift, L=LU-SQ10U
 KDHTX10:=0.0
 KDVTX10:=0.0
 DHTX10: HKICKER, KICK=KDHTX10
 DVTX10: VKICKER, KICK=KDVTX10
   Q10U: Drift, L=SQ10U
 BPMX10: Monitor
 BPMX13: Monitor
   Q13D: Drift, L=SQ13D
 KDVTX13:=0.0
 KDHTX13:=0.0
 DVTX13: VKICKER, KICK=KDVTX13
 DHTX13: HKICKER, KICK=KDHTX13
```

```
  UU13: Drift, L=LU-SQ13D
   UU1: Drift, L=LU-SQ1U-LSV1
  SSXL: Line = (UU9,UU,UU,UU10,DHTX10,DVTX10,Q10U,BPMX10,&
                QHX10,VV,QVX11,WW,WW)
  SSXR: Line = (WW,WW,QVX12,VV,QHX13,BPMX13,Q13D,DHTX13,&
                DVTX13,UU13,UU,UU,UU1)
  SSSX: Line = (SSXL,SSXR)
!-------------------------------------------------------------
   SPX: Line =(SSSX,ARCX)
!-------------------------------------------------------------
!   Assemble Superperiod A:
!-------------------------------------------------------------
 KSVA1:=0.0
  SVA1: Sextupole, L=LSV1, K2=KSVA1
 BPMA1: Monitor
 KDVTA1:=0.0
 DVTA1: VKICKER, KICK=KDVTA1
   QA1: Line = (SVA1,Q1U,QVA1,BPMA1,Q1D,DVTA1)
!-------------------------------------------------------------
 KSHA2:=0.0
  SHA2: Sextupole, L=LSH2, K2=KSHA2
 BPMA2: Monitor
 KDHTA2:=0.0
 DHTA2: HKICKER, KICK=KDHTA2
   QA2: Line = (SHA2,Q2U,QHA2,BPMA2,Q2D,DHTA2)
!-------------------------------------------------------------
 KDVTA3:=0.0
 DVTA3: VKICKER, KICK=KDVTA3
 BPMA3: Monitor
  SVA3: Sextupole, L=LSV3, K2=KSV3
   QA3: Line = (DVTA3,Q3U,QVA3,BPMA3,Q3D,SVA3)
!-------------------------------------------------------------
 KDHTA4:=0.0
 DHTA4: HKICKER, KICK=KDHTA4
 BPMA4: Monitor
  SHA4: Sextupole, L=LSH4, K2=KSH4
   QA4: Line = (DHTA4,Q4U,QHA4,BPMA4,Q4D,SHA4)
!-------------------------------------------------------------
  SVA5: Sextupole, L=LSV5, K2=KSV5
 BPMA5: Monitor
 KDVTA5:=0.0
 DVTA5: VKICKER, KICK=KDVTA5
   QA5: Line = (SVA5,Q5U,QVA5,BPMA5,Q5D,DVTA5)
!-------------------------------------------------------------
  SHA6: Sextupole, L=LSH6, K2=KSH6
 BPMA6: Monitor
 KDHTA6:=0.0
 DHTA6: HKICKER, KICK=KDHTA6
   QA6: Line = (SHA6,Q6U,QHA6,BPMA6,Q6D,DHTA6)
!-------------------------------------------------------------
  SVA7: Sextupole, L=LSV7, K2=KSV7
 BPMA7: Monitor
 KDVTA7:=0.0
 DVTA7: VKICKER, KICK=KDVTA7
   QA7: Line = (SVA7,Q7U,QVA7,BPMA7,Q7D,DVTA7)
!-------------------------------------------------------------
  OHA8: Octupole, L=LOH8, K3=KOH8
 BPMA8: Monitor
 KDHTA8:=0.0
 DHTA8: HKICKER, KICK=KDHTA8
   QA8: Line = (OHA8,Q8U,QHA8,BPMA8,Q8D,DHTA8)
!-------------------------------------------------------------
  OVA9: Octupole, L=LOV9, K3=KOV9
 BPMA9: Monitor
 KDVTA9:=0.0
 DVTA9: VKICKER, KICK=KDVTA9
```

```
    QA9: Line = (OVA9,Q9U,QVA9,BPMA9,Q9D,DVTA9)
!-----------------------------------------------------------
  ARCLA: Line = (QA1,Q1B1,BND,B1Q2,QA2,Q2B2,BND,B2Q3,QA3, &
                     Q3B3,BND,B3Q4,QA4,Q4B4,BND,B4Q5,QA5)
  ARCRA: Line = (Q5B6,BND,B6Q6,QA6,Q6B7,BND,B7Q7,QA7,Q7B8, &
                      BND,B8Q8,QA8,Q8B9,BND,B9Q9,QA9)
   ARCA: Line = (ARCLA,ARCRA)
!-----------------------------------------------------------
 KDHTA10:=0.0
 KDVTA10:=0.0
 DHTA10: HKICKER, KICK=KDHTA10
 DVTA10: VKICKER, KICK=KDVTA10
 BPMA10: Monitor
 BPMA13: Monitor
 KDHTA13:=0.0
 KDVTA13:=0.0
 DVTA13: VKICKER, KICK=KDVTA13
 DHTA13: HKICKER, KICK=KDHTA13
   SSAL: Line = (UU9,UU,UU,UU10,DHTA10,DVTA10,Q10U,BPMA10,&
                 QHA10,VV,QVA11,WW,WW)
   SSAR: Line = (WW,WW,QVA12,VV,QHA13,BPMA13,Q13D,DHTA13,&
                 DVTA13,UU13,UU,UU,UU1)
   SSSA: Line = (SSAL,SSAR)
!-----------------------------------------------------------
    SPA: Line =(SSSA,ARCA)
!-----------------------------------------------------------
!   Assemble Superperiod B:
!-----------------------------------------------------------
  KSVB1:=0.0
   SVB1: Sextupole, L=LSV1, K2=KSVB1
  BPMB1: Monitor
  KDVTB1:=0.0
  DVTB1: VKICKER, KICK=KDVTB1
    QB1: Line = (SVB1,Q1U,QVB1,BPMB1,Q1D,DVTB1)
!-----------------------------------------------------------
  KSHB2:=0.0
   SHB2: Sextupole, L=LSH2, K2=KSHB2
  BPMB2: Monitor
  KDHTB2:=0.0
  DHTB2: HKICKER, KICK=KDHTB2
    QB2: Line = (SHB2,Q2U,QHB2,BPMB2,Q2D,DHTB2)
!-----------------------------------------------------------
  KDVTB3:=0.0
  DVTB3: VKICKER, KICK=KDVTB3
  BPMB3: Monitor
   SVB3: Sextupole, L=LSV3, K2=KSV3
    QB3: Line = (DVTB3,Q3U,QVB3,BPMB3,Q3D,SVB3)
!-----------------------------------------------------------
  KDHTB4:=0.0
  DHTB4: HKICKER, KICK=KDHTB4
  BPMB4: Monitor
   SHB4: Sextupole, L=LSH4, K2=KSH4
    QB4: Line = (DHTB4,Q4U,QHB4,BPMB4,Q4D,SHB4)
!-----------------------------------------------------------
   SVB5: Sextupole, L=LSV5, K2=KSV5
  BPMB5: Monitor
  KDVTB5:=0.0
  DVTB5: VKICKER, KICK=KDVTB5
    QB5: Line = (SVB5,Q5U,QVB5,BPMB5,Q5D,DVTB5)
!-----------------------------------------------------------
   SHB6: Sextupole, L=LSH6, K2=KSH6
  BPMB6: Monitor
  KDHTB6:=0.0
  DHTB6: HKICKER, KICK=KDHTB6
    QB6: Line = (SHB6,Q6U,QHB6,BPMB6,Q6D,DHTB6)
!-----------------------------------------------------------
```

```
   SVB7: Sextupole, L=LSV7, K2=KSV7
  BPMB7: Monitor
  KDVTB7:=0.0
  DVTB7: VKICKER, KICK=KDVTB7
    QB7: Line = (SVB7,Q7U,QVB7,BPMB7,Q7D,DVTB7)
!-----------------------------------------------------------
   OHB8: Octupole, L=LOH8, K3=KOH8
  BPMB8: Monitor
  KDHTB8:=0.0
  DHTB8: HKICKER, KICK=KDHTB8
    QB8: Line = (OHB8,Q8U,QHB8,BPMB8,Q8D,DHTB8)
!-----------------------------------------------------------
   OVB9: Octupole, L=LOV9, K3=KOV9
  BPMB9: Monitor
  KDVTB9:=0.0
  DVTB9: VKICKER, KICK=KDVTB9
    QB9: Line = (OVB9,Q9U,QVB9,BPMB9,Q9D,DVTB9)
!-----------------------------------------------------------
  ARCLB: Line = (QB1,Q1B1,BND,B1Q2,QB2,Q2B2,BND,B2Q3,QB3, &
                     Q3B3,BND,B3Q4,QB4,Q4B4,BND,B4Q5,QB5)
  ARCRB: Line = (Q5B6,BND,B6Q6,QB6,Q6B7,BND,B7Q7,QB7,Q7B8, &
                      BND,B8Q8,QB8,Q8B9,BND,B9Q9,QB9)
   ARCB: Line = (ARCLB,ARCRB)
!-----------------------------------------------------------
 KDHTB10:=0.0
 KDVTB10:=0.0
 DHTB10: HKICKER, KICK=KDHTB10
 DVTB10: VKICKER, KICK=KDVTB10
 BPMB10: Monitor
 BPMB13: Monitor
 KDHTB13:=0.0
 KDVTB13:=0.0
 DVTB13: VKICKER, KICK=KDVTB13
 DHTB13: HKICKER, KICK=KDHTB13
   SSBL: Line = (UU9,UU,UU,UU10,DHTB10,DVTB10,Q10U,BPMB10,&
                 QHB10,VV,QVB11,WW,WW)
   SSBR: Line = (WW,WW,QVB12,VV,QHB13,BPMB13,Q13D,DHTB13,&
                 DVTB13,UU13,UU,UU,UU1)
   SSSB: Line = (SSBL,SSBR)
!-----------------------------------------------------------
    SPB: Line =(SSSB,ARCB)
!-----------------------------------------------------------
!   Assemble Superperiod C:
!-----------------------------------------------------------
  KSVC1:=0.0
   SVC1: Sextupole, L=LSV1, K2=KSVC1
  BPMC1: Monitor
  KDVTC1:=0.0
  DVTC1: VKICKER, KICK=KDVTC1
    QC1: Line = (SVC1,Q1U,QVC1,BPMC1,Q1D,DVTC1)
!-----------------------------------------------------------
  KSHC2:=0.0
   SHC2: Sextupole, L=LSH2, K2=KSHC2
  BPMC2: Monitor
  KDHTC2:=0.0
  DHTC2: HKICKER, KICK=KDHTC2
    QC2: Line = (SHC2,Q2U,QHC2,BPMC2,Q2D,DHTC2)
!-----------------------------------------------------------
  KDVTC3:=0.0
  DVTC3: VKICKER, KICK=KDVTC3
  BPMC3: Monitor
   SVC3: Sextupole, L=LSV3, K2=KSV3
    QC3: Line = (DVTC3,Q3U,QVC3,BPMC3,Q3D,SVC3)
!-----------------------------------------------------------
  KDHTC4:=0.0
  DHTC4: HKICKER, KICK=KDHTC4
```

```
  BPMC4: Monitor
   SHC4: Sextupole, L=LSH4, K2=KSH4
    QC4: Line = (DHTC4,Q4U,QHC4,BPMC4,Q4D,SHC4)
!-----------------------------------------------------------
   SVC5: Sextupole, L=LSV5, K2=KSV5
  BPMC5: Monitor
  KDVTC5:=0.0
  DVTC5: VKICKER, KICK=KDVTC5
    QC5: Line = (SVC5,Q5U,QVC5,BPMC5,Q5D,DVTC5)
!-----------------------------------------------------------
   SHC6: Sextupole, L=LSH6, K2=KSH6
  BPMC6: Monitor
  KDHTC6:=0.0
  DHTC6: HKICKER, KICK=KDHTC6
    QC6: Line = (SHC6,Q6U,QHC6,BPMC6,Q6D,DHTC6)
!-----------------------------------------------------------
   SVC7: Sextupole, L=LSV7, K2=KSV7
  BPMC7: Monitor
  KDVTC7:=0.0
  DVTC7: VKICKER, KICK=KDVTC7
    QC7: Line = (SVC7,Q7U,QVC7,BPMC7,Q7D,DVTC7)
!-----------------------------------------------------------
   OHC8: Octupole, L=LOH8, K3=KOH8
  BPMC8: Monitor
  KDHTC8:=0.0
  DHTC8: HKICKER, KICK=KDHTC8
    QC8: Line = (OHC8,Q8U,QHC8,BPMC8,Q8D,DHTC8)
!-----------------------------------------------------------
   OVC9: Octupole, L=LOV9, K3=KOV9
  BPMC9: Monitor
  KDVTC9:=0.0
  DVTC9: VKICKER, KICK=KDVTC9
    QC9: Line = (OVC9,Q9U,QVC9,BPMC9,Q9D,DVTC9)
!-----------------------------------------------------------
  ARCLC: Line = (QC1,Q1B1,BND,B1Q2,QC2,Q2B2,BND,B2Q3,QC3, &
                     Q3B3,BND,B3Q4,QC4,Q4B4,BND,B4Q5,QC5)
  ARCRC: Line = (Q5B6,BND,B6Q6,QC6,Q6B7,BND,B7Q7,QC7,Q7B8, &
                      BND,B8Q8,QC8,Q8B9,BND,B9Q9,QC9)
   ARCC: Line = (ARCLC,ARCRC)
!-----------------------------------------------------------
 KDHTC10:=0.0
 KDVTC10:=0.0
 DHTC10: HKICKER, KICK=KDHTC10
 DVTC10: VKICKER, KICK=KDVTC10
 BPMC10: Monitor
 BPMC13: Monitor
 KDHTC13:=0.0
 KDVTC13:=0.0
 DVTC13: VKICKER, KICK=KDVTC13
 DHTC13: HKICKER, KICK=KDHTC13
   SSCL: Line = (UU9,UU,UU,UU10,DHTC10,DVTC10,Q10U,BPMC10,&
                 QHC10,VV,QVC11,WW,WW)
   SSCR: Line = (WW,WW,QVC12,VV,QHC13,BPMC13,Q13D,DHTC13,&
                 DVTC13,UU13,UU,UU,UU1)
   SSSC: Line = (SSCL,SSCR)
!-----------------------------------------------------------
    SPC: Line =(SSSC,ARCC)
!-----------------------------------------------------------
!   Assemble Superperiod D:
!-----------------------------------------------------------
  KSVD1:=0.0
   SVD1: Sextupole, L=LSV1, K2=KSVD1
  BPMD1: Monitor
  KDVTD1:=0.0
  DVTD1: VKICKER, KICK=KDVTD1
    QD1: Line = (SVD1,Q1U,QVD1,BPMD1,Q1D,DVTD1)
```

```
!------------------------------------------------------------
  KSHD2:=0.0
   SHD2: Sextupole, L=LSH2, K2=KSHD2
  BPMD2: Monitor
  KDHTD2:=0.0
  DHTD2: HKICKER, KICK=KDHTD2
    QD2: Line = (SHD2,Q2U,QHD2,BPMD2,Q2D,DHTD2)
!------------------------------------------------------------
  KDVTD3:=0.0
  DVTD3: VKICKER, KICK=KDVTD3
  BPMD3: Monitor
   SVD3: Sextupole, L=LSV3, K2=KSV3
    QD3: Line = (DVTD3,Q3U,QVD3,BPMD3,Q3D,SVD3)
!------------------------------------------------------------
  KDHTD4:=0.0
  DHTD4: HKICKER, KICK=KDHTD4
  BPMD4: Monitor
   SHD4: Sextupole, L=LSH4, K2=KSH4
    QD4: Line = (DHTD4,Q4U,QHD4,BPMD4,Q4D,SHD4)
!------------------------------------------------------------
   SVD5: Sextupole, L=LSV5, K2=KSV5
  BPMD5: Monitor
  KDVTD5:=0.0
  DVTD5: VKICKER, KICK=KDVTD5
    QD5: Line = (SVD5,Q5U,QVD5,BPMD5,Q5D,DVTD5)
!------------------------------------------------------------
   SHD6: Sextupole, L=LSH6, K2=KSH6
  BPMD6: Monitor
  KDHTD6:=0.0
  DHTD6: HKICKER, KICK=KDHTD6
    QD6: Line = (SHD6,Q6U,QHD6,BPMD6,Q6D,DHTD6)
!------------------------------------------------------------
   SVD7: Sextupole, L=LSV7, K2=KSV7
  BPMD7: Monitor
  KDVTD7:=0.0
  DVTD7: VKICKER, KICK=KDVTD7
    QD7: Line = (SVD7,Q7U,QVD7,BPMD7,Q7D,DVTD7)
!------------------------------------------------------------
   OHD8: Octupole, L=LOH8, K3=KOH8
  BPMD8: Monitor
  KDHTD8:=0.0
  DHTD8: HKICKER, KICK=KDHTD8
    QD8: Line = (OHD8,Q8U,QHD8,BPMD8,Q8D,DHTD8)
!------------------------------------------------------------
   OVD9: Octupole, L=LOV9, K3=KOV9
  BPMD9: Monitor
  KDVTD9:=0.0
  DVTD9: VKICKER, KICK=KDVTD9
    QD9: Line = (OVD9,Q9U,QVD9,BPMD9,Q9D,DVTD9)
!------------------------------------------------------------
  ARCLD: Line = (QD1,Q1B1,BND,B1Q2,QD2,Q2B2,BND,B2Q3,QD3, &
                   Q3B3,BND,B3Q4,QD4,Q4B4,BND,B4Q5,QD5)
  ARCRD: Line = (Q5B6,BND,B6Q6,QD6,Q6B7,BND,B7Q7,QD7,Q7B8, &
                    BND,B8Q8,QD8,Q8B9,BND,B9Q9,QD9)
   ARCD: Line = (ARCLD,ARCRD)
!------------------------------------------------------------
 KDHTD10:=0.0
 KDVTD10:=0.0
 DHTD10: HKICKER, KICK=KDHTD10
 DVTD10: VKICKER, KICK=KDVTD10
 BPMD10: Monitor
 BPMD13: Monitor
 KDHTD13:=0.0
 KDVTD13:=0.0
 DVTD13: VKICKER, KICK=KDVTD13
 DHTD13: HKICKER, KICK=KDHTD13
```

```
   SSDL: Line = (UU9,UU,UU,UU10,DHTD10,DVTD10,Q10U,BPMD10,&
                 QHD10,VV,QVD11,WW,WW)
   SSDR: Line = (WW,WW,QVD12,VV,QHD13,BPMD13,Q13D,DHTD13,&
                 DVTD13,UU13,UU,UU,UU1)
   SSSD: Line = (SSDL,SSDR)
!-------------------------------------------------------------
    SPD: Line =(SSSD,ARCD)
!-------------------------------------------------------------
   SPAA: Line = (SSSA,ARCB)
   SPBB: Line = (SSSB,ARCC)
   SPCC: Line = (SSSC,ARCD)
   SPDD: Line = (SSSD,ARCA)
    RNG: Line = (SPAA,SPBB,SPCC,SPDD)
!-------------------------------------------------------------
!
Return
```

6.2.3 RTBT Optics File

```
" SNS RING TO TARGET TRANSFORT LINE (08/11/99)"
0 ;
PRINT, REFER ;
PRINT, BEAM, ON       ;
PRINT, TRANS, ON ;
PRINT, ACCEL, ON ;
PRINT, ONELINE   ;
BM:BEAM.0000,BETAX=.5311,ALPHAX=.0,BETAY=0.888,ALPHAY=0.0,P0=1.6960 ;
QF:=2.84631 ;
QD:=-2.84631 ;
QL1:=0.2500 ;
QL2:=0.5000 ;
QAR:=10.00 ;
STORE BX0=BETAX;
STORE BY0=BETAY;
STORE AX0=ALPHAX;
STORE AY0=ALPHAY;
LLK:  DRIFT.0,   L=2.0 ;
DR5:  ROTAT,  ANGLE=0.0 ;
DB3:  BEND, L=2.1, ANGLE=-16.8;
DR6:  ROTAT,  ANGLE=0.0 ;
LLL:  DRIFT, L=3.55 ;
Q01:  QUAD.00  L=QL2,B=-4.90232, APER=QAR ;
LL1:  DRIFT.,   L=0.36 ;
Q02:  QUAD.00  L=QL2,B=5.46685, APER=QAR ;
LL7:  DRIFT.0,   L=5.48810 ;
Q03:  QUAD.00, L=QL2, B=-2.88579, APER=QAR ;
LL7:  DRIFT,   L=3.3608 ;
Q04:  QUAD.00, L=QL2,B=3.45434, APER=QAR ;
LL7:  DRIFT,   L=3.3608 ;
Q05:  QUAD.00, L=QL1, B=-4.33670, APER=QAR ;
FPBT: -FIT, BETAX=0.2150,TOLER=0.001 ;
FPB1: -FIT, ALPHAX=0.000, TOLER=0.001 ;
FPB2: -FIT, BETAY=1.3132,TOLER=0.001 ;
FPB3: -FIT, ALPHAY=0.0000,TOLER=0.001 ;
Q05:  QUAD.00, L=QL1, B=-4.52748  , APER=QAR ;
LL7:  DRIFT,   L=3.3608 ;
Q06:  QUAD.00  L=QL2,B=4.46060, APER=QAR ;
LL7:  DRIFT,   L=3.3608 ;
Q07:  QUAD.00, L=QL2, B=-4.52748   , APER=QAR ;
LL7:  DRIFT,   L=3.3608 ;
Q08:  QUAD.00  L=QL2,B= 4.46060, APER=QAR ;
LL7:  DRIFT,   L=3.3608 ;
Q09:  QUAD.00, L=QL2, B=-4.52748   , APER=QAR ;
LL7:  DRIFT,   L=3.3608 ;
Q10:  QUAD.00  L=QL2,B= 4.46060, APER=QAR ;
LL7:  DRIFT,   L=3.3608 ;
Q11:  QUAD.00, L=QL2, B=-4.52748   , APER=QAR ;
LLP:  DRIFT.0, L=3.3608;
Q12:  QUAD.00  L=QL2, B= 4.43021, APER=QAR ;
LL7:  DRIFT.0, L=3.3608;
Q13:  QUAD.00,  L=QL2, B=-4.50216, APER=QAR ;
LL0:  DRIFT.0, L=1.0 ;
DR7:  ROTAT,  ANGLE=0.0 ;
DB4:  BEND, L=2.1, ANGLE=-16.8;
DR8:  ROTAT,  ANGLE=0.0 ;
LLP:  DRIFT.0, L=1.25 ;
-10 -1 6 0.0 0.000001 ;
-10 -2 6 0.0 0.000001 ;
Q14:  QUAD.00,  L=QL2, B=3.40055, APER=QAR ;
LL8:  DRIFT.0,   L=3.6400  ;
Q15:  QUAD.00, L=QL2, B=-3.82177, APER=QAR ;
LL8:  DRIFT,   L=5.2912
Q16:  QUAD.00,  L=QL2, B=2.82169, APER=QAR ;
```

```
LL2:  DRIFT,  L=5.2912 ;
Q17:  QUAD.00, L=QL2, B=-3.04264, APER=QAR ;
LLE:  DRIFT, L=5.2912 ;
Q18:  QUAD.00  L=QL1,B=2.91864, APER=QAR ;
FPB5: -FIT, BETAY=0.342700,TOLER=0.0001 ;
FPB6: -FIT, ALPHAX=0.000, TOLER=0.0001 ;
FPB7: -FIT, BETAX=1.9569,TOLER=0.0001 ;
FPB8: -FIT, ALPHAY=0.00000,TOLER=0.0001
Q18:  QUAD.00  L=QL1,B=QF, APER=QAR ;
LLF:  DRIFT, L=5.2912 ;
Q19:  QUAD.00, L=QL2, B=QD, APER=QAR ;
LLG:  DRIFT, L=5.2912 ;
Q20:  QUAD.00  L=QL2,B=QF, APER=QAR ;
LLH:  DRIFT, L=5.2912 ;
Q21:  QUAD.00, L=QL2, B=QD, APER=QAR ;
LLI:  DRIFT, L=5.2912 ;
Q22:  QUAD.00  L=QL2,B=QF, APER=QAR ;
LLJ:  DRIFT, L=5.2912 ;
Q23:  QUAD.00, L=QL2, B=QD, APER=QAR ;
LLC:  DRIFT, L=5.2912 ;
Q24:  QUAD.00  L=QL2,B=QF, APER=QAR ;
LLH:  DRIFT, L=5.1412 ;
Q25:  QUAD.00, L=QL2, B=QD, APER=QAR ;
LLH:  DRIFT, L=5.1412 ;
Q26:  QUAD.01, L=0.8, B=2.94198, APER=QAR ;
LLQ:  DRIFT, L=5.1412 ;
Q27:  QUAD.01  L=0.8,B=-2.31040, APER=QAR ;
LLR:  DRIFT, L=1.000000 ;
Q28:  QUAD.01, L=0.8, B=2.44457, APER=QAR ;
LLQ:  DRIFT, L=5.000000 ;
Q29:  QUAD.01  L=0.8,B=-1.59552, APER=QAR ;
LLR:  DRIFT, L=1.000000 ;
Q30:  QUAD.01, L=0.8, B=1.15648, APER=QAR ;
LLS:  DRIFT, L=5.000000 ;
LLT:  DRIFT, L=5.000000 ;
FPBT: FIT, BETAX=8.33000,TOLER=0.001 ;
FPB1: FIT, ALPHAX=0.000, TOLER=0.001 ;
FPB2: FIT, BETAY=1.02000,TOLER=0.001 ;
FPB3: FIT, ALPHAY=0.0000,TOLER=0.001 ;
SENTINEL
SENTINEL

Q13:  QUAD.00,  L=QL2, B=3.71940, APER=QAR ;
LL8:  DRIFT.0,   L=3.3608 ;
Q13:  QUAD.00,  L=QL2, B=-3.72278, APER=QAR ;
LL8:  DRIFT,   L=5.2912 ;
Q14:  QUAD.00, L=QL1, B=3.04844, APER=QAR ;
FPBT: -FIT, BETAX=1.6127,TOLER=0.001 ;
FPB1: -FIT, ALPHAX=0.000, TOLER=0.001 ;
FPB2: -FIT, BETAY=0.37418,TOLER=0.001 ;
FPB3: -FIT, ALPHAY=0.0000,TOLER=0.001 ;
Q14:  QUAD.00, L=QL1, B=2.25382, APER=QAR ;
LL8:  DRIFT,   L=1.0956
DR5:  ROTAT,  ANGLE=0.0 ;
DB3:  BEND, L=3.1, ANGLE=-22.5;
DR6:  ROTAT,  ANGLE=0.0 ;
LL8:  DRIFT,   L=1.0956
Q15:  QUAD.00,  L=QL2, B=-3.11005, APER=QAR ;
LL8:  DRIFT,   L=1.0956
DR5:  ROTAT,  ANGLE=0.0 ;
DB3:  BEND, L=3.1, ANGLE=-22.5;
DR6:  ROTAT,  ANGLE=0.0 ;
LL8:  DRIFT,   L=1.0956
Q16:  QUAD.00, L=QL1, B=2.25382, APER=QAR ;
Q14:  QUAD.00, L=QL1, B=3.18336, APER=QAR ;
LL8:  DRIFT,   L=5.2912
```

```
Q15:  QUAD.00,  L=QL2, B=-3.11005, APER=QAR ;
LL8:  DRIFT,   L=5.2912
Q14:  QUAD.00, L=QL1, B=3.18336, APER=QAR ;
Q16:  QUAD.00, L=QL1, B=2.25382, APER=QAR ;
LL8:  DRIFT,   L=1.0956
DR5:  ROTAT,  ANGLE=0.0 ;
DB3:  BEND, L=3.1, ANGLE=-22.5;
DR6:  ROTAT,  ANGLE=0.0 ;
LL8:  DRIFT,   L=1.0956
Q15:  QUAD.00,  L=QL2, B=-3.11005, APER=QAR ;
LL8:  DRIFT,   L=1.0956
DR5:  ROTAT,  ANGLE=0.0 ;
DB3:  BEND, L=3.1, ANGLE=-22.5;
DR6:  ROTAT,  ANGLE=0.0 ;
LL8:  DRIFT,   L=1.0956
Q16:  QUAD.00, L=QL1, B=2.25382, APER=QAR ;
-10 -1 6 0.0 0.000001 ;
-10 -2 6 0.0 0.000001 ;
Q14:  QUAD.00, L=QL1, B=2.25382, APER=QAR ;
LL8:  DRIFT,   L=5.2912
Q15:  QUAD.00,  L=QL2, B=-2.64994, APER=QAR ;
LL2:  DRIFT,  L=5.2912 ;
Q16:  QUAD.00, L=QL2, B=3.00141, APER=QAR ;
LLE:  DRIFT, L=5.2912 ;
Q15:  QUAD.00,  L=QL2, B=-2.55765, APER=QAR ;
LL2:  DRIFT,  L=5.2912 ;
Q15:  QUAD.00,  L=QL2, B=3.35064, APER=QAR ;
LL8:  DRIFT,   L=5.2912
Q17:  QUAD.00  L=QL1,B=QD, APER=QAR ;
FPB5: -FIT, BETAX=0.342700,TOLER=0.0001 ;
FPB6: -FIT, ALPHAX=0.000, TOLER=0.0001 ;
FPB7: -FIT, BETAY=1.9569,TOLER=0.0001 ;
FPB8: -FIT, ALPHAY=0.00000,TOLER=0.0001
Q17:  QUAD.00  L=QL1,B=QD, APER=QAR ;
LLF:  DRIFT, L=5.2912 ;
Q18:  QUAD.00, L=QL2, B=QF, APER=QAR ;
LLG:  DRIFT, L=5.2912 ;
Q19:  QUAD.00  L=QL2,B=QD, APER=QAR ;
LLH:  DRIFT, L=5.2912 ;
Q20:  QUAD.00, L=QL2, B=QF, APER=QAR ;
LLI:  DRIFT, L=5.2912 ;
Q21:  QUAD.00  L=QL2,B=QD, APER=QAR ;
LLJ:  DRIFT, L=5.2912 ;
Q22:  QUAD.00, L=QL2, B=QF, APER=QAR ;
LLC:  DRIFT, L=5.2912 ;
Q23:  QUAD.00  L=QL2,B=QD, APER=QAR ;
LLH:  DRIFT, L=5.1412 ;
Q24:  QUAD.00, L=QL2, B=QF, APER=QAR ;
LLG:  DRIFT, L=5.2912 ;
Q19:  QUAD.00  L=QL2,B=QD, APER=QAR ;
LLH:  DRIFT, L=5.2912 ;
Q20:  QUAD.01, L=QL2, B=3.20527, APER=QAR ;
LLI:  DRIFT, L=5.2912 ;
Q21:  QUAD.01  L=QL2,B=-2.88089, APER=QAR ;
LLJ:  DRIFT, L=5.2912 ;
Q22:  QUAD.01, L=QL2, B=2.94043, APER=QAR ;
LLC:  DRIFT, L=5.2912 ;
Q23:  QUAD.01  L=QL2,B=-2.81788, APER=QAR ;
LLH:  DRIFT, L=5.1412 ;
Q24:  QUAD.00, L=QL1, B=2.25382, APER=QAR ;
FPBT: FIT, BETAX=1.6127,TOLER=0.001 ;
FPB1: FIT, ALPHAX=0.000, TOLER=0.001 ;
FPB2: FIT, BETAY=0.37418,TOLER=0.001 ;
FPB3: FIT, ALPHAY=0.0000,TOLER=0.001 ;
Q14:  QUAD.00, L=QL1, B=2.25382, APER=QAR ;
LL8:  DRIFT,   L=1.0956
```

```
DR5:  ROTAT,  ANGLE=0.0 ;
DB3:  BEND, L=3.1, ANGLE=-22.5;
DR6:  ROTAT,  ANGLE=0.0 ;
LL8:  DRIFT,   L=1.0956
Q15:  QUAD.00,  L=QL2, B=-3.11005, APER=QAR ;
LL8:  DRIFT,   L=1.0956
DR5:  ROTAT,  ANGLE=0.0 ;
DB3:  BEND, L=3.1, ANGLE=-22.5;
DR6:  ROTAT,  ANGLE=0.0 ;
LL8:  DRIFT,   L=1.0956
Q16:  QUAD.00, L=QL1, B=2.25382, APER=QAR ;
Q14:  QUAD.00, L=QL1, B=3.18336, APER=QAR ;
LL8:  DRIFT,   L=5.2912
Q15:  QUAD.00,  L=QL2, B=-3.11005, APER=QAR ;
LL8:  DRIFT,   L=5.2912
Q14:  QUAD.00, L=QL1, B=3.18336, APER=QAR ;
Q16:  QUAD.00, L=QL1, B=2.25382, APER=QAR ;
LL8:  DRIFT,   L=1.0956
DR5:  ROTAT,  ANGLE=0.0 ;
DB3:  BEND, L=3.1, ANGLE=-22.5;
DR6:  ROTAT,  ANGLE=0.0 ;
LL8:  DRIFT,   L=1.0956
Q15:  QUAD.00,  L=QL2, B=-3.11005, APER=QAR ;
LL8:  DRIFT,   L=1.0956
DR5:  ROTAT,  ANGLE=0.0 ;
DB3:  BEND, L=3.1, ANGLE=-22.5;
DR6:  ROTAT,  ANGLE=0.0 ;
LL8:  DRIFT,   L=1.0956
Q16:  QUAD.00, L=QL1, B=2.25382, APER=QAR ;
-10 -1 6 0.0 0.000001 ;
-10 -2 6 0.0 0.000001 ;
Q14:  QUAD.00, L=QL1, B=2.25382, APER=QAR ;
LL8:  DRIFT,   L=5.2912
Q15:  QUAD.00,  L=QL2, B=-2.64994, APER=QAR ;
LL2:  DRIFT,  L=5.2912 ;
Q16:  QUAD.00, L=QL2, B=3.00141, APER=QAR ;
LLE:  DRIFT, L=5.2912 ;
Q15:  QUAD.00,  L=QL2, B=-2.55765, APER=QAR ;
LL2:  DRIFT,  L=5.2912 ;
Q15:  QUAD.00,  L=QL2, B=3.35064, APER=QAR ;
LL8:  DRIFT,   L=5.2912
Q17:  QUAD.00  L=QL1,B=QD, APER=QAR ;
FPB5: -FIT, BETAX=0.342700,TOLER=0.0001 ;
FPB6: -FIT, ALPHAX=0.000, TOLER=0.0001 ;
FPB7: -FIT, BETAY=1.9569,TOLER=0.0001 ;
FPB8: -FIT, ALPHAY=0.00000,TOLER=0.0001
Q17:  QUAD.00  L=QL1,B=QD, APER=QAR ;
LLF:  DRIFT, L=5.2912 ;
Q18:  QUAD.00, L=QL2, B=QF, APER=QAR ;
LLG:  DRIFT, L=5.2912 ;
Q19:  QUAD.00  L=QL2,B=QD, APER=QAR ;
LLH:  DRIFT, L=5.2912 ;
Q20:  QUAD.00, L=QL2, B=QF, APER=QAR ;
LLI:  DRIFT, L=5.2912 ;
Q21:  QUAD.00  L=QL2,B=QD, APER=QAR ;
LLJ:  DRIFT, L=5.2912 ;
Q22:  QUAD.00, L=QL2, B=QF, APER=QAR ;
LLC:  DRIFT, L=5.2912 ;
Q23:  QUAD.00  L=QL2,B=QD, APER=QAR ;
LLH:  DRIFT, L=5.1412 ;
Q26:  QUAD.01, L=0.8, B=2.53334, APER=QAR ;
LLQ:  DRIFT, L=5.1412 ;
Q27:  QUAD.01  L=0.8,B=-2.05333, APER=QAR ;
LLR:  DRIFT, L=1.000000 ;
Q28:  QUAD.01, L=0.8, B=2.13090, APER=QAR ;
LLQ:  DRIFT, L=5.000000 ;
```

```
Q29:  QUAD.01  L=0.8,B=-1.81646, APER=QAR ;
LLR:  DRIFT, L=1.000000 ;
Q30:  QUAD.01, L=0.8, B=1.44722, APER=QAR ;
LLS:  DRIFT, L=5.000000 ;
LLT:  DRIFT, L=5.000000 ;
FPBT: FIT, BETAX=8.33000,TOLER=0.001 ;
FPB1: FIT, ALPHAX=0.000, TOLER=0.001 ;
FPB2: FIT, BETAY=1.02000,TOLER=0.001 ;
FPB3: FIT, ALPHAY=0.0000,TOLER=0.001 ;
SENTINEL
SENTINEL
Q21:  QUAD.00  L=QL2, B=QD, APER=QAR ;
LLD:  DRIFT, L=5.2912 ;
Q22:  QUAD.00, L=QL2, B=QF, APER=QAR ;
LLE:  DRIFT, L=5.2912 ;
Q23:  QUAD.00  L=QL2,B=QD, APER=QAR ;
LLF:  DRIFT, L=5.2912 ;
Q24:  QUAD.00, L=QL2, B=QF, APER=QAR ;
LLG:  DRIFT, L=5.2912 ;

Q26:  QUAD.00, L=QL2, B=QF, APER=QAR ;
LLI:  DRIFT, L=5.2912 ;
Q27:  QUAD.00  L=QL2,B=QD, APER=QAR ;
LLJ:  DRIFT, L=5.2912 ;
Q28:  QUAD.00, L=QL2, B=QF, APER=QAR ;
LLC:  DRIFT, L=5.2912 ;
Q29:  QUAD.00  L=QL2, B=QD, APER=QAR ;
LLD:  DRIFT, L=5.2912 ;
Q30:  QUAD.00, L=QL2, B=QF, APER=QAR ;
LLE:  DRIFT, L=5.2912 ;
Q31:  QUAD.00  L=QL2,B=QD, APER=QAR ;
LLF:  DRIFT, L=5.2912 ;
Q32:  QUAD.00, L=QL2, B=QF, APER=QAR ;
LLG:  DRIFT, L=5.2912 ;
Q33:  QUAD.00  L=QL2,B=QD, APER=QAR ;
LLH:  DRIFT, L=5.2912 ;
Q34:  QUAD.00, L=QL2, B=QF, APER=QAR ;
LLI:  DRIFT, L=5.2912 ;
Q35:  QUAD.00  L=QL2,B=QD, APER=QAR ;
LLJ:  DRIFT, L=5.2912 ;
Q36:  QUAD.00, L=QL2, B=QF, APER=QAR ;
LLK:  DRIFT, L=1.3966367 ;
DR5:  ROTAT,  ANGLE=0.0 ;
DB3:  BEND, L=2.5, ANGLE=5.7297795;
DR6:  ROTAT,  ANGLE=0.0 ;
LLL:  DRIFT, L=1.3966367 ;
Q37:  QUAD.0F  L=QL2,B=-2.49755, APER=QAR ;
LLM:  DRIFT, L=5.2932734 ;
Q38:  QUAD.01, L=QL2, B=3.05585, APER=QAR ;
LLN:  DRIFT, L=5.2932734 ;
Q39:  QUAD.0F L=QL2,B=-2.49755, APER=QAR ;
LL0:  DRIFT, L=1.3966367 ;
DR7:  ROTAT,  ANGLE=0.0 ;
DB4:  BEND, L=2.5, ANGLE=5.7297795;
DR8:  ROTAT,  ANGLE=0.0 ;
10 -1 6 0.0000 0.01;
10 -2 6 0.0000 0.01 ;
LLP:  DRIFT, L=1.3966367 ;

10 -1 6 0.0000 0.01;
10 -2 6 0.0000 0.01 ;

10 -1 6 0.0000 0.01;
10 -2 6 0.0000 0.01 ;

10 -1 6 0.0 0.001;
```

```
10 -2 6 0.0 0.001;
SENTINEL
SENTINEL
QD1:  QUAD.00, L=QL1, B=-2.61351, APER=QAR ;
LL1:  DRIFT,   L=5.2912 ;
QF1:  QUAD.00, L=QL2, B=2.61351, APER=QAR;
LL2:  DRIFT, L=1.3966367;
DR1:  ROTAT,  ANGLE=0.0 ;
DD1:  BEND,   L=2.500, ANGLE=-5.7297795 ;
DR2:  ROTAT,  ANGLE=0.0 ;
LL3:  DRIFT,   L=1.3966367;
QD2:  QUAD.01, L=QL2, B=-2.71351 , APER=QAR ;
LLA:   DRIFT,   L=5.2912 ;
QF2:  QUAD.01, L=QL2, B=2.71351, APER=QAR ;
LL3:  DRIFT,   L=5.2912;
QD3:  QUAD.01,  L=QL2, B=-2.71351 , APER=QAR ;
LL2:  DRIFT, L=0.5 ;
DR1:  ROTAT,  ANGLE=0.0 ;
DD1:  BEND,   L=2.500, ANGLE=-5.7297795 ;
DR2:  ROTAT,  ANGLE=0.0 ;
LL3:  DRIFT,   L=2.2912;
QF3:  QUAD.01, L=QL2, B=2.71351, APER=QAR ;
10 -1 6 0.0000 0.01;
10 -2 6 0.0000 0.01 ;

FIT, NAME=BETAX-BX0, VALUE=0.0, TOLER=0.0001;
FIT, NAME=BETAY-BY0, VALUE=0.0, TOLER=0.0001;
FIT, NAME=ALPHAX-AX0, VALUE=0.0, TOLER=0.0001;
FIT, NAME=ALPHAY-AY0, VALUE=0.0, TOLER=0.0001;
SENTINEL
SENTINEL
FPBT: FIT, BETAX=0.32359,TOLER=0.001 ;
FPB1: FIT, ALPHAX=0.43412E-06, TOLER=0.001 ;
FPB2: FIT, BETAY=1.9778,TOLER=0.001 ;
FPB3: FIT, ALPHAY=0.56272E-06,TOLER=0.001 ;
SENTINEL
SENTINEL

FIT -11. 2. 0.5 0.0001 ;
FIT -13. 4. 0.5 0.0001
FIT, NAME=BETAX-BX0, VALUE=0.0, TOLER=0.0001;
FIT, NAME=BETAY-BY0, VALUE=0.0, TOLER=0.0001;
FIT, NAME=ALPHAX-AX0, VALUE=0.0, TOLER=0.0001;
FIT, NAME=ALPHAY-AY0, VALUE=0.0, TOLER=0.0001;
SENTINEL
SENTINEL
FPBT: FIT, BETAX=0.34246,TOLER=0.001 ;
FPB1: FIT, ALPHAX=0.29096E-03, TOLER=0.001 ;
FPB2: FIT, BETAY=1.9584,TOLER=0.001 ;
FPB3: FIT, ALPHAY=-0.11298,TOLER=0.001 ;
SENTINEL
SENTINEL

Q14:  QUAD.00, L=QL2, B=QF, APER=QAR ;
LLH:  DRIFT, L=5.2912 ;
Q15:  QUAD.00  L=QL2,B=QD, APER=QAR ;
LLF:  DRIFT, L=5.2912 ;
Q16:  QUAD.00, L=QL2, B=QF, APER=QAR ;
LLH:  DRIFT, L=5.2912 ;
Q17:  QUAD.00  L=QL2, B=QD, APER=QAR ;
LLH:  DRIFT, L=5.2912 ;
Q18:  QUAD.00, L=QL2, B=QF, APER=QAR ;
LLI:  DRIFT, L=5.2912 ;
Q19:  QUAD.00  L=QL2,B=QD, APER=QAR ;
LLJ:  DRIFT, L=5.2912 ;
Q20:  QUAD.00, L=QL2, B=QF, APER=QAR ;
```

```
LLC:  DRIFT, L=5.2912 ;
Q21:  QUAD.00  L=QL2, B=QD, APER=QAR ;
LLD:  DRIFT, L=5.2912 ;
Q22:  QUAD.00, L=QL2, B=QF, APER=QAR ;
LLE:  DRIFT, L=5.2912 ;
Q23:  QUAD.00  L=QL2,B=QD, APER=QAR ;
LLF:  DRIFT, L=5.2912 ;
Q24:  QUAD.00, L=QL2, B=QF, APER=QAR ;
LLG:  DRIFT, L=5.2912 ;
Q25:  QUAD.00  L=QL2, B=QD, APER=QAR ;
LLH:  DRIFT, L=5.2912 ;
Q26:  QUAD.00, L=QL2, B=QF, APER=QAR ;
LLI:  DRIFT, L=5.2912 ;
Q27:  QUAD.00  L=QL2, B=QD, APER=QAR ;
LLJ:  DRIFT, L=5.2912 ;
Q14:  QUAD.00, L=QL2, B=QF, APER=QAR ;
LLC:  DRIFT, L=5.2912 ;
Q15:  QUAD.00  L=QL2, B=QD, APER=QAR ;
LLD:  DRIFT, L=5.2912 ;
```

6.3 Index of Design Technical Notes

6.3.1 BNL Technical Notes

No.	Author(s)	Title	Date
1	A.G. Ruggiero,et al	The NSNS Accumulator Ring	08/05/96
2	D. Raparia, et al	NSNS Ring System Design Study	10/09/96
3	L.N. Blumberg, Y.Y.Lee	H- Charge Exchange Injection into the 1 GeV NSNS Accumulator	11/01/96
4	A. Luccio, et al	Injection and RF Capture in the NSNS A Numerical Simulation in 6 Dimensions	12/05/96
5	H. Ludewig et al	NSNS Ring Systgem Design Study - Collimation and Shielding	11/01/96
6	D. Raparia, et al	The NSNS Ring to Target Beam Transport Line	10/29/96
7	A. G. Ruggiero	Space Charge and Coherent Effects in the NSNS Storage Ring	06/06/96
8	A. G. Ruggiero, M. Blaskiewicz	The Electron-Proton Effects in Intense Proton Bunches	01/15/97
9	M. Blaskiewicz, et al	RF Options for the NSNS	12/05/96
15	H. C. Hseuh	Design of the NSNS Accumulator Ring Vacuum System	02/12/97
17	R. Witkover	NSNS Ring Beam Diagnostic Instrumentation	02/14/97
18	H. Ludewig, et al	Design of the NSNS Collimator System	03/18/97
20	J. Smith	NSNS Ring and Transfer Lines Control System	04/21/97
23	A. U. Luccio	Numerical Calculation of the Tune Spread Induced by Transverse Space Charge in a Synchrotron	01/29/97
24	A. G. Ruggiero	Tuneability of the NSNS Accumulator Ring	02/12/97
25	A. G. Ruggiero	Closed Orbit Distortion and Correction in the NSNS Accumulator Ring	02/14/97
26	Y.Y Lee	The 4 Fold Symmetric Lattice for the NSNS Accumulator Ring	02/19/97
27	A. G. Ruggiero, M. Blaskiewicz	Estimate of the Longitudinal Coupling Impedance for the NSNS Accumulator Ring	04/21/97
28	A. G. Ruggiero, M. Blaskiewicz	Fast Transverse Instability in the NSNS Accumulator Ring	04/24/97
29	A. G. Ruggiero	Longitudinal Stability of the Beam Bunch in the NSNS Accumulator Ring	05/20/97
30	A. G. Ruggiero	Fast Transverse Damper for the NSNS Accumulator Ring	06/02/97
31	C. J. Gardner	Closed Orbit Distortion and Correction in the Four-Fold Symmetric NSNS Ring	04/14/97
32	S. Y. Zhang	NSNS Space Charge Effect	04/24/97
33	S. Y. Zhang	NSNS Transverse Instability	04/24/97
34	S. Y. Zhang, W.T. Weng	NSNS Transverse Microwave Instabilities	06/06/97
35	A.G.Ruggiero, M. Blaskiewicz	Electron-Proton Effects in Intense Proton Bunches Second Edition	05/12/97
36	M. Blaskiewicz, J.M. Brennan, A. Zaltsman	The NSNS RF System	05/12/97
37	C. J. Gardner	Some Notes on Tuning the NSNS Ring Lattice	08/12/97
38	J. Beebe-Wang, A.U. Luccio, R. Witkover	Simulations of SNS Accumulator Ring Beam Position Monitor Signals	11/07/97
39	C. J. Gardner	Skew Quadrupole Corrections for the SNS Ring	12/17/97
40	C. J. Gardner	Some Notes on the Placement of Correctors	12/29/97
41	C. J. Gardner	Sextupole Corrections for the SNS Ring	01/14/98
42	M. Blaskiewicz	Impedance and Stability considerations for the SNS	02/17/98
43	S. Y. Zhang, W. T. Weng	SNS Longitudinal Space Charge Effect	04/06/98
44	H. Ludewig, et al	Revised Conceptual Design for the Collimator	04/24/98
45	C.J. Liaw, Y.Y.Lee, J. Alessi,J. Tuozzolo	Maximum Temperature on the Carbon Striping Foil in the Spallation Neutron Source	06/18/98
46	M. Blaskiewicz	Impedance and Stability Considerations for the SNS: Part II	08/09/98
47	J. Smith, J. Yu, S. Kuznetsov	BNL EPICS Development System	09/16/98
48	R. Shafer	Proposal for the SNS Ring Beam Synchronous Timing System	09/21/98
49	R. Witkover	Considerations in Designing a “beam-In-Gap” Monitor for the Spallation Neutron Source	09/23/98
50	S. Y. Zhang	Secondary Electron Emission at the SNS Storage Ring Collimator	10/05/98
51	J. Mi	SNS Accumulator Ring Extraction Fast Kicker Modulator Initial Simulation	09/25/98
52	D. Raparia, J. Alessi, Y.Y. Lee, W. T. Weng	The SNS High Energy Beam Transport Line	09/20/98

No.	Author(s)	Title	Date
53	C. J. Gardner	Three-Dimensional Field Expansions in Magnets: A Primer	11/19/98
54	N. Tsoupas, J.Brodowski, Y. Y. Lee, J. Tuozzolo	Preliminary Study of the Magnetic Field of the SNS Lambertson-Type Extraction Septum Magnet	12/22/98
55	N. Tsoupas, et al	The SNS Injection Septum Magnet	12/22/98
56	J.Smith	SNS Networking at BNL	01/24/99
57	P. Thieberger	Proposed Magnetic Suppression of Secondary Electrons for the SNS Collimators	02/08/99
58	D. Raparia	Estimated Beam Loss Due to Energy Straggling Through the Charge Exchange Injection Foil	02/08/99
59	R.Connolly, P. Cameron, T. Shea, R. Witkover	Ionization Profile Monitor for SNS	03/01/99
60	R. Witkover	Considerations for the SNS Ring BLM System Design	03/01/99
61	S. Y. Zhang	SNS Storage Ring Impedances, 2-17-90	03/26/99
62	M. Kesselman	Study of Ring BCM Requirements, Parameters and Feasibility	05/20/99
63	M. Blaskiewicz, et al.	Barrier Cavities in the Brookhaven AGS	05/20/99
64	P. Thieberger, et al.	Secondary electron yields & their dependence on the angle of incidence on stainless steel surfaces for three energetic ion beams	08/18/99
65	D. Raparia, J. Alessi, Y.Y. Lee	Collimation in the HEBT	08/19/99
66	J.Wei	Preliminary Change Request for the SNS Ring Hybrid Lattice	10/12/99
67	H. Ludewig	Preliminary Estimate of Dose Following Machine Shutdown from Collimators, Vacuum Chamber Walls, and Adjacent Magnets	10/18/99
68	M. Meth, A. Zaltsman	Stability and Neutralization of the SNS RF Output Amplifier	12/15/99
69	S. Y. Zhang	SNS Ring BPM	12/15/99
70	D. Raparia, et al	Impact of the Suuperconducting Linac on the HEBT and Ring	01/14/2000
71	R. Lambiase, B. Oerter, J. Smith	Description of the Power Supply Control Scheme for the Spallation Neutron Source	02/04/2000
73	D. T. Abell	Bugs in UAL/TEAPOT Map for a Sector Bend	04/04/2000
74	S. Sathe	Report on SNS Magnet Database	04/15/2000
75	Y. Papaphilippou, N. Tsoupas	Preliminary Change Request for the Chromatic Sextupoles and Trim Quadrupole Elements of the SNS Accumulator Ring	05/30/2000 05/30/2000
76	J. Wei (Editor)	Preliminary Change Request for the SNS 1.3 GeV-Compatible Ring	05/04/2000
77	H. Ludewig, et al	Preliminary Estimates of Dose and Residual Activation of Selected Components in Ring Collimation Straight	06/06/2000 06/06/2000
78	A. V. Fedotov	Effect of Boundary Conditions at the Walls of a Beam Pipe on Present SNS Space-Charge Simulations	06/01/2000
79	J. G. Wang, S. Y. Zhang	Measurements of Coupling Impedance for the SNS Accumulator Ring	06/09/2000
80	J. Beebe-Wang, C. R. Prior	Injection Mismatch for the SNS Accumulator Ring	06/01/2000
81	J. Beebe-Wang	Oscillating Injection Painting and Related Technical Issues	06/01/2000
82	C. J.Gardner	Closed Orbit Distortion and Correction in the 248 Meter SNS Accumulator Ring Lattice	07/18/2000
83	H. Ludewig et al	Preliminary Estimates of the Residual Dose in the Vicinity of the First Doublet Following Machine Shutdown	12/1999
84	H. Hahn	On the Validity of Coupling Impedance Bench Measurements	09/05/2000
85	N. Malitsky	A Prototype of the SNS Optics Database	11/09/2000
86	A.V. Fedotov, N. Malitsky, J. Wei	Space-Charge Simulations for the Spallation Neutron Source Ring Using Unified Accelerator Libraries	01/25/2001
88	D. Davino, H. Hahn	Transverse Impedance Measurement of a Simplified Model of the SNS Extraction Kicker	03/2001
89	I. Papaphilippou, et al	Preliminary Change Request for the Low-Field Corrector Power Supplies of the SNS Ring	03/23/2001
90	G. Parzen	Choosing the Working Point in the SNS	03/05/2001
91	A.Fedotov, I. Papaphilippou, J. Wei, J.A. Holmes	Space-Charge and Resonance considerations for Choosing the SNS Ring Working Points	03/23/2001
92	Y. Papaphilippou, et al	Preliminary Change Request for the Powering of the 21Q40 and 26Q40 Focusing Arc Quadrupoles	04/02/2001
93	Y. Papaphilippou, Y. Y. Lee, N. Tsoupas, J.Wei	Preliminary Change Request for including chromaticity sextupoles in the SNS accumulator ring	04/06/2001

No.	Author(s)	Title	Date
94	N.Tsoupas, D. Raparia, Y.Y. Lee, J. Wei	Survey and Orientation of Beam-Coordinate System Near the Extraction Region of the SNS Ring	04/25/2001
95	N. Catalan-Lesheras, D. Raparia	The Collimation System of the Ring to Target Beam Transfer (RTBT) Line	07/03/2001
96	N. Tsoupas, J. Wei, C.J.Gardner, Y.Y. Lee	Sextupole Families and Optical Compensations for SNS Ring	07/17/2001
97	N. Catalan-Lasheras, D. Raparia	The Collimation System of the High Energy Beam Transfer (HEBT) Line	07/27/2001
98	G. Parzan	Electric Fields of a Uniformly Charged Elliptical Beam	08/03/2001
100	A.V. Fedotov, I. Hofmann	Half-Integer Resonance Crossing in high-Intensity Rings	09/26/2001
101	G. Parzen	Estimates of the Linear Coupling Effects	10/03/2001
102	D. Davino, H. Hahn	Measurement and Analysis of the Transverse Coupling Impedance of the SNS Extraction Kickers	10/22/2001
103	H. Hahn, D. Davino	Resistive Coatings on Layered Accelerator Structures with Rectangular Cross-Section	01/08/2002
104	M. Kesselman	Considerations for the Design of the Beam Current Monitor System for the SNS	03/05/2002
105	G. Parzen	Non-Linear Effects Due to Sextupoles	02/26/2002
106	D. Raparia	Linac Dump Optics with Window Near Quadrupoles	03/12/2002
107	D. Raparia	RTBT Collimators Re-Visisted	03/21/2002
108	D. Raparia, A. Hershcovitch	Plasma Window for SNS Target	04/03/2002
109	H. Hahn, D. Davino	SNS Extraction Kicker Magnet With Low -m Ferrite	06/28/2002
110	N. Tsoupas, et al	A Large-Aperture Narrow Quadrupole for the SNS Accumulator Ring	05/21/2002
111	G. Parzen	Guidelines for Injection Dipole Multipole	05/24/2002
112	D. Davino, J-L. Mi, N. Tsoupas	Reduced Transverse Impedance of SNS Ring Extraction Kickers	07/17/2002
113	J. Mi, J. Sandberg, A. Zhang	SNS Extraction Kicker BPFN Output Current Waveform for Low-μ Ferrite Magnet Current	07/26/2002
114	S. Tepikian, C. J. Gardner	Multipole Polarities for the SNS Accumulator Ring	07/2002
115	D. Davino, H. Hahn, M. Blaskiewicz	Coupling Impedance Measurements of the SNS RF Cavity	08/27/2002
116	R. Talman, N. Malitsky	Beam-Based BPM Alignment	

6.3.2 ORNL Ring-Related Technical Notes

No.	Author(s)	Title	Date
AP.TN13	V. Danilov et al	Closed Orbit Instability Seen as a Transition Process During and After Injection	2001
AP.TN8	J. Wei	SNS Convention on Coordinate System, Console Display, and Magnet Polarity	2001
AP.TN7	N.Catalan-Lasheras (Editor)	Expected beam losses along the SNS accelerator facility during normal operation	2001
AP.TN4	A.V.Aleksandrov	Effect of TiN Coating on SNS AR Kicker Performance	2001
AP.TN3	D.Raparia et al	Plasma Window for SNS Target	2001
AP.TN2	J. Wei (editor)	Preliminary change request for the SNS 1.3 GeV-compatible ring	2001
AP.TN1	W.Wan et al	Global Coordinates of the SNS Accelerator Complex	2001
ORNLAP.TN011	J.D. Galambos et al	ORBIT User Manual	1999
ORNLAP.TN010	D. Jeon et al	SNS accumutator ring collimator optimization with beam dynamics	1999
ORNLAP.TN009	J.D.Galambos et al	Beam profile broadening in PSR due to transverse space charge: simulation and comparison with experiment	1999
ORNLAP.TN007	J.A. Holmes et al	AN RMS Particle Core Model for Rings	1998
ORNLAP.TN006	J.A. Holmes et al	Dynamic Space Charge Models for Computational Applications in Rings	1998
ORNLAP.TN005	J.D. Galambos et al	Preliminary SNS H$^-$ injection calculations with space charge using a PIC model	1998
ORNLAP.TN004	J. A. Holmes et al	Space charge calculations in rings for uniform focusing, FODO, and doublet lattices	1998
ORNLAP.TN002	J.D. Galambos et al	Uncontrolled Ho Excited State Losses for SNS Injection	1997
ORNLAP.TN001	J.D.Galambos et al	Longitudinal Injection Studies for the ESS and SNS	1997

6.4 Abbreviations and Acronyms

3-D	three-dimensional
AAA	Advanced Accelerator Applications, LANL
ac	alternating current
AGS	Alternating Gradient Synchrotron
AHF	Advanced Hydrotest Facility, LANL
ANL	Argonne National Laboratory
BEPC	Beijing Electron Positron Collider
BIG	beam-in-gap
BNL	Brookhaven National Laboratory
BPM	beam position monitor
CERN	European Organization for Nuclear Research
cm	10^{-2} m
CNGS	CERN Neutrinos to Gran Sasso
CONCERT	Combined Neutron Centre for European Research and Technology
CPU	central processing unit
cw	continuous wave
dc	direct current
DOE	Department of Energy, US
DTL	drift-tube linac
EA	energy amplifier
e.g.	for example
EM	electromagnetic
EPICS	Experimental Physics and Industrial Control System
e-p	electron-proton
ESS	European Spallation Source
eV	electron-volt
FFAG	fixed-field alternating-focusing
FNAL	Fermi National Accelerator Laboratory
FODO	focusing/defocusing lattice structure with drift sections
FWHM	full width at half maximum

GeV	10^9 electric volts
GHz	10^9 Hertz
H	horizontal
H^-	hydrogen ion with a negative charge
H^+	hydrogen ion with a positive charge
H^0	neutral hydrogen
HEBT	high-energy beam transport
Hz	Hertz
IBS	intra-beam scattering
ICS	integrated control system
ICSWG	integrated control system working group
i.e.	namely
IGBT	insulated-gate bipolar transistor
I/O	input / output
IPM	ionization profile monitor
IPNS	Intense Pulsed Neutron Source (ANL)
ISIS	spallation neutron facility at RAL
ISR	Intersecting Storage Ring, CERN
JAERI	Japan Atomic Energy Research Institute
JHF	Japan Hadron Facility
JKJ	JAERI/KEK Joint Project
KAON	Kaon, Antiproton, Other hadron, Neutrino Factory
KEK	High Energy Accelerator Research Organization (Japan)
KEKB	KEK *B*-factory facility
keV	10^3 electric volts
kHz	10^3 Hertz
kW	10^3 Watt
L	longitudinal
LANL	Los Alamos National Laboratory
LAR	full-energy linac plus accumulator ring
LBNL	Lawrence Berkeley National Laboratory
LHC	Large Hadron Collider
linac	linear accelerator

m	meter
MeV	10^6 electric volts
MHz	10^6 Hertz
MI	Main Injector (Fermilab)
mrad	milli-radian
ms	10^{-3} second
mSv/hour	10^{-3} sievert per hour
MURA	Midwest University Research Association
MW	10^6 Watt
ns	10^{-9} second
ORNL	Oak Ridge National Laboratory
Pa	Pascal; 7.5×10^{-3} Torr
PD	proton driver
PEP-II	SLAC B-factory facility
PF	photon factory
PFN	pulse-forming network
PIC	particle in cell
PLC	programmable logic controller
ppp	particles per pulse
PS	Proton Synchrotron (CERN)
PSR	Proton Storage Ring
R&D	research and development
RAL	Rutherford-Appleton Laboratory
RCS	rapid-cycling synchrotron
RF	radio frequency
RFQ	radio-frequency quadrupole
RHIC	Relativistic Heavy Ion Collider
rms	root mean squared
RTBT	ring-to-target beam transport
SEY	secondary-emission yield
SI	(Systèm International, MKSA)

SLAC	Stanford Linear Accelerator Center
SNS	Spallation Neutron Source
SPL	Superconducting Proton Linac (CERN)
SPS	Super Proton Synchrotron (CERN)
Sv	sievert; 100 rem
V	vertical
VME	Standarized computer I/O crate
VXI	VME crate adapted for instrumentation
W	Watt
WBS	work break-down structure
Δ	difference
μm	10^{-6} meter
μs	10^{-6} second
$\sum$	summation symbol
Ω	Ohm

6.5 List of Symbols

Latin letters

a	average beam radius
a_2	skew quadrupole strength
a_i, b_i, d_i	IBS geometric factors
A_{im}	Laslett tune-shift factor
A_{s1}, A_{s2}	Lorentz stripping coefficients
b	average radius of vacuum pipe
B	magnetic field amplitude
$\tilde{B}$	magnetic field (frequency domain)
$\dot{B}$	rate of change of magnetic field
B_0	nominal guiding magnetic-field
$B_0\rho$	rigidity of a particle
B_f	ratio of average and peak proton density; $B_f \leq 1$
B_x	horizontal component of magnetic field
B_y	vertical component of magnetic field
c	speed of light
C_l	envelope-oscillation coefficient
d_w	thickness of vacuum pipe wall
D	lattice dispersion function
D^+	maximum dispersion
$D_\parallel$	longitudinal microwave-instability threshold
$D_\perp$	transverse microwave-instability threshold
dP_r/ds	power generated in a resistive loop
e	unit electric charge
$\tilde{E}$	electric field (frequency domain)
E_s	synchronous energy of the beam
E_s^{max}	proton energy corresponding to maximum secondary-emission of electrons
f_{sc}	space-charge form factor
g	gap height of dipole-magnet

g_0	space-charge geometric factor
h	rf harmonic number
h_r	height of a resistive loop
I	average beam current in ring
$\hat{I}$	peak beam current
$\tilde{I}$	beam current in frequency domain
j	$\sqrt{(-1)}$
k	excited resonance harmonics
$K_\perp$	transverse-focusing strength
$\Delta K_\perp$	deviation in transverse-focusing strength
$K_\perp^{(l)}$	strength of $2l$-th pole error
l	resonance order
L_c	FODO cell length
$\mathcal{L}_c$	IBS Coulomb logarithm
m, n	integers
m_0	rest mass of proton
m_e	rest mass of electron
M	number of lattice superperiods
N_0	number of protons per bunch
P	pressure
q	electric-charge number
r_0	classical radius of proton; $e^2/4\pi\epsilon_0 m_0 c^2$
r_e	classical radius of electron; $e^2/4\pi\epsilon_0 m_e c^2$
$\mathcal{R}$	longitudinal resistive-impedance
R_0	average radius of ring circumference
s	azimuthal displacement along ring circumference
S	longitudinal phase-space area of the bunch
s_b	center-to-center distance between subsequent bunches
$S_{\rm rms}$	rms longitudinal bunch area

t	time in laboratory frame
T_c	characteristic transition-crossing time
T_{mw}	duration time of microwave instability near transition
T_{nl}	chromatic nonlinear time near transition
V_{rf}	rf peak voltage
w_r	width of a resistive loop
x	horizontal displacement
x'	dx/ds
x_{sep}	transverse displacement at the septum
X	normalized horizontal displacement, $X \equiv x/\sqrt{\beta_x}$
X'	$dX/d\mu = (\alpha x + \beta x')/\sqrt{\beta_x}$
y	vertical displacement
y'	dy/ds
Y	normalized vertical displacement, $Y \equiv y/\sqrt{\beta_y}$
Y'	$dY/d\mu = (\alpha y + \beta y')/\sqrt{\beta_y}$
Y_{ee}	electron SEY upon electron impact
Y_{ep}	electron SEY upon proton impact
Y_{ep}^{max}	maximum electron SEY yield upon proton impact
z	longitudinal displacement
$Z_{\parallel}$	longitudinal coupling impedance
$Z_{\perp}$	transverse coupling impedance
Z_0	$(\varepsilon_0 c)^{-1} = 377$ (ohms)
$Z_{\parallel}^{\mathrm{rw}}$, $Z_{\perp}^{\mathrm{rw}}$	coupling impedances due to resistive wall
$Z_{\parallel}^{\mathrm{sc}}$, $Z_{\perp}^{\mathrm{sc}}$	coupling impedances due to space charge

Greek letters and other symbols	
$\vert\ \vert$	absolute value
$\langle\ \rangle$	average value
α_0	momentum compaction factor, $\alpha_0 = \gamma_T^2$
α_1	first-order non-linear momentum compaction factor
$\alpha_\perp$	transverse α lattice function
α_e	electron survival rate in the bunch gap
α_x	horizontal lattice function
$\alpha_{x,i}$	horizontal lattice function of injecting beam
β	relativistic factor; βc is beam velocity
β'	$d\beta/ds$
$\beta_\perp$	transverse-amplitude function
$\beta_\perp^+$	maximum transverse-amplitude function in FODO cell
$\beta_\perp^-$	minimum transverse-amplitude function in FODO cell
β_e	electron relativistic factor; $\beta_e c$ is the electron velocity
β_{kick}	transverse-amplitude function at the kicker
β_{sep}	transverse-amplitude function at the septum
β_x	horizontal-amplitude function
$\beta_{x,i}$	horizontal-amplitude function of injecting beam
β_Z	average Courant-Snyder β-function at location of impedance
γ	relativistic factor; $\gamma = (1 - \beta^2)^{-1/2}$
$\dot{\gamma}$	rate of γ variation in time
γ_T	relativistic factor corresponding to the transition energy
$\dot{\gamma}_T$	rate of γ_T variation in time during transition jump
$\gamma_{x,y}$	horizontal and vertical lattice-functions
ΔE_e	energy gained by electron
δ_s	skin depth
$\Delta p/p$	relative momentum deviation
ΔS	change in longitudinal phase-space area of the bunch
$\Delta x_0'$	change of x' due to main magnetic field

$\Delta x'_{fr}$	change of x' due to fringe field
$\Delta\mu$	betatron phase-advance
$\Delta\nu$	transverse tune shift
$\Delta\nu^{(m,n)}$	stop-band width
$\Delta\nu_{\rm sc}$	transverse incoherent space-charge tune-shift
$\Delta\nu_{x,y}$	horizontal or vertical tune-shift
$\Delta\nu_{\rm coh}$	coherent tune shift
$\epsilon_\perp$	transverse unnormalized (or geometric) emittance
$\epsilon_{\rm rms}$	rms transverse emittance
ϵ_x	horizontal unnormalized (or geometric) emittance
$\epsilon_{x,i}$	horizontal unnormalized (or geometric) emittance of injecting beam
ζ_m	multibunch electron-cloud multipacting parameter
ζ_s	single-bunch electron-cloud multipacting parameter
η	phase-slip factor
η_e	electron-neutralization factor
θ_g	grazing angle
$\theta_{\rm kick}$	transverse momentum deflection from the kicker
κ	resonance strength
λ_e	electron line density
λ_s	mean decay length due to Lorentz stripping
μ	permeability
μ_0	permeability in vacuum
μ_c	betatron phase-advance per FODO cell
ν_0	unperturbed transverse tune
ν_x	horizontal tune
ν_y	vertical tune
$\nu_{x,0}$, $\nu_{y,0}$	unperturbed horizontal- or vertical-tune
$\xi_\perp$	transverse chromaticity of the ring
ρ_m	molecular density
ρ_r	volume resistivity
σ_p	rms spread in relative momentum deviation $\Delta p/p$
$\sigma_{\rm ion}$	ionization cross section
σ_ϕ	rms spread in RF phase
ϕ	RF phase
ϕ_c	bending angle per FODO cell
ϕ_s	synchronous RF phase
ψ_x	horizontal betatron-oscillation phase
ψ_y	vertical betatron-oscillation phase
ω_e	electron bounce frequency
ω_s	synchronous angular-revolution frequency

References

[1] *Spallation Neutron Source Design Manual*, June 1998.

[2] *Preliminary Change Request for the SNS Ring Hybrid Lattice*, SNS/BNL Technical Note 66, edited by J. Wei, October 1999.

[3] Raparia, D, Alessi, J., Lee, Y.Y., Ruggiero, A.G., Soukas, A., Tuozzolo, J., Weng, W.T., Witkover, R.L., 97, NSNS/BNL Tech. Note 2.

[4] Raparia, D. 1997, NSNS/BNL Tech. Note 6.

[5] D. Raparia, et al., "The NSNS High Energy Beam Transport Line", Proc. 1997 Particle Accelerator Conference, p. 162.

[6] J. Beebe-Wang, et al., "Transverse Phase Space Painting for SNS Accumulator Ring Injection", , Proc. 1999 Particle Accelerator Conference, p. 1743.

[7] H. Grote and F. C. Iselin, "The Mad Program (Version 8.19) User's Reference Manual, CERN/SL/90-13 (AP), (CERN, Geneva, Switzerland, 1996).

[8] A. Fedotov, N. Malitsky, Y. Papaphilippou, J. Wei, and J. Holmes, PAC 2001, Paper RPAH004, (Chicago, 2001).

[9] Y. Papaphilippou, A. Fedotov, N. Malitsky, A. Shishlo, and J. Wei, PAC 2001, Paper TPPH008, (Chicago, 2001).

[10] J. Wei, J. Beebe-Wang, J. Brodowski, A. Fedotov, C. Gardner, Y. Lee, D. Raparia, V. Danilov, J. Holmes, C. Prior, G. Rees, and S. Machida, PAC 2001, Paper WPPH050, (Chicago, 2001).

[11] J. Galambos *et al*, ORBIT Users Manual, http://www.sns.gov//APGroup/Codes/Codes.htm. J. Holmes et al., Proceedings of PAC'99, p. 109 (1999).

[12] D. Davino et al., BNL/SNS Tech Note 112 (2002).

[13] H. Hahn et al., BNL/SNS Tech Note 117 (2002).

[14] S. Kurennoy, LANL Tech Memo SNS:2000-016 (2000).

[15] D. Davino et al., BNL/SNS Tech Note 115 (2002).

[16] J. Galambos et al., Proceedings of PAC'99, p. 3140 (1999).

[17] J. Holmes et al., Phys. Rev. ST AB 2, 114202 (1999).

[18] J. Beebe-Wang et al., Proceedings of EPAC'00, p.1286 (2000).

[19] A.V. Fedotov et al., Proceedings of EPAC'00, p.1289 (2000).

[20] A.V. Fedotov et al., Proceedings of PAC'01, p. 2851 (2001).

[21] A.V. Fedotov et al., Proceedings of PAC'01, p. 2848 (2001).

[22] A.V. Fedotov et al., Phys. Rev. ST AB 4, 084202 (2001).

[23] M. Blaskiewicz, Phys. Rev. ST AB 4, 044202 (2001).

[24] A.V. Fedotov and I. Hofmann, Phys. Rev. ST AB 5, 024202 (2002).

[25] N. Malitsky et al. Proceedings of EPAC'02, p. 1646 (2002).

[26] S.Y. Zhang, BNL/SNS Tech. Note 061 (1999).

[27] M. Blaskiewicz, Proceedings of PAC'99, p.1611 (1999).

[28] K. Woody et al., Proceedings of PAC'01, p. 2057 (2001).

[29] V. Danilov et al., Proceedings of PAC'01, p. 1752 (2001).

[30] D. Davino et al., Proceedings of PAC'01, p. 1838 (2001).

[31] J. Wei et al., Proceedings of EPAC'02, p. 1067 (2002)

[32] A.V. Fedotov et al., Proceedings of EPAC'02, p. 1350 (2002).

[33] D. Davino et al., Proceedings of EPAC'02, p. 1467 (2002).

[34] V. Danilov, SNS project ASAC Review,unpublished (2002).

[35] A.V. Fedotov, SNS project ASAC Review, unpublished (2002)

[36] M. Blaskiewicz, SNS project ASAC Review, unpublished (2002).

[37] H. Hahn, Phys. Rev. ST Accel. Beams 3, 122001 (2000)

[38] L.S. Walling, D.E. McMurry, D.V. Neuffer and H.A. Thiessen, Nuclear Instruments & Methods A **281**, p. 433-447 (1989).

[39] C.J. Gardner, BNL/SNS Technical Note 31, 1997; C.J. Gardner, BNL/SNS Technical Note 82, 2000.

[40] S. Mashida and Y. Shoji, AIP Conf.Proc., **377**, 160-168, 1995.

[41] Y. Shoji and H. Sato, *Nucl. Instr. Meth. Phys. Res.*, **399**, 5-10, 1997.

[42] J. Holmes, *et al.*, to be presented in PAC'2001, Chicago, 2001.

[43] C.J. Gardner, BNL/SNS Technical Note 37, 1997.

[44] Y. Papaphilippou and N. Tsoupas (eds.), BNL/SNS Technical Note 75, 2000.

[45] A.V. Fedotov, *et al.*, ICAP'00 Proceedings, Darmstadt, Germany, September 2000; A.V. Fedotov, *et al.*, BNL/SNS Technical Note 86, 2001.

[46] N. Tsoupas, *et al.*, EPAC 2000 Proceedings, Vienna, 2000.

[47] Y. Papaphilippou and D.T. Abell, EPAC 2000 Proceedings, Vienna, 2000.

[48] A. Dragt et al., MaryLie 5, Un. of Maryland, 2000.

[49] J. Jackson et al, BNL-AM-MD-303, 2001.

[50] N. Malitsky and R. Talman, AIP 391, 1996.

[51] Y. Papaphilippou, EPAC 2000, Vienna, 2000.

[52] Y. Papaphilippou, PAC 2001, Chicago, 2001.

[53] Y. Papaphilippou et al., PAC 2001, Chicago, 2001.

[54] J. Beebe-Wang, et al., EPAC 2000, Vienna, 2000.

[55] A. Fedotov et al., Halo and space-charge issues in the SNS accumulator ring, these Proceedings.

[56] J. Wei, R. Talman, Part. Accel. 55, 339, 1996; Y. Papaphilippou, J. Wei, R. Talman, Phys. Rev. E, (submitted).

[57] E. Forest, J. Milutinovic, Nucl.Inst. and Meth. A269, 474, 1988.

[58] E. Forest, *Beam Dynamics - A new attitude and framework*, Harwood Acad. Pub., Amsterdam, 1998.

[59] G.E. Lee-Whiting, Nucl.Inst. and Meth. 103, 117, 1972.

[60] M. Venturini, A. Dragt, Nucl.Inst. and Meth. A427, 387, 1999.

[61] J. Laskar, Physica D 67, 257 (1993); J. Laskar and D. Robin, Part. Acc. 54, 183 (1996).

[62] Vector Fields, Ltd, Oxford England.

[63] K.G. Steffen, *High Energy Beam Optics*, Interscience, New York, 1965.

[64] V. Danilov et al., Proceedings of PAC'01, p.1749 (2001).

[65] M. Blaskiewicz, Proceedings of EPAC'00, p. 1110 (2000).

[66] J. Wei and R. Macek, Proceedings of ECLOUD'02 Workshop (2002).

[67] M. Blaskiewicz, J.M. Brennan, Y.Y. Lee SNS tech note # 9, (1996).

[68] M. Blaskiewicz, J.M. Brennan, A. Zaltsman SNS tech note # 36, (1997).

[69] M. Blaskiewicz, J.M. Brennan, J. Brodowski, J. Delong, M. Meth, E. Onillon, A. Zaltsman , 7th European Particle Accelerator Conference,pg 1942, (2000).

[70] M. Blaskiewicz, J.M. Brennan, J. Brodowski, J. Delong, M. Meth, K. Smith, A. Zaltsman , PAC01.

[71] National Spallation Neutron Source, Conceptual Design Report, 4-64, (1997).

[72] J. Wei, 7th European Particle Accelerator Conference,pg 123, (2000).

[73] F. Pederson, IEEE, TNS, Vol. NS-22, No. 3, pg 1906, (1975).

[74] R. Garoby, Fontiers of Particle Beams: Intensity Limitations, US-CERN School on Particle Accelerators, Springer-Verlag, pg 509, (1990).

[75] D. Boussard, CERN 91-04 (1991).

[76] S. Koscielniak, TRI-DN-97 (1997) *and references therein*

[77] S.Y. Zhang, SNS Tech Note # 43 (1999).

[78] J. Wei et al., Phys. Rev. ST Accel. Beams 3, 080101 (2000).

[79] J.B. Jeanneret and T. Trenkler, "K2: A Software Package Evaluating Collimation Systems in Circular Colliders", CERN SL 94-105 AP.

[80] MCNPX Users Manual - Version 2.1.5, L.S. Waters, ed., LANL, Los Alamos, TPO-E83-G-UG-X-00001, 1999.

[81] C.M. Warsop, AIP Conf. Proc. 448.

[82] R.J. Macek, AIP Conf. Proc. 448.

[83] ANSYS Engineering Analysis of Systems, Swanson Analysis Systems Inc., 1997.